Neutron Scattering Studies of Some Unconventional Magnets



Philip G. Welch

University College

University of Oxford

A thesis submitted for the degree of

Doctor of Philosophy

Hilary 2021

Abstract

The identification and characterisation of low-dimensional and frustrated magnetic systems is an area of great importance in the field of solid-state chemistry. If we intend to design and control the magnetic properties of frustrated magnets, we must first understand the microscopic interactions responsible for the formation of these disordered magnetic phases. This is of fundamental interest due to the potential for frustrated magnets to form *e.g.* quantum spin liquid materials.

Frustrated and low-dimensional phases are not solely of fundamental interest; a number of properties have been identified as stemming directly, or indirectly, from disordered magnetic states. Correlated magnetic disorder has been implicated in the formation of, for example, high-temperature superconducting, multiferroic, and magnetocaloric systems. The analysis of neutron scattering is of pivotal importance in understanding such systems. In disordered phases, we cannot rely on Bragg peaks in neutron scattering patterns, since the long-range order is suppressed by frustration. Instead we must turn to the diffuse magnetic neutron scattering created by local, short-range, correlations.

In this thesis I present investigations of several frustrated and low-dimensional magnetic systems using a variety of neutron scattering techniques. In Chapters 3 and 4 I explore the structures of two triangular lattice antiferromagnets, $CsCoCl_3$ and the metal–organic framework $Tb(HCO_2)_3$. In Chapter 5 I present the first neutron scattering investigation of $Gd_2Pt_2O_7$; a recently reported magnetic pyrochlore system. I have employed both polarised diffuse neutron scattering and inelastic

neutron scattering measurements in order to quantify the microscopic interactions which serve to relieve the frustration, relative to other gadolinium pyrochlores. Finally, in Chapter 6, I have investigated the spin-chain compound Er_2BaNiO_5 using a combination of single-crystal neutron diffraction, and bulk magnetic and electrical property measurements.

Acknowledgements

This thesis would not have been possible without the help and support of Professor Andrew Goodwin and Dr Ross Stewart. The ever-present encouragement and drive to work on brilliant and engaging projects means that there has rarely been a dull moment over the course of this DPhil. Thank you for being great mentors and imparting some of your wisdom to me.

I also wish to extend my gratitude to all of the collaborators who have worked with me on these projects. My thanks go to: Daniel Harcombe and Paul Saines for their work on $Tb(HCO_2)_3$; Joe Paddison for his incredible support with all things related to diffuse magnetic neutron scattering, and in particular his work on $Gd_2Pt_2O_7$; Robin Perry for his synthesis of Er_2BaNiO_5 and his assistance with the synthesis of $CsCoCl_3$; Arkadiy Simonov for fruitful discussions and advice about supercell dynamics, and for his assistance in collecting single-crystal X-ray data for Er_2BaNiO_5; and Roger Johnson and Francis Chmiel for their introduction to, and assistance with, electrical measurements. Without all the beamline and support staff who have supported this research this would be a very minimalist thesis. In particular, I must thank: all of the team on WISH, namely Pascal Manuel, Fabio Orlandi, and Dimitry Khalyavin; everyone on D7, especially, Andrew Wildes, Lucile Mangin-Thro, and the ILL cryogenic support team; Matthias Gutmann and Silvia Capelli on SXD; and all of the excitations and polarised neutrons group at ISIS.

I must also thank all of the members of the Goodwin group present and past, including, but not limited to: Harry, Ella, Arianna, Simon, Emma, Johny, Emily

M, John, and Tom; Hanna, Hamish, Chloe, Ali, Phil M, Emily R, and Peter; and everyone else who has been a part of the group over the past six years. Thank you also to Ana for being an organisational genius. There are too many Part II students to mention, but you've all contributed to and helped shape this amazing group of people. Thank you all for being fantastic colleagues.

Having been in Oxford for roughly nine years now, there would be far too many people to thank them individually: "I don't know half of you half as well as I should like; and I like less than half of you half as well as you deserve." It would be remiss of me not to mention my friends from undergrad who are some of the nicest people you could ever hope to meet. It is sometimes said that it is not the destination which is the most important, but the friends we make along the way; to all the friends I have gained from the Maths and Stats departments, thank you (especially for the board games). A special mention has to go to Maria for always providing the much-needed reassurance that the difficult parts of a DPhil will all work out well in the end. I must also thank everyone in the Oxford University Karate Club for being a wonderful group of people, and especially Sensei Spiros for almost getting me to my Dan grading (if a pandemic hadn't got in the way).

I also have to thank my parents for their constant and unwavering support. You've always been there for me and believed in me, and this thesis belongs to you as much as it does to me. Finally, I have to thank my partner, Alex. I couldn't have wished to go through this strange year of pandemic and writing up with someone as kind, caring, and wonderful as you. You've been a rock for me this year, and you mean the world to me.

For my parents

Contents

1 Introduction **1**

1.1 Overview 1

1.2 Conventional magnetic order 2

1.3 Low-dimensional magnetism 20

1.4 Geometrically frustrated magnetism 28

1.5 Thesis structure and aims 40

2 Methods **42**

2.1 Scattering Techniques 42

2.2 Physical Property Measurements 61

2.3 Computational Methods 63

2.4 Synthesis 71

3 One-dimensional magnetic order in the metal-organic framework $Tb(HCO_2)_3$ **77**

3.1 Introduction 77

3.2 Results and Discussion 85

3.3 Conclusions 104

4 One-dimensional antiferromagnetism in $CsCoCl_3$ **107**

4.1 Introduction . . . 107

4.2 CsCoCl3 . . . 111

4.3 Supercell Spin Dynamics (SCSD) . . . 122

4.4 Conclusions . . . 130

5 Enhanced exchange interactions in the Heisenberg pyrochlore antiferromagnet – $Gd_2Pt_2O_7$ 132

5.1 Introduction . . . 132

5.2 Results and Discussion . . . 138

5.3 Conclusion . . . 157

6 Magnetic and electrical properties of single-crystalline spin chain compound Er_2BaNiO_5 159

6.1 Introduction . . . 159

6.2 Results and Discussion . . . 165

6.3 Conclusions . . . 184

7 Conclusion 187

Bibliography 191

Appendix A 210

A1 $Q = 0$ magnetic scattering and susceptibility . . . 211

A2 DMC grid search for $Gd_2Pt_2O_7$ . . . 214

Appendix B 214

B1 SpinW code used for the calculation of a dynamical matrix for use in supercell spin dynamics calculations 215

Appendix C **222**

C1 Python code used for supercell spin dynamics calculations 223

Chapter 1

Introduction

1.1 Overview

Features of magnetic order have been exploited for centuries in the form of lodestones and compasses, although it is only in the last century that a microscopic understanding of magnetism has been developed. Given that much of the development in the modern Anthropocene relies on the use of magnets in applications that drive the information era, continuing to further the collective understanding of magnetic systems is of great importance. As with other areas of solid-state chemistry and materials science, the focus is not solely on ordered systems; understanding and controlling disorder on the microscopic level is becoming increasingly important to further develop memory devices,[1] or to generate substitutes for increasingly scarce liquid helium coolants.[2]

Neutron scattering has long provided a method for the microscopic determination of magnetic structures. One of the earliest and most profound uses of neutron scattering was the experimental observation of antiferromagnetism in MnO.[3] In the wake of this observation, the number of magnetic materials investigated using neutrons has increased dramatically. The majority of these investigations make use of long-standing crystallographic approaches based on the magnetic symmetry of single-crystal or powder samples determined *via* the Bragg reflections of the ordered phase.

Bragg reflections allow us to understand ordered magnetic phases; however if the magnetic structure does not contain long-range order, the magnetic scattering

is dominated by non-Bragg features. Therefore we become reliant on this diffuse magnetic neutron scattering in order to analyse the magnetic structure. In this thesis I will apply a variety of neutron scattering techniques to the identification of disordered magnetic states, and the interactions from which they arise.

This Chapter is structured as follows. First I will present some phenomenological aspects of conventional magnetic order and the simple interactions that give rise to these states. This will be followed by a description of some aspects of low-dimensional magnetic order, in particular in one-dimensional chains. I will then discuss geometrically frustrated magnetism in both two- and three-dimensional space, including an overview of triangular Ising antiferromagnets and pyrochlore systems. Finally, I will present an outline of the remainder of this thesis.

1.2 Conventional magnetic order

I will begin this thesis with a phenomenological description of collective order in crystalline solids. These models are well covered in standard textbooks on the subject.[4,5]

If we first consider that a magnetic moment can be associated with a current loop, we can imagine that an orbiting electron will describe a current loop, and hence possesses a magnetic moment. This moment, $\boldsymbol{\mu}$, is defined by

$$\boldsymbol{\mu} = \gamma \mathbf{L}, \tag{1.1}$$

where $\mathbf{L}$ is the angular momentum of the electron, and γ is the gyromagnetic ratio. When dealing with an isolated electron, we can rewrite $\gamma = g\mu_{\mathrm{B}}/\hbar$, where $g \approx 2$

is the electron g-factor, μ_{B} is the Bohr magneton, and $\hbar = h/2\pi$ is the reduced Planck constant. Therefore the magnetic moment for a particle possessing only spin angular momentum, $\mathbf{S}$, becomes

$$\boldsymbol{\mu} = -\frac{g\mu_{\mathrm{B}}}{\hbar}\mathbf{S}. \tag{1.2}$$

The energy of this magnetic moment, when placed in a magnetic field, $\mathbf{B}$, is given by

$$E = -\boldsymbol{\mu} \cdot \mathbf{B}, \tag{1.3}$$

such that it is minimised when the field and the moment are aligned parallel.

When electrons are situated in the orbitals of an atom, we would, in theory, have to take into account both the orbital angular momentum of the atom and the spin angular momentum of the electron. However, if we consider a first-row transition metal, the valence electrons in the $3d$ orbitals, when situated in a crystal field, will have their orbital angular momentum "quenched" by the size of the anisotropic internal electric field. Thus, in such cases we need only consider the electron spin angular momentum. However, if the valence electrons are in $4f$ orbitals, for example, the magnitude of the spin-orbit coupling will dominate the interaction, and needs to be taken into account.

In what is known as the Curie Limit, *i.e.* $k_{\mathrm{B}}T \gg E$, the thermal population of the Zeeman levels is approximately equal, and the spin behaves in a classical fashion. This means that Equation 1.2 can be written as

$$m_{\mathrm{eff}} = g\mu_{\mathrm{B}}[S(S+1)]^{\frac{1}{2}}, \tag{1.4}$$

where we can treat the spin angular momentum vector as a simple scalar quantity. In a vacuum there is a linear relationship between $\mathbf{B}$ and another vector field, $\mathbf{H}$, given as

$$\mathbf{B} = \mu_0 \mathbf{H}. \tag{1.5}$$

In a material with magnetisation, $\mathbf{M}$, defined as the magnetic moment per unit volume, these two vector fields are no longer linearly related, with the relationship now being

$$\mathbf{B} = \mu_0 (\mathbf{H} + \mathbf{M}). \tag{1.6}$$

In the special case of a so-called linear material, it is possible to define the magnetisation as a linear response to an external magnetic field,

$$\mathbf{M} = \chi \mathbf{H}, \tag{1.7}$$

where χ is the magnetic susceptibility.

Curie's law tells us that for high temperature,

$$\chi \propto \frac{1}{T}, \tag{1.8}$$

where the proportionality constant, C, is the material-dependent Curie constant. This is itself related to the size of the magnetic moment,

$$C = \frac{\mu_0 N_\mathrm{A}}{3kT} m_\mathrm{eff}^2. \tag{1.9}$$

Therefore we can readily calculate the magnitude of the effective magnetic moment

in units of μ_B if we are able to measure the susceptibility of our material in the high temperature limit.

By dealing with materials in the high temperature limit, we are implicitly assuming that they are behaving paramagnetically. If this is not the case, then the Curie law will not hold, as we will see in Chapter 6. In a paramagnetic state, the thermal motion of the magnetic moments (spins) is sufficient to overcome the interactions between them, leading to a disordered state. In the absence of an applied field, such a system will have no bulk magnetic moment, as the random alignment and motion of the spins will serve to cancel the overall moment. Considering the susceptibility as a function of temperature, we can intuitively suggest that as a paramagnetic system is cooled, the decreasing thermal motion will cause the uncorrelated spins to develop a preference of being oriented towards the direction of the small applied field, and we would expect to see a smoothly increasing curve as the temperature is lowered. This is the classical conclusion of the Curie law.

1.2.1 Phenomenological descriptions of ordered states

Most magnetic systems with three-dimensional magnetic interactions will not remain paramagnetic at all temperatures; as thermal motion is decreased, the internal energy can fall below the level associated with the interactions between the spins. In the simplest case to visualise, this may lead to a cooperative state, where all spins are oriented in the same direction; known as ferromagnetism. This will give rise to a sharp increase in the susceptibility on cooling, which will continue to rise, as the individual ferromagnetic domains of the sample grow larger and align with the field direction.

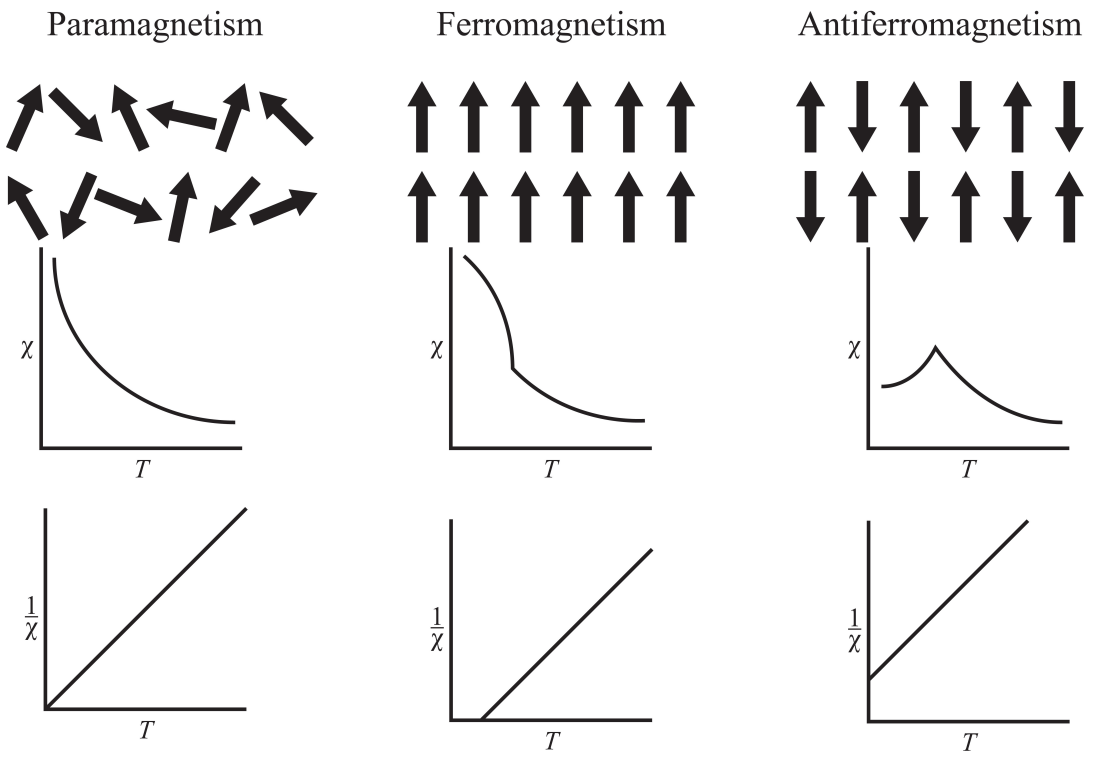


Figure 1.1: Cartoon depictions of the types of magnetic order outlined in the text, where the black arrows represent spin vectors decorating a two-dimensional grid. Each panel also shows a schematic representation of the change in susceptibility as the temperature changes. The bottom panel shows the inverse susceptibility, extrapolated from temperatures above the critical temperature, associated with these forms of magnetism. Adapted from Kittel.[6]

If, rather than promoting a completely aligned state, the interactions within the system favour anti-alignment, the system is defined as antiferromagnetic. In such a state, the preference is for each spin to be oppositely aligned with its neighbours, as shown in Figure 1.1. If the susceptibility of such a state is measured, the point at which the interactions outweigh thermal fluctuations will be marked by a reduction in susceptibility. As thermal fluctuations decrease further, the system will become perfectly anti-aligned, and will have no bulk magnetic moment. This arrangement of spins can be imagined as a pair of interpenetrating sublattices, where the bulk magnetisation of the lattices, $\mathbf{M}_x$, are opposed, such that $\mathbf{M}_1 = -\mathbf{M}_2$.

We are not, however, solely dependent upon the direction of change in the susceptibility as these critical temperatures are traversed, as in all but the simplest

cases, the exact form of the susceptibility will likely be complex enough to potentially obscure these features. Another method of extracting information from such measurements is to make use of the Curie-Weiss law for modelling the susceptibility in the paramagnetic regime:

$$\chi = \frac{C}{T - \Theta_{\mathrm{CW}}}. \tag{1.10}$$

Here C is the material dependent Curie constant, and Θ_{CW} is the Weiss temperature, describing the overall nature of the interactions. If the Weiss constant is positive, then we can say that the net interactions are ferromagnetic, when it is negative they are antiferromagnetic. Often, a plot of the inverse susceptibility, $1/\chi = \frac{1}{C}(T - \Theta_{\mathrm{CW}})$, will be used, since in the paramagnetic regime it should be linear, with a slope of $1/C$, and an x-intercept of Θ_{CW}.[6]

It is also common to perform measurements of the susceptibility at a fixed temperature, but with a variable field strength. This allows for the determination of how the magnetisation of the sample depends on the applied field strength, which is often plotted as M *vs* H. From such measurements it is possible to observe whether the magnetisation saturates with increasing field, whether there are any field induced transitions, and whether there is a component of the magnetisation which is remnant after cycling the field, requiring a coercive field to overcome. Often the large internal fields created when a ferromagnet is saturated—with all individual ferromagnetic domains oriented parallel with the field direction—cause a barrier to the magnetisation being reversed by applying a field in the opposite direction. This leads to such ferromagnets requiring large fields to be applied in the opposite direction in order to reverse the directions of the spins.

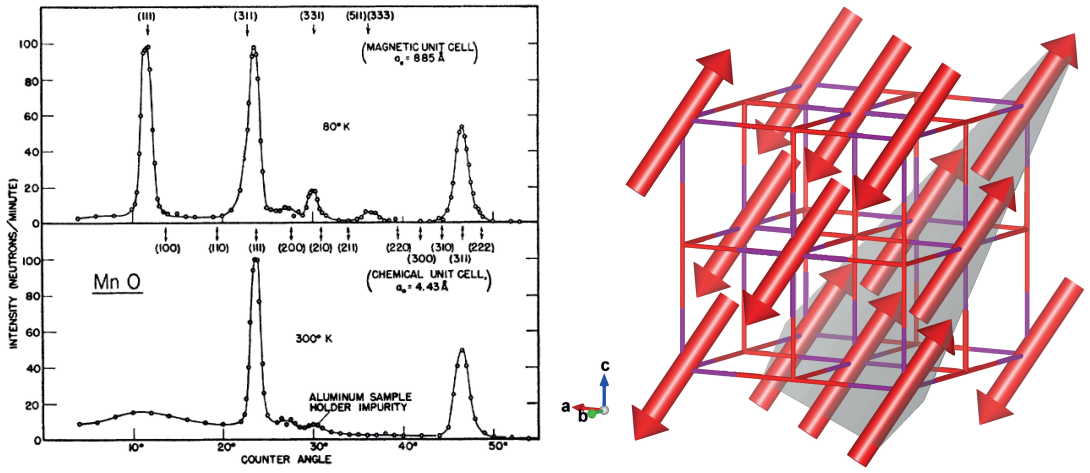


Figure 1.2: Shull and Smart's first observation of antiferromagnetic order in MnO using neutron diffraction. As shown in Ref. 3. In particular, a magnetic Bragg peak emerges near 10°, which was not observed in X-ray measurements. This peak is characteristic of the antiferromagnetic order on the face-centered cubic Mn^{2+} sublattice. The right hand panel shows the magnetic structure of MnO, (111) planes show ferromagnetic correlations, and these planes are antiferromagnetically aligned along the [111] direction.

While the existence of ferromagnetism has been exploited for centuries—for example in compasses—antiferromagnetism is a comparatively modern discovery, as the ordered phase has no net magnetic moment. Prior to Néel's discovery of antiferromagnetism,[7] a handful of authors had determined how neutron diffraction could be used to detect magnetic structures,[8–10] and the observation of antiferromagnetism in MnO in 1949 by Shull and Smart helped to establish neutron diffraction as a vital technique for determining the structures of magnetic crystals.[3] Their key result is shown in Figure 1.2.

Since the types of order outlined above are associated with periodic arrangements of spins, we can expect them to give rise to Bragg peaks in neutron diffraction, associated with the periodicity of the magnetic order. If the system is ferromagnetic then the repeating unit of the magnetic structure will be coincident with the underlying nuclear structure. Therefore the corresponding magnetic reflections occur at the nuclear reciprocal lattice points. In a ferromagnetic state, the magnetic scat-

tering appears as an extra contribution to the intensity of at the nuclear reciprocal lattice points. In the case of an antiferromagnet with only one magnetic atom per unit cell, the magnetic unit cell will be larger than the nuclear unit cell, due to the interpenetration of the second sublattice. In the diffraction pattern we would expect this to lead to peaks at the Brillouin zone boundaries. This can be seen in Figure 1.2, where the magnetic Bragg peaks associated with antiferromagnetic order in MnO occur between the nuclear Bragg reflections.

The forms of ordered magnetic states presented above are merely a small subset of all the possible ordered magnetic states; however, they are the key types that we will encounter in this thesis. It is nonetheless relevant to highlight further types of magnetic order that can arise. If we take the two sublattices of an antiferromagnet and suppose that it is composed of two different magnetic ions with different magnetic moments, a state may be formed where one sublattice is only partially cancelled by the other, leading to a reduced, but non-vanishing, bulk magnetisation. This is known as ferrimagnetism.[7,11] It is also possible to form a similar magnetic state by canting the spins so that full cancellation does not occur, as can be found in sperimagnetic compounds.[12] Similar situations can occur where ferromagnetic and antiferromagnetic materials possess an axis around which the magnetic moment can vary from site to site, such systems are termed asperomagnetic and speromagnetic, respectively.[13] As will be shown below, it is also possible to favour canted antiferromagnetic states, where components of the spin can be rotated due to antisymmetric interactions. Other ordered systems such as spin density waves and helical spin arrays are also possible, shown in Figure 1.3.

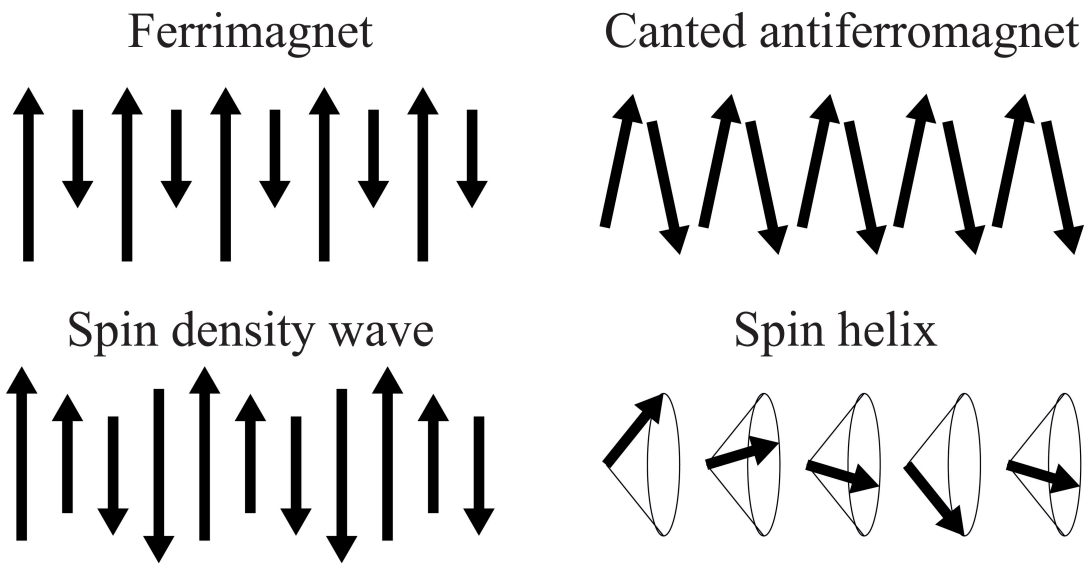


Figure 1.3: Cartoon representations of other types of magnetic order which can arise.

1.2.2 Magnetic space group notation

Descriptions of magnetic symmetry can be considered an extension of the more familiar space groups for nuclear structures.[14] The key difference lies in the application of time-reversal symmetry to the axial vectors associated with spins. The operation $1'$, for example, has the effect of reversing the direction of the axial vector. If we imagine that our axial vector can take one of two opposite values, we can describe it in terms of possessing a colour; either black or white.

The idea of colouring lattices can be used to give rise to the so-called Shubnikov groups, of which there are four types:*

I Colourless groups, which are simply the crystallographic space groups without additional symmetry.

II Grey groups, the direct product of a crystallographic space group with the time-reversal operator, which therefore possess identical and overlapping distribution of two colours.

III Black and white groups, which are the subdirect products of the crystallographic space groups with $1'$. In this specific type, the subgroup is *translationengleich* (the translations of the space group and subgroup are the same) to the space group.

IV Black and white groups where the subgroup is *klassengleich* (the point group of the subgroup and space group are the same) to the space group.

*If the time-reversal operator is used, rather than a colour-change operation, these are known as type 1, 2, $3a$, and $3b$ magnetic groups.

In total, there are 1651 magnetic space groups, now tabulated in the same fashion as the 230 crystallographic space groups.[15] There are, however, two different naming conventions, the Opechowski–Guccione (OG) notation, and the Belov–Neronova–Smirnova (BNS) notation, which differ in their notations for the *klassengleiche* black and white groups (type IV). In this case, there are some translations which are associated with spin reversal, and therefore the magnetic primitive cell is larger than the crystal primitive cell. In the OG notation, the cell labels are associated with the unit cell where magnetic order has been neglected. Therefore it is necessary to consider 'primed' operators in the space group symbol (the combination of a crystallographic operation and the time-reversal operator). The BNS notation considers that the magnetic cell is, in general, different than the paramagnetic parent, and thus we do not find 'primed' operators in BNS symbols.

In this thesis, two magnetic space groups are used. In Chapter 3 we will see that $Tb(DCO_2)_3$ has been described in the $P3m'1$ space group, while in Chapter 6 we will see that Er_2BaNiO_5 forms an ordered magnetic structure in the C_c2/c space group. In $P3m'1$, the crystallographic space group $P3m1$ has had the mirror planes combined with the time-reversal operator. This is a type III group, and the OG and BNS settings are the same. The type IV group C_c2/c is written in BNS notation (the equivalent OG notation would be $C_{2c}2/m'$). If we only consider the lattice centring, *e.g.* C_c, we have a C-centred monoclinic cell, where there is a change in colour (or time-reversal) between the base and top (in the **c**-direction) of the parent crystallographic unit cell.

1.2.3 Types of magnetic exchange

The ground states of all of these magnetic systems will be those which minimise the energy associated with the Hamiltonian for that system. In the simplest case, for example, a Hamiltonian associated with a ferromagnetic state may promote like interactions, and penalise unlike ones:

$$\mathcal{H} = J \sum_{\langle i,j \rangle} \mathbf{S}_i \cdot \mathbf{S}_j. \tag{1.11}$$

In this expression for the nearest-neighbour Heisenberg model,[16] J is the exchange constant between two spins, $\mathbf{S}_i, \mathbf{S}_j$, where the sum runs over nearest neighbour spin pairs, $\langle i, j \rangle$. In the ferromagnetic case considered, J would be required to take a negative sign in order to promote parallel alignment of spins. Equivalently, in order to promote anti-alignment of spins, a positive J is required.*

The exchange interactions characterised by J can arise due to direct overlap of the metal atomic orbitals—as may be the case in MnO, where there is debate over whether the $3d$ orbitals overlap[17,18]—or due to a mediated exchange, commonly via oxygen. This gives rise to M–O–M interactions known as superexchange, and shown in Figure 1.4.[19] Given that often it is not possible for direct overlap of orbitals to be responsible for inducing magnetic order—*e.g.* as in insulating rare-earth compounds the partially-filled $4f$ orbitals lack the necessary radial extent—superexchange can often be the dominant mechanism. Since such interactions are dependent on the crystal structure, a number of different exchange types and directions are possible,

*The convention of whether to state that a negative J is ferromagnetic varies between authors, *e.g.* $\mathcal{H} = -J \sum_{\langle i,j \rangle} \mathbf{S}_i \cdot \mathbf{S}_j$. There is no material difference between these two forms.

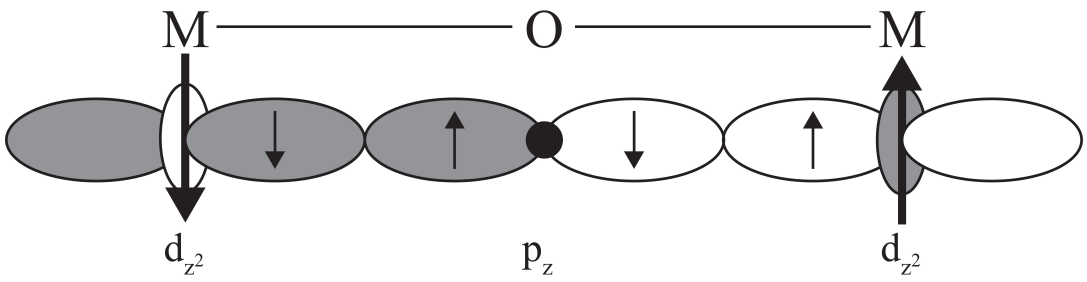


Figure 1.4: Superexchange between two metals connected by an oxygen atom.

M–O–M Angle	Orbitals	Interaction
180°	Filled ↔ Filled	Strongly AFM
180°	Filled ↔ Empty	Weakly FM
90°	Filled ↔ Filled	Weakly FM

Table 1.1: Summary of the GKA rules for octahedrally coordinated magnetic ions.

and the rules for whether these tend to be ferromagnetic or antiferromagnetic in nature are known as the Goodenough-Kanamori-Anderson (GKA) rules, summarised in Table 1.1.[20,21]

For simple systems, the Hamiltonian can easily be evaluated as the result of nearest-neighbour pairwise interactions. Unfortunately, few magnetic systems follow such simple rules. In most cases, there will be many different interactions which need to be accounted for.

In Equation 1.11 we have made the assumption that the spins are simply vectors which can terminate anywhere on the surface of a sphere. This is the Heisenberg formalism, and provides a general model for a variety of systems. There are, however, cases where the spins can only take on one of two values, *e.g.* $S = \pm 1$. These are referred to as Ising systems, and are essentially a simplification of the Heisenberg model, where each spin vector now has binary degrees-of-freedom, rather than being continuous.[22] In a system where the spins are oriented in n directions, this is known as an n-state Potts model.[23,24]

The Ising model is effectively the limit of an anisotropic Heisenberg model when the anisotropy is oriented along a single axis. This can be further generalised with the inclusion of a single-ion anisotropy term in the Hamiltonian, of the form

$$\mathcal{H}_{\mathrm{SI}} = -\Delta \sum_i S_{iz}^2, \tag{1.12}$$

where Δ captures the strength of the anisotropy, and z denotes the local anisotropy axis. Such a single-ion anisotropy is often the result of spin-orbit coupling.[25] For $\Delta > 0$ we would expect to have an 'easy-axis' anisotropy, while for $\Delta < 0$ the anisotropy would be expected to lie in a plane—so called XY anisotropy. This term can have profound implications on the magnetic properties of a system, and as we will see, is can be one of the driving forces for the formation of spin-ice phases.[26]

Another interaction which is always present in systems with unpaired electrons is a longer-range dipolar coupling,

$$\mathcal{H}_{\mathrm{dip}} = \frac{D r_1^3}{2} \sum_{i,j} \frac{\hat{\mathbf{S}}_i \cdot \hat{\mathbf{S}}_j - 3(\hat{\mathbf{S}}_i \cdot \hat{\mathbf{r}}_{ij})(\hat{\mathbf{S}}_j \cdot \hat{\mathbf{r}}_{ij})}{r_{ij}^3}, \tag{1.13}$$

where r_1 is the nearest-neighbour distance, $r_{ij} = |\mathbf{r}_{ij}|$, and $\hat{\mathbf{S}}_i$ is the unit vector of the ith spin. The interaction constant is defined by both the geometry of the lattice, and the nature of the magnetic ion,

$$D = \frac{\mu_0 (g\mu_{\mathrm{B}})^2}{4\pi r_1^3}. \tag{1.14}$$

We make use of the unit-length vector between spins i and j: $\hat{\mathbf{r}}_{ij} = (\mathbf{r}_j - \mathbf{r}_i)/|\mathbf{r}_j - \mathbf{r}_i|$, where $\mathbf{r}_i, \mathbf{r}_j$ represent the positions of the ith and jth spins, respectively. This

long-range interaction is a very important perturbation to the general Heisenberg exchange model, particularly in pyrochlore magnets with rare earth ions.[27] When dealing with transition metal systems, it is often possible to effectively ignore the dipolar interaction, as the small magnetic moments will give rise to a dipolar exchange constant significantly smaller than direct exchange interactions. By contrast, in lanthanide compounds, the dipolar and exchange terms often have comparable strengths.[28]

There are many other types of magnetic interactions which can occur in solids. RKKY interactions,[29] for example, involve coupling between spins mediated by the conduction electrons in metals. Biquadratic exchange $\propto (\mathbf{S}_i \cdot \mathbf{S}_j)^2$ is of relevance to $S = 1$ systems.[30,31] While the antisymmetric Dzyaloshinsky-Moriya (DM) interaction, where $\mathcal{H}_{\mathrm{DM}} = \mathbf{D}_{\mathrm{DM}}[\mathbf{S}_i \times \mathbf{S}_j]$,[32,33] favours spin-canting of otherwise antiferromagnetic spins, and leads to weakly ferromagnetic components. These interactions can be very important, for example, with the DM interaction being responsible for the formation of skyrmions in ferromagnetic systems.[34] We do not consider these interaction types further in this thesis.

1.2.4 Excitations

In the previous section, we have examined the ground states of ordered magnetic systems, while neglecting the excitations of those systems. Perturbing a magnetically ordered state will lead to fluctuations which are collective in nature, due to the correlations present in the structure. An analogy can be drawn to the collective vibrations of nuclear structures, known as phonons.

Phonon excitations are quantised, and there is a relationship between the frequency, ω, and wavevector, $\mathbf{Q}$, known as a dispersion relation. Those phonons where $\omega = 0$ at $\mathbf{Q} = 0$—*i.e.* where long wavelength excitations can be produced for vanishingly small energies—are known as acoustic phonons, as they are primarily responsible for sound transport through materials. These are in contrast to optic phonons, which have a finite frequency at $\mathbf{Q} = 0$.[35]

In the magnetic sense, these quantised fluctuations are known as spin waves or magnons. If we consider a one-dimensional Heisenberg ferromagnetic chain [Fig. 1.5], the dispersion relation of which is shown in Figure 1.6, flipping a single spin would create a high energy state, and the perturbation would have a very short wavelength—and is not a state which is allowed by the system as it is no longer an eigenstate. If we instead take that same perturbation, but distribute the energy along a large section of the chain, each spin needs only precess with a very small deviation from its equilibrium position. Flipping a spin in a ferromagnetic chain is associated with an overall change in spin of $\Delta S = 1$, and can therefore be induced by a neutron.[4] Examples of magnon dispersion relations are shown for ferro- and antiferromagnetic chains in Figure 1.6. These examples were generated using SpinW, and are based on a linear chain, with neighbouring Ising spins (oriented perpendicular to the chain axis) separated by 3 Å, with an interaction parameter of $J = \mp 1$, respectively. At low values of $\mathbf{Q}$, ferromagnetic and antiferromagnetic spin wave dispersions have very different forms. By following, for example, a semi-classical approach to determine the dispersion relation—as shown by *e.g.* Blundell[4]—the

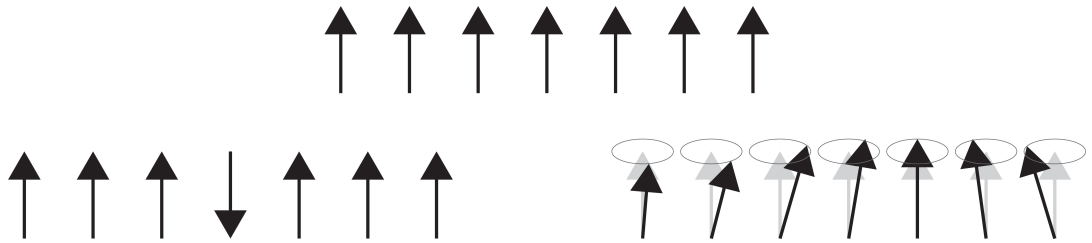


Figure 1.5: Top: Ground state of a ferromagnetic linear chain. Bottom left: A single spin is flipped relative to the ground state, at large energy cost. Bottom right: Spin wave mode, where the excitation is distributed to a periodic precession of the spin waves around their equilibrium direction (shown as the grey arrows).

dispersion relation for a ferromagnetic chain is

$$\hbar\omega = 4JS(1 - \cos(qa)). \tag{1.15}$$

In the limiting case where $qa \ll 1$,

$$\hbar\omega \approx 2JS(qa)^2, \tag{1.16}$$

and the dispersion behaves as x^2 at low $\mathbf{Q}$. For the antiferromagnetic chain,

$$\hbar\omega = 4JS|\sin(qa)|, \tag{1.17}$$

and for $qa \ll 1$,

$$\hbar\omega \approx 4JS(qa), \tag{1.18}$$

giving a linear dispersion at low $\mathbf{Q}$.

By measuring the change in energy of a neutron undergoing an inelastic scattering process, it is possible to measure the frequency and wavevector dependence of an variety of excitation types *e.g.* crystal-field levels,[36] phonon dispersion curves,[37]

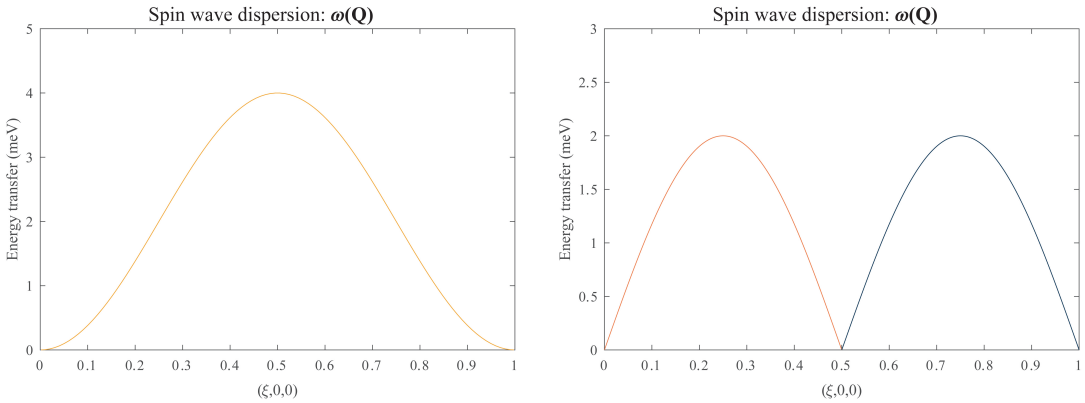


Figure 1.6: Examples of ferromagnetic **a)**, and antiferromagnetic **b)** spin-wave dispersions.

and magnon dispersion curves.[38] Since the dispersion relation for magnons can be defined by knowledge of the magnetic Hamiltonian and the magnetic structure of the system, it is, in theory, possible to extract the various exchange parameters from the inelastic scattering pattern. One method of modelling the spin wave dispersions is using SpinW,[39] which implements linear spin-wave theory (LSTW) in a MATLAB package.

The basic ingredients of LSWT are that the Hamiltonian is first expressed in terms of the raising and lowering operators for the spins. It is then mapped onto an expression for an harmonic operator *via* the Holstein-Primakoff transformation, which expresses the Hamiltonian in terms of bosonic creation and annihilation operators, $a, a^{\dagger}$.[40] The key part of LSWT is taking only those terms in a series expansion of the transformed Hamiltonian which are linear in the creation and annihilation operators. Finally, the Hamiltonian is Fourier transformed and diagonalised, producing the eigenvectors and eigenvalues of the spin waves.

LSWT is a robust method for the calculation of spin waves, however it does have a few limitations. Since it only contains terms linear in $a^{\dagger}a$ we are naturally discarding some information about the dynamics of the system, *e.g.* multi-magnon

processes. Furthermore, as implemented, the method neglects more complicated crystal-field interactions than those which give rise to a single-ion anisotropy, *e.g.* two-magnon interactions, or the creation of ghoston modes.[41,42]

Considering the interactions I have discussed above, we can start to map features of the inelastic magnetic neutron spectrum back to the exchange parameters. One simple mapping is that when there is a gap at low energy in the spectrum, this feature can often be mapped back onto the presence of spin-orbit coupling and anisotropic interaction in the Hamiltonian, as a finite amount of energy will be required to displace a spin from lying parallel with the direction of the anisotropy.[43]

1.3 Low-dimensional magnetism

Low-dimensional magnets have long provided an important playground for the discovery and exploitation of unconventional physics[44]—from the earliest studies of soliton excitations in $CsNiF_3$ (Refs. 45–47) to contemporary research into quantum information transport in spin-chain compounds.[48] The sensitivity of these systems to small perturbations results in a rich diversity of phase transitions and complex ordering phenomena. For example, the Ising spin-chain compound $Ca_3Co_2O_6$ exhibits a variety of equilibrium and non-equilibrium states,[49–51] characterised by *e.g.* long-wavelength incommensurate spin density modulations and field-induced magnetisation plateaux reminiscent of Hofstadter fractionalisation.[52,53] Arguably the strongest scientific interest from both experimental and theoretical perspectives has always been in the limit of strict 1D order.[54–59] Yet even in canonical systems such as $Ca_3Co_2O_6$ the divergence of correlation lengths along 1D spin chains is always accompanied by full 3D magnetic order.[51,60] So the realisation and experimental

characterisation of genuine partially-ordered low-dimensional magnetic phases remain an important challenge in the field.[61]

1.3.1 Overview of one-dimensional order

As a starting point, I will consider the basic properties of a one-dimensional Ising chain, for which it can be shown that at $T > 0$ there is no magnetic order. The Hamiltonian for a nearest-neighbour model is given as in Equation 1.11. If this is restricted to an Ising degree of freedom then $S_i = \pm 1$. For a ferromagnetic system ($J < 0$) with N spins, the minimum energy is given as $E = -2NJ$. If a single spin is flipped—forming two domain walls—the energy increases by $4J$. This change in energy is constant for the flipping of a contiguous block of spins of length L, as there will always be two domain walls formed at the edges of the block. If we consider the entropy gain for the creation of such domain walls, we see that for a block of L spins, the entropy gained scales as: $S = k_{\mathrm{B}} \ln L$. Therefore at finite temperature the free energy of the system can always be lowered by the insertion of domain walls, and the chain will not be ordered.[62]

The case of the antiferromagnetically coupled $S = 1/2$ Heisenberg spin-chain was solved exactly by Bethe.[63] In such a state, there is a long-range entanglement of the singlet ground state, leading to antiferromagnetic domains approaching infinite length as $T \to 0$. An excitation of a single spin from this state corresponds to a change in total spin of $\Delta S = 1$. In the Ising case, this forms two domain walls which can propagate freely along the chain without energy penalty. Since this excitation requires the production of two domain walls, it costs a finite amount of energy, and therefore there exists a gap in the excitation spectrum. If we consider each domain

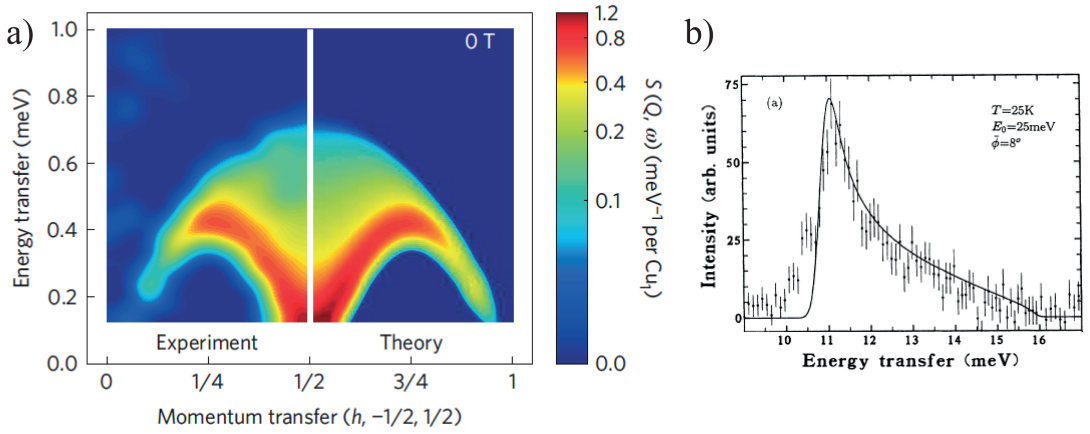


Figure 1.7: a) Measurement of the spinon continuum in $CuSO_4{\cdot}5D_2O$ across momentum and energy space, as presented by Mourigal *et al.*[65] **b)** The spinon continuum measured in $CsCoCl_3$ at 25 K. From Goff *et al.*[68]

wall separately, it can be shown that it carries $S = 1/2$, and is known as a spinon. Since each spinon carries $S = 1/2$, a neutron can only interact with a pair of these excitations, and therefore a continuum in the excitation spectrum is seen [Figure 1.7 a)].[64,65] In this case, the excitations are gapless since the dispersion relation ($\hbar\omega = \pi|J \sin(qa)|$) tends to zero as $q \to 0$.[66]

$CsCoCl_3$ has long been investigated as an $S = 1/2$ one-dimensional Ising-like antiferromagnet.[54,67–69] Chains of Co^{2+} ions lie parallel with the crystallographic c-axis, have an Ising-like anisotropy, and are antiferromagnetically coupled. Indeed, it has been found to possess solitons—effectively a propagating domain wall—which travel along the c-axis, as shown in Figure 1.7 b).

1.3.2 Haldane chains

In 1983, Haldane proposed that there should be a difference between the excitations of chains with $S = 1/2$ and $S = 1$.[70] As outlined above, $S = 1/2$ antiferromagnetic spin-chains—unless they possess perfect Ising anisotropy—will show gapless excitations. However, Haldane's conjecture was that those chains with $S = 1$ should

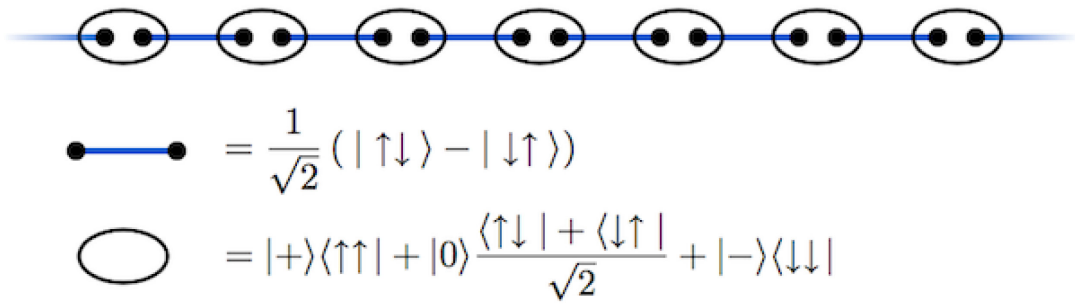


Figure 1.8: The AKLT ground state of an $S = 1$ chain. The blue bonds indicate where an $S = 0$ state is formed from the two $S = 1/2$ components of the $S = 1$ chain, shown in the ovals. Image used under Creative Commons CC0 1.0 license.

have a gap in their magnetic excitation spectrum. This is due to the spins forming a singlet ground state, which has an excitation gap to the excited state. The first soluble model of an $S = 1$ spin chain was proposed by Affleck, Kennedy, Lieb, and Tasaki.[71] The AKLT model proposes that each each $S = 1$ site can be constructed from two $S = 1/2$ degrees of freedom, which, in turn, couple into an $S = 0$ state, which behaves as a valence bond solid [Fig. 1.8].

Various compounds have been investigated as potential Haldane chains, with two of the earliest being $Ni(C_2H_8N_2)_2NO_2ClO_4$ (NENP),[72,73] and Y_2BaNiO_5.[74,75] In both cases Ni^{2+} forms $S = 1$ antiferromagnetic chains, and inelastic neutron scattering shows that there is an energy gap [Figure 1.9], as predicted by Haldane. Y_2BaNiO_5, especially, has been studied extensively with regards to substitution of non-magnetic yttrium with *e.g.* neodymium,[75] or substituting magnetic Ni^{2+} with nonmagnetic Zn^{2+} in order to induce chain terminations.[76]

1.3.3 Overview of two-dimensional systems

Two-dimensional magnets also exhibit a range of unusual physics. One clear distinction from the 1D case is that long-range order is possible in 2D. Consider a 2D system with Ising anisotropy and ferromagnetic interactions. If we assume that

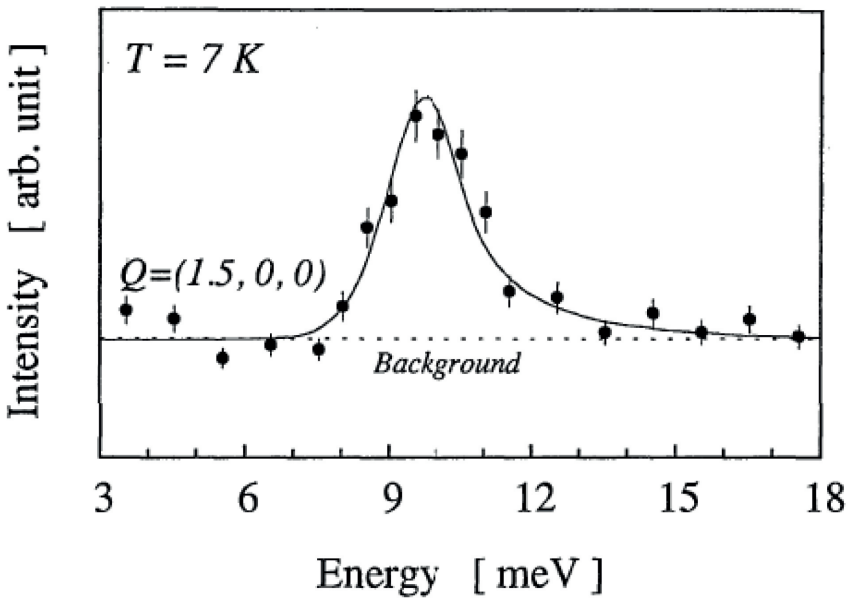


Figure 1.9: Inelastic neutron scattering data at constant-**Q**, showing the Haldane gap of 9.6 meV. Presented by Yokoo *et al.*[74]

there exists a domain of flipped spins, this time with a perimeter of L spins, the energy of the system will be $E = E_0 + 2JL$. The energy now depends on L, and there will be $\Sigma \sim c^L$ possible configurations (where $2 < c < 3$). The free energy of the system now has the form $F = E_0 + 2JL - TL \ln c$. Therefore, in the case that $T < \dfrac{2J}{\ln c}$, we would expect a transition to the fully aligned state.[77] Hence the 2D Ising FM(AFM) has the potential order at low temperature.

If we instead consider an XY 2D ferromagnet—*i.e.* where continuous rotation of the spins in the xy-plane is allowed—the behaviour is very different. The Mermin-Wagner theorem states that for $T > 0$ there are no phases which break the continuous symmetry—*i.e.* which order—as the correlation function at sufficiently large distances will decay to zero, and there is no long-range order.[62] There is, however, a difference in the scaling of the correlation function between low and high temperatures. At low temperature there is a power-law dependence, whereas at high temperature, the correlation function decays exponentially.

It is often possible for a 2D XY system to lower its energy by forming vortex pairs, where the spin vectors show a continuous rotation in the plane around a point, due to the gain in entropy associated with them. At high temperature, these vortex pairs are deconfined from each other, and able to move through the 2D plane. At low temperature it was found that these vortex pairs could form a tightly bound state. The works of Berezinskii, Kosterlitz, and Thouless, determined that despite the lack of spontaneous symmetry-breaking in a 2D XY system, a phase transition can be seen between the confined and deconfined vortex states, now known as the Berezinskii–Kosterlitz–Thouless (BKT) transition.[78,79] The work on these topologically protected phase transitions was awarded the Nobel prize in 2016. BKT transitions have been implicated in a number of different systems, including in superconducting states,[80] thin magnetic films,[81] Josephson junction arrays,[82] and superfluid phases.[83]

Finally, we will also take a brief overview of 2D systems composed of triangular motifs, which will be explored in more detail in the following section. A key observation of 2D Heisenberg (or XY) antiferromagnets on triangular lattices (with no external field) is that there exists a unique ground state, known as a 120° structure [Fig. 1.10].[84]

Such systems have also provoked a substantial amount of interest due to their magnetic-field-induced transitions,[85] which give rise to frustrated phases, as the spins can no longer be maximally opposed in the 2D plane. Such phases, when a DM interaction is included, have also been found to form skyrmion crystals.[86]

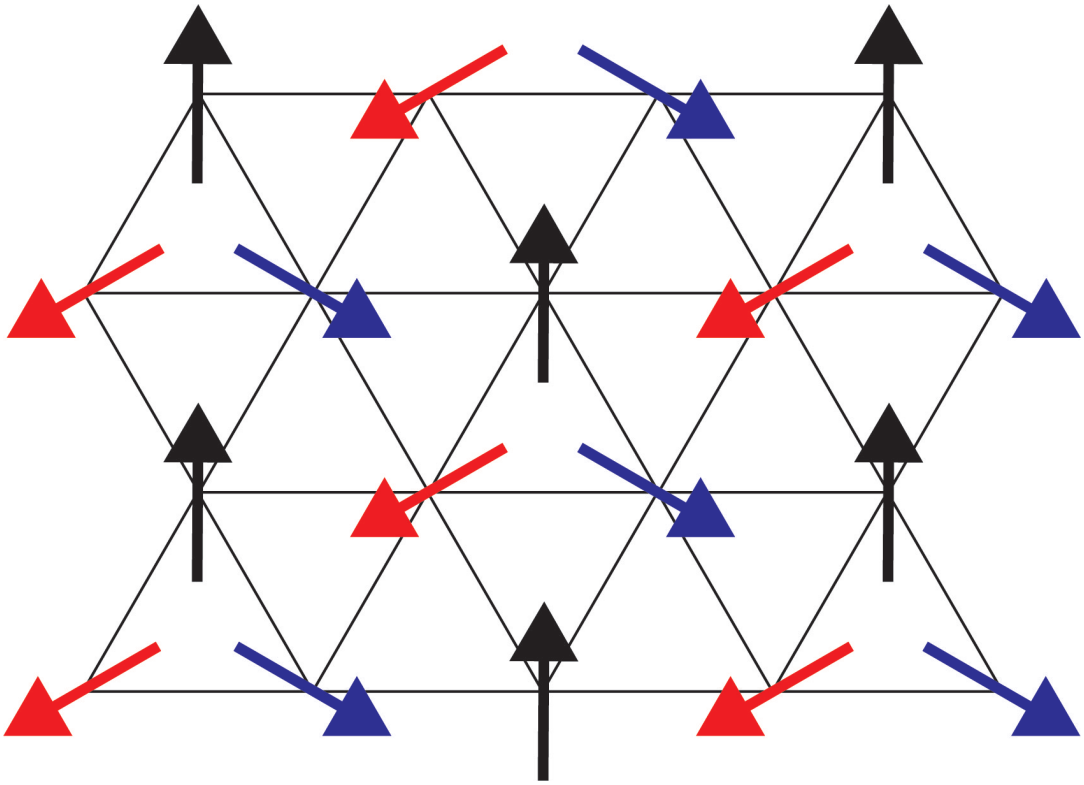


Figure 1.10: 120° order in the Heisenberg triangular lattice antiferromagnet.

1.3.4 Metal-organic frameworks as hosts of low dimensional order

Since most of the structures discussed above can be found in traditional inorganic compounds, it can be a particular challenge to construct systems where the required structural and magnetic features coincide. While it is possible to use well established rules to tune structures in order to create certain states—such as using a chiral lattice with ferromagnetic and DM interactions to create a host for skyrmions[87]—the interplay of lattice geometry, magnetic interactions, and the appropriate degrees of freedom can be difficult to design. One way to solve this challenge is to combine the established design rules of metal-organic framework (MOF) chemistry with transition-metal or rare-earth ions.

A simplified view of MOF design is to suppose that the metal ions used act as nodes, while organic motifs act as linkers to form particular structures. A canonical example is MOF-5 where Zn_4O clusters are linked by linear 1,4-benzodicarboxylate ions (BDC^{2-}, $C_8H_4O_4^{2-}$) into a cubic structure, as shown in Figure 1.11.[88–90] Since historically MOF chemistry has focused on porosity and gas uptake properties, tuning the structures is common practice.[91] Thus it is possible to design systems with chains,[92] sheets,[93] ladders,[94] or more complex 3D structures.[95]

The scope for geometric control of MOF design allows the materials chemist to introduce particular magnetic interactions that favour unconventional magnetic order. For example, it may be possible to create antiferromagnetic chains,[97] design 2D magnetic structures,[98] use host–guest interactions to induce spin crossover effects,[99] and host Kitaev spin liquid interactions.[100]

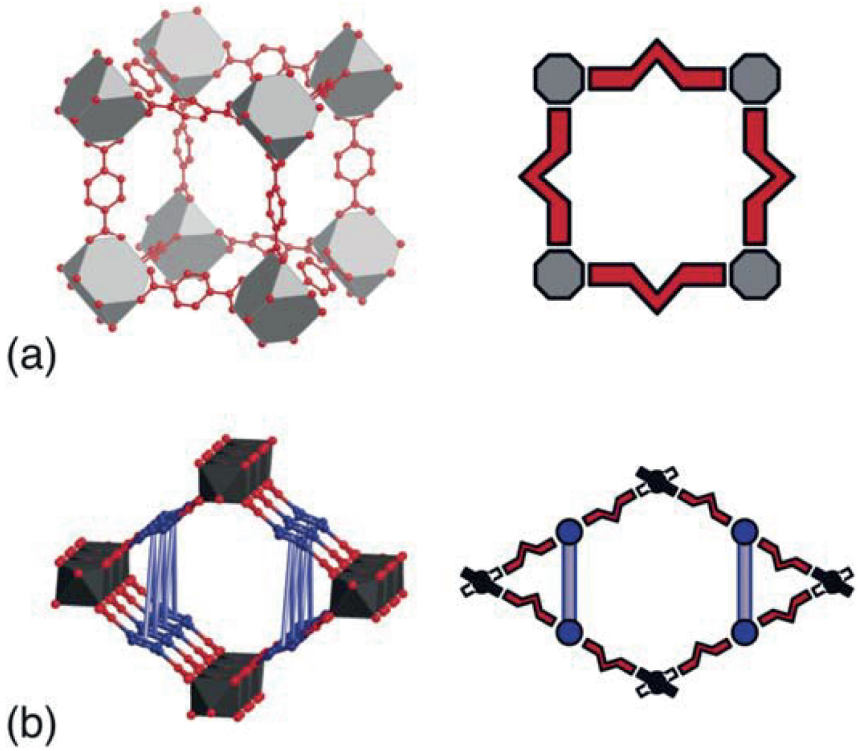


Figure 1.11: Schematic representations of MOF-5, **a)**, and MIL-53, **b)**, where we see that MOFs may be thought of as being constructed of metal nodes and organic linkers. Reproduced from Ogborn *et al.*[96]

1.4 Geometrically frustrated magnetism

Geometrical magnetic frustration is commonly defined as the inability of a magnetic system to satisfy all magnetic interactions simultaneously.[101] The most recognisable example of this arises when Ising spins are placed on the vertices of an equilateral triangle and have nearest-neighbour antiferromagnetic interactions. It is straightforward to align two spins opposite to each other, however the third spin will then not satisfactorily anti-align with both of the other spins, leading to a degeneracy in the system's ground state. Frustration tends to lead to a suppression of magnetic order below the temperature scale determined by the Weiss temperature, and we can define a frustration parameter $f = \frac{|\Theta_{\mathrm{CW}}|}{T_{\mathrm{N}}}$, describing the suppression of the ordering temperature.[101]

1.4.1 Triangular lattice antiferromagnets

As I have discussed above, certain geometries of magnets are particularly good at hosting frustrated magnetic interactions. If we restrict ourselves to two dimensions, it is generally systems containing triangular motifs which exhibit the most frustration.

We have already seen that when spins on an edge sharing triangular network have XY or Heisenberg degrees of freedom, then it is possible to form a unique, 120°, ground state.[102] If, however, there is a strong Ising-like anisotropy, then the system can be described as a triangular Ising antiferromagnet (TIA). In 1950, Wannier derived the statistical mechanical properties of an antiferromagnetic triangular Ising net, as part on an investigation into the non-trivial aspects of antiferromagnetism.[103] It was determined that such as system does not feature a long-range ordered ground state, and that there is a residual entropy at absolute zero. Keen and Goodwin have given an overview of some the types of systems which have been described as analogues of TIA models.[104] It has been determined that in the ground state of the TIA system, there is a local, short-range, order, but long-range disorder.[105] Each triangular unit has a 'two-up-one-down/two-down-one-up' or 'no three alike' arrangement of spins, but over the 2D plane the system is disordered, as shown in Figure 1.12.

1.4.2 Magnetic Pyrochlores

Some of the most studied magnetic systems which are frustrated over three-dimensional space form on the pyrochlore lattice.[106] The mineral known as pyrochlore, $(Na,Ca)_2Nb_2O_6(OH,F)$, was originally described in the early 19th cen-

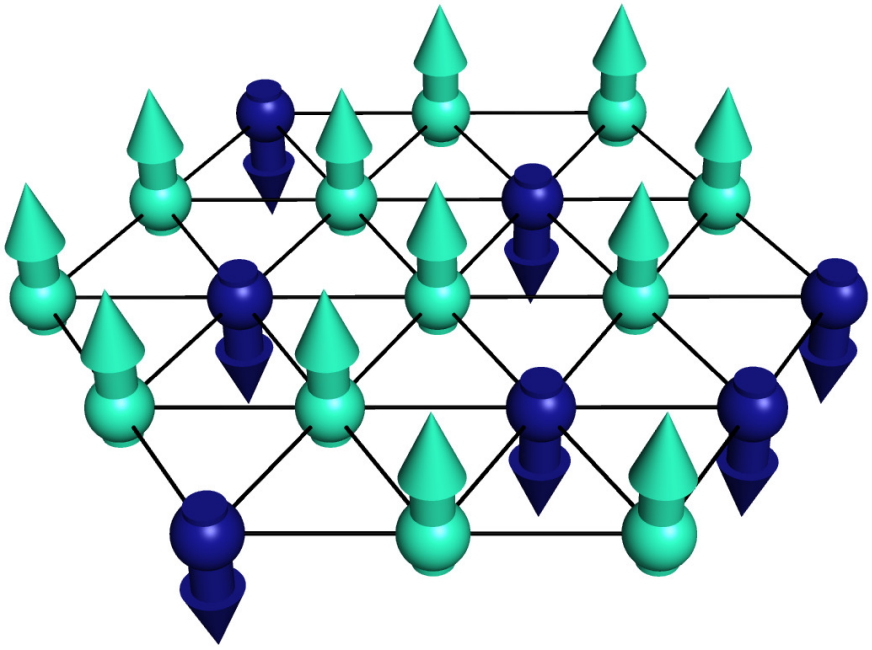


Figure 1.12: A possible arrangement of spins within a TIA system, where for each triangular unit there are two spins in one orientation, and one pointing in the opposite direction.

tury[107] and the structure was defined in the early 20th century.[108] The name now more generally refers to systems of the form $A_2^{3+}B_2^{4+}O_7$. Structurally, pyrochlores form networks of corner-sharing tetrahedra, usually in the cubic $Fd\bar{3}m$ space group, as shown in Figure 1.14 a). This structure is the medial lattice of the diamond lattice, *i.e.* the centres of the tetrahedra in a pyrochlore describe the diamond structure. In this thesis, I will restrict discussion to pyrochlore systems containing magnetically-active A or B ions, examples of which are shown in Figure 1.13.

Within the subset of magnetic pyrochlore oxides, there is still a large variety of magnetic structures which can be formed. Not only can we form long-range ordered structures, but also spin-glass, spin-liquid, and spin-ice phases.[106,109] All of these phases arise due to a variety of different effects, with the frustration of the magnetic interactions being one of the key drivers. I will briefly review the different types

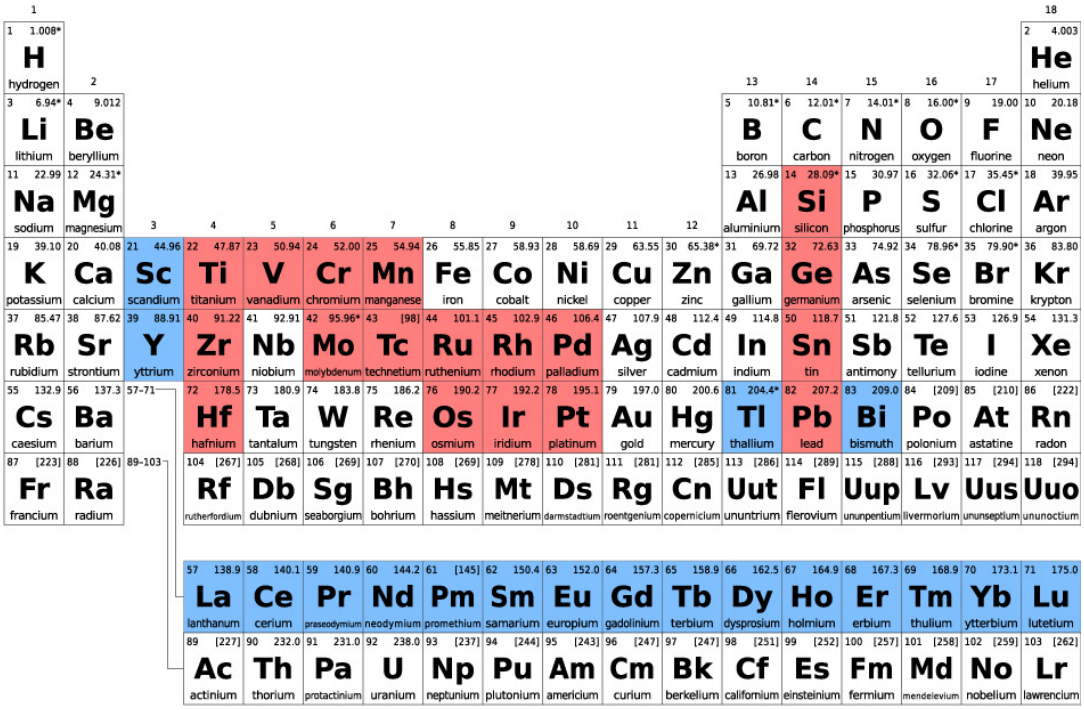


Figure 1.13: Depiction of the variety of ions which can form pyrochlore structures, with the A^{3+} ions shown in blue, and the B^{4+} ions shown in red. Adapted from Hallas *et al.*[109]

of pyrochlore systems, and the driving forces of their formation, before focusing on those pyrochlores which form long-range ordered magnetic structures, as they are the most relevant to this thesis.

Arguably the most famous magnetic state adopted by some pyrochlore magnets is the "spin-ice" phase.[110] The name of this phase arises due to Anderson's suggestion that the ordering of these spin systems was analogous to the orientations of hydrogen bonds in cubic ice-VII.[111] In the ice structure in question, the short covalent O–H bonds and longer O...H hydrogen bonds are oriented towards the corners of a tetrahedron, such that each tetrahedron has two short covalent bonds, and two long hydrogen bonds. In the spin-ice structure, this is reflected in each pyrochlore tetrahedron hosting two spins oriented towards the centre of it, and two oriented towards the centres of two adjacent tetrahedra, as shown in Figure 1.14 b).

The simplest model for this type of system involves the ferromagnetic coupling of spins with a strong anisotropy directing them to lie parallel to the local-$\langle 111 \rangle$ directions for each tetrahedron. The lowest energy state for each tetrahedron is six-fold degenerate, and it is this degeneracy which gives rise to frustration in a ferromagnetic material. The first example of this was shown in $Ho_2Ti_2O_7$.[112] In this system, the dipolar coupling and exchange strengths are comparable. It is a peculiarity of the pyrochlore lattice that the long-range dipolar interactions are dominated by the nearest-neighbour term, which can be reformatted as an effective exchange interaction. Therefore it is possible to realise an effectively ferromagnetic interaction with an antiferromagnetic nearest-neighbour exchange.[110] For example, in $Ho_2Ti_2O_7$, $J_{\mathrm{nn}} = 0.52\,\mathrm{K}$, while the dipolar interaction $D = -2.35\,\mathrm{K}$, giving rise to an effective, ferromagnetic, $J_{\mathrm{eff}} = -1.83\,\mathrm{K}$.[110] The spin-ice phase may also emerge

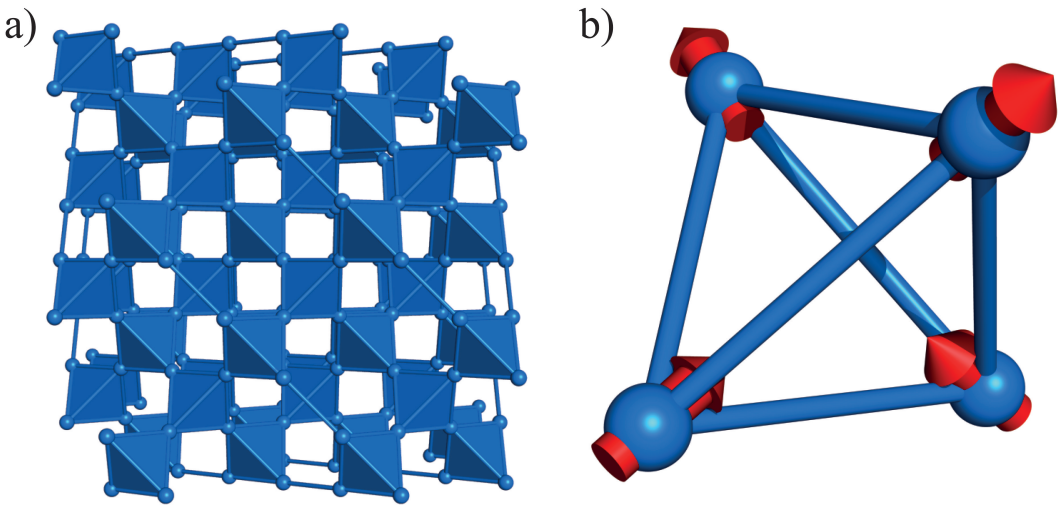


Figure 1.14: a) The pyrochlore structure of corner sharing tetrahedra (the A and B sites form two interpenetrated networks of this type). **b)** The spin-ice ground state, 'two-in-two-out', structure, shown here on a single tetrahedral unit of the pyrochlore net.

in systems with Heisenberg spins, *i.e.* away from the strict Ising limit.[113]

Those pyrochlores which form long-range ordered phases will often possess specific interactions which are capable of relieving the frustration inherent within the corner-sharing tetrahedra. One example of this is the promotion of order by long-range dipolar interactions, as proposed by Palmer and Chalker.[114] Taking this addition to the nearest-neighbour interactions in isolation, they find that order along $\mathbf{k} = (000)$ becomes favoured at certain ratios of the nearest-neighbour and dipolar exchanges.

There are several well studied examples of magnetic pyrochlores which display a transition, at finite temperature, into long-range ordered states. These include the gadolinium pyrochlores $Gd_2Ti_2O_7$[115–117] and $Gd_2Sn_2O_7$,[118,119] as well as $Er_2Ti_2O_7$,[120,121] $Tb_2Sn_2O_7$,[122–124] and a number of rare-earth ruthenates. Within the systems which order at low temperatures, there is still a great deal of diversity in how they order. As demonstrated by Wills *et al.*[119] even within structures with $\mathbf{k} = (000)$ many irreducible representations are possible [Fig. 1.15]. They also

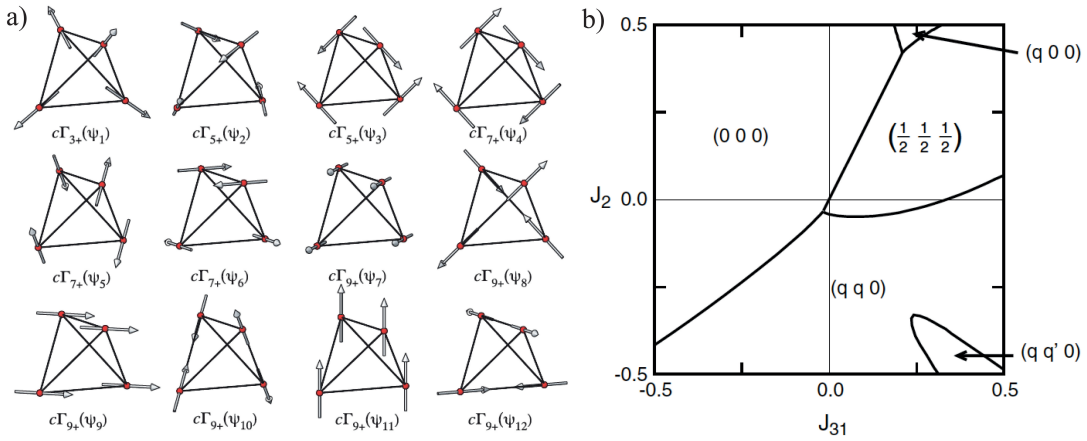


Figure 1.15: **a)** The magnetic structure basis vectors associated with a $\mathbf{k} = (000)$ pyrochlore ground state. **b)** The instability wavevectors for different ratios of next-nearest and third-neighbour exchange constants, for antiferromagnetic, dipolar, pyrochlores. Both panels presented by Wills *et al.*[119]

determine that depending on the ratios of further neighbour exchange constants, different magnetic propagation vectors become favoured.

Fixing the A-site cation and varying the B-site cation can also lead to stark differences in how pyrochlores order. For example, in the two gadolinium-based pyrochlores $Gd_2Ti_2O_7$ (GTO) and $Gd_2Sn_2O_7$ (GSO), there is a significant difference in the ground state configuration. In GSO, there is a phase transition at $T_c = 1\,\mathrm{K}$ into the $\mathbf{k} = (000)$, 'Palmer-Chalker' state, while in GTO, there are two successive transitions at $T_{c1} = 1\,\mathrm{K}$ and $T_{c2} = 0.7\,\mathrm{K}$. This low temperature state has been shown to involve two propagation vectors, and the ordered moment shows complex modulations.[125] In both cases, Hamiltonains involving three near-neighbour interactions, dipolar coupling, and single-ion anisotropy, have been used, with the exchange constants shown in Table 1.2.

1.4.3 Overview of other key frustrated systems

Further to triangular lattice antiferromagnets and pyrochlores, there are a number of other systems which display the hallmarks of frustrated magnetism. One

	J_1	J_2	J_{3b}	D	Δ
GTO	4.80	0.192	0	0.653	1.500
GSO	3.91	0	−0.02	0.575	1.715

Table 1.2: Comparison of the interaction parameters for both GTO and GSO. All values are given in K, and correspond to the 'classical' values—*i.e.* modified by $S(S+1)$ or S^2—as presented in Chapter 5.

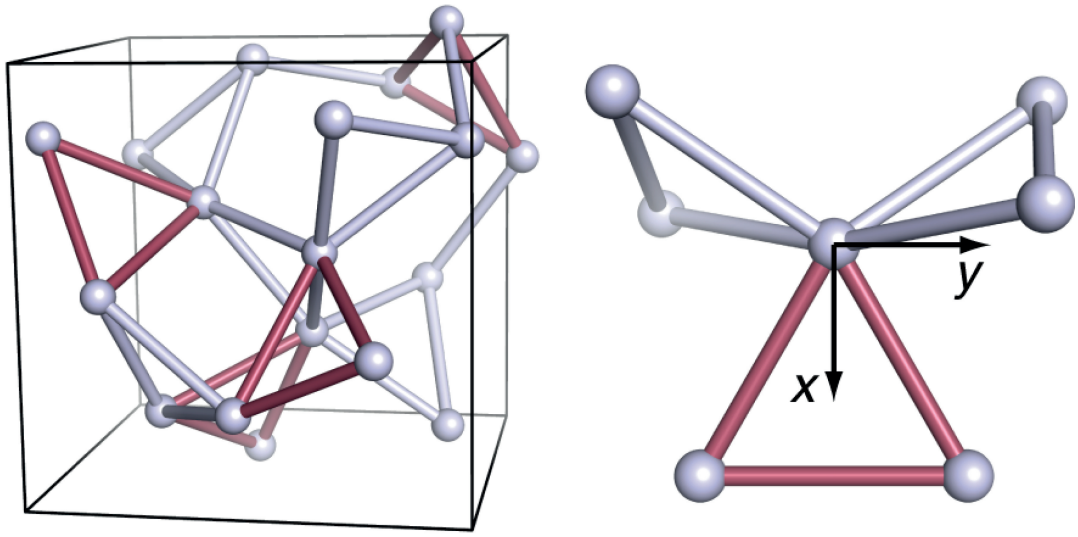


Figure 1.16: Vertex sharing triangle arrangement in β-Mn. The local Mn environment is made up of 'windmill' units, as shown in the right panel. Figure from Paddison *et al.*[130]

way of arranging triangular units in three dimensions is to create a structure in the 'hyperkagome' family.[126] In such structures there are triangular units which form a vertex-sharing network in three dimensions. One pertinent example of a hyperkagome structure is β-Mn, which has received interest as the only known elemental quantum spin liquid.[127] β-Mn itself features antiferromagnetic spin-fluctuations and behaves as a non-Fermi liquid.[128,129] There has also been a significant interest in doped forms of β-Mn, for example with cobalt, which produces an emergent, frustrated, spin structure, mimicking the triangular lattice antiferromagnet, shown in Figure 1.16.[130]

Another compound in which vertex sharing triangles give rise to frustration is gadolinium gallium garnet (GGG, $Gd_3Ga_5O_{12}$). The interactions of this system

are of great interest from a fundamental standpoint, as there is a 'hidden-order' transition as a result of cooperative interactions of 10-spin loops.[131] GGG has also seen practical use as a magnetic refrigerant due to producing a large magnetocaloric effect (MCE) at low temperature.[132]

Frustration is also seen in honeycomb lattices, such as Na_2IrO_3.[133,134] This system has been proposed to possess a Kitaev-Heisenberg model,[135] where bond-dependent interactions and nearest-neighbour interactions are in competition with each other, and the relative magnitude of the interaction terms gives rise to different ground states, as shown in Figure 1.17.

1.4.4 Frustrated magnets as magnetocalorics

The magnetocaloric effect allows for heat to be removed from a system by the cycling of a magnetic field. An MCE material is first placed in a strong magnetic field, saturating the spins parallel to the field direction. The heat produced during this transition is removed (*e.g.* by liquid helium) while the field is held constant. Removal of the magnetic field under insulating conditions allows the spins to disorder and gain entropy, causing a loss of thermal energy, thus causing the sample to cool down, allowing it to remove heat from the target of the refrigeration. This returns the refrigerant back to the original state, and the cycle can be repeated. An example of this cycle is shown in Figure 1.18. Such materials may play an important future role due to the rising cost of helium for refrigeration.

Since the MCE relies upon the disordering of spins at zero field and low temperature, materials which lack order under these conditions are required. Hence it is hypothesised that frustrated magnets will play a large part in this field.[136–138]

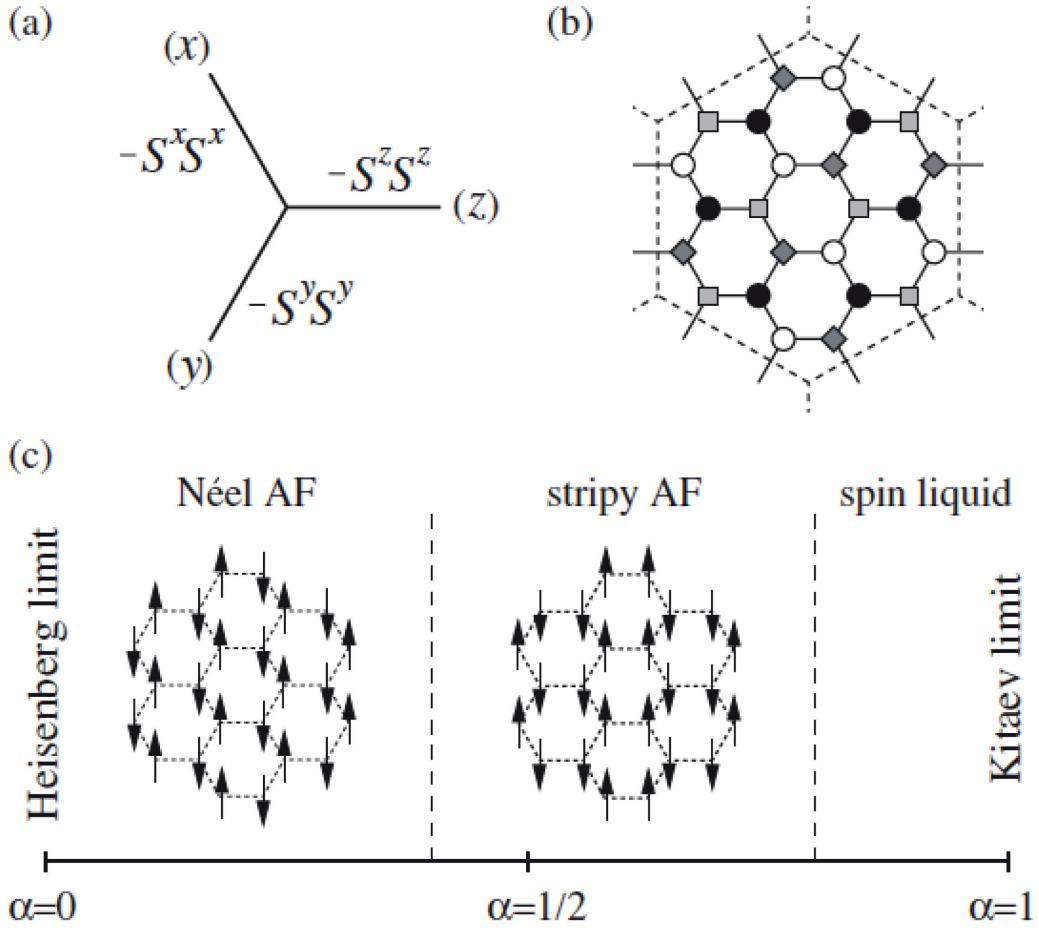


Figure 1.17: **a)** The three directional bonds in the Kitaev system. **b)** An example of a four-sublattice model on the honeycomb network. **c)** A schematic phase diagram for the Kitaev-Heisenberg model, where, as α increases, the Kitaev contribution increases, and the Heisenberg contribution decreases. Figure from Chaloupka *et al.*[135]

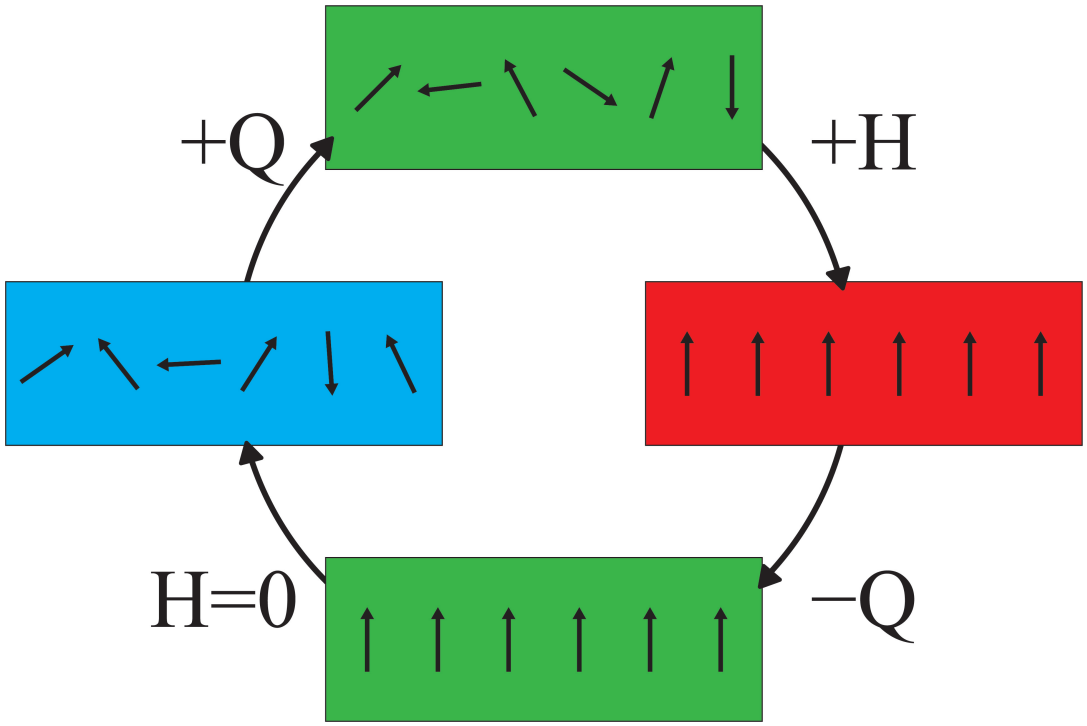


Figure 1.18: Cartoon representation of a magnetocaloric cooling cycle. Starting from the paramagnetic state shown at the top, spins are first ordered by an applied magnetic field, $+\mathbf{H}$, causing the temperature to increase. This extra heat is removed by an external coolant, $-Q$. The magnetic field is then removed ($\mathbf{H} = 0$) and the spins disorder, gaining entropy and cooling the system. This allows heat to be transferred from the target of the cooling, which is gained by the MCE material, $+Q$.

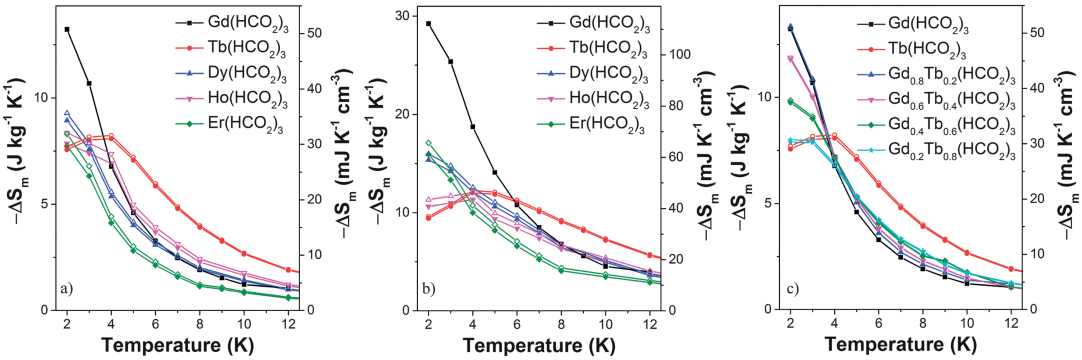


Figure 1.19: Change in magnetic entropy for the $Ln(\mathrm{HCO_2})_3$ series for **a)** $\Delta B = 1 - 0\,\mathrm{T}$, **b)** $\Delta B = 2 - 0\,\mathrm{T}$. **c)** Shows the change for the $\mathrm{Gd}_{1-x}\mathrm{Tb}_x(\mathrm{HCO_2})_3$ series, with $\Delta B = 1 - 0\,\mathrm{T}$.

In particular, the lanthanide formates are of interest to this thesis. As demonstrated by Saines *et al.*, most of the $\mathrm{Ln(HCO_2)_3}$ series crystallises in a rhombohedral, $R3m$, structure.[137] This distributes chains of $\mathrm{Ln^{3+}}$ in the *ab*-plane, forming an effective triangular lattice. One method for the measurement of the MCE is to use the Maxwell relation, $\Delta S_\mathrm{m}(T) = \int [\partial M(T,B)/\partial T]_B \mathrm{d}B$, to calculate the magnetic entropy change, which is closely related to the MCE.[137] From this, it was found that the $\mathrm{Gd(HCO_2)_3}$ system shows the largest ΔS_m at low temperatures, and that $\mathrm{Tb(HCO_2)_3}$ outperforms it at higher temperatures [Fig. 1.19]. To investigate how the incorporation of $\mathrm{Tb^{3+}}$ into $\mathrm{Gd(HCO_2)_3}$ impacted the size and position of the maximum in ΔS_m, Saines *et al.* created a solid solution of $\mathrm{Gd}_{1-x}\mathrm{Tb}_x(\mathrm{HCO_2})_3$, which showed that incorporating $\mathrm{Tb^{3+}}$ could improve the various MCE properties.

A partial explanation for the relative change in MCE performance is that while $\mathrm{Gd(HCO_2)_3}$ contains antiferromagnetic chains along the *c*-axis, $\mathrm{Tb(HCO_2)_3}$ appears to have significant ferromagnetic correlations along the chains, and both appear to have antiferromagnetic correlations in the *ab*-plane. Therefore doping $\mathrm{Tb^{3+}}$ into the system may induce changes in the nature of the interactions along, or between, chains, which contribute to an improvement in MCE performance.[137]

1.5 Thesis structure and aims

The overall aim of this thesis is to use neutron scattering to understand unconventional magnetic order in a variety of materials. To this end, I have studied several different frustrated magnetic systems where the underlying lattice geometry strongly influences the nature of the magnetic states observed.

The structure of this thesis will follow the following format. In Chapter 2 I will introduce and describe the methods of analysis which have been used in my studies. These include the neutron scattering techniques used, the computational analysis of the data collected, and the synthesis of the compounds of interest in this thesis.

In Chapters 3 and 4 I will present our investigations of two triangular lattice antiferromagnets—$Tb(HCO_2)_3$ and $CsCoCl_3$—and our reinterpretation of their magnetic structures. In particular I show both to be triangular Ising antiferromagnets comprising, respectively, ferro- and antiferromagnetic Ising chains. In Chapter 4 I also detail an implementation of a supercell dynamics based approach for the calculation of spin waves in locally ordered, frustrated, systems, using $CsCoCl_3$ as a proof-of-concept.

Chapter 5 demonstrates how inelastic neutron scattering, polarised neutron magnetic diffuse scattering, and Monte Carlo techniques can be used to determine the ground state and interaction parameters of a new gadolinium-based pyrochlore system, $Gd_2Pt_2O_7$.

Then, in Chapter 6 I present an investigation into the coupling of short range magnetic order and ferroelectric polarisation in single crystal samples of a compound related to the Haldane chain compound Y_2BaNiO_5. I have used a combination of

single-crystal neutron diffraction, SQUID magnetometry, heat capacity, and electrical measurements to study Er_2BaNiO_5.

Finally, Chapter 7 will present my conclusions and provide an outlook for future work in these areas.

Chapter 2

Methods

2.1 Scattering Techniques

2.1.1 General Scattering Theory

At the core of this thesis lies a variety of diffraction techniques. X-ray crystallography finds its roots in the works of W. H. Bragg and W. L. Bragg, who first formulated how the diffraction of X-rays by a crystal can provide insights into the underlying atomic structure.[139] If magnetic structures are to be analysed, an extension of the original work of the Braggs needs to be made, and it is generally necessary to use neutrons, rather than X-rays, as our incident radiation. Neutrons are well suited to nuclear structure studies, since, unlike X-rays, they can interact with atomic nuclei, rather than electron clouds. They can also be diffracted by magnetic moments as they are $S = \frac{1}{2}$ particles. Therefore, they can be used for the determination of magnetic structures.[3]

Our goal is to be able to locate the positions of nuclei, or determine the locations of magnetic moments, in a crystal structure, that is, determine a density function, $\rho(\mathbf{r})$, at each point, $\mathbf{r}$, in real space. We can equivalently consider the function $F(\mathbf{Q})$ describing the waves of periodicity, $\mathbf{Q}$, where $|\mathbf{Q}| = Q = \dfrac{2\pi}{\lambda}$, required to reconstruct the same distribution, where λ is the wavelength. $F(\mathbf{Q})$ is known as the structure factor, and is nothing more than the Fourier transform of the density function,

$$F(\mathbf{Q}) = \int \rho(\mathbf{r}) \exp\left(\mathrm{i}\mathbf{Q} \cdot \mathbf{r}\right) \mathrm{d}\mathbf{r}. \tag{2.1}$$

In principle, measurement of $F(\mathbf{Q})$ at sufficiently many values of $\mathbf{Q}$ should allow us to perform a reverse Fourier transform to recover the density function in real space. In practice, however, this is not so simple, as will be described in due course.

In order to measure the structure factor, we must first consider the geometry of a neutron or X-ray scattering experiment, as shown in Figure 2.1. We have an incident wave defined by its wave vector $\mathbf{k}_\mathrm{i} = \frac{2\pi}{\lambda}\hat{\mathbf{k}}_\mathrm{i}$, which interacts with a sample and takes on final wave vector, $\mathbf{k}_\mathrm{f}$. Clearly, different considerations must be taken in the cases where $|\mathbf{k}_\mathrm{i}| = |\mathbf{k}_\mathrm{f}|$ (elastic scattering) and $|\mathbf{k}_\mathrm{i}| \neq |\mathbf{k}_\mathrm{f}|$ (inelastic scattering). The momentum transfer to the sample is defined as $\mathbf{Q} = \mathbf{k}_i - \mathbf{k}_f$, which can be represented by a "scattering triangle", as shown in Figure 2.2.

The value measured by the detector in a scattering experiment is the intensity of the radiation, which is proportional to the square-modulus of the structure factor: $I(\mathbf{Q}) \propto |F(\mathbf{Q})|^2$. Since $F(\mathbf{Q})$ is a complex number, we lose the information containing the phase of $F(\mathbf{Q})$. This is known as the "phase problem" and is principally what prevents simply using a reverse Fourier transform to directly determine the density function from our scattering data.

First, we can consider the scattering from a crystalline material. We can think of a crystal structure as the tiling of a repeating unit—the unit cell—on the points of a lattice which describe the tessellation. This can also be described as the convolution of a motif with the lattice. The Fourier transform of a crystal is therefore the product of the Fourier transforms of the motif and the lattice, as the Fourier transform of a convolution is the product of the individual Fourier transforms.

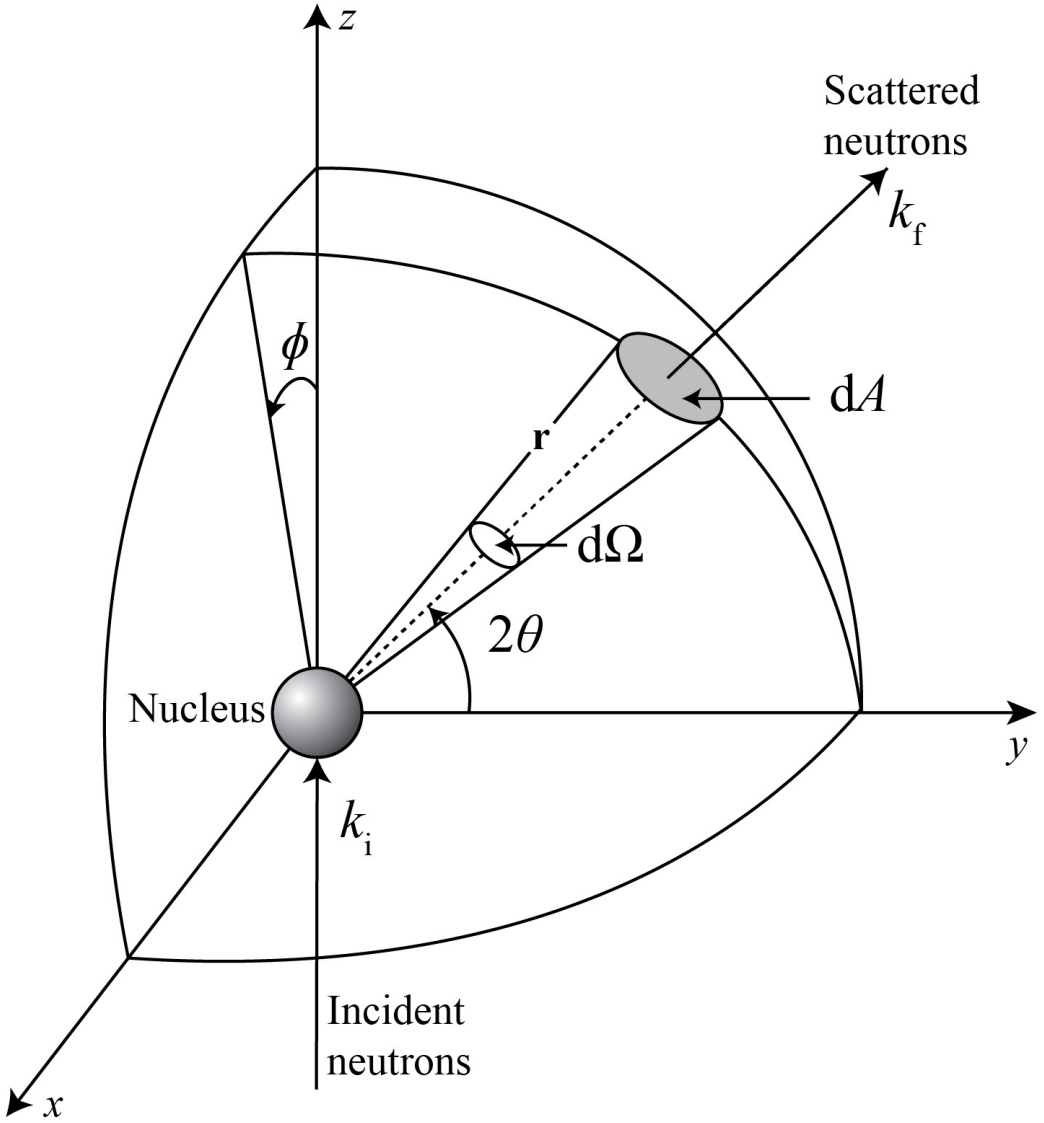


Figure 2.1: The typical geometry of a scattering experiment. Adapted from Fig. 2.4 of Ref. 140.

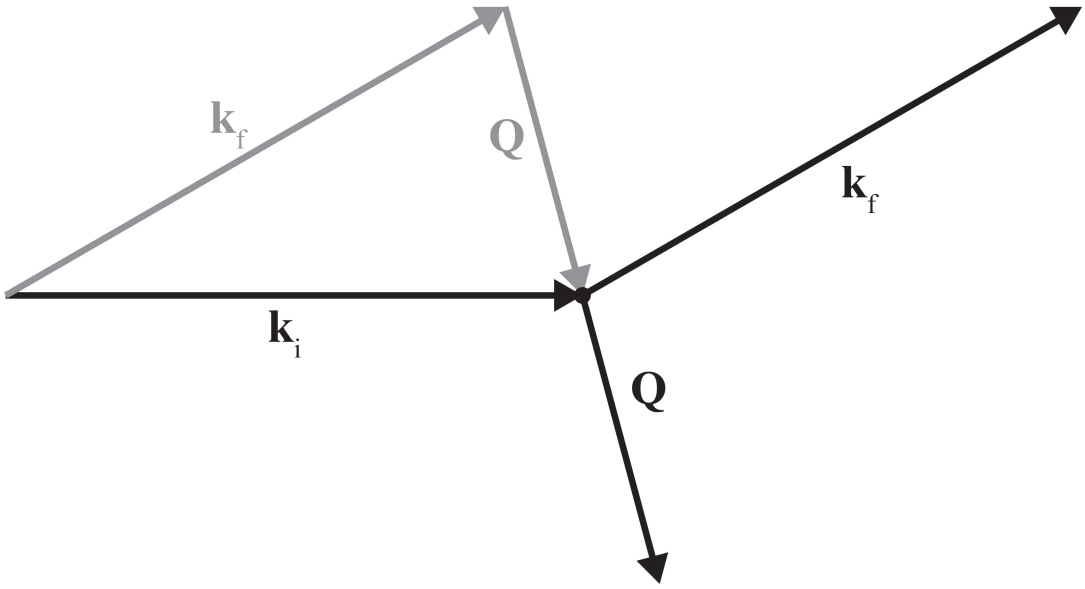


Figure 2.2: Isosceles scattering triangle showing the momentum transferred to the sample as the difference of the initial and final wavevectors.

The lattice is defined as a series of delta-functions,

$$\mathcal{L}(\mathbf{r}) = \sum_{UVW} \delta[\mathbf{r} - (U\mathbf{a} + V\mathbf{b} + W\mathbf{c})], \tag{2.2}$$

where $\mathbf{a}$, $\mathbf{b}$, and $\mathbf{c}$ are the vectors describing the unit cell, and U, V, W are integers. The Fourier transform of this function produces the reciprocal lattice we need to consider:

$$\mathcal{R}(\mathbf{Q}) = \sum_{hkl} \delta[\mathbf{Q} - (h\mathbf{a}^* + k\mathbf{b}^* + l\mathbf{c}^*)], \tag{2.3}$$

where $\mathbf{a}^*$, $\mathbf{b}^*$, and $\mathbf{c}^*$ are known as the reciprocal lattice vectors.

Combining the equations above, and making use of the convolution theorem (see *e.g.* Ref. 141), the structure factor for the crystal can be written as:

$$\begin{aligned} F_{\text{crystal}}(\mathbf{Q}) &= F_{\text{unitcell}}(\mathbf{Q}) \times \mathcal{R}(\mathbf{Q}) \\ &= \int_{\text{unitcell}} \rho(\mathbf{r}) \exp(\mathrm{i}\mathbf{Q}\cdot\mathbf{r}) \mathrm{d}\mathbf{r} \times \sum_{hkl} \delta[\mathbf{Q} - (h\mathbf{a}^* + k\mathbf{b}^* + l\mathbf{c}^*)]. \end{aligned} \tag{2.4}$$

This function is then non-zero only when

$$\mathbf{Q} = \mathbf{G}_{hkl} = h\mathbf{a}^* + k\mathbf{b}^* + l\mathbf{c}^*, \tag{2.5}$$

where the set of all $\{\mathbf{G}_{hkl}\}$ is the reciprocal lattice. If we now consider the fractional coordinates of nuclei in the unit cell, $x\mathbf{a}+y\mathbf{b}+z\mathbf{c}$, then the structure factor becomes

$$\mathbf{F}_{hkl} = \sum_{\mathrm{n}=1}^{N} b_{\mathrm{n}} \exp\left[\mathrm{i}(h\mathbf{a}^* + k\mathbf{b}^* + l\mathbf{c}^*) \cdot (x_{\mathrm{n}}\mathbf{a} + y_{\mathrm{n}}\mathbf{b} + z_{\mathrm{n}}\mathbf{c})\right], \tag{2.6}$$

where $\mathbf{F}_{hkl}$ is known as the structure factor for the reflection (hkl).

In the case of elastic scattering, which we will return to shortly, no energy is transferred to the sample, and we can determine $\mathbf{Q}$ based on the angle, θ, through which the radiation is diffracted

$$\begin{aligned} Q^2 = |\mathbf{Q}|^2 &= k_i^2 + k_f^2 - 2k_i k_f \cos 2\theta \\ &= 2\left(\frac{2\pi}{\lambda}\right)^2 - 2\left(\frac{2\pi}{\lambda}\right)^2 \cos 2\theta. \end{aligned} \tag{2.7}$$

Therefore

$$Q = \frac{4\pi}{\lambda} \sin\theta. \tag{2.8}$$

We can compare this with the scenario presented in Figure 2.3. A path length difference of an integer number of wavelengths is needed in order to give constructive interference of the plane waves incident on the crystal, therefore we arrive at Bragg's law

$$n\lambda = 2d \sin\theta, \tag{2.9}$$

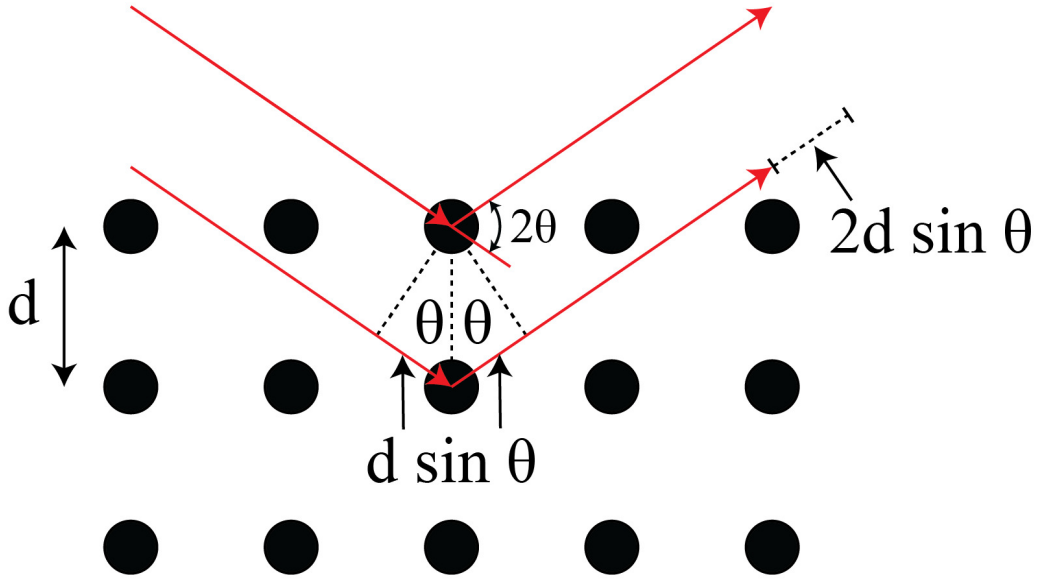


Figure 2.3: Diagrammatic derivation of Bragg's Law for a 2D assembly of fixed particles and two incident plane waves of wavelength λ.

where d is the inter-planar spacing, and θ is half of the total scattering angle. Thus we can relate Q to the inter-planar spacing,

$$Q = \frac{2\pi}{d}. \tag{2.10}$$

If we were to measure the scattering from a non-crystalline material, such as a liquid, we will not observe peaks which are effectively delta-functions in reciprocal space. There is no underlying lattice upon which the motif sits, therefore the density function will not be localised in real space. Such systems tend to produce scattering consisting of smoothly continuous, broad, peaks (or rings, when measured using an area detector).[104] The difference is shown in Figure 2.4. This diffuse scattering still contains a great deal of information about the system, since the intensity is still $I(\mathbf{Q}) \propto |F(\mathbf{Q})|^2$, where $F(\mathbf{Q})$ is the structure factor as defined in Equation 2.1.

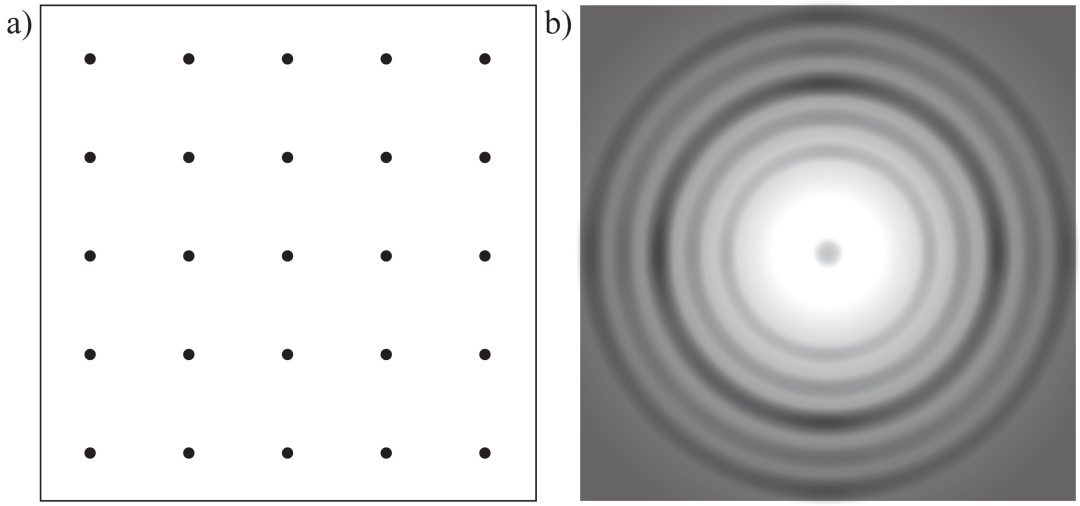


Figure 2.4: Stylised depiction of the scattering from a single crystal, **a)**, compared with the stylised scattering from a disordered system, such as a liquid or glass, **b)**.

Expanding the square-modulus shows that

$$|F(\mathbf{Q})|^2 = \int\int \rho(\mathbf{r}_i - \mathbf{r}_j) \exp\left[\mathrm{i}\mathbf{Q}\cdot(\mathbf{r}_i - \mathbf{r}_j)\right] \mathrm{d}\mathbf{r}_i \mathrm{d}\mathbf{r}_j. \tag{2.11}$$

The scattered intensity, therefore, contains information relating to the separations of all particle pairs.

2.1.2 Elastic neutron scattering

If the incident radiation for a scattering experiment is a neutron, we can use the de Broglie relationship to give the wavelength of the neutron

$$\lambda = \frac{h}{m_n v}, \tag{2.12}$$

where h is Planck's constant, m_n is the mass of the neutron, and v is the particle velocity. As introduced above, neutrons have a number of advantages and disadvantages, when compared with other types of radiation, for example, X-rays. In the

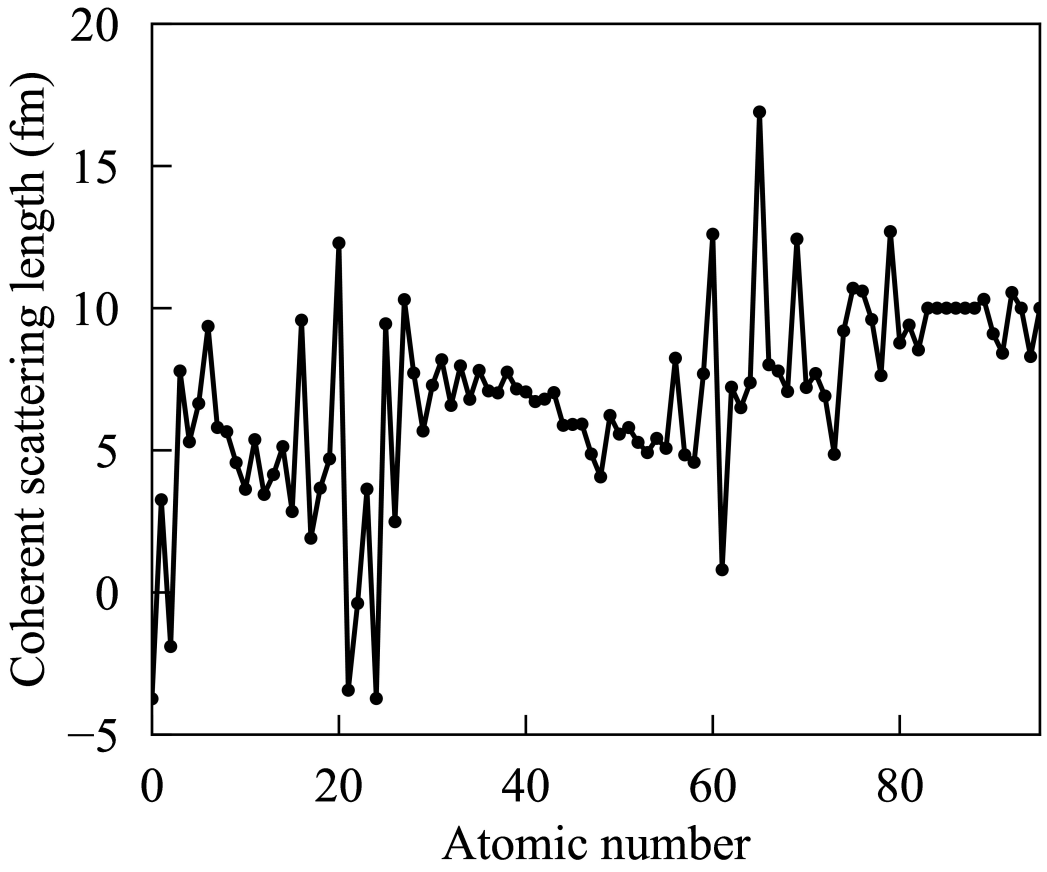


Figure 2.5: Variation of the (real part of the) coherent scattering length of (the natural abundance of) elements with atomic number. Notably this is not a linear increase as seen for X-ray scattering lengths, and in several cases a negative scattering length is observed.

study of nuclear structures, neutrons are of great use, as they can interact directly with the nuclei in the structure. The density function we are measuring in an experiment is known as the "scattering length" of the nucleus. The scattering lengths of nuclei are not linear in atomic number, or necessarily similar for different isotopes of the same element, nor do they have the same sign for all isotopes. An example of the variation of b with atomic number is shown in Figure 2.5.

The scattering length itself is related to the Fermi-pseudopotential, $V(\mathbf{r}) = \frac{2\pi\hbar^2}{m} \cdot b \cdot \delta(\mathbf{r})$, which approximates the neutron–nucleus interaction as an effective hard-sphere collision. The sign of the scattering length tells us whether this

pseudopotential is repulsive, $b > 0$, or attractive, $b < 0$.

In the case where the nucleus which is acting as a scattering centre has a non-zero nuclear spin, two possible combinations of nuclear and neutron spin are possible, depending on whether the combination of the spins is parallel or anti-parallel. The ensemble averaging of these two combinations can be separated into two different cases for scattering: coherent and incoherent. Coherent scattering originates from the correlations between both identical and different nuclei, and gives us information on the structure as well as the collective dynamics. The incoherent scattering, on the other hand, does not contain any information about the structure, instead it can be thought of as a 'flat background' for the purposes of our measurements (it does contain information on single particle dynamics, however those is beyond the scope of this thesis). Values of the coherent and incoherent scattering-lengths are tabulated and are often presented as the coherent and incoherent scattering cross-sections

$$\begin{aligned} \sigma_{\text{coh}} &= 4\pi\bar{b}^2 \\ \sigma_{\text{inc}} &= 4\pi(\overline{b^2} - \bar{b}^2), \end{aligned} \tag{2.13}$$

where the averages, $\overline{b^2}$ and $\bar{b}^2$, arise from the ensemble average of the spin-states in the system, and where we define the total cross-section for a scattering event as

$$\sigma_{\text{tot}} = \frac{\text{number of neutrons scattered in all directions per second}}{\text{incident flux } (I_0)}, \tag{2.14}$$

where the incident flux is the number of neutrons which are incident per unit area of sample in unit time. One important example of the importance of isotopes having

different scattering cross-sections is the case of hydrogen, which has a small coherent scattering length and a large incoherent scattering length, with $\frac{\sigma_{\text{inc}}}{\sigma_{\text{coh}}} \approx 40$. Thus, the presence of hydrogen in a sample generally leads to a large incoherent background which can act to partially or completely obscure features of interest in the diffraction pattern.

When a scattering experiment is performed, the diffractometer measures the differential cross-section,

$$\frac{\mathrm{d}\sigma}{\mathrm{d}\Omega} = \frac{\text{number of neutrons scattered per sec into a solid angle } \mathrm{d}\Omega}{I_0 \mathrm{d}\Omega}. \tag{2.15}$$

If we know the momentum transfer to our sample, we can use this to measure the intensity of our scattered radiation for a given $\mathbf{Q}$ as $I(\mathbf{Q}) = \frac{\mathrm{d}\sigma}{\mathrm{d}\Omega}$. We can now relate this scattering cross-section back to the structure factor in Section 2.1.1.

Neutron production

In order to generate neutrons for use in structural or dynamical studies, two methods are commonly used. The first method employed is to simply use the excess neutrons coming from a nuclear reactor, as a uranium reactor (using ^{325}U as the fissile material) will, on average, produce 2.7 fast neutrons per fission event.[140] This is more than enough for the reaction to be self-sustaining, and the remaining neutrons can be moderated down to the speeds required for diffraction measurements. The ILL in Grenoble uses a high-flux reactor (HFR) to supply neutrons to two experimental guide halls.[140] There are a number of different moderators surrounding the reactor core, but the majority of moderation is done by the coolant (*i.e.* light water), and the main moderator, D_2O. For elastic scattering measurements at a reactor source

often a single wavelength of neutrons is selected using *e.g.* a single-crystal graphite monochromator.

Another method of producing neutrons, which eliminates the need for a nuclear reactor—which is becoming a significant consideration for the future development of neutron scattering facilities, particularly in densely populated areas—is to use a pulsed accelerator source and rely on neutron spallation. The key advantage in this technique is that the neutrons are generated in a time-period significantly shorter than the time between pulses, allowing for appropriate cooling of the target. Here I will focus on the spallation technique, as that is what is used at ISIS, but other techniques are possible.

Essentially, spallation involves the bombardment of a heavy-metal target (*e.g.* mercury at the ESS, and tungsten at ISIS) with protons. This causes an internal nucleon cascade within the target nucleus, followed by an internuclear cascade where particles are ejected and absorbed within the target, and finally, the ejection of neutrons from the excited nuclei in a process known as "evaporation", giving lower-energy neutrons. In order to accelerate and direct the protons towards the target, ISIS makes use of a synchrotron to store H^+ ions, formed by stripping electrons from H^- ions accelerated using a linear accelerator (linac). These protons are stored and accelerated in the synchrotron before being kicked into the extracted proton beamline where they are directed towards the target. From there, the neutrons are generated, as described above, and can be moderated to the desired energy range.

The continuous production of neutrons in a reactor naturally gives rise to a high average flux. Therefore it is possible to monochromate the full (white) beam—with the loss of neutrons that implies—and still have a high enough flux to the sample

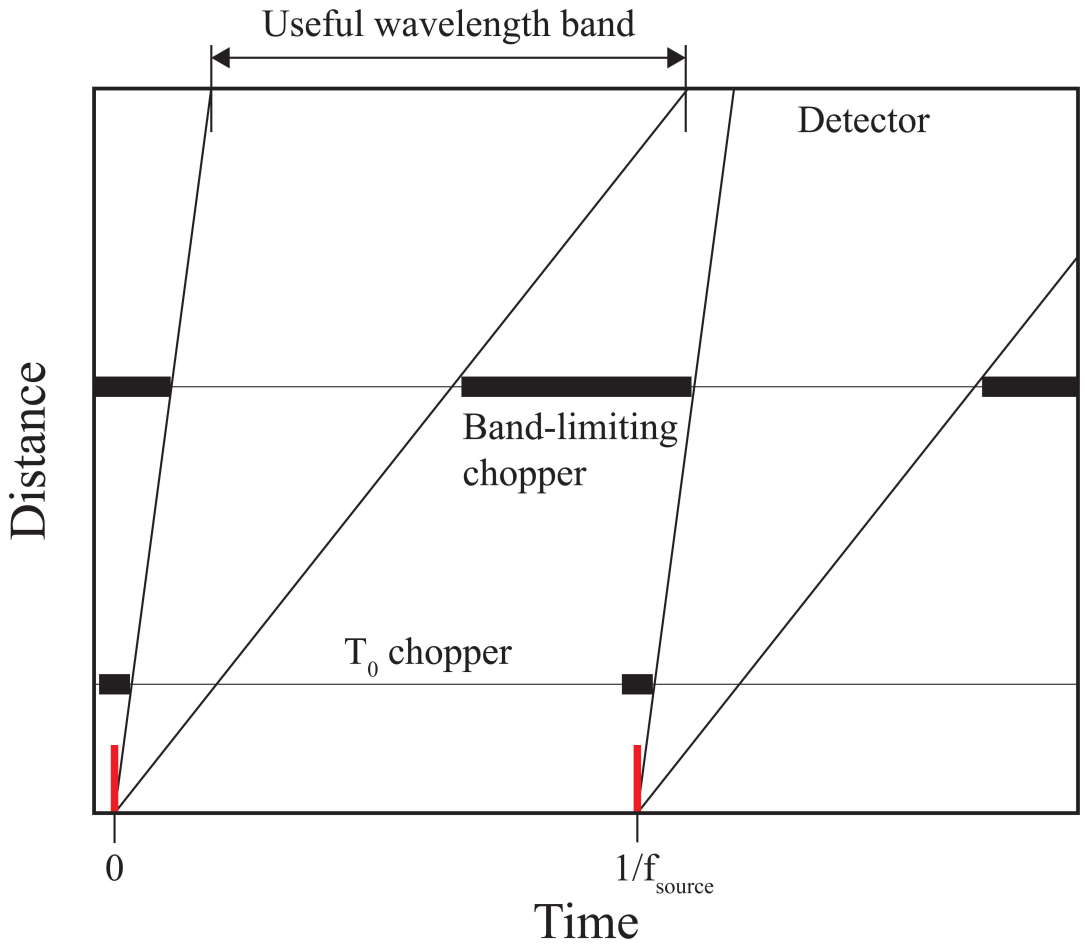


Figure 2.6: Representation of neutron pulses (shown in red) propagating in time and distance, showing the usable wavelength distribution at the detector.

to allow data collection in a reasonable time frame. Pulsed sources, on the other hand, have a relatively low average flux due to the fact that for the majority of the time, the flux from the target is effectively zero. In order to make use of this time between neutron pulses in a spallation source, neutrons of different energies are allowed to disperse in time before they are incident on the sample. This allows for the white beam to be used. Since the time of generation is known, instruments can be designed which record the time difference between generation and detection, giving the time of flight (ToF) of the neutrons. A schematic time-distance plot for a spallation source is shown in Figure 2.6.

2.1.3 X-Ray scattering

The derivations above assume that the incident radiation is scattered from a point scatterer. This holds for the case of neutrons scattering from nuclei, however it does not fully describe the interaction of X-rays with electron density. Rather than having a scattering length which depends on the specific nucleus involved, a *form factor*, $f(\lambda, \theta)$, where θ is the scattering angle, is now required to describe the diffraction. A useful analogy is given by Sivia:[141] in the same way as diffraction through a slit, if the slit is made wider, the spherical waves diffracted become more planar, and thus there is a diminishing of intensity as the scattering angle increases. There are two other principle factors which describe the form factor for X-ray diffraction: (i) it has the same sign for all elements (ignoring anomalous scattering), and (ii) the magnitude is proportional to the atomic number Z.

This implies that if we wish to determine the positions of two ions with the same number of electrons, *e.g.* Si^{4+} and Al^{3+}, or if we wish to locate very light elements such as hydrogen, X-rays may not be as good a probe as neutrons. However, X-rays have the advantage that they can be produced relatively cheaply compared with neutrons, and a substantial portion of X-rays used for routine scattering studies can be produced by small, in-house, X-ray tubes situated in user-friendly instruments.

2.1.4 Elastic Magnetic Neutron Scattering

At the start of this chapter I noted that neutrons have a magnetic moment with $S = \frac{1}{2}$, but no charge, thus making them an ideal probe of the magnetic fields within a sample—*e.g.* unpaired electrons. In general, the theory is very similar to that of scattering from the nuclei in the sample, however the key difference is that there is

now a vector interaction between the magnetic dipole moments

$$V_{\mathrm{M}}(\mathbf{r}) = -\boldsymbol{\mu}_{\mathrm{n}} \cdot \mathbf{B}(\mathbf{r}), \tag{2.16}$$

where $\mathbf{B}(\mathbf{r})$ is the magnetic field created by the system. Two of the most important points regarding magnetic neutron scattering are that the neutron is only sensitive to the component of the magnetic moment perpendicular to the scattering vector, $\mathbf{Q}$, and that the neutrons are interacting with the magnetic fields produced by electrons in atomic orbitals which are distributed in space, *i.e.* the scattering is no longer from a point-charge. Therefore, a form-factor is needed to describe how the intensity of the scattered neutrons decreases at high angle, similar to the atomic form-factor used in X-ray scattering. Therefore our magnetic structure factor is given as

$$F_{\mathrm{M}}(\mathbf{Q}) = \sum_{j} \boldsymbol{\mu}_j f_j(\mathbf{Q}) \exp\left(\mathrm{i}\mathbf{Q} \cdot \mathbf{r}_j\right). \tag{2.17}$$

Paddison *et al.* provide a method for the computational calculation of the magnetic scattering cross-section, based on the work of Blech and Averbach,[142] which we will also return to later.[143] The key equation from this work gives the measured intensity of magnetic neutron scattering, after performing the spherical averaging appropriate for a powder, as

$$\begin{aligned} I(Q) = C[\mu f(Q)]^2 \Bigg\{ \frac{2}{3} + \frac{1}{N} \sum_{i,j} \Bigg[A_{ij} \frac{\sin Qr_{ij}}{Qr_{ij}} \\ + B_{ij} \left(\frac{\sin Qr_{ij}}{(Qr_{ij})^3} - \frac{\cos Qr_{ij}}{(Qr_{ij})^2} \right) \Bigg] \Bigg\}, \end{aligned} \tag{2.18}$$

where

$$A_{ij} = S_i^x S_j^x,$$
$$B_{ij} = 2S_i^z S_j^z - S_i^x S_j^x. \tag{2.19}$$

In these equations, i and j label the spins, r_{ij} gives the separation of the spins, $f(Q)$ is the magnetic form-factor, and μ is the effective magnetic moment. The proportionality constant, $C = \left(\frac{\gamma_n r_e}{2}\right)^2 = 0.07265$ barns, where γ_n is the neutron magnetic moment, and r_e is the classical electron radius.

This is the equation used by the program SPINVERT to which we will return later. From this equation we can interpret the real-space effects related to a configuration of spins, *e.g.* the spin anisotropy, or pairwise spin correlation functions.

One of the principal problems related to the measurement of magnetic neutron scattering is that the magnitude of the interaction of a neutron with a magnetic field may be much smaller than when a neutron interacts with a nucleus. The intensity of the scattering now depends on the magnetic moment of the scatterers, and thus depends on their spin. Therefore, the intensity of magnetic neutron scattering can be significantly smaller than the intensity of nuclear scattering. One of the main challenges when analysing magnetic neutron scattering is the separation of nuclear and magnetic scattering intensity.

Three methods for the separation of magnetic and nuclear scattering are used in this thesis. The first, and conceptually most straightforward, approach is to manually remove regions of the scattering pattern associated with nuclear scattering. This is only possible if there is little overlap of the magnetic and nuclear scattering, and therefore not possible for *e.g.* a ferromagnet. The second method is to col-

lect datasets of the scattering in the paramagnetic and ordered magnetic regimes. We can then subtract the lower-temperature dataset containing both the magnetic and nuclear scattering from the dataset containing the nuclear scattering and the paramagnetic scattering (which should simply contain a form-factor dependence of uncorrelated magnetic scattering). This subtraction should leave only the magnetic scattering. There are, however, several assumptions made with this approach. The first assumption is that the nuclear structure does not change significantly between the two temperatures. Even if the nuclear structure retains its symmetry, lattice contraction (or expansion) may cause the nuclear Bragg peaks to move sufficiently that sharp artefacts remain after subtraction. A second assumption is that there are no strong magnetic correlations in the nominally paramagnetic regime, as these could give rise to structured diffuse magnetic scattering which may not be present in the lower temperature dataset. This method has been used for the analysis of data presented in Chapter 4, where we encounter some of these drawbacks. Performing a temperature subtraction is a more accessible method for the isolation of magnetic scattering than xyz polarisation analysis, discussed below, as a standard instrument set-up may be used, and there is no reduction in neutron flux due to polarisation.

The third method used for the separation of the nuclear and magnetic scattering is xyz polarisation analysis, where we make use of the measurement of the orientation of polarised neutron spins in order to separate these components. The neutrons produced by reactor and spallation sources are not spin polarised. It is, however, possible to consider the situations in which the neutron spin may be aligned with, or anti-aligned to, an external field—which are called spin-up and spin-down, respectively. An overview of the production of polarised neutrons is given in several

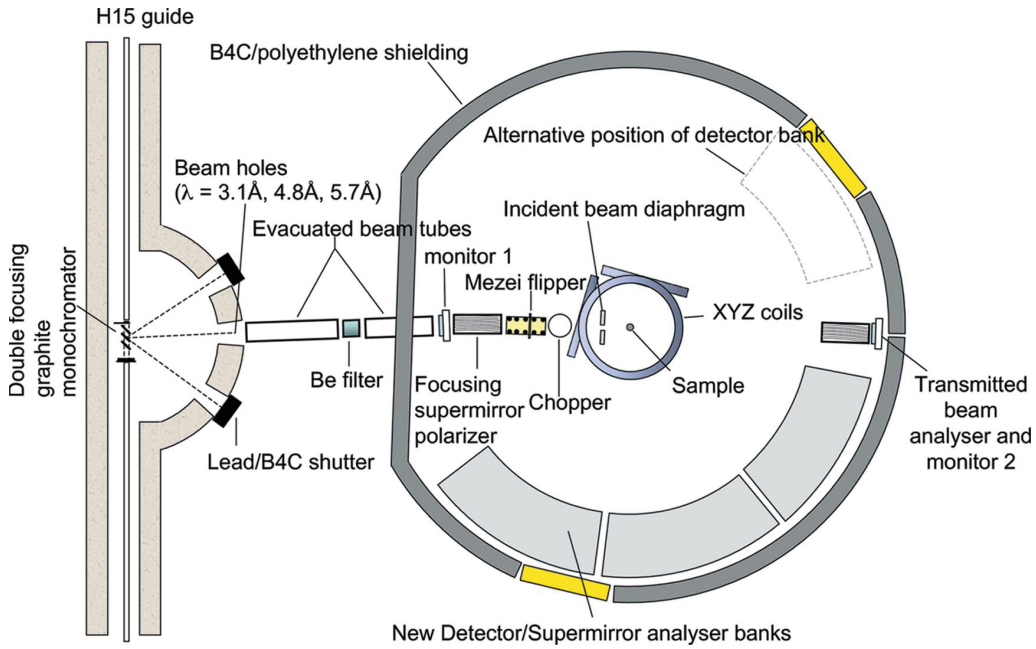


Figure 2.7: Schematic view of the D7 spectrometer at the ILL, Grenoble. The key components for the polarisation of the incident neutrons are the supermirror polariser array, and the Mezei-type flipper. Source: Ref. 144

textbooks *e.g.* Ref. 140. I will restrict the discussion of polarisation and analysis method to those pertaining to the D7 spectrometer at the ILL, Grenoble [Fig. 2.7], as this is where our polarised neutron scattering experiments were carried out.

To produce a polarised beam of neutrons, D7 makes use of a supermirror bender polariser, using a multilayer assembly of Co/Ti supermirrors to polarise and guide the beam, by exploiting the difference in reflectivity for spin-up and spin-down neutrons. The polarised beam is then passed through a Mezei-type flipper to set the incident polarisation.[145] Around the sample position there are xyz coils which set the magnetic field. For each orientation of the field, both the spin-flip (sf) and non-spin-flip (nsf) scattering are measured, giving a total of six measurements. Using the equations developed by Schärpf and Capellmann[146] as well as Moon, Riste, and Koehler,[147] and the extension of these given by Stewart *et al.*[144] we can—for a well-defined number of cases—separate out the spin-incoherent, the nuclear, and

the magnetic scattering. Full details of the equations used in the standard data reduction and processing steps on D7 are given in Ref. 144. The main equations of interest to this thesis are those which allow for two independent calculations of the magnetic cross-section [Eq. 36 in Ref. 144], given by

$$\begin{aligned}\left(\frac{\mathrm{d}\sigma}{\mathrm{d}\Omega}\right)_{\mathrm{mag}} &= 2\left(\frac{\mathrm{d}\sigma}{\mathrm{d}\Omega}\right)^{x}_{\mathrm{sf}} + 2\left(\frac{\mathrm{d}\sigma}{\mathrm{d}\Omega}\right)^{y}_{\mathrm{sf}} - 4\left(\frac{\mathrm{d}\sigma}{\mathrm{d}\Omega}\right)^{z}_{\mathrm{sf}}, \\ \left(\frac{\mathrm{d}\sigma}{\mathrm{d}\Omega}\right)_{\mathrm{mag}} &= 4\left(\frac{\mathrm{d}\sigma}{\mathrm{d}\Omega}\right)^{z}_{\mathrm{nsf}} - 2\left(\frac{\mathrm{d}\sigma}{\mathrm{d}\Omega}\right)^{x}_{\mathrm{nsf}}\left(\frac{\mathrm{d}\sigma}{\mathrm{d}\Omega}\right)^{y}_{\mathrm{nsf}}.\end{aligned} \tag{2.20}$$

D7 was designed with this principle in mind, and has been optimised to collect data which can be handled in this way. Both supermirror arrays and ferromagnetic single crystals are optimised for the polarisation of neutrons of a relatively narrow range of wavelengths. This is of benefit when polarising a monochromatic beam at, for example, a reactor source, however it is less suited to the white beams typically used in spallation sources. In these cases, a polariser is required which is effective for a large range of wavelengths. One such method commonly used at the ISIS Neutron and Muon source, is a spin-polarised ^{3}He filter. Low pressure spin polarised ^{3}He can be produced using metastable-exchange optical pumping using high-powered lasers, which can then be compressed using a piston compressor, and then transported to the beamline for use.

The chief drawback of neutron polarisation analysis is that the initial polarisation, whether by a supermirror, polarising single crystal, or ^{3}He spin-filter, will remove approximately half of the neutrons in the unpolarised incident beam. Further loss of neutrons will occur in the analyser, as that will also only accept one spin-state. Therefore, such polarisation analysis is best performed at sources with

a high incident flux, as otherwise the signal-to-noise ratio for the given measurement time may not be good enough, especially for the analysis of diffuse magnetic scattering.

2.1.5 Inelastic Neutron Scattering

The equations above have described the elastic scattering of neutrons, however it is possible for $|\mathbf{k}_i| \neq |\mathbf{k}_f|$. In this case, both the momentum transfer and the energy transfer need to be considered:

$$\hbar\omega = \mathrm{E}_i - \mathrm{E}_f = \frac{\hbar^2}{2m}(k_i^2 - k_f^2), \tag{2.21}$$

where E_i and E_f are the initial and final energies of the neutron, and ω is the angular frequency. Therefore, the scattering event is now characterised by both $\mathbf{Q}$ and ω.

The scattering triangle [*e.g.* Fig. 2.2] is no longer isosceles and so,

$$\begin{aligned} Q^2 &= k_i^2 + k_f^2 - 2k_i k_f \cos 2\theta \\ &= \frac{2m}{\hbar^2}\left(\mathrm{E}_i + \mathrm{E}_f - 2\sqrt{\mathrm{E}_i \mathrm{E}_f}\cos 2\theta\right). \end{aligned} \tag{2.22}$$

If we suppose that our *spectrometer* can analyse both the momentum and the energy of the neutrons, we need to consider the double differential cross-section

$$\frac{\mathrm{d}^2\sigma}{\mathrm{d}\Omega \mathrm{dE}} = \frac{\begin{array}{r}\text{total number of neutrons scattered per second into solid} \\ \text{angle } \mathrm{d}\Omega \text{ with final energies between } E_\mathrm{f} \text{ and } E_\mathrm{f} + \mathrm{d}E_\mathrm{f}\end{array}}{I_0 \times \mathrm{d}\Omega \times \mathrm{dE_f}.} \tag{2.23}$$

The numerator is dependent on the bandwidths of $\mathrm{d}\Omega$ and $\mathrm{dE_f}$, as well as the number of incident neutrons (as defined in Eq. 2.14). Using the Van Hove formalism,[148] this

simplifies the double differential cross-section to

$$\frac{\mathrm{d}^2\sigma}{\mathrm{d}\Omega\mathrm{dE}} = b^2\frac{k_f}{k_f}NS(\mathbf{Q},\omega), \tag{2.24}$$

where we have a system of N atoms, and $S(\mathbf{Q},\omega)$ is the scattering function for the system. The function $S(\mathbf{Q},\omega)$ contains all the information related to the scattering response to inelastic events, such as scattering from phonons or magnons.

2.2 Physical Property Measurements

Throughout my studies, I have used a variety of physical property measurements, especially in the study reported in Chapter 6. These techniques are well established, and only a brief overview of the pertinent points will be given here.

2.2.1 Magnetisation Measurements

We have used a Quantum Design (QD) MPMS 3 magnetometer with a vibrating sample magnetometer (VSM) insert in order to collect magnetisation data. This type of magnetometer uses a superconducting quantum interference device (SQUID) to measure very small magnetic fields induced in a sample. Essentially the operation of a SQUID involves a superconducting ring containing a pair of parallel strips of insulating material forming Josephson junctions. These allow for the tunneling of Cooper pairs across the junction and thus small changes in the applied current can disrupt the tunneling and be detected. The sample itself is moved through a series of pickup coils, which are themselves connected to an input coil adjacent to the SQUID. For more details of the operation of SQUID magnetometers, see *e.g.* Ref. 149. For our powder measurements, the sample was packed into a gelatine capsule

and straw, both with small diamagnetic moments, and secured in place using further capsules and Kapton tape. Our single crystal measurements were performed using the Quantum Design single-crystal stage for the MPMS 3—a quartz paddle—to which the crystal is attached using GE varnish. This allows for very good control over which axis of the crystal is mounted parallel to the applied field.

2.2.2 Thermal and Electrical Measurements

A Quantum Design (QD) physical property measurement system (PPMS) has been used to collect data on the heat capacity of our sample of Er_2BaNiO_5. In principle, the QD PPMS can be used to collect data for a variety of different physical properties—*e.g.* electrical transport, AC susceptibility, torque magnetometry—however we have employed it solely for the purpose of measuring thermal transport properties, in the form of the heat capacity. The sample stage for this measurement option is a *puck* containing a calorimeter and a sample mounting platform. In order to ensure that there is good thermal contact between the sample and the platform, a layer of Apiezon grease is used to attach the sample. The rest of the puck then forms a thermal bath around the sample platform. QD supply software which controls the data collection, which includes a routine for the measurement and subtraction of the background signal of the puck and grease, as well as the fitting algorithms which convert the measured thermal response from the heat pulse into the experimental heat capacity of the sample.

In order to perform electrical measurements on Er_2BaNiO_5, a custom designed set-up was used. The sample environment used is, again, a PPMS allowing cooling from room temperature to 5 K. Samples were attached to a custom sample holder

with GE varnish, and electrodes were connected using silver paint. The sample is then connected in series with a DC high-voltage power supply and a current-to-voltage amplifier (IV amplifier). A Keithley 6517B electrometer was used to record *e.g.* time, sample temperature, and current flow, which was collected using custom Python scripts.[150] This experiment was performed with the generous assistance of Dr Roger Johnson and Dr Francis Chmiel. Prior to measurement, a powder sample was compressed into a disk and sintered at 1000 °C for 12 hours. In the case of the single crystal, the contact area of each axis was $\sim$ 1 mm^2, while $d = 4$ mm for the sintered powder disk. For pyrocurrent measurements, a bias voltage was set up across the sample using the power supply. The sample was then cooled under the bias voltage to 10 K, at which point the electric field was removed and the sample shorted for sufficient time to allow the background to stabilise. The pyrocurrent was then measured as a function of temperature while heating in zero electric field. In order to confirm our measurements we additionally performed a pyrocurrent measurement with a bias electric field applied, as described in Reference 151. For this measurement, the sample is cooled in zero field, and then a bias voltage is applied while the temperature is increased.

2.3 Computational Methods

2.3.1 Metropolis Monte Carlo

Analysis of a large amount of our neutron diffraction data and physical properties has been performed using Monte Carlo (MC) techniques. The techniques used in this thesis have been detailed extensively elsewhere (*e.g.* Ref. 152), however, it will

be instructive to review the methods that have been used in the analysis of the data collected in this thesis.

The basic Monte Carlo technique employed is the Metropolis-Hastings algorithm.[153,154] The flow-chart in Figure 2.8 gives an overview of the method used. A box of randomly generated vectors representing the classical magnetic spins of the system is generated. Spins are then randomly selected and randomly rotated around the surface of the sphere they describe. A cost function is then calculated; which may, for example, be the energy change of the system as a result of the move carried out. If the move improves the cost function, it is accepted, however if the cost function is not improved, the move may still be accepted based on a given probability (which, in many cases, is related to the temperature of the system: *e.g.* if a random number, $r < \exp\left(\frac{-\Delta E}{k_{\mathrm{B}}T}\right)$, where $0 \leq r \leq 1$. In this thesis I have made use of two different implementations of MC techniques.

The first is the forward (or direct) MC simulation. Here a system is modelled based on a proposed Hamiltonian. As will be expanded on in subsequent chapters, this Hamiltonian can take many different forms depending on the system, with an illustrative example being

$$\begin{aligned}\mathcal{H} =& \frac{1}{2}\sum_{i,j} J_{ij}\hat{\mathbf{S}}_i \cdot \hat{\mathbf{S}}_j + \Delta \sum_i (\hat{\mathbf{S}}_i \cdot \hat{\mathbf{z}}_i)^2 \\ &+ \frac{Dr_1^3}{2}\sum_{i,j} \frac{\hat{\mathbf{S}}_i \cdot \hat{\mathbf{S}}_j - 3(\hat{\mathbf{S}}_i \cdot \hat{\mathbf{r}}_{ij})(\hat{\mathbf{S}}_j \cdot \hat{\mathbf{r}}_{ij})}{r_{ij}^3}.\end{aligned} \tag{2.25}$$

In this particular case, we are considering pairwise interactions with exchange constants J_{ij}, a single-ion anisotropy parallel or perpendicular to the local z-axis, Δ, and a long-range dipolar interaction characterised by the dipolar coupling strength,

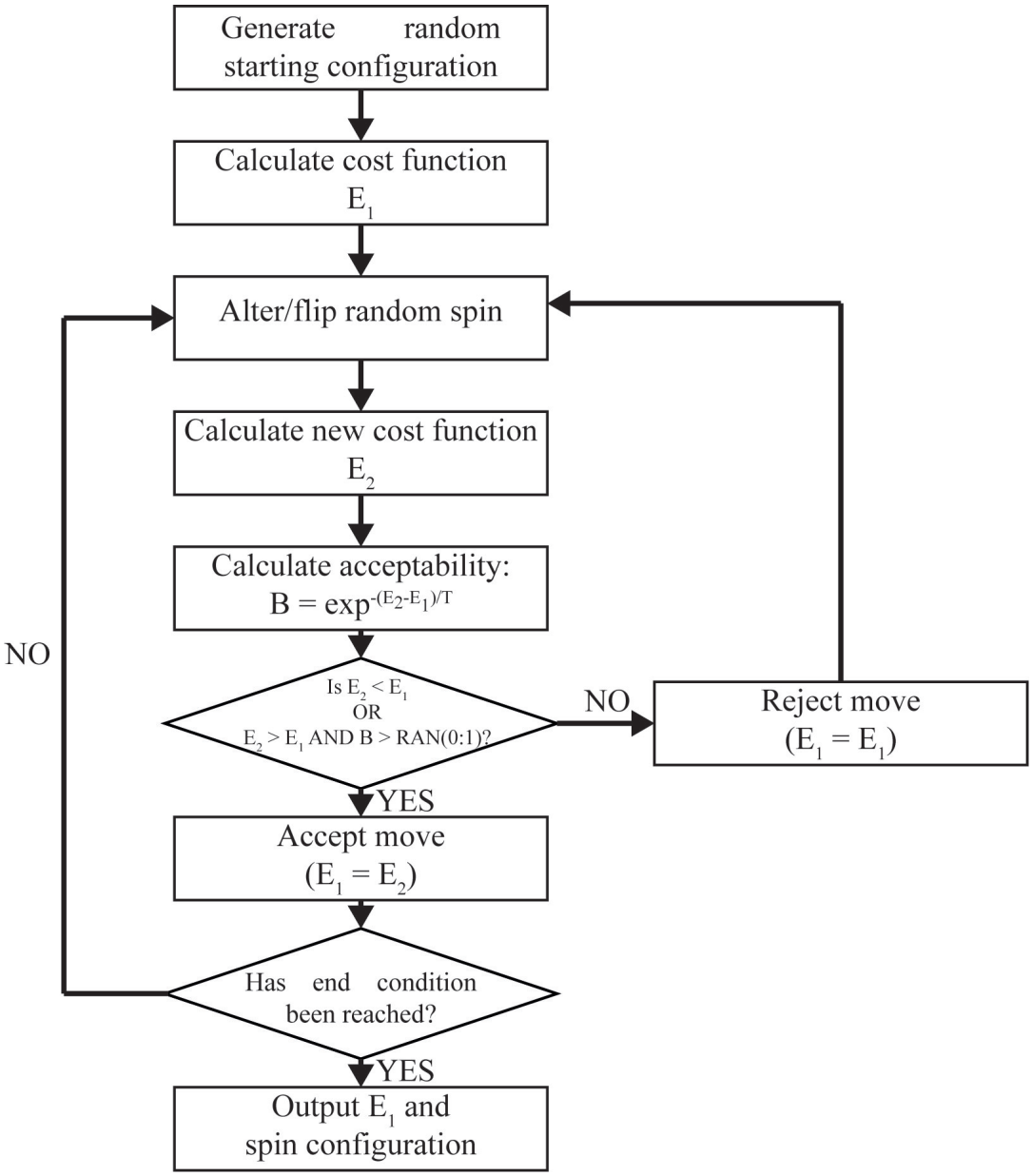


Figure 2.8: Flow chart showing a high-level overview of the Monte Carlo methods used in this thesis.

D. Using this Hamiltonian, we are able to calculate the energy of our system, and then use the Metropolis-Hastings method to simulate spin configurations at a given temperature. Other, simpler, Hamiltonians are used throughout this thesis, particularly in Chapters 3 and 4.

2.3.2 Reverse Monte Carlo

The second Monte Carlo method used in this thesis is magnetic reverse Monte Carlo (RMC). In this technique, the cost function which is being minimised is the least-square difference between the calculated diffuse magnetic scattering and the measured data. This approach allows for the analysis of diffuse scattering data without the requirement of defining a Hamiltonian, and thus we can avoid biasing our conclusions. As implemented in SPINVERT,[152] the technique does, however, rely on a number of assumptions in order to limit degrees of freedom of the system to avoid spurious results. (i) The nuclear positions need to be fixed, with the spins fixed to these positions, (ii) the experimental data must be solely magnetic in origin, (iii) there must be no magnetoelastic coupling, and (iv) all of the spins are required to have the same magnetic properties. It is by using these assumptions that SPINVERT is often able to recover a three-dimensional diffuse scattering pattern from spherically averaged data.

I have made use of the SPINVERT implementation of magnetic RMC throughout this thesis.[152] The cost function to be minimised is given by

$$\chi^2 = W \sum_{i=1}^{N_\mathrm{d}} \left(\frac{I_i^\mathrm{expt} - s I_i^\mathrm{calc}}{\sigma_i} \right)^2 . \tag{2.26}$$

The parameters required for this function are the experimental diffuse scattering

intensity at point i, I_i^{expt}; the calculated diffuse scattering intensity, I_i^{calc}, given by Eq. 2.18, modified by a supplied (or refined) scale factor, s (related to the magnitude of the spins); the experimental uncertainty, σ_i; and an empirical weight factor, W. By making use of this cost function, and simulating a large enough number of spins, we can refine our model to the data collected.

SPINVERT, and the RMC approach in general, has a number of advantages and disadvantages when compared with methods such as direct Monte Carlo simulations. Since it is a model-free method, it is only biased by the experimental data collected. This means that we will not be biased by an incorrect model, however, it also implies that the results of the refinement will only be as good as the data collected. If our data contain random or systematic errors, then the spin configurations generated may contain spurious features if our choice of parameters is poor. Despite fitting to only powder magnetic neutron diffraction data, SPINVERT can be used to generate 3D real-space spin configurations, which may then be used to calculate a single-crystal diffuse magnetic neutron scattering pattern.[131,152]

2.3.3 Linear Spin Wave Calculations

For the calculations of magnetic inelastic neutron scattering, I have made use of the code contained in SpinW;[39] a MATLAB package which calculates magnetic excitations using linear spin-wave theory (LSWT). The full details of the code are given in Ref. 39, however it is illustrative to detail certain parts of it as, particularly in Chapter 4, we have made direct use of the dynamical matrix generated, rather than use the code for the calculation and visualisation of the excitations.

As described in Chapter 1, LSWT is based on transforming the Heisenberg

Hamiltonian into ladder operators, and then mapping this onto an harmonic operator. This is then expressed in terms of Bosonic creation (annihilation) operators and then Fourier transformed, once non-linear parts are excluded. The Fourier transformed version of the Hamiltonian becomes an eigenvector/eigenvalue problem, which together allow for the calculation of the pairwise correlation functions, and thus the calculation of the neutron scattering intensity.

The SpinW package makes use of MATLAB processing and plotting routines to implement LSWT. The methods implemented by the SpinW class provide tools for the calculation of a wide variety of spin structures, which can be defined in terms of the magnetic propagation vector, the angle of a spin helix, the rotation of a collinear structure, or by the direct input of the spin vectors, as I have used in this thesis. An example of the SpinW code used is presented in Appendix B1.

In general, the diagonalisation of the spin dynamical matrix is performed in the background when the `spinwave` method is called from a SpinW object, which then allows for easy visualisation by the `sw_plotspec` function. In Chapter 4, it is necessary to access the spin dynamical matrix directly, as we only need to calculate the eigenvectors and eigenvalues at $\mathbf{k} = 0$. This is facilitated by use of the `saveH` property of the `spinwave` method.

2.3.4 Band Unfolding

Recent work by Overy *et al.* demonstrated that strongly correlated structural disorder is intimately linked to physical properties which depend on periodicity.[155] They also showed that the zone-centre excitations of a supercell can be used in conjunction with band-unfolding to calculate the full phonon spectrum.[156] A schematic

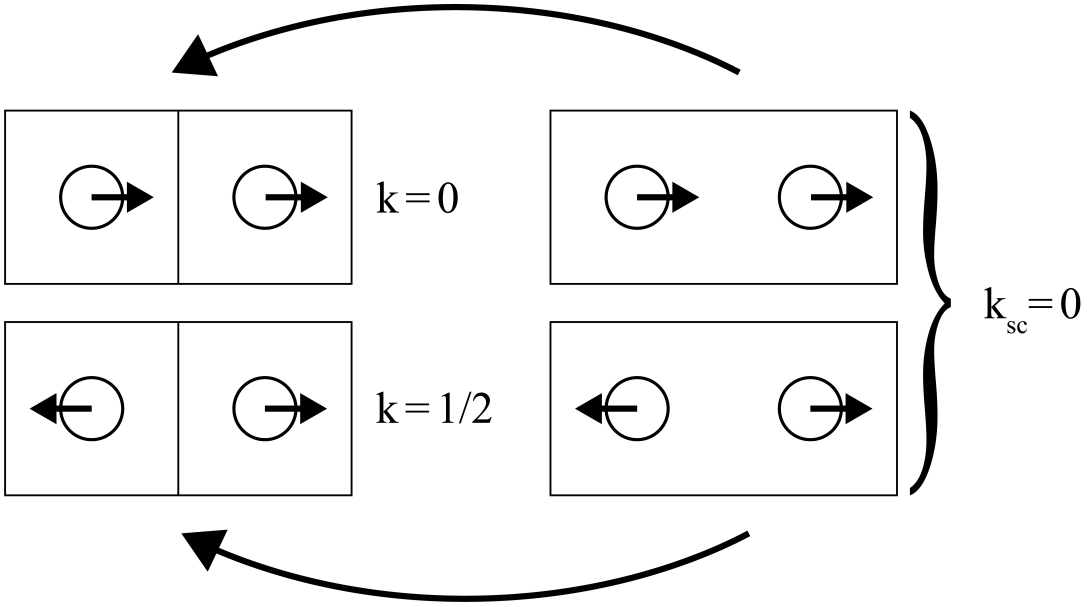


Figure 2.9: The left hand panel shows two wavevectors for the displacements of two unit cells each containing one atom in a 1D chain. The right hand panel shows the same displacements within a two atom supercell of the left hand unit cells. Both sets of displacements occur at the zone centre, however we can use band-unfolding to map these displacements back to those stemming from the original unit cells.

representation of this process is shown in Figure 2.9, and is known as supercell lattice dynamics (SCLD).

We reproduce the essential equations of this method below, noting the differences required for our calculations. The backbone of this calculation is the generation of a dynamical matrix $\mathbf{D}(\mathbf{k})$, which is defined at wave-vector $\mathbf{k}$ as:

$$D_{\alpha j,\beta j'}(\mathbf{k}) = \frac{1}{(m_j m_{j'})^{1/2}} \sum_{\ell'} \left[\Phi_{\alpha\beta}\left(\begin{smallmatrix} j & j' \\ 0 & \ell' \end{smallmatrix}\right) \times \exp\left\{ \mathrm{i}\mathbf{k} \cdot [\mathbf{r}(j'\ell') - \mathbf{r}(j0)] \right\} \right], \tag{2.27}$$

where

$$\Phi_{\alpha\beta}\left(\begin{smallmatrix} j & j' \\ 0 & \ell' \end{smallmatrix}\right) = \frac{\partial^2 W}{\partial u^{\alpha}_{j0} \partial u^{\beta}_{j'\ell'}}, \tag{2.28}$$

is the force-constant matrix relating atomic displacements, u, to the lattice energy, W. The diagonalisation of the dynamical matrix yields the eigenvalues of $D(\mathbf{k})$,

which are the square of the normal mode frequencies, $\omega^2(\mathbf{k}, \nu)$, and the eigenvectors, $\mathbf{e}(\mathbf{k}, \nu)$, give the atomic displacements for a particular phonon mode, ν. When the unit cell contains Z atoms, there will be $3Z$ eigenvalues in the dynamical matrix.

In the SCLD method, a supercell containing N conventional unit cells is used. The diagonalisation of the dynamical matrix at the zone-centre, $\mathbf{D}(\mathbf{k} = \mathbf{0})$, yields the $3ZN$ frequencies and eigenvectors that are associated with the normal modes of the supercell. Each eigenvector also contains $3ZN$ components, labelled as e^a_{jl}, where each component now describes the displacements of a single atom in the supercell along a cartesian direction.

These can then be projected onto the N $\mathbf{k}$-points allowed by the dimensions of the configuration. For example, in a cubic supercell with cell length $L = \sqrt[3]{N}$, the allowed $\mathbf{k}$-vectors are

$$\mathbf{k} = 2\pi \left(\frac{n_1}{L}, \frac{n_2}{L}, \frac{n_3}{L} \right); \quad n_i \in \{0, 1, \ldots, L-1\}. \tag{2.29}$$

In order to project these frequencies to the appropriate $\mathbf{k}$-point in reciprocal space, the band unfolding equation used by Reference 156 gives the projection, ρ, for all ω as,

$$\rho(\mathbf{k}, \omega) = \sum_{\nu} \left\{ \frac{\delta[\omega - \omega(\nu)]}{N} \times \sum_{\alpha} \left| \sum_{jl} e^a_{jl}(\nu) \exp\left[\mathrm{i}\mathbf{k} \cdot \mathbf{r}(jl) \right] \right|^2 \right\}. \tag{2.30}$$

Here the projection, ρ, is effectively stating the extent to which the eigenvector of the phonon mode, ν, projects at each appropriate $\mathbf{k}$-point. If $\rho = 0$ the eigenvector is orthogonal to the $\mathbf{k}$-vector, while a value of $\rho = 1$ means that the $\mathbf{k}$-vector

chosen fully describes the motion of the phonon mode. By averaging over symmetry-equivalent **k**-vectors and multiple configurations, the accuracy of the calculations can be improved. Figure 2.10 shows the application of this method to an ordered supercell, where the projections are strictly in $\{0, 1\}$, as presented by Overy *et al.*[156]

In summary, SCLD provides a means for mapping the zone-centre excitations of a supercell back to the phonon modes which would be calculated in a single unit cell. This means that, in principle, we are able to, with relatively small computational expense, calculate the phonon modes of a disordered supercell, up to the limit of the reciprocal space resolution given by the number of **k**-points.

2.4 Synthesis

Two of the components of interest to this thesis were synthesised by collaborators, and I synthesised the remaining two. Both Er_2BaNiO_5 and $CsCoCl_3$ were produced during the course of this work. Both of these compounds have been synthesised by others in the past, however to the best of my knowledge, we have presented the first reports of the growth of single crystals of Er_2BaNiO_5 large enough for single-crystal neutron diffraction measurements. The synthesis of Er_2BaNiO_5 was performed with Dr Robin Perry.

2.4.1 Er_2BaNiO_5

Single-crystal samples of Er_2BaNiO_5 have been prepared for the first time using a flux method similar to that used by Yokoo *et al.* for the synthesis of single crystals of Y_2BaNiO_5.[74] Such a flux growth requires an inorganic solvent and high temperatures to allow a reaction to take place. This technique is generally a very good option

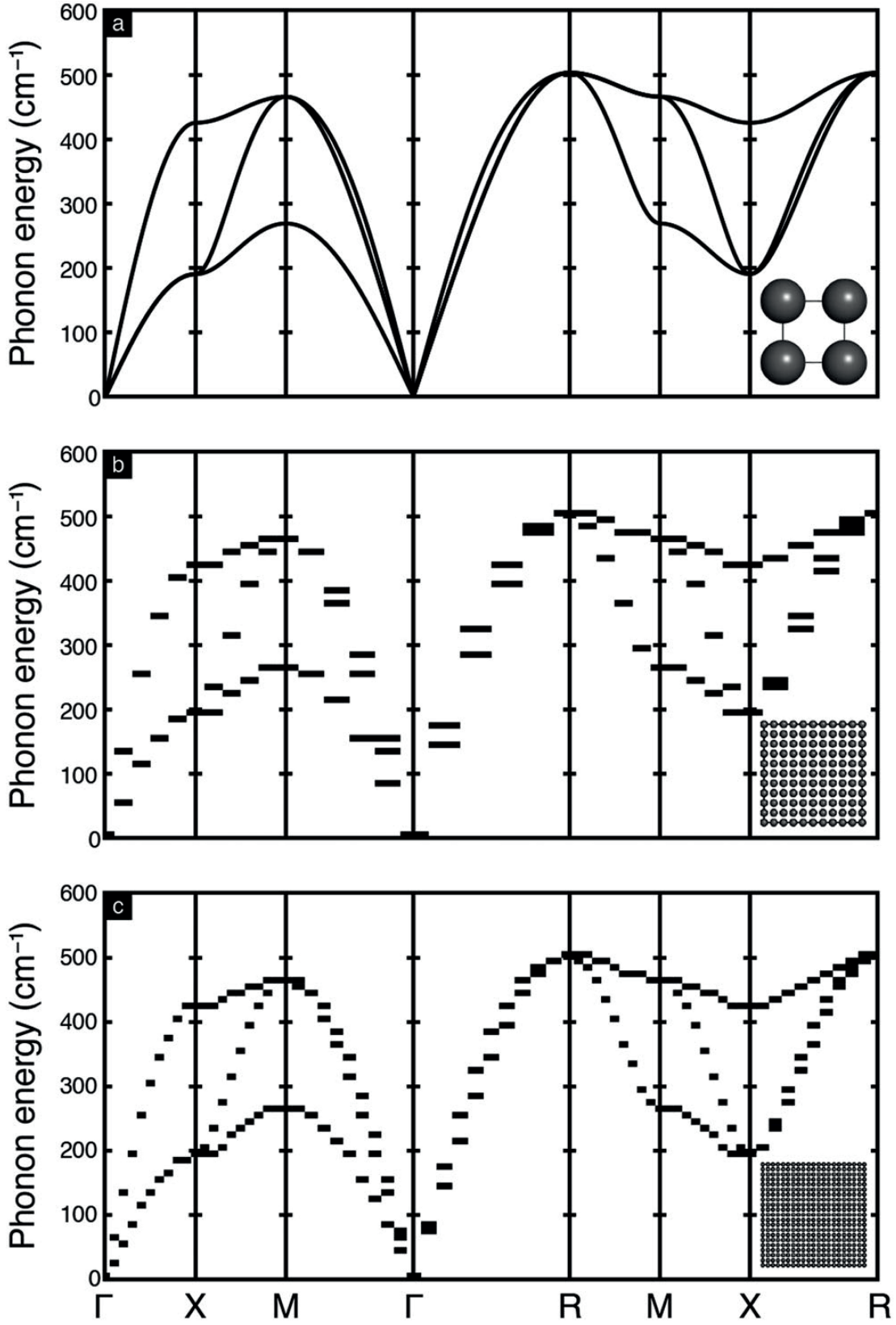


Figure 2.10: **a)** Phonon dispersion curves for a cubic unit cell containing one atom, as calculated using GULP.[157] Comparison is made with phonon dispersion curves calculated using SCLD, with **b)** a $10 \times 10 \times 10$ and **c)** a $20 \times 20 \times 20$ supercell. As presented by Overy *et al.*[156]

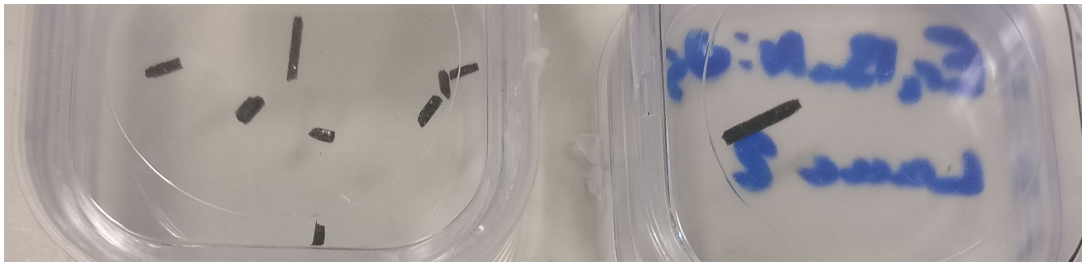


Figure 2.11: Single-crystal samples of Er_2BaNiO_5 formed using the synthesis method described in the text. The longest samples are on the order of 20 mm in length.

when the reagents melt incongruently, as appears to be the case with this system, however, it requires a fine control of the reaction conditions in order to produce large single crystals, as the short timescales often lead to mm-sized crystals. A 45 : 45 : 10 mixture of NiO:$BaCO_3$:Er_2O_3 was ground intimately and pre-reacted at 900 °C. The resulting mixture was then reground and heated at 1600 °C for 6 hours and then cooled to 1450 °C at 1 °C/hr. This led to formation of single crystals of Er_2BaNiO_5 from the flux. Dilute nitric acid was used to dissolve the remaining unreacted flux while preserving the Er_2BaNiO_5 crystals. An example of the crystals produced is shown in Figure 2.11.

2.4.2 $CsCoCl_3$

For the synthesis of $CsCoCl_3$ a number of techniques were attempted, based on methods published by other groups. Several very early reports of this compound exist and give evidence that it is possible to form $CsCoCl_3$ from aqueous solution of CsCl and $CoCl_2$, however all of our attempts at this synthesis method gave a mixture of products, mostly including the related compound Cs_2CoCl_4 and hydrated forms of the starting materials, as determined by powder X-ray diffraction. This is most likely due to the dissolution and reaction of $CsCoCl_3$ and left-over starting materials in the vacuum filtration and washing step of our synthesis to give Cs_2CoCl_4 as the

major product—a problem which is exacerbated if methanol is used as the solvent for washing. In order to avoid this problem, we turned to the approach published by Seifert in 1961 where they used a straightforward melt growth to form $CsCoCl_3$.[158] The binary phase diagram presented in Figure 2.12 shows that there is a eutectic point in the melting of CsCl and $CoCl_2$. As the resulting product is reported to be hygroscopic, a 1:1 molar ratio of CsCl and $CoCl_2$ was mixed and ground intimately in an Ar glovebox.[159] The mixture was then loaded into a borosilicate tube and sealed under Ar, removed from the glovebox and finally sealed under vacuum using an oxy-acetalene torch. Heating the sealed tube to 600 °C for 24 hours and cooling slowly to room temperature afforded a pale blue powder. This sample was removed from the tube in the glovebox, ground under Ar, and 13.46 g was loaded into a 8 mm vanadium sample can. Phase composition of our powder was confirmed using powder X-ray diffraction on a Brucker D8 Eco diffractometer using a Cu source.

2.4.3 Other Compounds

The other two compounds of interest in this thesis were synthesised by collaborators; an overview is presented below, with full details for $Tb(HCO_2)_3$ given in Ref. 137. The sample of $Gd_2Pt_2O_7$ used in our neutron scattering experiments was synthesised using high-pressure, high-temperature (HPHT) techniques by Dr Jason Gardner and Dr Wei-Tin Chen. For these experiments we required a sample of $Gd_2Pt_2O_7$ which has been made using ^{160}Gd in order to reduce the absorption cross-section of our sample, as natural abundance gadolinium is one of the most strongly absorbing elements. A stoichiometric amount of starting materials was intimately ground and filled into a gold capsule, and subsequently treated at 1100 °C

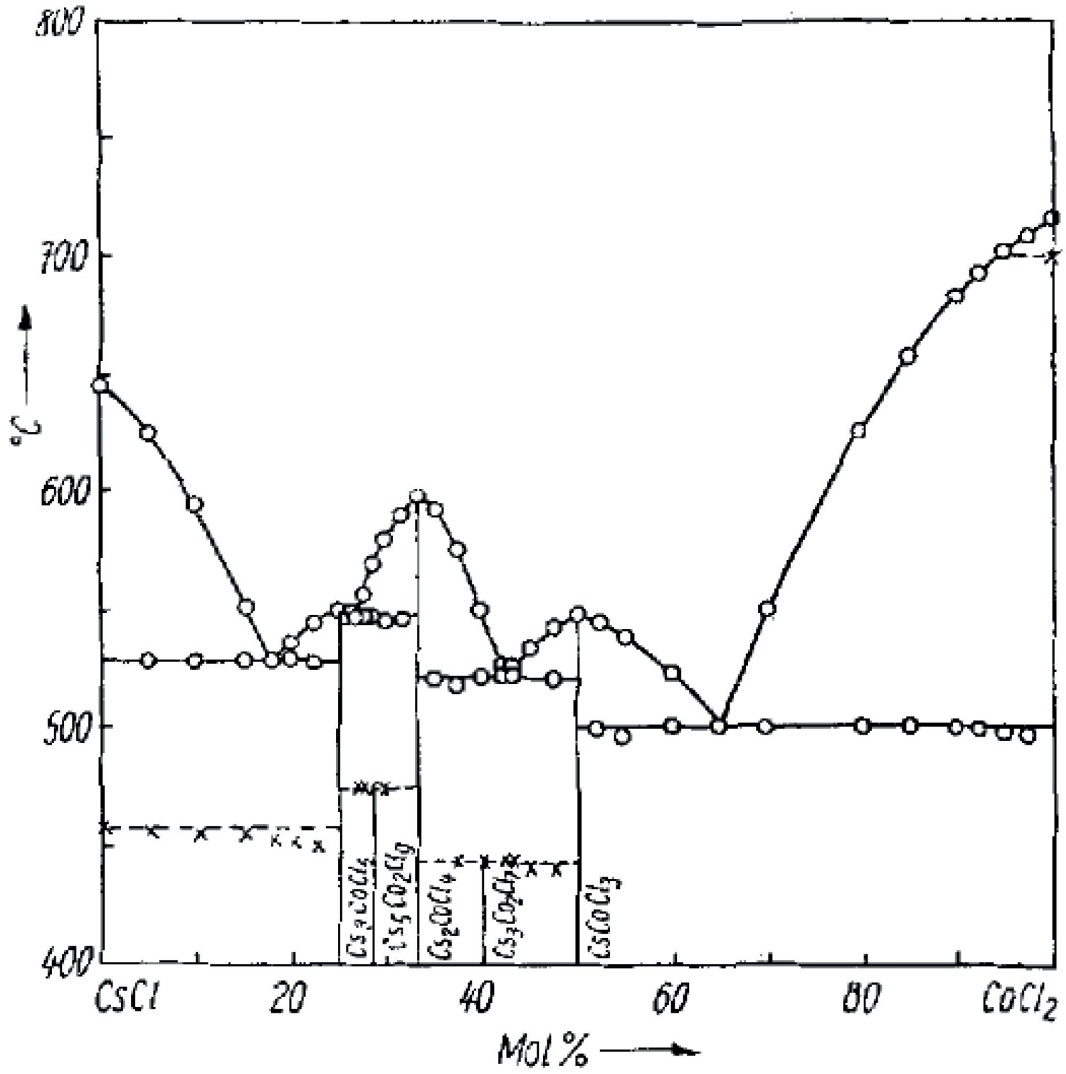


Figure 2.12: Binary phase diagram for the $CsCl/CoCl_2$ system, as presented by Seifert.[158]

and 6 GPa in a DIA-type cubic anvil high pressure apparatus.

$$^{160}Gd_2O_3 + 2PtO_2 \rightarrow {}^{160}Gd_2Pt_2O_7. \tag{2.31}$$

In this case, an HPHT synthesis was employed in order to prevent the decomposition of PtO_2 at the temperatures required. In order to confirm the phase purity of the polycrystalline sample, X-ray and neutron diffraction data were collected at both beamline I11, Diamond, Didcot, UK, and the POLARIS instrument, ISIS Neutron an Muon Source, Didcot, UK, respectively.

Chapter 3

One-dimensional magnetic order in the metal-organic framework $Tb(HCO_2)_3$

An investigation into the low-dimensional magnetic structures of $Tb(HCO_2)_3$ has been carried out using a combination of variable-temperature neutron scattering measurement, reverse Monte Carlo (RMC) analysis, and direct Monte Carlo (DMC) simulation of the evolution of magnetic order in $Tb(HCO_2)_3$ on cooling from 100 K to 1.6 K. The key result is that the spin transition at T_N involves antiferromagnetic ordering of 1D ferromagnetic Tb^{3+} spin-chains to give a short-range ordered state equivalent to the triangular Ising antiferromagnet (TIA). The spin chains decorate a triangular motif and only exhibit long-range order along the chain dimension. This stands in contrast to the long-range ordered models previously proposed—we show that these models are an artefact of applying conventional crystallographic approaches to a state that does not possess 3D order, and that therefore these models do not describe the true magnetic structure below T_N.

The work in this chapter was performed in close collaboration with a Part II student (Daniel Harcombe), under my supervision.

3.1 Introduction

The influence of partial, and low-dimensional, order on the magnetic structure of metal–organic frameworks (MOFs) is a field of ongoing research. In such MOFs, magnetically-active transition-metal or rare-earth ions are connected *via* organic ligands to form framework structures that extend in 1D, 2D, or 3D. It is the incor-

poration of these ligands into such frameworks which allows for the possibility of superexchange interactions that span a broad energy range to give rise to interesting magnetic properties. Since, in general, there exist well-established design rules for such systems, the possibility for the inclusion of low-dimensional structural motifs (*e.g.* chains, ladders, layers) is opened up. As shown in Chapter 1, the partial magnetic ordering of low-dimensional systems is of great interest for a variety of reasons, not least of which is the observation that even in systems where there is well-established 1D order, there is almost always a transition to full 3D order as a result. Taken together, the combination of design rules for MOF systems, and the ongoing interest in low-dimensional magnetic order, suggest that MOFs may be ideal candidates to host low-dimensional magnetism.[160] Indeed the magnetic response of a number of key MOF families—including formates,[161] oxalates,[162] and succinates[163,164]—can be interpreted in terms of low-dimensional behaviour.

Almost all of our collective understanding of magnetic order in MOFs is based on indirect experimental techniques, such as magnetic susceptibility, heat capacity, and dielectric constant measurements.[161–165] The combination of such measurements with neutron studies for traditional—*e.g.* oxide—systems allows us to identify features in indirect measurements related to low-dimensional order. However, this is not yet the case for MOFs. The magnetic interactions observed within MOF systems are markedly different than in dense, oxide based, materials, primarily due to the length, and nature, of the exchange pathways between metal centres. These differences have spurred a recent increase in the number of neutron experiments performed on MOF and MOF–like systems (*e.g.* Ref. 166), however it remains the case that such investigations are challenging both synthetically and experimentally. The

presence of organic ligands in such frameworks generally gives rise to a number of hydrogen atoms, which, due to their large incoherent neutron scattering cross-section, add a large 'background' to most neutron measurements, easily overwhelming the magnetic response for low-spin, and low spin-density, systems. Therefore, a great deal of care must be taken to appropriately dueterate such systems, and the removal of any protic solvents must also be considered.

In spite of the difficulties in collecting neutron scattering data for MOFs, recently the number of neutron experiments performed on MOF systems has increased significantly. In general, this increase has been motivated by the fact that neutron scattering measurements can help establish the nature of cooperative magnetic order directly, while other measurements may only be able to provide a basic measure of bulk interaction strength, or the presence of magnetic transitions. One example of a MOF which has been investigated by neutron scattering is $Tb(HCO_2)_3$.[137,167,168]

One key reason for the interest into the $R(HCO_2)_3$ (R = rare earth) series, is the evidence that the Gd^{3+} member exhibits a magnetocaloric effect (MCE) superior even to that of the canonical MCE system $Gd_3Ga_5O_{12}$.[137] At higher temperatures (4–10 K), which is the more relevant regime for *e.g.* cooling the superconducting magnets used in medical resonance imaging and nuclear magnetic resonance facilities, $Tb(HCO_2)_3$ has a better MCE performance than the Gd analogue.[137] Local ferromagnetic ordering offers a natural explanation for why magnetisation can be induced under field with such ease—and hence why it is that $Tb(HCO_2)_3$ exhibits strong MCE at temperatures for which the antiferromagnetically-correlated Gd analogue is relatively unresponsive. Thus, understanding the nature of the magnetic order in $Tb(HCO_2)_3$ may help aid the search for other materials which present supe-

rior MCE responses. It was in this context that terbium(III) formate, $Tb(HCO_2)_3$, was chosen as an appropriate target of study.

Under ambient conditions, $Tb(HCO_2)_3$ crystallises in the rhombohedral space group $R3m$.[137,169,170] All Tb^{3+} cations are crystallographically equivalent, and are connected by the O atoms of bridging formate ions to form 1D chains that lie coincident with the crystallographic threefold rotation axes [Fig. 3.1 a)]. The Tb...Tb separation along a given chain is 3.97 Å with the corresponding Tb–O–Tb angle 105.5°—a geometry that favours ferromagnetic coupling and provides a uniaxial crystal field at the Tb^{3+} site (point symmetry $3m$).[137] The chains pack on a perfect triangular lattice with inter-chain separation $a/\sqrt{3} = 6.02$ Å. Extended Tb–OCO–Tb bridges connect neighbouring chains; one end of the formate bridge has a bifurcated coordination, giving two inequivalent Tb...Tb superexchange pathways (distances 6.16 and 6.57 Å) for each pair of chain neighbours [Fig. 3.1 b)]. There is no experimental evidence for any change in space group symmetry between room temperature and 1.4 K.[137,167,171]

The presence of hydrogen in $Tb(HCO_2)_3$ means that neutron scattering measurements have been focused on the deuterated analogue: $Tb(DCO_2)_3$. Neutron diffraction has been used to characterise the magnetic structure of both the antiferromagnetic ($T < T_N \simeq 1.6$ K) and paramagnetic ($T = 3$ K) regimes [Fig. 3.2].[137,168] The system orders magnetically on cooling to 1.4–1.6 K, and conventional symmetry analysis of the magnetic Bragg scattering observed in this ordered phase identifies $P3m'1$ as the unique magnetic space group.[137,167,168] When the system transitions to this ordered magnetic phase on cooling below T_N, the magnetic Bragg peaks that emerge are subtly broader than the non-magnetic Bragg reflections and are accom-

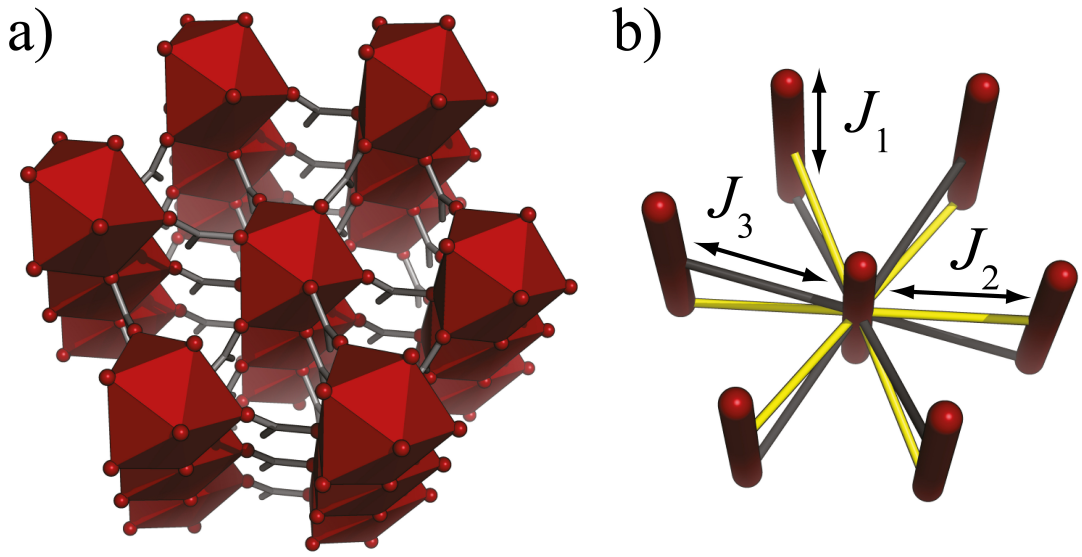


Figure 3.1: Crystal structure and key magnetic interaction pathways of $Tb(HCO_2)_3$. a) Tb^{3+} coordination environments (tricapped trigonal prisms; polyhedra) form face-sharing columns parallel to the crystallographic c-axis. Columns are arranged on a triangular lattice and are connected by formate ions, shown here in stick representation. b) Intra-chain exchange pathways are ferromagnetic (J_1), and the two inequivalent inter-chain exchange pathways (J_2, J_3) are collectively antiferromagnetic.

panied by a substantial diffuse scattering component that is highly structured in reciprocal space and thereby indicative of strongly correlated disorder.[104]

The $P3m'1$ magnetic unit-cell has the same size as the nuclear cell, however, the rhombohedral centering is lost. Two distinct spin ordering patterns (and their linear combinations), shown in Figure 3.3, are consistent with the observed magnetic Bragg reflection conditions and intensities. Both cases demand single-ion anisotropy with local moments aligned parallel to the c-axis; both require FM correlations along the Tb chains; and both correspond to antiferromagnetic (AFM) ordering patterns with zero net magnetisation. Ref. 168 gives a concise description of the magnetic structure using a basis vector approach, which is illustrative of the order presented in the left panel of Figure 3.3, and which I will use as an explanatory guide. The ordering vector given is $\mathbf{k} = (1, -1, 0)$ for which there are two possible irreps: we will focus in the $\boldsymbol{\Gamma}_2$ irrep, which is 1D in nature. Using this irrep, the atom at (0,0,0) has a magnetic moment, $\boldsymbol{\mu} = (0, 0, w)$ while the atoms at $(2/3, 1/3, 1/3)$ and $(1/3, 2/3, 1/3)$ have moments, $\boldsymbol{\mu} = (0, 0, -w/2)$. These values are directly equivalent to the schematic representation provided in the left panel of Figure 3.3. The second model can be partitioned into three sublattices where two ferromagnetic chains are coupled antiferromagnetically, and the remaining chain being disordered, which has been described as both a spin-idle structure[137] and, in the collinear limit describes the average structure of a partially disordered antiferromagnet (PDA), as described by Mekata.[54,172]

Both of the magnetic structures presented above were proposed on the basis of conventional crystallographic analysis. In both cases, as shown in Figure 3.3, a modulation in Tb^{3+} moment is required, which has no obvious physical origin. In the

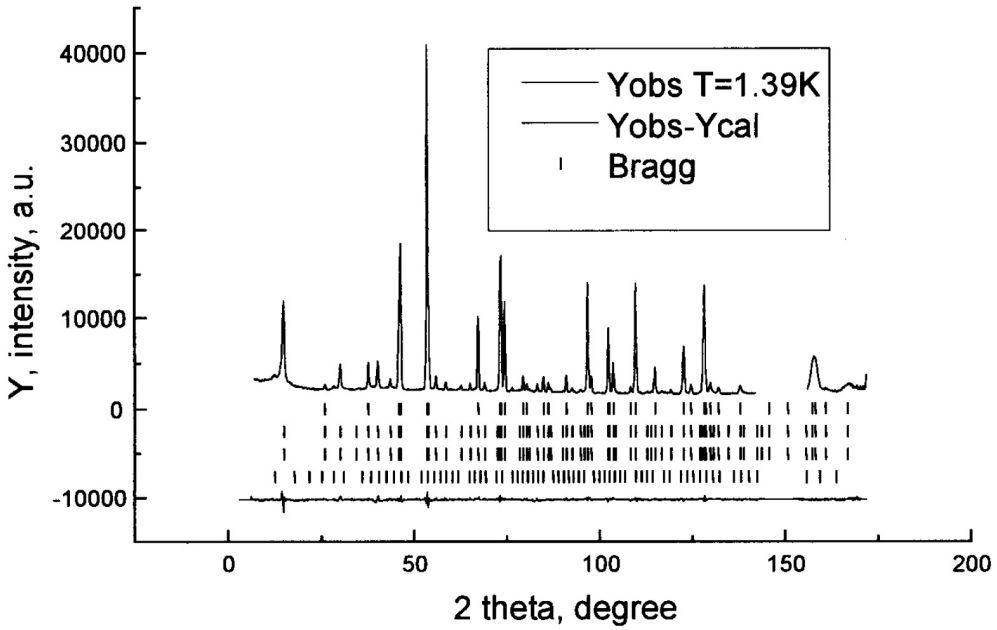


Figure 3.2: Observed and calculated diffraction patterns for $Tb(DCO_2)_3$ presented by Kurbakov *et al.* in Ref. 168. The middle two rows of tick marks define the reflections of the magnetic structure, with the second of these being necessary to account for the broad nature of the observed reflections.

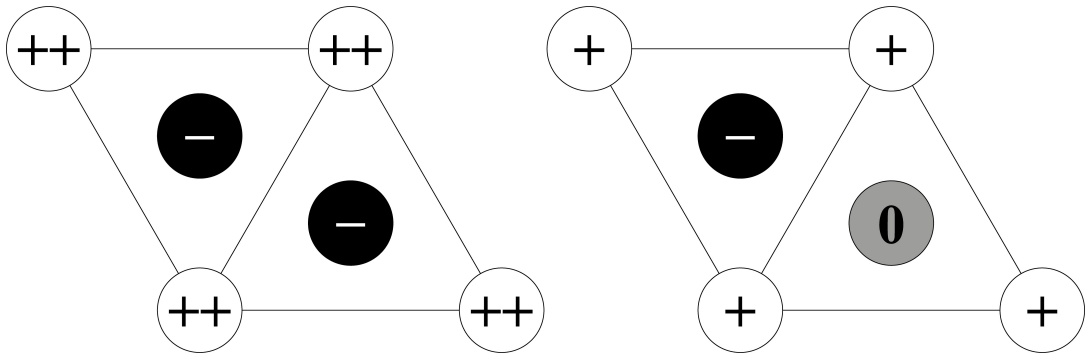


Figure 3.3: The two—crystallographically equivalent—magnetic unit cells proposed for $Tb(HCO_2)_3$ on the basis of magnetic Rietveld refinement below 1.6 K. Circles represent Tb chains projected onto the (a, b) plane, symbols '+' and '−' denote ferromagnetic chains with magnetisations along $\mathbf{c}$ and $-\mathbf{c}$, respectively, and '0' denotes the absence of any ordered moment. Based on Refs. 137,167.

study of disordered (non-magnetic) materials it is recognised that low-dimensional order often gives Bragg-like scattering features, interpretation of which by conventional crystallographic means leads to spurious structural models.[173,174]

In this chapter we remeasure the neutron total scattering patterns of $Tb(HCO_2)_3$ as a function of temperature in both the paramagnetic and magnetically ordered regimes. We then analyse these data using a combination of reverse Monte Carlo refinement and direct Monte Carlo modelling in order to ascertain the extent to which the previously proposed models provide an accurate description of the magnetic interactions in $Tb(HCO_2)_3$. As set out at the start of this chapter, our key observation is that the low temperature transition at T_N involves 1D ferromagnetic (FM) order along Tb^{3+} spin-chains to give a partially-ordered state equivalent to the triangular Ising antiferromagnet (TIA). In this low-T phase, the direction of chain magnetisation tends to alternate between neighbouring chains but this alternation is frustrated and is not itself ordered. This state—which emerges also in DMC simulations—is distinct from the 3D "partially disordered antiferromagnet" (PDA) model.[54] Its magnetic scattering pattern contains both Bragg-like and structured

diffuse features, with the Bragg intensities indistinguishable from those calculated either from the multiple-moment models suggested in previous Rietveld studies or from the PDA model. The existence of a well-defined 1D state in $Tb(HCO_2)_3$ distinguishes this system from other spin-chain triangular antiferromagnets such as $Ca_3Co_2O_6$,[51,60] $CsNiF_3$,[175,176] and CoV_2O_6[59] and suggests its low-temperature physics may be of particular interest in the study of 1D magnetism.

3.2 Results and Discussion

3.2.1 Neutron Total Scattering

Neutron powder total scattering data for $Tb(DCO_2)_3$ were collected across a temperature range spanning 300–1.6 K using the WISH diffractometer at ISIS.[177] The sample used was that reported in Ref. 137. For data collection, the sample was placed into a vanadium can of 6 mm diameter and loaded on the diffractometer. Temperature was controlled using a low-background ^{4}He cryostat. Typical data collection strategies involved neutron counts of *ca.* 20 μA h. Data were corrected using standard protocols as implemented in the Mantid software, merging banks at constant scattering geometry in order to improve counting statistics. The scattering from an empty 6 mm vanadium can was also measured under identical conditions, processed using the same protocols, and used for background subtraction.

The nuclear scattering contribution is well confined to nuclear Bragg peaks, which could be fitted using GSAS[178] and subtracted from the total scattering data collected with the 27.1° and 58.3° banks. These corrected data were merged, placed on an absolute scale (using the GSAS scale factor), and rebinned at intervals of

$\Delta Q = 0.02\,\text{Å}^{-1}$. The final total usable Q-range spanned 0.1–3.7 Å^{-1}, although within this range a total of five regions contaminated with nuclear scattering contributions were excised and omitted from our subsequent analysis. The corrected data are shown in Figure 3.4.

These data show no evidence of long-range magnetic order for $T > 1.6\,\text{K}$, which is consistent with the earlier studies of Refs. 167 and 137. As we approach $T = 1.6\,\text{K}$, we observe that the diffuse scattering becomes gradually more structured around several points in reciprocal space, with the region around $Q \approx 0.7\,\text{Å}^{-1}$ showing the largest increase in intensity. This gradual increase resolves itself into peaks siting atop a diffuse base at $T = 1.6\,\text{K}$ (see inset to Figure 3.4). We first analysed these sharp reflections as in Refs. 167 and 137, in terms of conventional magnetic Bragg scattering analysis, but we will come to rationalise their nature in terms of a partially ordered magnetic structure in due course.

3.2.2 Average Structure Refinement

The nuclear and magnetic structures of $Tb(DCO_2)_3$ were refined against the neutron scattering data collected at 1.6 K using GSAS.[178,179] Basic crystallographic details are given in Table 3.1 and the refined atomic positions and magnetic moments are listed in Table 3.2. The magnetic model used for these refinements is that proposed by Kurbakov *et al.*[168] In this long-range ordered model, the magnetic space group is $P3m'1$, which constrains the Tb^{3+} moments to lie along **c**. An illustration of the Rietveld fit obtained is given in Fig. 3.5. By using the same profile parameters for both the nuclear and magnetic Bragg reflections we can see that there is a small additional broadening to the magnetic component, which is observed in the residual

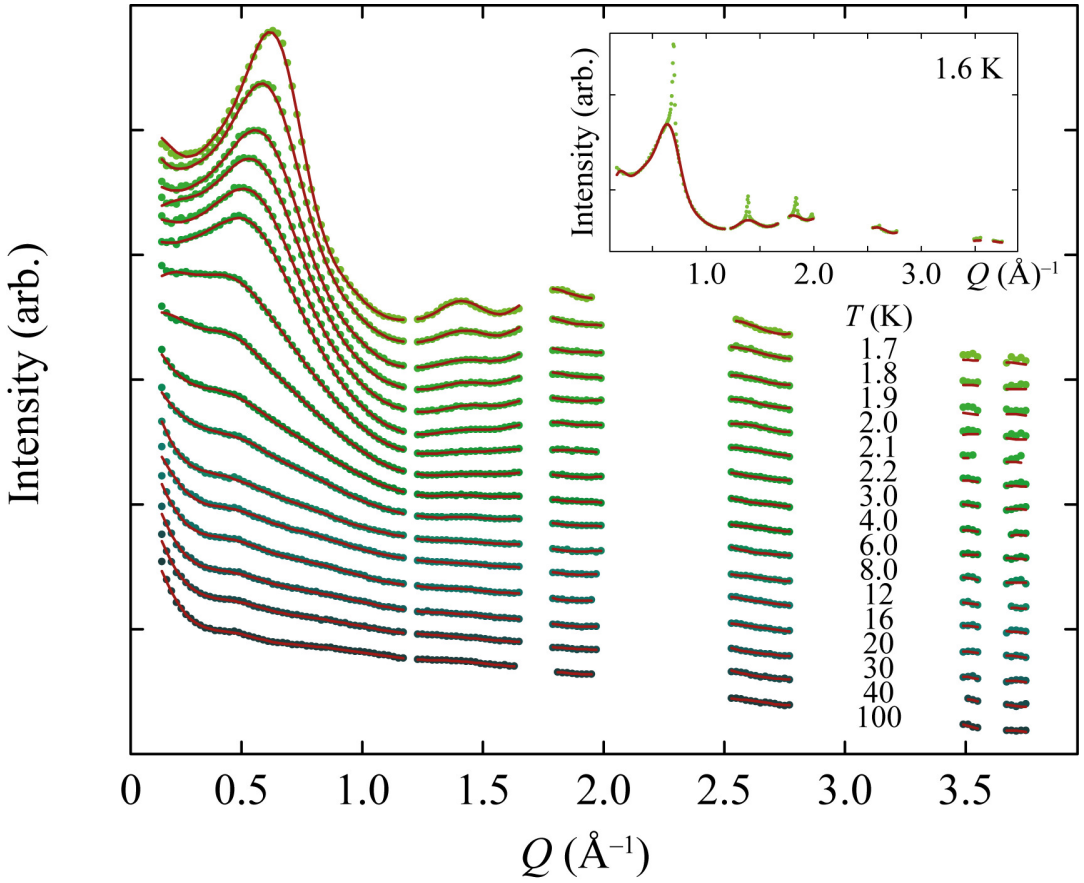


Figure 3.4: Temperature-dependent magnetic scattering in $Tb(DCO_2)_3$ and its SPINVERT analysis. Scattering data are shown as filled circles, with SPINVERT fits shown as red solid lines. Regions of the scattering pattern contaminated with nuclear scattering have been excluded. The inset shows scattering data collected at 1.6 K within the partially ordered regime together with a small-box SPINVERT fit.

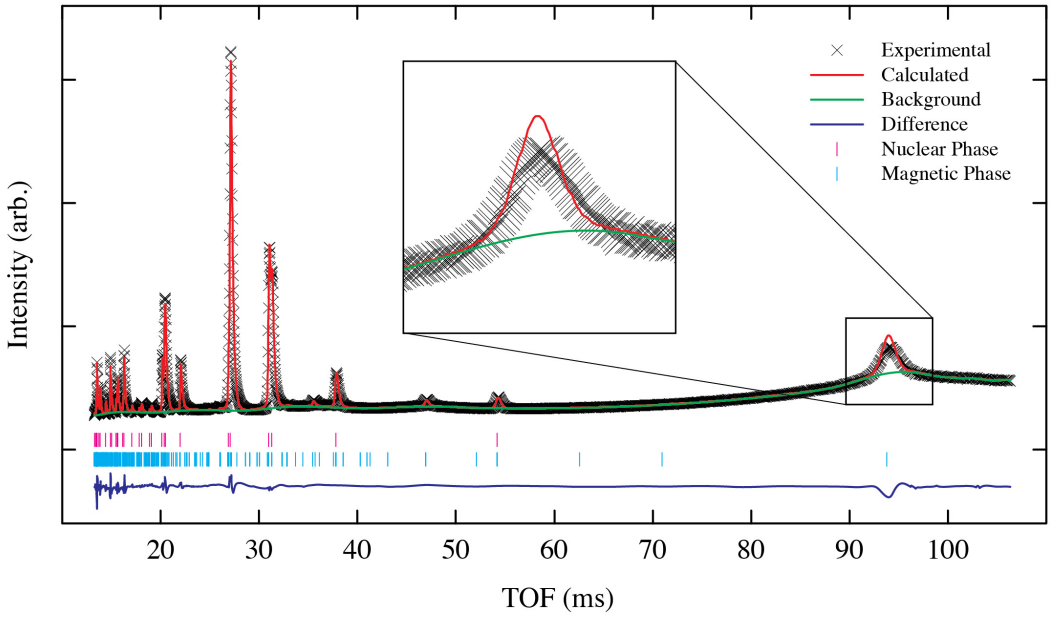


Figure 3.5: Rietveld fit to neutron diffraction data measured at 1.6 K for the $Tb(DCO_2)_3$ structural parameters given in Tables 3.1 and 3.2. Inset is a larger representation of the low-Q magnetic peak.

function for the highest d-spacing reflections, as shown in Fig. 3.5. We find that the magnitude of the magnetic moment matches well with that previously measured by Saines *et al.*[180]

3.2.3 Reverse Monte Carlo

For magnetic neutron scattering data collected in the paramagnetic regime, $T > T_N$, the absence of magnetic Bragg reflections necessitataed the use of an RMC approach. We have used the SPINVERT code,[143,152] applying the analytical approximation to the Tb^{3+} form factor given in Ref. 181 and a linear-in-Q background function.[143] For our initial refinements, we used RMC spin configurations representing a $\sim(50\,\text{Å})^3$ supercell of the nuclear $R3m$ cell (1170 spins); larger configurations gave equivalent results at greater computational expense. The precise

Empirical formula	$TbC_3D_3O_6$
Formula weight ($g\,mol^{-1}$)	296.957
Crystal system	Rhombohedral
Nuclear space group	$R3m$ (No. 160)
Magnetic space group	$P3m'1$ (Fedorov space group No. 156)
Radiation	neutron, time of flight
Temperature (K)	1.6
a (Å)	10.42047(12)
c (Å)	3.96889(5)
Number of observations	15 569
R_p	0.0459
wR_p	0.0452
χ^2	53.91

Table 3.1: Crystallographic details determined by time of flight neutron powder diffraction.

Atom	Wyckoff site	x	y	z	U_{iso} (Å^2)
Tb	$3a$	0	0	0*	0.0121(5)
C	$9b$	0.51342(7)	0.48658(7)	0.2167(5)	0.0107(3)
O1	$9b$	0.46669(7)	0.53331(7)	−0.0130(5)	0.0103(3)
O2	$9b$	0.58314(6)	0.41686(6)	0.1715(6)	0.0099(3)
D	$9b$	0.49501(7)	0.50499(7)	0.4778(5)	0.0267(5)

Atom	Moment (μ_B)
Tb	−2.351(17)
	1.176(8)

Table 3.2: Refined structural model determined using time-of-flight powder neutron diffraction. *This coordinate was fixed, as required in the polar space group $R3m$.

supercell used for RMC refinements was given by the transformation

$$\begin{bmatrix} \mathbf{a} \\ \mathbf{b} \\ \mathbf{c} \end{bmatrix}_{\mathrm{RMC}} = \begin{bmatrix} 3 & -3 & 0 \\ 5 & 5 & 0 \\ 0 & 0 & 13 \end{bmatrix} \begin{bmatrix} \mathbf{a} \\ \mathbf{b} \\ \mathbf{c} \end{bmatrix}_{R3m} . \tag{3.1}$$

This choice of supercell yields orthogonal and approximately isotropic configurations. Fits of the SPINVERT refinements are shown in Fig. 3.4. Using the same configuration size, a SPINVERT refinement of the 1.6 K data set—*i.e.* within the ordered regime—manages to account satisfactorily for the diffuse component of the scattering but cannot reproduce the Bragg-like features [see inset to Fig. 3.4]. This is to be expected[143] as the reciprocal-space resolution $\Delta Q \sim 0.01\,\text{Å}^{-1}$ required to describe Bragg scattering is many times smaller than the resolution afforded by the size of the RMC supercells ($\Delta Q \simeq 2\pi/r_{\mathrm{max}} = 0.2\,\text{Å}^{-1}$).

If we wish to analyse our refinements in more detail, we can turn to the real-space properties of the spins in our simulation box. One of the simplest properties we can extract is the orientations of the spins. To do this, we take the stereographic projection of the spin vectors on the surface of a sphere. Our results for three representative temperatures (1.7, 2.2, and 8 K) are shown in Figure 3.6. We see that, at the lowest temperatures, there is a strong preference for the spins to lie coincident with the c-axis. This Ising-like anisotropy is not unexpected for Tb^{3+} and was previously noted for this compound in Ref. 137. We see that there is clear evidence of this anisotropy at both 1.7 and 2.2 K, but is not obvious at 8 K, where the distribution of spins in the supercell takes on a more isotropic form. Since RMC is an inherently random approach it tends to produce a lower bound on the true

extent of single-ion anisotropy, and we would expect the true degree of this single-ion effect to persist to higher temperatures than evident from RMC.[131,143]

It is possible to define the ratio of maximum and minimum orientational distribution densities of the spins in our RMC configurations as $\Delta \ln(p) = \ln(p_{\max}) - \ln(p_{\min})$. The temperature dependence of this function is shown in Fig. 3.6 b) for our SPINVERT refinements. We find an approximate power-law dependence below 10 K, with vanishing anisotropy at higher temperatures.

Given that RMC predicts that there should be a large, Ising-like, single-ion anisotropy if the refinement allows spins to have Heisenberg degrees of freedom, we have repeated our SPINVERT refinements with the spins restricted to have Ising degrees of freedom across our whole temperature range. These fits are shown in Figure 3.7. Across the whole temperature range studied, Ising spins are able to reproduce the diffuse scattering observed. Naturally, the greater number of degrees of freedom when Heisenberg spins are used in the refinement should provide a better fit than if the spins are constrained to lie coincident to the c-axis. However, when the constraint of Ising spins was enforced in our refinements, we still produce acceptable fits to datasets collected at all but the lowest temperature measured. Thus we cannot rule out that Ising-like behaviour persists to much higher temperatures than suggested by the stereographic projections obtained for unconstrained RMC fits.

Further to the stereographic projections of the spins, we can calculate the spin-spin correlations within our refined spin configurations. We decompose the correlation functions, by calculating them across two orthogonal directions: along the chains of Tb^{3+} ions, and perpendicular to those chains. Our results are shown in Figure 3.8 a), again given for three representative temperatures. From these plots

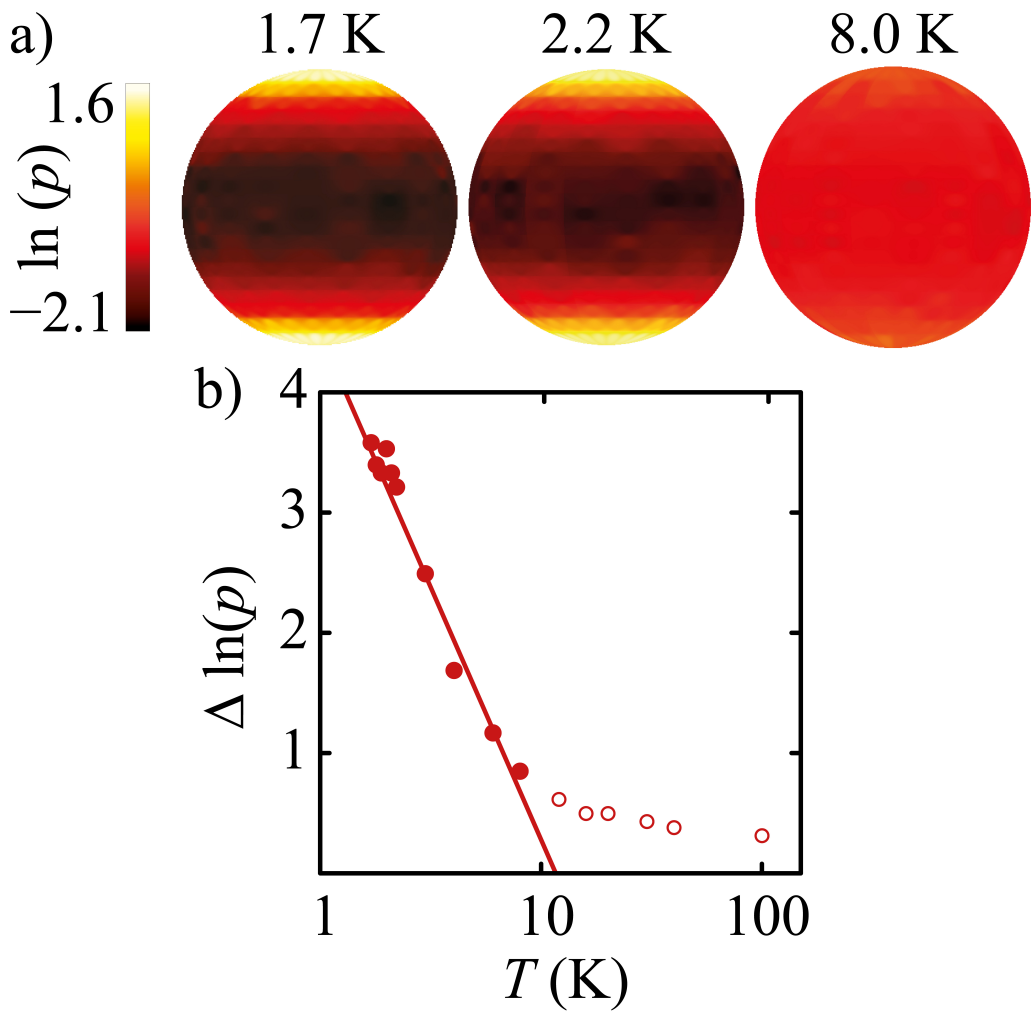


Figure 3.6: a) The single-ion spin orientation functions are shown in stereographic projection, with colours indicating relative distribution probability $p(\theta, \phi) = \rho(\theta, \phi)/\mathrm{d}(\cos\theta)\mathrm{d}\phi$; here $\rho(\theta, \phi)$ is the fraction of total spins within the angular region $\mathrm{d}(\cos\theta), \mathrm{d}\phi$. b) Temperature dependence of the single-ion anisotropy, as determined from the SPINVERT refinements. The solid line shows the fit to the low-T experimental values (filled symbols).

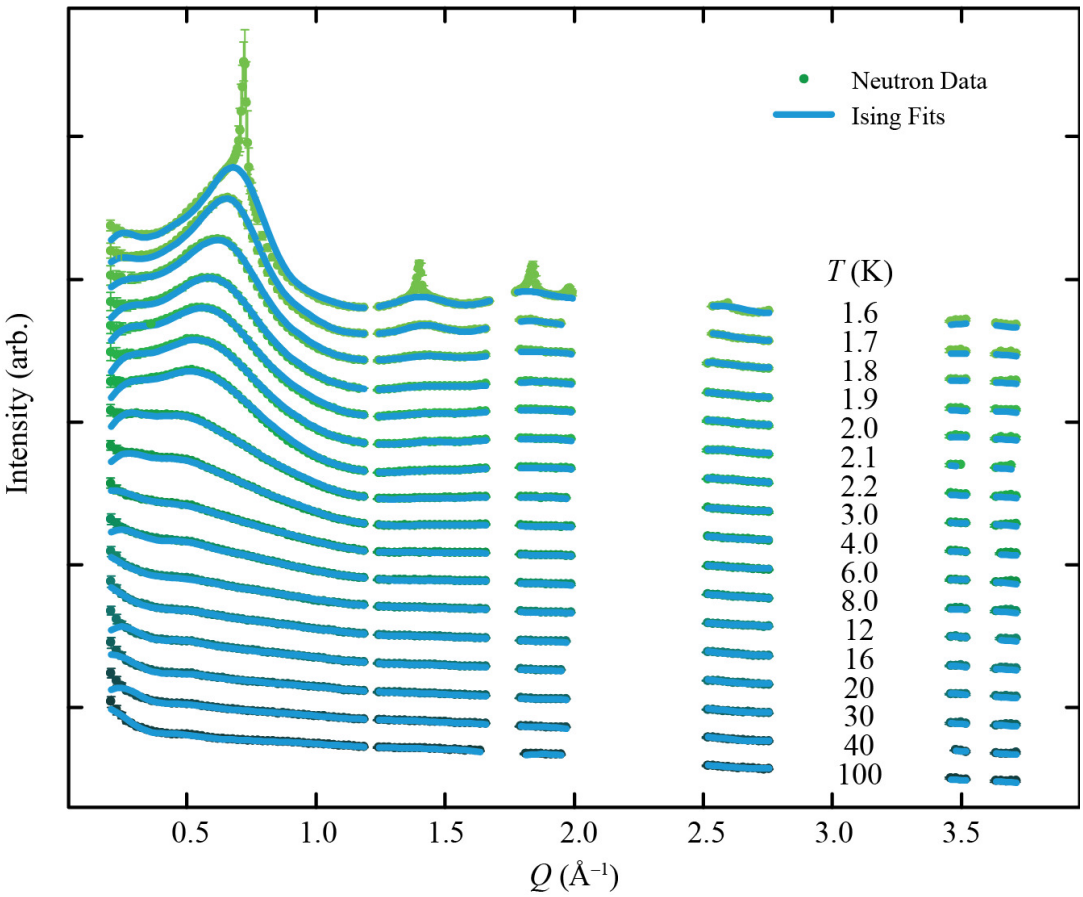


Figure 3.7: Temperature-dependent magnetic scattering in $Tb(DCO_2)_3$ and its SPINVERT analysis with spins constrained to be Ising spins. Scattering data are shown as filled circles, with SPINVERT fits shown as blue solid lines. Regions of the scattering pattern contaminated with nuclear scattering have been excluded.

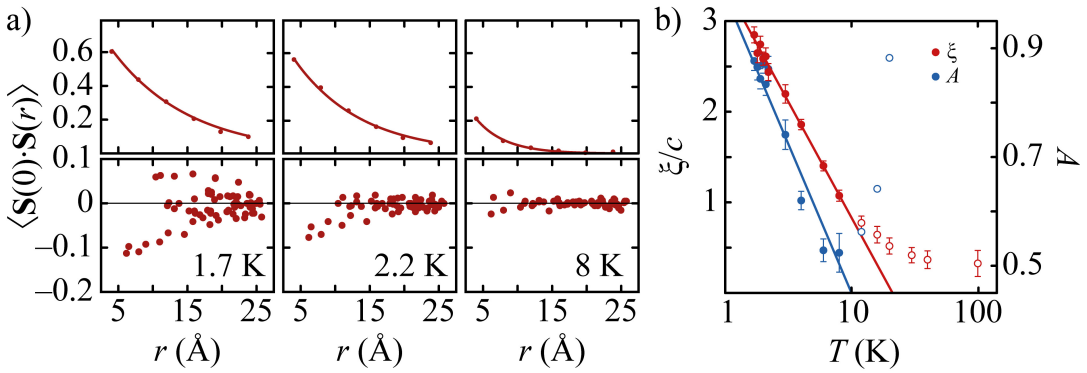


Figure 3.8: a) Pairwise correlation functions at three representative temperatures spanning the paramagnetic regime as generated from RMC refinement. Spin correlation functions have been separated into intra-chain (top panels) and inter-chain (bottom panels) terms. The lines show the fits generated using the stretched-exponential given in Eq. 3.2. The uncertainties on all points are smaller than the symbols. **b)** T-dependence of the intra-spin correlation length and prefactor, extracted from the fits shown in **a)**. The solid lines show fits to the low-T experimental values (filled symbols).

we see the low temperature evolution of strong FM correlations along the chains. We see that at 1.7 K there is an exponential decay of the intra-chain pairwise spin-spin correlation function which extends out to beyond 20 Å.

By contrast, at the lowest temperatures measured, the inter-chain correlations are antiferromagnetic, as evidenced by the negative values of $\langle \mathbf{S}(0) \cdot \mathbf{S}(r) \rangle$ for $r =$ 6.16 and 6.57 Å. These interactions are necessarily frustrated, and lead to net FM correlations for next-nearest inter-chain neighbours (*e.g.*, $r = a = 10.42$ Å), which are most noticeable at 1.7 K. Spin correlations corresponding to spin pairs taken from chains that are neither nearest-neighbours nor next-nearest neighbours are very weak: these account for the series of data points around $\langle \mathbf{S}(0) \cdot \mathbf{S}(r) \rangle = 0$ for $r > 12$ Å.

It is also possible to investigate the intra-chain spin correlation functions analytically by fitting our experimental values using the empirical expression

$$\langle \mathbf{S}(0) \cdot \mathbf{S}(r, T) \rangle = A(T) \exp[-r/\xi(T)]. \tag{3.2}$$

Here ξ can be interpreted as a measure of the spin correlation length, and $A < 1$ allows for the population of spin waves ($A \to 1$ in the classical Ising limit). Fits to the correlation functions and the corresponding values of the parameters ξ, A for our SPINVERT configurations are shown in Fig. 3.8 a, b). We find an approximate power-law dependence for both ξ and A for $T < 10\,\mathrm{K}$; the fits are not well constrained above 10 K. The Ising formalism $c/\xi = \ln[\coth(J/T)]$ [182] could not provide a convincing fit to our SPINVERT correlation functions; we interpret this failure of the strict Ising model as an indication of the relevance of the energy scale of the single ion anisotropy, which distinguishes this system from systems such as $Ca_3Co_2O_6$ where Ising behaviour is sufficient to fit the experimental spin correlation functions. [51,60]

3.2.4 Direct Monte Carlo

On the basis of the correlation functions presented above, it is possible to propose that the basic spin physics of the system might be captured by a combination of Ising-like single-ion anisotropy, FM intra-chain interactions and AFM inter-chain interactions. The simplest Hamiltonian containing these ingredients is

$$\mathcal{H} = J_{\parallel} \sum_{\langle i,j \rangle} \mathbf{S}_i \cdot \mathbf{S}_j + J_{\perp} \sum_{\langle\langle i,j \rangle\rangle} \mathbf{S}_i \cdot \mathbf{S}_j - D \sum_i S_{iz}^2, \tag{3.3}$$

where $\langle \cdots \rangle$ and $\langle\langle \cdots \rangle\rangle$ denote sums over neighbouring spins within and between chains, respectively. The prefactors $J_{\parallel} = J_1 < 0$ and $J_{\perp} = J_2 \equiv J_3 > 0$ are as shown in Fig. 3.1 b), and $D > 0$ is the single-ion term. To the best of our knowledge, there is no general theory for this interaction model on the rhombohedral lattice that would allow us to extract the J_i, D parameters directly from the experimental spin correlation functions, even if specific realisations are well understood. [183,184] Conse-

quently, one of the best approaches is to use Eq. 3.3 to drive DMC simulations and perform a grid search with different parameter sets in order to attempt to reproduce the basic temperature dependence of the experimental spin correlation functions. The correlation functions are shown in Figure 3.9. We can thereby identify a set of J_i, D values which capture the key behaviour of paramagnetic $Tb(DCO_2)_3$.

Using such a grid search approach, a variety of candidate J_i, D values were tested, carrying out DMC simulations using the code developed in Ref. 131 and described in Section 2.3. Parameter sets were ranked according to the fidelity of reproduction of the pairwise spin correlation functions at all measured temperatures. The DMC spin configurations were the same size and geometry as in the original SPINVERT refinements. Simulations were initialised with random spin orientations, with T systematically lowered from 100 K to 1.7 K following equilibration at each step. Simulations were repeated 100 times and the correlation functions averaged over these independent runs. We found the closest match to experiment for $J_{\|} = -1.5(5)$ K, $J_{\perp} = 0.03(1)$ K, $D = 70(20)$ K (note that the S^2 term has been subsumed within these J_i, D values).

While the match to the AFM inter-chain interactions observed using RMC is improved by distinguishing J_2 and J_3 (see Fig. 3.10) this effect appears to be marginal. Importantly we do not require this additional complexity for the conclusions we draw here as they do not significantly affect the features observed. We do note, however, that the $J_{\|}$ and D parameters showed strong covariance, such that reasonable fits could be obtained with larger $|J_{\|}|$ and smaller D. Because the RMC spin orientation distributions underestimate anisotropy, we cannot use these distributions to help quantify D (other than to act as an indication of the tested value being too

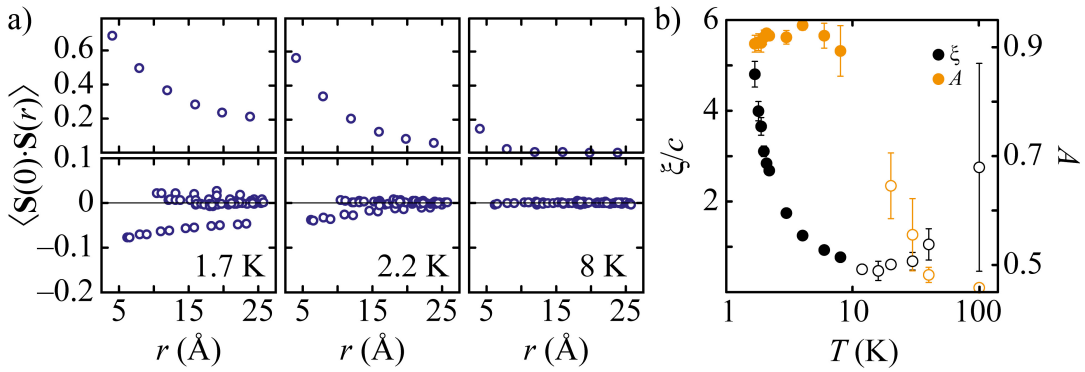


Figure 3.9: a) Pairwise correlation functions at three representative temperatures spanning the paramagnetic regime as generated from DMC simulation. Spin correlation functions have been separated into intra-chain (top panels) and inter-chain (bottom panels) terms. b) T-dependence of the intra-spin correlation length and prefactor, extracted from the fits to the intra-chain correlations shown in a).

low, which is not the case here). Nevertheless the value of D we obtain is consistent with that obtained elsewhere for Tb^{3+} in axial crystal fields,[185] and the qualitative behaviour of the DMC simulations themselves is the same for all acceptable $J_{\parallel}, D$ combinations we identified.

By driving the simulation through a temperature equivalent to the experimentally determined transition temperature, it is observed that the Hamiltonian also gives rise to a phase transition on cooling below ∼1.6 K for all J_i, D values consistent with the neutron scattering measurements of the paramagnetic phase. Surprisingly, these simulations give rise to states which are not long-range ordered, as would be expected based on the models presented in Refs. 137,168. Instead, direct interrogation of the DMC configurations reveals only partial order. Individual chains exhibit FM order with their magnetisation aligned either parallel or antiparallel to **c**; the chain magnetisation tends to alternate between neighbouring chains but this alternation is frustrated by the underlying triangular lattice and so there is no 3D magnetic order. We determine this state to be a representation of a triangular Ising antiferromagnet (TIA).[103] Long-range order is suppressed in this state, and it

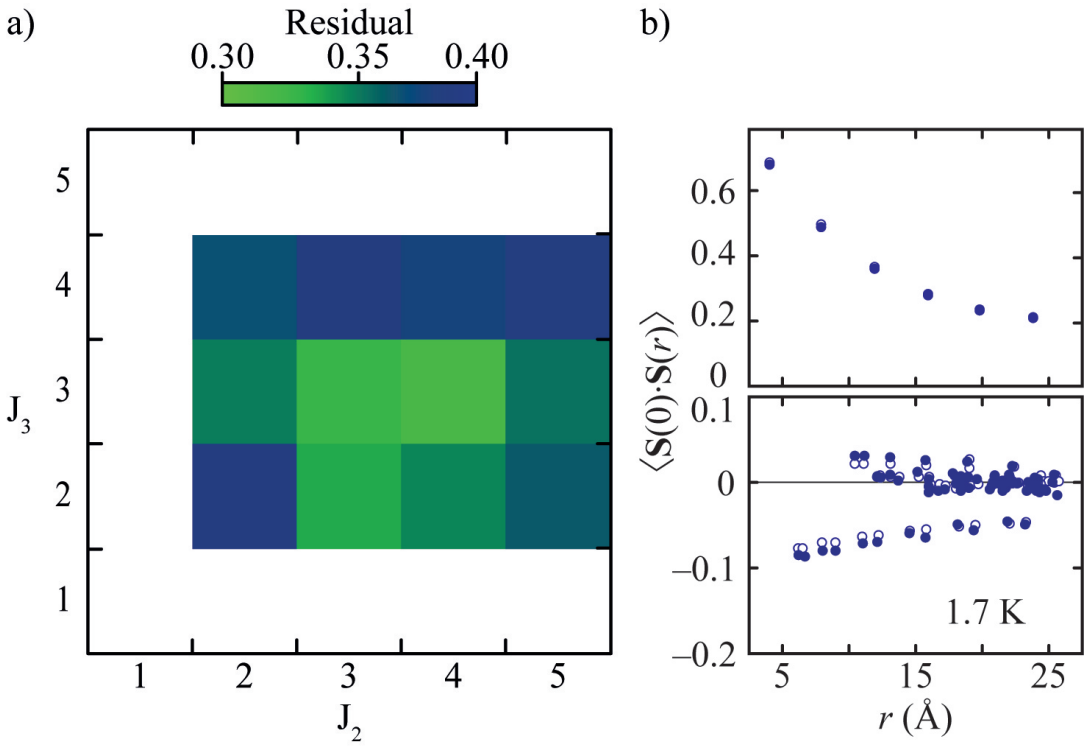


Figure 3.10: a) Graphical representation of a DMC parameter grid search used to explore J_2, J_3 space. Here $J_{\|}$ and D have been constrained to equal -1.5 and $70\,\mathrm{K}$, respectively. **b)** The resulting pairwise spin correlations at $T = 1.7\,\mathrm{K}$ for the optimum parameter set obtained in **a)**: *i.e.*, $J_2 = 0.03\,\mathrm{K}$, $J_3 = 0.04\,\mathrm{K}$. Open symbols show the correlation terms obtained in the approximation $J_2 = J_3$ and filled symbols show the same terms obtained for independent J_2, J_3. Uncertainties are smaller than the symbols in all cases.

is local rules on each triangle in a 2D motif which specify the spin directions. In this realisation of a TIA, it is the collective chain magnetisations which are mapped onto the individual Ising variables. We find no evidence of sublattice ordering which would be necessary to satisfy either of the equivalent PDA models [Fig. 3.12]. Hence we sought to determine whether this TIA state might rationalise the coexistence of Bragg and diffuse scattering observed experimentally at 1.6 K.

As discussed above, the issue of finite—and relatively small—box size prevents the simulations which have passed through the low-temperature phase transition from describing the sharp features in the magnetic scattering at 1.6 K. A significantly larger simulation box would be required to afford the resolution needed; a problem which is not computationally feasible at this time. If, however, an assumption is made that the state below T_{N} contains only the local ordering of Ising spin-chains, a simpler model can be proposed, which can afford the required reciprocal-space resolution. By turning the problem into a 2D representation of the triangular Ising antiferromagnet, a new interaction Hamiltonian can be applied:

$$\mathcal{H} = \sum_{p} \big(\big(\sum_{i} S_i \big)^2 - 1 \big), \tag{3.4}$$

where the sums run over all individual triangles, p, and the three spins in each triangle, i. This allows the derivation of a large 2D configuration corresponding to a ground-state of the TIA. The configuration size used corresponded to a 4×4 supercell of the (001) projection of the original SPINVERT configuration. By assigning the spin of an atom in the 3D supercell to be the same as that of its projection on to the (001) plane, it is easy to expand this 2D Ising configuration into a 3D Heisenberg

spin configuration. In doing so each Ising state ϵ of the 2D configuration was used to generate the spin vector $\mathbf{S}$ of a column of spins in the 3D configuration:

$$\epsilon \in \{-1, +1\} \rightarrow \mathbf{S} = (0, 0, \epsilon). \tag{3.5}$$

This configuration now corresponds to a $4 \times 4 \times 4$ supercell of the original SPINVERT/DMC configuration, improving the reciprocal space resolution to $\sim 0.06\text{Å}^{-1}$.

The 3D spin configuration generated was then used as an input for an additional SPINVERT refinement, now allowing small reorientations of the spins; with the aim to introduce small fluctional movements of the spins as would be permitted at finite temperature. Note that the size of the configuration meant that a full SPINVERT refinement from a random spin arrangement was computationally unfeasible. Instead the aim was simply to show that a sensible spin configuration based on the intermediate ordered state identified in DMC simulations could account for the observed neutron diffraction pattern. This process introduced small spin reorientations but preserved the basic TIA spin structure. After sufficient SPINVERT refinement cycles to allow 25 proposed moves/spin, we obtained a calculated magnetic diffraction pattern that was in good agreement with the experimental data. Crucially, we find that this intermediate order TIA state can account for the entire experimental scattering pattern, including the appearance of Bragg-like peaks with the correct reflection conditions and relative intensities [Fig. 3.11 a)]. By construction, this model requires no unphysical modulation of the Tb^{3+} moment. Rather the *magnitude* of chain magnetisation is homogeneous throughout the configuration; our model contains an average spin projection $|\langle S_z \rangle| = 0.662(4)$ along the chain axes

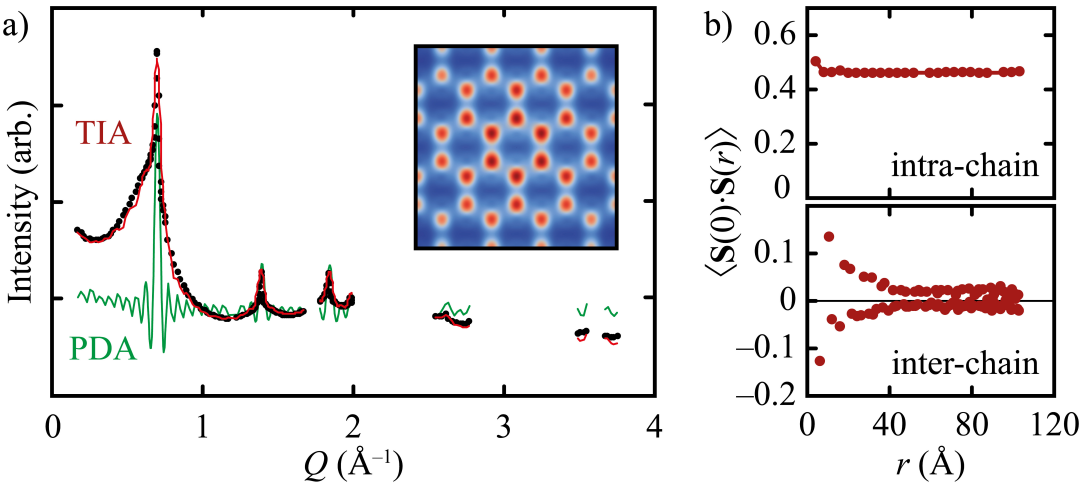


Figure 3.11: a) Comparison of experimental neutron scattering data (black symbols) with neutron scattering patterns calculated for $Tb(DCO_2)_3$ configurations corresponding to TIA (red line) and PDA (green line) states; the 'ripples' are a finite-size effect [186] and are more noticeable for the PDA model because it contains 3D order. Bragg-like features appear at the regions of reciprocal space associated with maxima in the TIA diffuse scattering pattern (inset). b) The pairwise spin correlation functions for the TIA model separated into intra-chain (top) and inter-chain (bottom) terms. 1D order has two clear signatures in these correlation functions: the correlation length diverges for intra-chain spin pairs, and the inter-chain correlations vanish as inter-chain separation increases.

with standard deviation = 0.136. A PDA model with the same spin projection values gives a diffraction pattern with the same Bragg reflection conditions and relative Bragg intensities but cannot account for the structured diffuse scattering observed experimentally [Fig. 3.11 a)]. Hence the TIA model reproduces both the Bragg and diffuse components of the magnetic intensities, but the PDA model accounts only for the Bragg component.

It is worth asking ourselves what form we would have expected the magnetic neutron scattering to take, if we had been designing a TIA state *ab initio*. A number of sources have tackled this question, including Keen and Goodwin[104] and Yoon and Millane.[105] In both of these cases, the authors propose that (if we had access to 3D reciprocal space) continuous diffuse scattering would be observed around the Brillouin zone boundary, with a greater intensity localised on its vertices. This is further

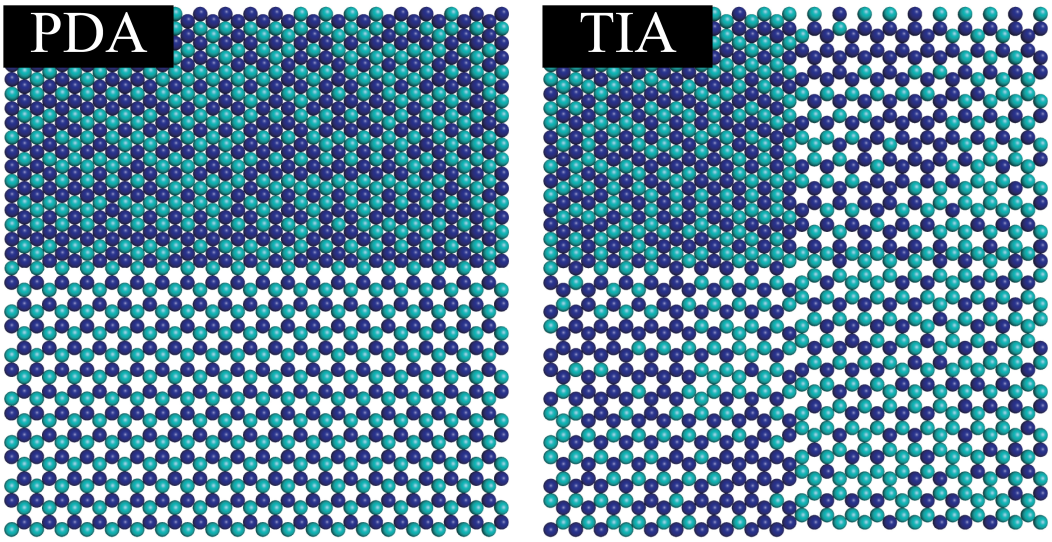


Figure 3.12: Comparison of the TIA and PDA states with Ising variables represented by green and blue spheres. In both cases every triplet of neighbouring Ising states $\epsilon = \pm 1$ obeys the sum rule $|\sum_i \epsilon_i| = 1$, but the PDA model contains a honeycomb sublattice (shown as the lower half) with strict antiferromagnetic order. Sites not included in this sublattice adopt random Ising states. For the TIA state, none of the three sublattices exhibit long-range order. Illustrated here by showing three different representations the TIA configuration, each with one of the three sublattices omitted.

supported by the latter paper, where it is derived that the TIA state should feature correlations which decay algebraically, the Fourier transform of which gives sharp reciprocal-space features accompanied by a characteristic broad base, as we see here. In both of these papers, the key outcome is that the powder averaged scattering pattern of a triangular Ising antiferromagnet would be expected to show sharp maxima in the continuous diffuse-scattering function, which are only marginally broadened relative to the structural Bragg reflections.

If we turn now to the spin correlation functions extracted from our TIA configuration [Fig. 3.11 b)] we see the aforementioned form of the correlation function. The correlation length diverges (over the $\sim$10 nm scale of the configurations) for *intra*-chain spin pairs, reflecting long-range 1D ferromagnetic order. Since the coupling between these (ordered) chains is antiferromagnetic and frustrated, they tend to anti-align; the *inter*-chain spin correlations are antiferromagnetic for spin pairs taken from neighbouring chains, and positive for next-nearest chain neighbours. The effects of frustration suppress the long-range order in this plane, and so the spin correlation becomes vanishingly small for successively distant spins. The divergence of the 1D ferromagnetic spin correlation length between 1.6 and 1.7 K [*cf.* Figs. 3.4 b) and 3.11 b)] is consistent with the second-order phase transition postulated on the basis of the analysis of magnetic Bragg scattering using conventional crystallographic approaches.[137] Data collection at (even) finer temperature intervals around T_{N} would allow more detailed characterisation of the critical behaviour of this unusual transition.

3.3 Conclusions

The interest in this system was initially sparked by an unusual magnetic scattering pattern, as shown in the inset to Fig. 3.4 a), containing a superposition of Bragg-like features and structured diffuse scattering. RMC analysis of these data was computationally intractable, as the size of the box of spins required to account for the Bragg-like features ($\sim 10^5$ spins) means that refinement from a randomly-oriented spin configuration is simply too expensive. DMC simulations not only allow us to explore phase behaviour at reduced computational expense, but also allow for the inference of a Hamiltonian from the experimental data. Therefore, we have used DMC simulations to generate spin configurations for $T = 1.5\,\mathrm{K} < T_\mathrm{N}$, driven by the Hamiltonian in Eq. 3.3 parameterised so as to match the experimental (RMC) spin correlation functions measured within the paramagnetic regime ($T \geq 1.7\,\mathrm{K}$). At the simulation temperature of 1.5 K, the DMC configuration shows 1D FM order along spin chains but TIA-like disorder between chains; the "TIA model" shown in Fig. 3.12. A large spin configuration corresponding to an idealised TIA model was then generated, and allowed to relax using small spin reorientations during an RMC refinement against the experimental data. The resulting spin configuration accounts entirely for the experimental scattering pattern [Fig. 3.11 a)]. The spin correlation functions shown in Fig. 3.11 b) are derived from this RMC-refined TIA model and so represent the experimental spin correlations at 1.6 K. Finally, we verified explicitly that a PDA model (partial 3D order) with intra-chain spin correlations identical to those in our RMC model cannot account for the experimentally-observed diffuse scattering.

This analysis indicates that in the magnetically ordered state of $Tb(HCO_2)_3$, accessed below 1.6 K, is 1D in nature, such that the remnant spin degrees of freedom map this system onto the 2D TIA. The sharp reflections observed in the neutron scattering patterns are not true Bragg reflections, but correspond to maxima in the continuous scattering function [inset to Fig. 3.11 a)] with precisely the form expected for TIA phases.[187] It was shown in Ref. 105 that interpretation of these "reflections" using conventional crystallographic approaches leads to a three-sublattice average structure model (*viz.* PDA) as portrayed in Fig. 3.3. Consequently, the modulation in magnitude of ordered moment from chain to chain given by such a model is an artefact of applying conventional crystallographic tools to a state with no true 3D order.

There are a number of implications which can be drawn from the identification of 1D magnetic order in $Tb(HCO_2)_3$; some of which are further explored in Chapter 4. By analogy to $CsNiF_3$ the signature of emergent phenomena in its excitation spectrum may be anticipated;[45–47] indeed the contrast in single-ion anisotropy between these two systems (easy-axis *vs* easy-plane) provides a means of testing key aspects of the theory of anisotropic 1D ferromagnets.[44,183] The TIA state observed in $Tb(HCO_2)_3$ may also provide an explanation for the large magnetocaloric response observed previously. As we will see in Chapter 4, the TIA model possesses a greater residual entropy than the PDA model, which we would expect to give rise to a larger MCE.

Despite conceptual similarities to $Ca_3Co_2O_6$, there is an order-of-magnitude difference in $J_{\parallel}/J_{\perp}$ which acts to stabilise the intermediate order state observed in $Tb(HCO_2)_3$.[60] Comparison must be made with the work of Dixey *et al.* in which the

low-temperature response of $Tb(HCO_2)_3$ was investigated further.[188] Their neutron diffraction measurements below $T = J_\perp \sim 30\,\mathrm{mK}$ suggest that an "emergent charge ordered state"[189] is established, containing elements of 3D order, as would have been expected from the magnitude of the exchange constants determined above. From a materials design perspective, the 1D behaviour of $Tb(HCO_2)_3$ is a direct consequence of the underlying MOF architecture. Chemical substitution of the formate ions for longer bridging ligands may allow even more extreme $J_\parallel/J_\perp$ values to be realised, presumably stabilising 1D behaviour over a larger temperature range. Substitution at the Tb^{3+} site may also be of interest:[169] $Gd(HCO_2)_3$ exhibits AFM intra-chain coupling, and so the $Gd_{1-x}Tb_x(HCO_2)_3$ series (Ref. 137) may allow realisation of random-chain 1D magnets.[190]

Chapter 4

One-dimensional antiferromagnetism in $CsCoCl_3$

Following on from the study of $Tb(HCO_2)_3$ of the previous chapter, I use this chapter to present our investigation into $CsCoCl_3$. The chapter contains two distinct, but related, sections. First, I make use of techniques analogous to those used in the previous chapter to study the partial magnetic order in $CsCoCl_3$. We find that, as with $Tb(HCO_2)_3$, this structure can be described in terms of a TIA, where the chains of Co^{2+} ions themselves are, again, antiferromagnetically coupled, but the coupling within a given chain is antiferromagnetic rather than ferromagnetic. I show that the TIA arises due to frustration of the effective phase of antiferromagnetic order from chain to chain. Secondly, I have examined the key differences between the TIA and PDA phases in terms of the magnetic excitations we would expect. To do this, I have expanded the technique of supercell lattice dynamics and band unfolding in order to calculate the magnetic inelastic neutron spectra which would be expected for these states.

4.1 Introduction

As we have previously determined, the application of traditional crystallographic techniques to systems where there is only short-range order may lead to misidentification of the true magnetic structure. Since the previous chapter focused on a rare-earth MOF, we wish to extend the methods we have developed to more traditional, dense, inorganic systems. Our starting point was to perform a literature

search to identify whether other compounds have been reported to possess partially disordered structures on a triangular lattice. From our search we identified that a range of materials had been described as supporting partial order, with some being identified directly as partially disordered antiferromagnets (PDAs). These systems included $CaCoRhO_6$,[191,192] $RbCoBr_3$,[193–195] and the $CsCoX_3$ (X = Co, Br) family.[67,196–198] A common theme in these earlier studies is that when these materials undergo transitions into their partially disordered states, the magnetic Bragg peaks that appear are often described as being relatively broad—we will return to this theme later.

Here we focus on $CsCoCl_3$. Its nuclear structure contains chains of face-sharing $CoCl_6$ octahedra which lie parallel with the crystallographic c-axis of its hexagonal unit-cell. The $P6_3/mmc$ space-group distributes these chains in the ab-plane so as to form an edge-sharing triangular network. This is equivalent to an hexagonal perovskite structure. All Co^{2+} ions are crystallographically equivalent and separated by $a = 7.202\,\text{Å}$ in the ab-plane, and by $c/2 = 3.016\,\text{Å}$ along the c-axis at ambient temperatures, as shown in the schematic in Figure 4.1 a).

The material exhibits three magnetic ordering temperatures: 20.82 K, 14 K, and 5 K. At the very lowest temperatures (*e.g.* 4 K) the magnetic space-group of $CsCoCl_3$ is given as $P6'_3/m'cm'$.[198] This corresponds to a structure with two active magnetic propagation vectors,

$$\begin{aligned} \mathbf{k}_1 &= (1/3, 1/3, 0) \\ \mathbf{k}_2 &= (0, 0, 0), \end{aligned} \tag{4.1}$$

Atom	x	y	z	$\mathbf{m}_x$	$\mathbf{m}_y$	$\mathbf{m}_z$
Co_1	0	0	0	0	0	-2.80
Co_2	1/3	2/3	0	0	0	2.66

Table 4.1: The positions of the magnetically active ions in $CsCoCl_3$ in fractional coordinates along with the components of the magnetic moment in μ_B, as given by Mekata and Adachi.[198]

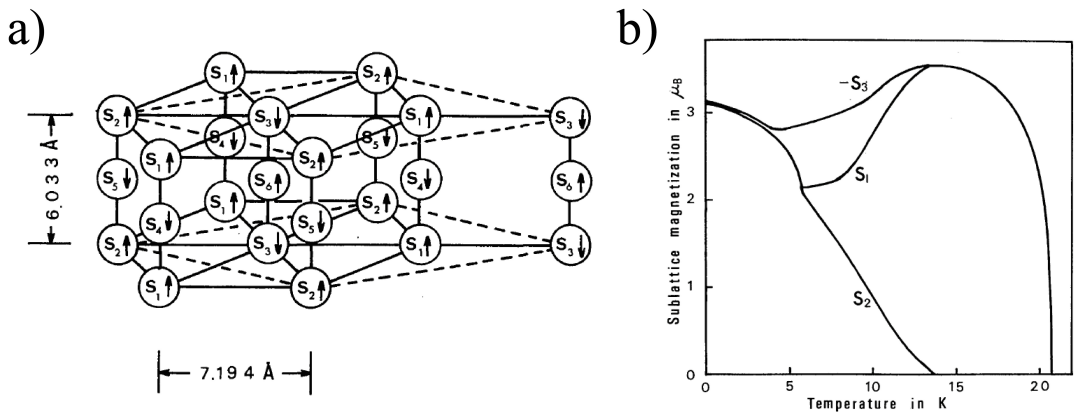


Figure 4.1: a) Magnetic structure of $CsCoCl_3$. The dotted lines show the relationship between the magnetic and the crystallographic unit cell in the ab-plane. b) The probable temperature dependence of the sublattice magnetisations. Both panels from Mekata and Adachi, Ref. 198

and two magnetically inequivalent Co^{2+} ions at $(0, 0, 0)$ and $(1/3, 2/3, 0)$. The magnetic moment of each site, determined by magnetic neutron diffraction measurements, is given in Table 4.1. If only $\mathbf{k}_1$ were active in this magnetic structure, $Co_2(\mathbf{m}_z) = -Co_1(\mathbf{m}_z)/2$. Using the nomenclature of Ref. 198 we can describe this state in terms of three sublattices where (at 4 K), $S_1 = S_2 \neq S_3$ [Figure 4.1 b)]. At higher temperatures, there is a complex dependence of the sublattice magnetisation on the temperature [Figure 4.1 b)]. However, our interest is in the highest-temperature regime—$14 < T < 21$ K—in which the sublattice magnetisations are given as $S_1 = -S_3$, $S_2 = 0$. Note that there is a strong similarity between this average magnetic structure and that of the PDA state proposed for $Tb(DCO_2)_3$ [Figure 3.3].

In this structure, the chains themselves are thought to be good realisations of

antiferromagnetic Ising $S = \frac{1}{2}$ chains, and previous investigations have shown that along the chains, the fundamental exications are solitons—*i.e.* domain-wall pairs—which can propagate along the chain directions.[68,69,199] These observations are consistent with predictions that the lowest-energy excitations of an antiferromagnetic Ising $S = \frac{1}{2}$ spin-chain should be the propagation of domain walls.[200]

Any finite size representation of the PDA and TIA models will form part of a large manifold of ground-states and predicting the inelastic neutron scattering associated with these representations is not trivial. Since *e.g.* linear spin-wave theory as implemented in SpinW[39] requires a unit-cell descriptor of the magnetic state we are interested in, it would not, in general, be possible to calculate the magnetic excitations using this well documented method. It is therefore necessary to develop an approach which can be used if we are presented with a magnetic supercell of the original unit cell. Such a technique has previously been applied to phonon calculations where mass, or force-constant, disorder is treated as either random or correlated, using 'supercell lattice dynamics' (SCLD).[156] Here we have expanded this technique to calculate magnetic excitations in order to facilitate the comparison of the theoretical inelastic neutron scattering patterns of TIA and PDA states.

This chapter will initially follow the same general outline as Chapter 3. We will present the results of our neutron diffraction measurements for $CsCoCl_3$, and analyse them using simulations of the possible magnetic states. Following on from this, we will investigate more generally the differences in the inelastic neutron scattering spectra of systems which can be described as possessing either PDA or TIA phases. We will present our conversion of SCLD to deal with magnetic systems along with proof-of-concept calculations. Finally we will determine whether PDA and TIA

phases would be distinguishable using inelastic neutron scattering.

4.2 $CsCoCl_3$

4.2.1 Synthesis

A melt-based synthesis for $CsCoCl_3$ was used as described in Section 2.4.2. Phase composition of our powder was confirmed using powder X-ray diffraction on a Brucker D8 Eco diffractometer using a Cu source, and by neutron diffraction on WISH at 300K [Fig. 4.2]. We find an approximately 0.5% contribution to the scattering from Cs_2CoCl_4, which we can model in the general refinements, but are able to ignore in any temperature subtracted magnetic calculations, as $T_N = 217\,mK$, *i.e.* well below the temperature of our measurements.[201]

4.2.2 Neutron Total Scattering

Our neutron total scattering measurements were collected on WISH, using a standard ^4He (ILL orange) cryostat. 13.46 g was loaded into an 8 mm vanadium sample can in an Ar glovebox and quickly transferred to the beamline. Data were collected at the base temperature of the cryostat (1.5 K), in 2 K intervals between 5 K and 25 K, and at 300 K. Our data were corrected using measurements of an empty can and the standard reduction scripts used on WISH. At 300 K our neutron diffraction data and Rietveld refinement confirm the sample composition [Fig. 4.2]. We refined against all banks of WISH simultaneously using FULLPROF.[202] Both caesium and cobalt lie on special positions with fixed fractional coordinates. Chlorine sits on the 6*h* Wyckoff site, with a free x coordinate. Our refinement of this coordinate to $x = 0.1546(1)$ matches the value reported previously by Melamud *et al.*,

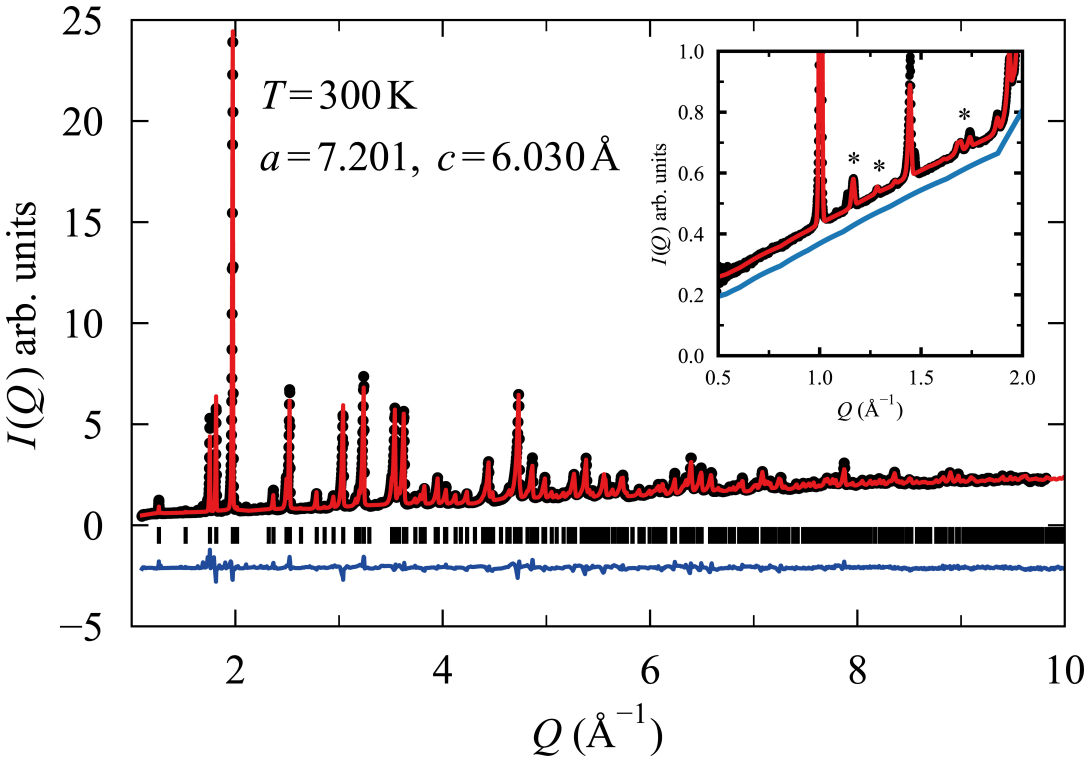


Figure 4.2: Neutron diffraction data at 300K, as measured on the backscattering banks of WISH, with Rietveld refinement shown in red, the difference in blue, and the reflections for $P6_3/mmc$ shown as black tick-marks. Inset: Low-Q data from lower angle banks, showing the interpolated background (light blue line) as calculated in FULLPROF. The * indicate the $\sim 0.5\%$ Cs_2CoCl_4 impurity.

within error.[67]

In our low temperature measurements, we begin to observe additional intensity in both the diffuse scattering, and as additional peaks, due to magnetic interactions. Since the magnetic propagation vector is reported to be $\mathbf{k} = (1/3, 1/3, 0)$ we would expect to have some magnetic intensity coincident with the nuclear Bragg reflections. We found that the structural and magnetic features are not well separated and it was not simply possibly to exclude regions of the pattern contaminated with nuclear scattering. We therefore make use of temperature subtraction in order to isolate the magnetic scattering. In order for this technique to be effective, we would ideally have a dataset slightly above T_N—so that there is only a slight difference in the position of the nuclear scattering—where the system is purely paramagnetic. Due to the

amount of lattice compression between 300 K and $T \leq 25$ K, it was not possible to perform a temperature subtraction from the ambient temperature data. For this reason we performed a temperature subtraction of our low-temperature datasets relative to the data collected at 25 K in order to isolate the magnetic scattering. We will come to show that the system is not truly paramagnetic at 25 K, and discuss the implications for our interpretation of the data.

In Figure 4.3, we present our temperature-subtracted data. At 21 K we start to see structured diffuse scattering appearing, which has resolved itself into sharp peaks at 19 K. We note, as seen for $Tb(DCO_2)_3$, these peaks appear to have a relatively broad base. Between 13 and 11 K, we see a further set of sharp reflections appear in our diffraction pattern. If we compare these transitions with the approximate phase diagram shown in Figure 4.1 b), we can see that we appear to be observing changes in the magnetic structure at temperatures very similar to those measured in Ref. 198. If we assume that in this work and previous reports the thermometry is accurate, it would appear that above the previously determined T_N we still see evidence of structured diffuse scattering, indicating that there is likely to be a correlated paramagnetic regime extending above T_N. In order to determine this more conclusively, it would be necessary to measure these data at much finer temperature steps than we have used here.

4.2.3 Preliminary comparison with idealised PDA and TIA

In the remainder of this section, I will focus on the 19 K dataset, as earlier studies indicate that at this temperature the system should have transitioned into

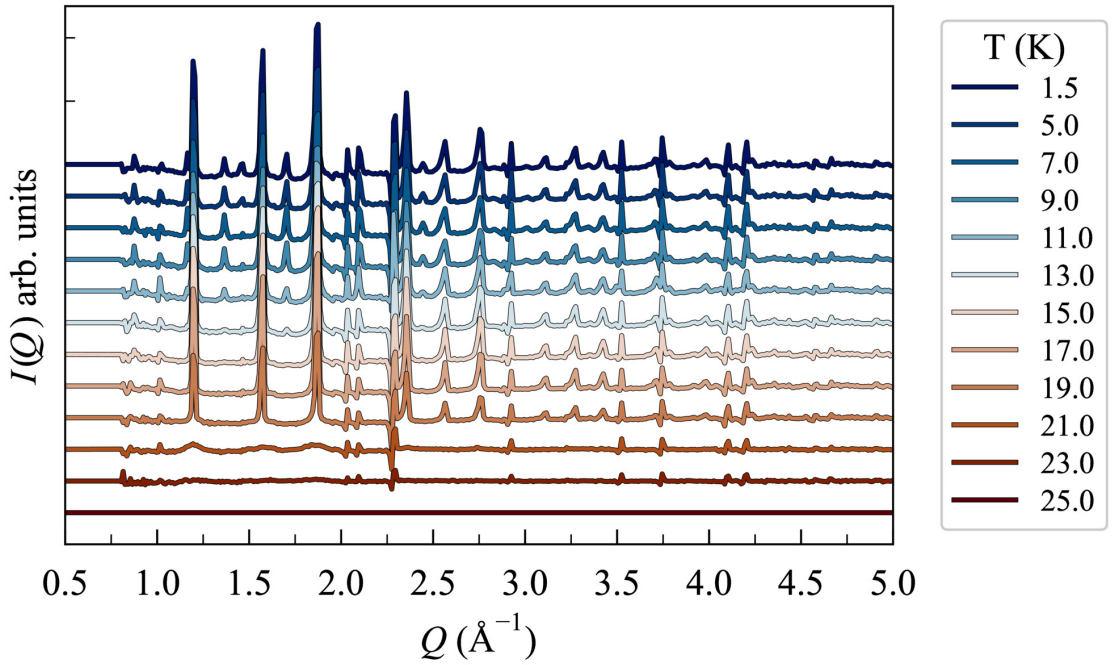


Figure 4.3: Temperature dependence of the temperature subtracted magnetic neutron scattering for $CsCoCl_3$, relative to $25\,K$. Two transitions are observable at 19 and 11 K.

the proposed PDA state, while also being sufficiently far away from any lower-temperature transitions.

In order to test whether the magnetic scattering at 19 K is characteristic of partial magnetic order, we have generated idealised models for both PDA and TIA states. We have used an orthogonal supercell of the hexagonal unit cell given by the transformation:

$$\begin{bmatrix} \mathbf{a} \\ \mathbf{b} \\ \mathbf{c} \end{bmatrix}_{\text{Orth.}} = \begin{bmatrix} 96 & 48 & 0 \\ 0 & 84 & 0 \\ 0 & 0 & 100 \end{bmatrix} \begin{bmatrix} \mathbf{a} \\ \mathbf{b} \\ \mathbf{c} \end{bmatrix}_{P6_3/mmc} . \tag{4.2}$$

The overall box size was chosen in order to give an approximately isotropic configuration, which we have populated with Ising spins. As with $Tb(HCO_2)_3$, the Hamiltonian used for the simulation of the TIA state was Equation 3.4, so that we can build a zero-defect state of the TIA. Since the PDA state is defined by a unit cell, the supercell required can be given as an arbitrary expansion of it. Once the supercell has been generated, the disordered sites in (a layer of) the unit cell can be randomly assigned as either spin-up, or spin-down, which therefore determines the phase of the antiferromagnetic spin-chain when expanded into 3D. In this case, when we expand the system from its 2D representation to the full 3D configuration used to calculate the magnetic scattering, we assign each layer to have an opposite sign to the preceding one, accounting for the well defined intrachain antiferromagnetism. The magnetic neutron scattering calculated for both of these phases is compared to the temperature subtracted data collected at 19 K and is presented in Figure 4.4.

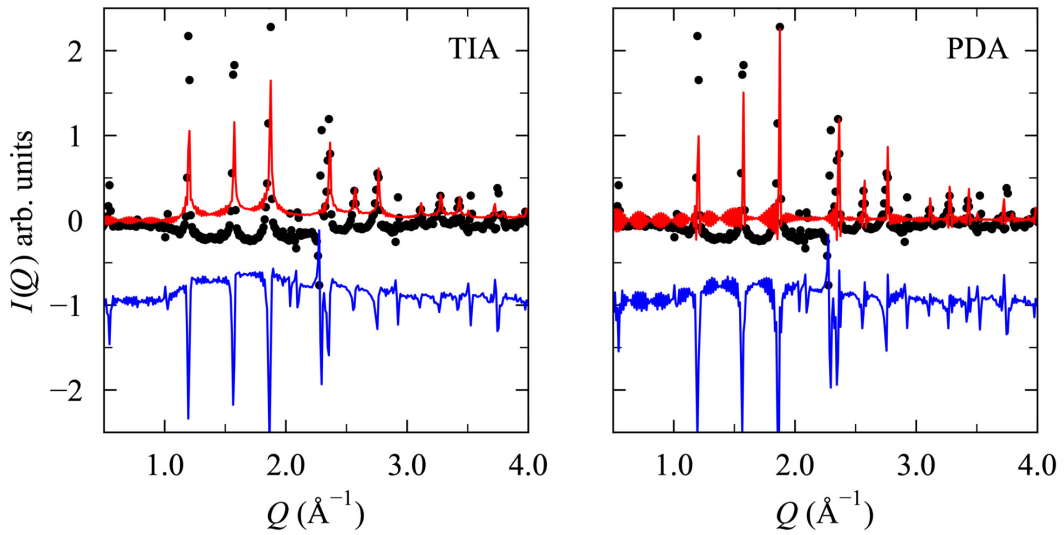


Figure 4.4: Comparison of the calculated diffraction patterns for the TIA and PDA models with the temperature subtracted data at 19 K for $CsCoCl_3$. The difference between the calculated and observed data is shown in blue (offset for clarity).

Both our PDA and TIA models account correctly for the number and approximate intensities of the Bragg-like features observed in our temperature-subtracted neutron diffraction data. In both cases, however, we see that there are non-trivial difference functions between the observed and calculated scattering.

We observe that the long-range order of the PDA state, when modelled as a finite-size box in real space, gives rise to high-frequency (Fourier) ripples in reciprocal space, as artefacts of the Fourier transform. Such features arise due to a convolution of a sinc-function with the Bragg peaks, where the sinc-function is produced from the Fourier-transform of the rectangular box-function.[203,204] These serve to obscure the exact level of the background, as they are convoluted with the Bragg-peak delta-functions. It appears, however, that in both cases our models give rise to difference functions which do not behave in the manner expected. Below approximately 1 Å^{-1}, the difference function is flat and approximately zero, while above this value of Q, there is a smoothly varying curve which does not behave in the same manner as

the magnetic form-factor. We can also observe that the TIA model gives rise to a difference function where the main differences are the intensity of the peaks, and the level of the background function. Between the difference function of the Bragg-like features in this model, we see a relatively smooth curve. However, in the PDA model, we see that the broadening at the base of the peaks is not captured well by the model. A number of different strategies were attempted to rectify the problem with the level of the background function, *e.g.* background refinement using SPINVERT, however no method was able to satisfactorily account for the level of the background.

4.2.4 Revisiting the temperature subtraction

It proved to be instructive to take a closer look at the dataset at 25 K which we have used as the reference for our temperature subtraction. As shown in Figure 4.5, we can see that at around 1 Å^{-1} there is a subtle change in the gradient of the interpolated background function, which isn't present in the 300 K dataset [inset to Fig. 4.2]. As we have already observed that there is a correlated paramagnetic regime above T_{N}, it is possible that our 25 K data are not purely paramagnetic. Considering that $Q = 1\,\text{Å}^{-1} \approx 6.28\,\text{Å}$, a magnetic feature appearing at this point is likely associated with antiferromagnetic order along the c-axis. Furthermore, since the feature seems to be broad and diffuse in nature, it is unlikely to be associated with long-range, 3D, order.

We have proposed a possible magnetic state at 25 K based on the assumption that the intrachain exchanges are stronger than those between chains. Simulating a state where each chain is perfectly antiferromagnetic along the c-axis, but with no correlations between the chains—*i.e.* random spins in the ab-plane—we observe, in

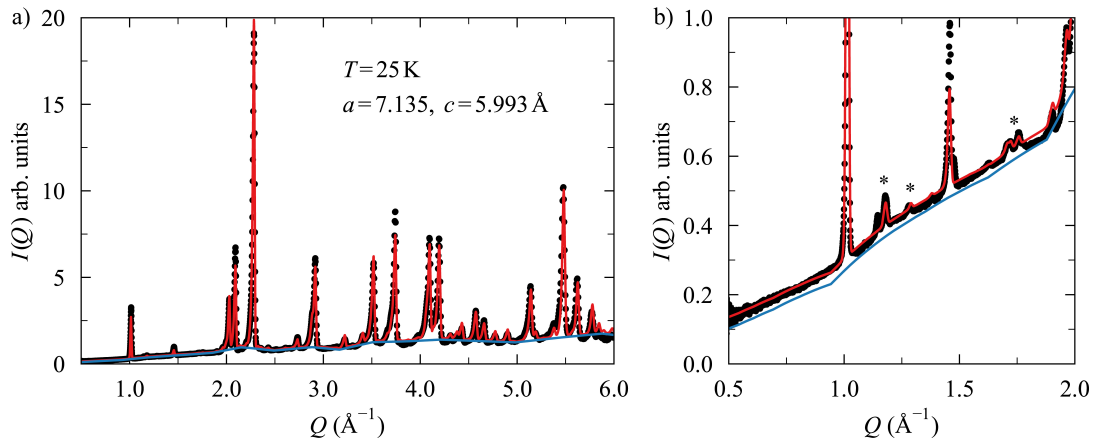


Figure 4.5: a) Rietveld refinement of our 25 K dataset. Data are shown in black and the fit is shown in red. The pale blue line indicates the interpolated background. b) Low-Q data showing the change in slope of the background function at approx. 1 Å^{-1}. The * indicate the scattering from $\sim 0.5\%$ Cs_2CoCl_4 impurity.

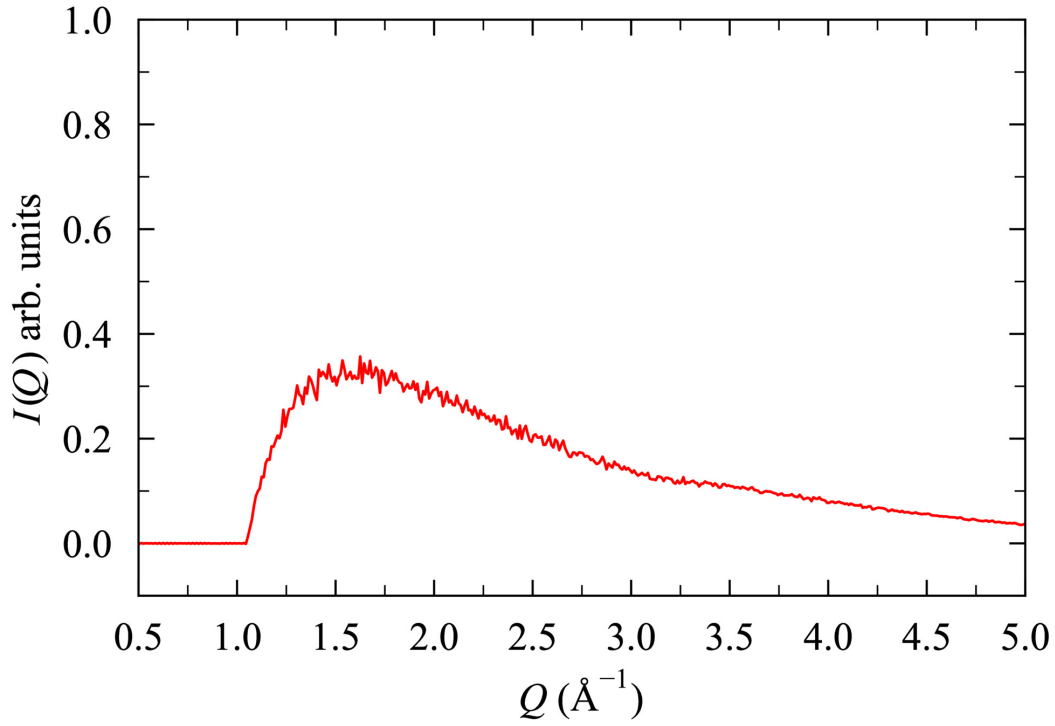


Figure 4.6: Calculated magnetic neutron scattering for our model of antiferromagnetic chains distributed with random phases over the triangular lattice. The scale factor applied here is arbitrary, and not comparable to *e.g.* Fig. 4.5.

the calculated scattering, a sudden increase of intensity at 1 Å^{-1}, as shown in Figure 4.6. We also see that there is a relatively broad and long tail to this peak, which matches very well with the observed difference function for our idealised PDA and TIA states and the temperature subtracted data. We therefore hypothesised that the state at 25 K contains antiferromagnetic chains, relatively strongly correlated along the c-axis, but with little to no correlation between these chains. We note that there is a strong correspondence between this state, and our results for $\text{Tb}(\text{DCO}_2)_3$, where the presence of ferromagnetic intrachain correlations was observed above T_N.

Since, in all cases, we have subtracted the $T < 25\,\text{K}$ data from a state which is not perfectly paramagnetic, we must now take this 'random' antiferromagnetic state into account. Therefore we have subtracted the scattering contribution of this

state from the scattering generated for our idealised model systems. In order for there to be no scaling issues when dealing with the different states, which have different magnetic moments,[137] we have subtracted the calculated scattering for the random antiferromagnet model, before the scale factor is refined for the sum of the scattering. Ideally, it would be possible to refine the magnetic moment, and hence the scale factor, by comparison of the data at 25 K with data at a higher temperature, in a fully paramagnetic regime, or by collecting diffuse magnetic scattering data at 25 K using xyz polarisation, in order to isolate the magnetic scattering completely. Since such data were not available to us, we deemed that subtracting this scattering before the refinement of the scale factor provided a suitable compromise. The results of our revised calculations are shown in Figure 4.7. We now correctly match the level of the background of our temperature subtracted data, and we can make a much clearer comparison between the calculated scattering for PDA and TIA states.

We have now demonstrated that the TIA model gives a better description of the observed magnetic scattering. The model captures correctly the broadening of the base of the peaks, and the associated level of the background better than the PDA model. Since both of our states are essentially idealised, defect-free, models, extracting the spin-correlation functions from them does not give us any more information than was built-in to the models, and is therefore not shown here. We can, however, see that the TIA state gives a better description of the diffuse scattering, and so we propose that at intermediate temperatures, $CsCoCl_3$ contains antiferromagnetic chains, which are locally ordered in 2D, but do not contain long-range, 3D, order.

As with $Tb(HCO_2)_3$ we have shown that there is a measurable difference in the magnetic neutron diffraction patterns expected for TIA and PDA states. In the TIA

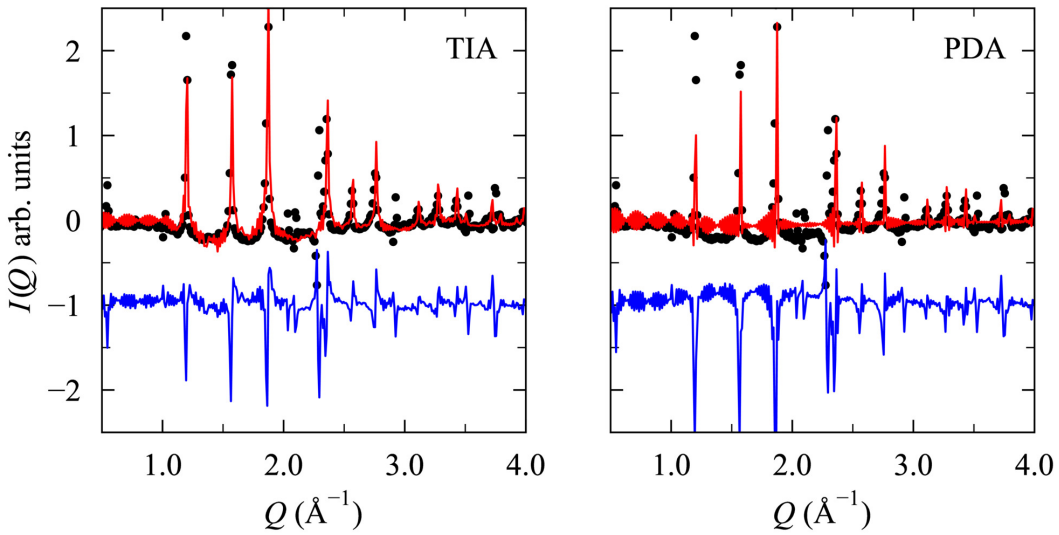


Figure 4.7: Comparison of the calculated diffraction patterns for the TIA and PDA models when the contribution of the random antiferromagnetic phase is subtracted, with the temperature subtracted data at 19 K for $CsCoCl_3$.

state, the maxima in the continuous diffuse scattering function could be viewed as a Lorentzian component convoluted with the δ-function of a Bragg peak. Since there are a variety of crystallographic features which could produce such a component, it could easily be overlooked and subsumed into a standard magnetic Rietveld refinement, giving rise to the PDA model being assigned to that diffraction pattern. We have determined that in the vicinity of $T \geq 25\,\mathrm{K}$, $CsCoCl_3$ behaves as a collection of randomly phased antiferromagnetic chains on a triangular lattice. We also note that above $T_\mathrm{N} \approx 20\,\mathrm{K}$ there exists a temperature region where $CsCoCl_3$ behaves as a correlated paramagnet with an increasing correlation strength to interchain neighbours as the temperature decreases. Finally we determine that $CsCoCl_3$ would appear to be described better as a TIA between 20 K and 14 K. These observations are summarised in our schematic phase diagram shown in Figure 4.8.

In our analysis, we have only considered the idealised structures, and make no comment on the magnitudes of the exchange parameters, or whether there would be

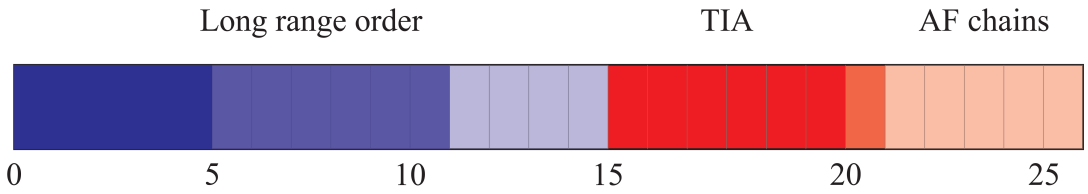


Figure 4.8: Proposed magnetic phase diagram for $CsCoCl_3$ at zero field. The nature of the low-temperature long-range ordered phases were not explored in this thesis.

any thermal disorder at intermediate temperatures. As in the case of $Tb(DCO_2)_3$, one might be able to allow SPINVERT to introduce such fluctuations to obtain a better fit to the data in due course. While it generally appears that there are only subtle differences in the static structure of these types of systems, the influence on the excitations has not yet been determined.

4.3 Supercell Spin Dynamics (SCSD)

4.3.1 Overview

Having established meaningful differences between the static structures of PDA and TIA states, it is natural to question whether these differences affect physical properties. One example of the differences between the PDA and TIA states is their configurational entropy. In a PDA unit cell, one-third of the spin-chains take on a random phase, while the other two-thirds are ordered, meaning that this state will have an entropy of $S = \frac{R}{3}\ln 2$. The entropy of a TIA has been calculated by Wannier[103] as

$$\begin{aligned} S &= R\frac{2}{\pi}\int_0^{\pi/3} \ln\left(2\cos\omega\right)d\omega \\ &= 0.3383R. \end{aligned} \tag{4.3}$$

That the PDA state has a lower entropy than the TIA state is not entirely unexpected. Looking at *e.g.* Fig. 3.12, we can see that, by inspection, a PDA state obeys the same local rules as a TIA—*i.e.* that no three spins in a triangle can be oriented in the same direction—but with an additional ordered component. Alternatively, we can state that the set of PDA states is a subset of the set of TIA states.

Given the difference in entropy for these states, we might expect there to be a difference in other physical properties, such as their magnetic excitation spectra. As described above, generally the interest into the excitations of systems such as $CsCoCl_3$ have been limited to those which appear as a result of the antiferromagnetic Ising chains.[69] Our focus is instead on the interactions and excitations involving the orthogonal component. As a result, the calculations in this section have generally been performed on isolated 2D representations of the states given, and we have not expanded our representations to include the chain axis.

As outlined in Section 2.3 it is possible to use linear spin-wave theory to calculate the dynamical matrix and then diagonalise to extract the eigenvalues and eigenvectors of the magnetic excitations. However, the general method for this is to begin with a unit-cell representation of the system; something which both the PDA and TIA states lack.* We could, of course, turn to density-functional theory (DFT) and calculate the interactions in a configuration large enough to capture the differences in structure between the two systems. This method would be very computationally expensive, and require careful choice of appropriate functionals. Is it possible for us to make use of the computational speed and simplicity of LSWT and still be able

*In order to use SpinW for the calculation of the magnon dispersions for a PDA system, we would be required to select a particular configuration of the random sublattice.

to calculate the excitations of disordered systems?

In order to answer this question, we can first think about the mapping between structural (correlated) disorder and the phonon spectra and densities of states. Overy *et al.* have presented detailed studies on how correlated disorder can influence the phonon dispersion curves.[155,156] They have also presented a method for the calculation of phonon dispersion curves using supercells of the disordered structure and applying the band unfolding method described in Section 2.3.4.

4.3.2 Implementation

If we wish to make use of this technique in a magnetic system, we must first consider what the dynamical matrix looks like if we are dealing with spins and magnetic exchanges, rather than force constants between atoms. The spin dynamical matrix is presented in Ref. 205 (see also Note 24 therein) as,

$$\begin{aligned} \Delta_{j,j'}(\mathbf{k}) = -2\sum_{\ell}\Big[&\frac{\sqrt{S_j S_{j'}}}{\hbar} J\left(\begin{smallmatrix} j & j' \\ 0 & \ell \end{smallmatrix}\right) \\ &\times \exp\left\{\mathrm{i}\mathbf{k}\cdot[\mathbf{r}(j'\ell)-\mathbf{r}(j0)]\right\} - \delta(j,j')\sum_{j''}\frac{S_{j''}}{\hbar}\left(\begin{smallmatrix} j & j'' \\ 0 & \ell \end{smallmatrix}\right)\Big]. \end{aligned} \tag{4.4}$$

Comparing this dynamical matrix with the one given in Section 2.3.4 shows us that rather than weighting the calculation by $m^{-1/2}$ it is scaled by $S^{1/2}$; and that we use the exchange-constant matrix, J, instead of the force-constant matrix, Φ. The eigenvalues of Equation 4.4 are the frequencies of the spin-waves, $\omega(\mathbf{k},\nu)$, while the eigenvectors give the normal mode spin-wave displacements.

This dynamical matrix is what SpinW calculates using LSWT. The dynamical matrix itself is usually processed in the background and then the magnon spectrum is

plotted by the software, however we require direct access to the matrix itself. We can extract the matrix, and make use of functions built-in to MATLAB to diagonalise it directly and hence extract the eigenvalues and corresponding eigenvectors at $\mathbf{k} = 0$. For an example of the MATLAB/SpinW code used see Appendix B1. Once these values have been extracted, we have used a custom written Python script which applies the band-unfolding equation [Eq. 2.30] to the eigenvectors and eigenvalues calcualted. This script can then take these projections and produce plots of both the magnon-dispersion pattern, and the density-of-states.

4.3.3 Proof of concept

In order to confirm that this method works correctly for the type of spin systems we are interested in, we first performed a proof-of-concept calculation on a system for which we can directly calculate the magnon dispersion curves; a triangular lattice ferromagnet. For our analytical calculations, we have generated a single unit-cell of a 2D representation of a triangular lattice structure, with $a = b = 2\,\text{Å}$, $c = 8\,\text{Å}$ ($\alpha = \beta = 90°$, $\gamma = 120°$). The exchange matrix used in the calculation is the 3×3 identity matrix, I_3, and the spin waves are calculated along high-symmetry directions in reciprocal space. For our supercell representation, we have generated a $12\times12\times1$ supercell using SpinW, and we have used the same exchange matrix. From this calculation, we can extract the eigenvalues and eigenvectors of the dynamical matrix directly from SpinW. We have then applied our band unfolding algorithm as defined above.

Up to the limit of the reciprocal space resolution described in Section 2.3.4, the analytical result and the dispersion curves produced by band unfolding match very

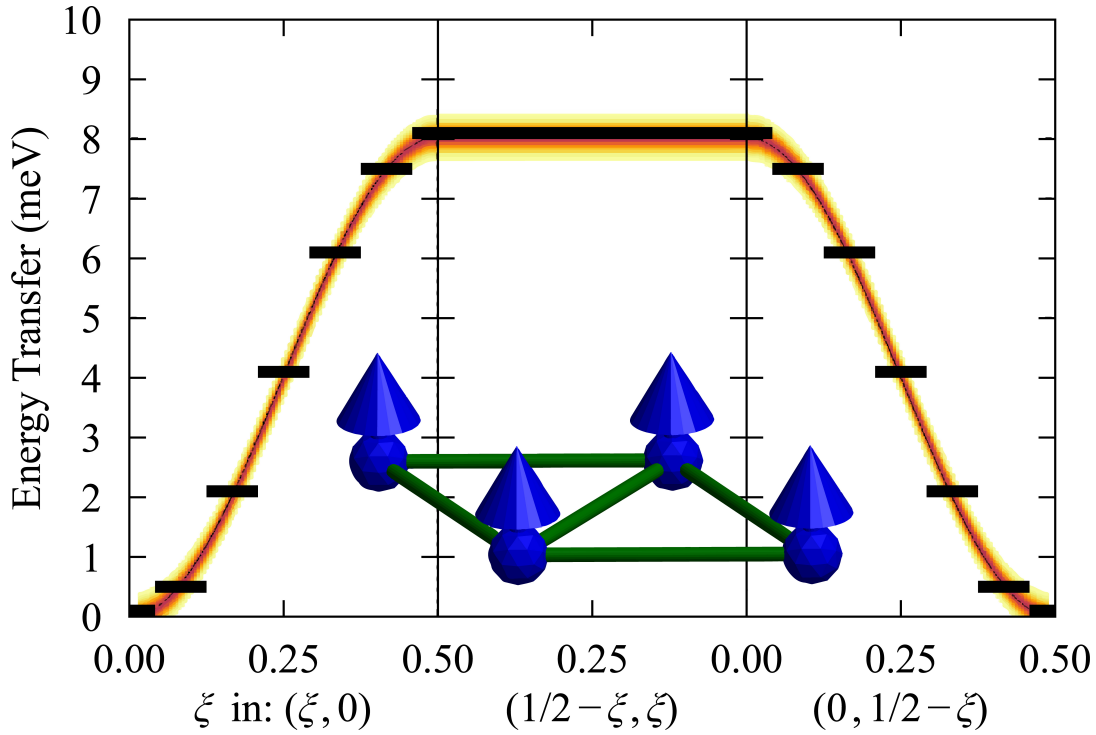


Figure 4.9: Analytical calculation of the magnon dispersion curves for a triangular ferromagnet as calculated using SpinW (orange curve) overlaid with the results of our band-unfolding calculations for a 12×12 supercell of the original configuration (black bars). The inset shows the configuration used in SpinW for the analytical calculation of the spin waves.

well, as shown in Figure 4.9.

We have also compared our results with other analytically soluble dispersion curves. One of the simplest antiferromagnetic structures that can exist on frustrated triangular motifs is a stripe phase, involving a doubling of the unit cell along a given axis (in this case, the b-axis). Once again both calculations give analogous results [Fig. 4.10]. We note here that the excitations of this model, in particular the flat band along $((0, \frac{1}{2}) \rightarrow (0, 0))$, will be relevant in our discussion of the TIA and PDA states.*

*Which edge of the Brillouin zone this band follows is determined by the real-space axis containing the magnetic propagation vector.

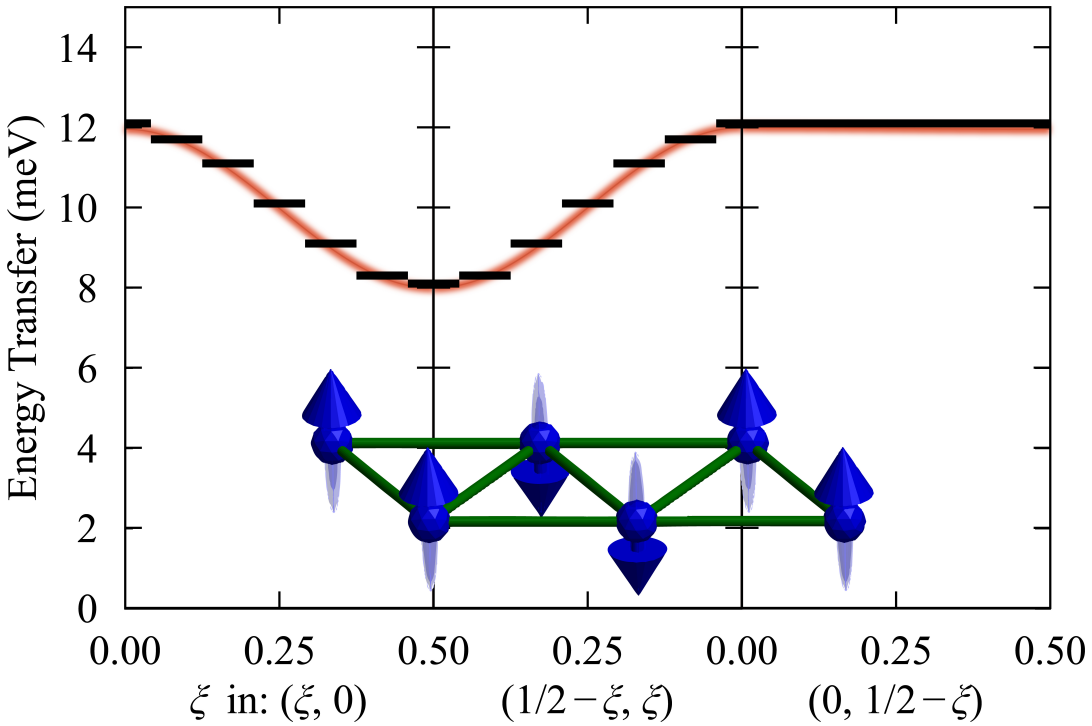


Figure 4.10: Analytical calculation of the magnon dispersion curves for a an antiferromagnetic stripe phase, as calculated using SpinW (orange curve) overlaid with the results of our band-unfolding calculations for a 12×12 supercell of the original configuration (black bars). The inset shows the configuration used in SpinW for the analytical calculation of the spin waves.

4.3.4 Comparison of the TIA and PDA states

Now that we have established that combining a supercell and band unfolding approach will work for this type of system, we can investigate the PDA and TIA structures. In order to use SpinW to generate the eigenvectors and eigenvalues, we need to first set-up our disordered supercell. This has been either done by hand (for the long-range ordered models, *e.g.* stripe phases), or by reading in a file generated form the preceding Monte Carlo calculations. In order to calculate our dynamical matrices, it is necessary to perform a perturbation of spins from an 'ordered' supercell, where the easy-axis anisotropy is significantly (arbitrarily) greater than the interaction terms. In our example, $|D|/|J| = 100$, which is approximately an order of magnitude smaller than the equivalent ratio for $Tb(HCO_2)_3$. This term ensures

that the configurations are stable with respect to spin flips. The dynamical matrices generated in this way contain only real values, and this prevents us having to deal with imaginary modes in the spin-wave spectrum.* Once the dynamical matrix has been extracted for our model, we can simply make use of the band-unfolding method to plot the calculated spin waves in reciprocal space. In Figure 4.11 the plots produced are placed on an arbitrary scale by scaling to the minimum calculated value in the most disordered supercell; this has been done as the absolute energy scale includes the arbitrarily large single-ion anisotropy.

In order to better compare our models, we have also generated a random structure with antiferromagnetic exchange and the same single-ion anisotropy. This allows us to provide a disordered bound to the position of intensity in reciprocal space. Comparison of the calculated spin waves and corresponding densities-of-states shows that there are several features which are consistent across all of our supercells. These include flat features at around 12 and 14 meV which appear in all of our models, and which we may be able to attribute to locally ordered sections within the models, *e.g.* the aforementioned flat feature in Figure 4.10. Notably the low-intensity flat excitation at 13 meV appears in the TIA model and in the random structure, yet is absent in the PDA structure. The key difference we observe is that gaps appear in the PDA model, which do not feature in either the TIA model or a random antiferromagnet. Hence the PDA and TIA states are characterised by different excitation spectra, with implications for corresponding thermal and spin-transport properties.

As with the static structures, we turn to the question of whether it would be possible to observe these differences in an experiment. Based on the calculated

*There is precedent for being able to disregard imaginary modes *e.g.* Paddison *et al.*[189]

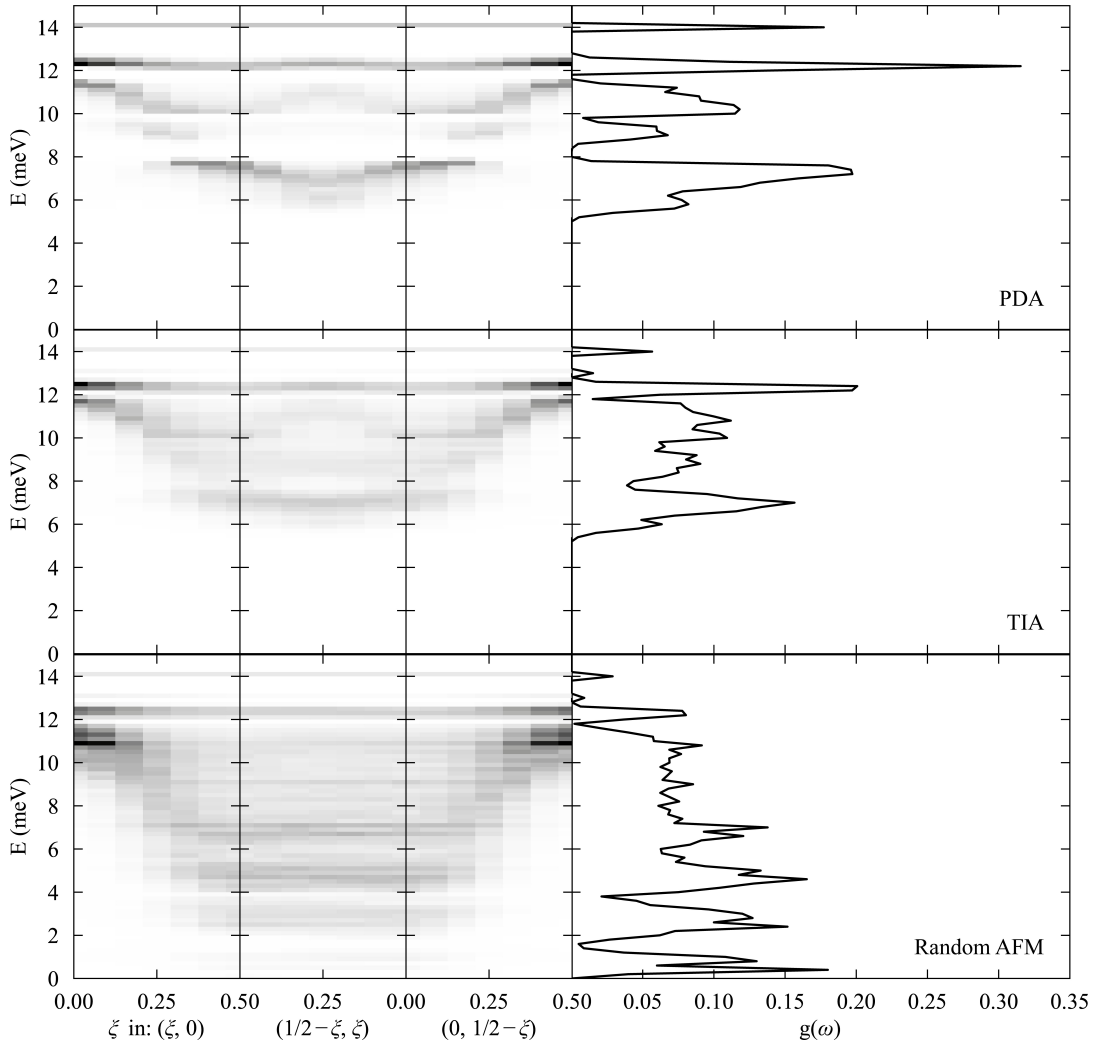


Figure 4.11: Magnon dispersion curves calculated using our supercell-based approach for PDA, TIA, and random antiferromagnetic states. The right hand panels shows the density-of-states for each system.

inelastic scattering, we would need to have an energy resolution less than 0.5 meV at the energy of the excitations. Since our calculations are based on an arbitrary exchange constant and single-ion anisotropy, we don't know what incident energy (E_i) we would require. If we take the paper by Shiba *et al.* as a reference, they report an interchain exchange constant of 0.93 meV and a single-ion term of 4.14 meV.[206] Using these values directly in our SpinW calculations, we find that the energy scale due to our energy normalisation matches very well with the experimental values. We would therefore expect to see most of the inelastic signal below 15 meV. Using the tools available in the MANTID software,[207] we can calculate the theoretical flux and energy resolution for a given E_i across a variety of instruments at ISIS. For this resolution and this E_i we would expect LET to be able to resolve the presence of energy gaps as calculated.

As I have stated above, the key difference between the PDA and TIA is the presence of gaps in the inelastic spectrum of the PDA state. Based on both arbitrary and 'realistic' values of the interaction constants we may expect that the presence or absence of gaps would be measurable experimentally.

4.4 Conclusions

In this chapter, I have extended the methods devised from experimental observations in Chapter 3 to cover a broader area of theoretical interest. The primary result is that $CsCoCl_3$ can also be described as a realisation of a triangular Ising antiferromagnet, and that the partially disordered antiferromagnet state previously reported is likely an artefact of applying a traditional crystallographic approach to a system containing only short-range magnetic order. This may have far broader

applications than explored within this thesis, as there are still a great number of systems which are directly described in terms of the PDA state, not least of which is $CsCoBr_3$ which we also attempted to synthesise. The reagents proved to be significantly more hygroscopic than those for $CsCoCl_3$, causing the sealed reaction tube to fail. Not only are there many magnetic examples of this state, but there are also several cases where charge[208] and orbital order[209] can be described in the same way. It is necessary to note that the identification of a TIA state in such systems may be significantly harder to determine, and it is possible that there are more rational physical driving-forces behind the formation of a long-range disordered state. I have also demonstrated that not only is there a difference in the observed static magnetic neutron scattering between TIA and PDA states—there is a meaningful difference in the dynamics of them. This has been shown through both a simple derivation of the entropy differences, as well as the differences which could be expected in an inelastic neutron scattering experiment.

Chapter 5

Enhanced exchange interactions in the Heisenberg pyrochlore antiferromagnet – $Gd_2Pt_2O_7$

The Heisenberg pyrochlore antiferromagnet $Gd_2Pt_2O_7$ is one of a series of gadolinium pyrochlore compounds with various B-site cations (B = Ti, Sn, Ir, Ge, and Pt). Despite the expected simplicity of a pure spin-only Gd^{3+} Heisenberg interaction model, the gadolinium pyrochlore series exhibits various complex magnetic ground states at low temperature. $Gd_2Pt_2O_7$ displays the highest temperature magnetic order of the series with $T_N = 1.6\,K$ which has been attributed to enhanced superexchange pathways facilitated by empty $5d$ e_g Pt^{4+} orbitals. In this study we use various neutron scattering techniques on an isotopically-enriched polycrystalline $^{160}Gd_2Pt_2O_7$ sample to examine the magnetic structure and spin-wave excitation spectrum below T_N in order to extract the dominant exchange interactions. We find that the ground state magnetic structure is the Palmer-Chalker state previously seen in $Gd_2Sn_2O_7$. The associated gapped excitation spectrum is consistent with enhanced exchange interactions between next-nearest-neighbour Gd^{3+} ions and an increased single-ion anisotropy. We confirm this exchange model with analysis of the magnetic diffuse scattering in the paramagnetic regime using polarised neutrons.

5.1 Introduction

In the previous two chapters, we have investigated the effects of frustration on two-dimensional lattices. In this chapter, we will turn to a system where the

frustration extends over all three spatial dimensions: namely $Gd_2Pt_2O_7$, where the frustrated network extends over 3D-space, in the form of corner-sharing tetrahedra. We have measured both the inelastic neutron spectrum in the ordered regime, and also the magnetic neutron diffraction patterns below and above T_N. In this way we characterise the interactions that govern its magnetic behaviour.

The magnetic pyrochlore lattice—in which magnetic ions sit on the vertices of corner-sharing tetrahedra—is commonly studied as an archetypal example of three-dimensional geometrical frustration. These studies have uncovered a large variety of emergent low temperature magnetic states, including spin-liquids and spin-ices,[210,211] fragmented spin-structures,[212] and complex partially ordered structures.[117] Geometric frustration suppresses the magnetic ordering temperature (T_N) below the Curie-Weiss temperature (Θ_{CW}). One measure of the degree of geometrical frustration in a system is the frustration parameter: $f = \frac{|\Theta_{CW}|}{T_N}$.[101] A frustration parameter of $f > 10$ generally indicates a highly frustrated material, which would typically not be describable using mean-field theory.[213] In a model system with only nearest-neighbour, antiferromagnetic, interactions on a perfect pyrochlore lattice, we would expect a spin-liquid ground state, due to the large degree of frustration.[214,215] It is perturbations to this simple nearest-neighbour exchange—such as further-neighbour interactions, dipolar exchange, or single-ion anisotropies—which cause most real systems to enter long-range ordered states at finite temperatures.

$Gd_2Pt_2O_7$ (GPO) is an interesting example where a combination of nearest- and next-nearest-neighbour exchange, dipolar-interactions, and single-ion anisotropy, serve to relieve the frustration and give rise to long-range magnetic order at accessible temperatures. $Gd_2Pt_2O_7$ crystallises in the cubic, $Fd\bar{3}m$, space group, with

$a \approx 10.26\,\text{Å}$ at room temperature,[216,217] and forms a pyrochlore network of corner-sharing tetrahedra, with a number of dominant exchange pathways, as shown in Figure 5.1. In the cubic pyrochlore system, there are two third-neighbour interaction pathways at the same separation—one which passes through another Gd^{3+} ion, and one which crosses the hexagon formed of corner-sharing tetrahedra, and therefore also passes through the Pt^{4+} ion which lies in the centre of the hexagon. Reports of other gadolinium pyrochlores indicate that the interaction passing through another Gd^{3+} ion can generally be assumed to be negligible compared to the other parameters.[119,218] We therefore neglect this interaction pathway in our analyses, using only the cross-hexagon third-neighbour interaction, J_3.

In related, highly frustrated, materials—and as we have observed in $CsCoCl_3$—the temperature range just above the magnetic ordering temperature has been of significant interest, and it has been possible to observe a 'cooperative paramagnet' state over the temperature range $T_N < T \lesssim |\Theta_{\text{CW}}|$ (previous reports give $\Theta_{\text{CW}}(\text{GPO}) = -9.4(1)\,\text{K}$).[216,219] In contrast with other Gd pyrochlores, GPO orders at $T_{\text{N}} = 1.6\,\text{K}$, an ∼60% enhancement relative to both $Gd_2Sn_2O_7$ (GSO) ($T_{\text{N}} = 1.0\,\text{K}$) and $Gd_2Ti_2O_7$ (GTO) ($T_{\text{N1}} = 1.0\,\text{K}$).[216] GPO can therefore said to be moderately frustrated with $f = 5.9$. Due to similarities in both the heat capacity and magnetic susceptibility measurements of GPO and GSO, it is suggested by Hallas *et al.* that GPO will also order into the so-called Palmer-Chalker ($\mathbf{k} = (0\,0\,0)$) state.[114,216] From their heat capacity measurements, they also extract a value of the spin-wave gap as $\Delta_{\text{gap}} = 0.245(1)\,\text{meV}$.

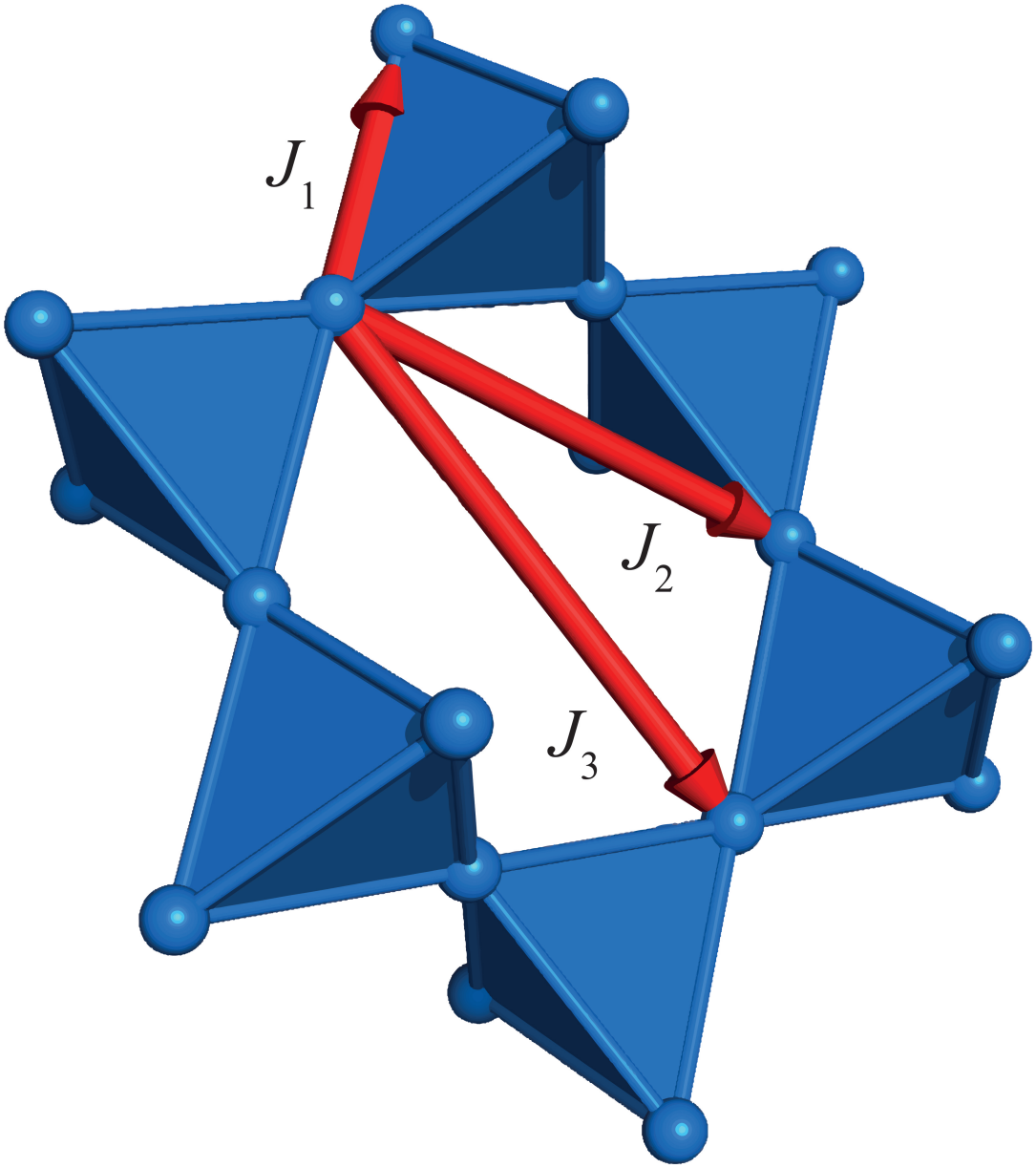


Figure 5.1: The arrangement of Gd^{3+} ions (blue spheres) in $Gd_2Pt_2O_7$. The network of corner-sharing tetrahedra is illustrated in blue. Principal exchange interaction pathways are shown in red. There are two interactions with the same separation as J_3. Only the 'cross-hexagon' J_3 is shown. The Pt^{4+} ions are situated in the centre of these hexagonal structures. The Pt^{4+} ion lies in the centre of the hexagon.

The gadolinium pyrochlore systems have previously been analysed using a Hamiltonian of the form:

$$\begin{aligned}\mathcal{H} =& \frac{J_1'}{2}\sum_{\langle i,j\rangle}\hat{\mathbf{S}}_i\cdot\hat{\mathbf{S}}_j + \frac{J_2'}{2}\sum_{\langle\langle i,j\rangle\rangle}\hat{\mathbf{S}}_i\cdot\hat{\mathbf{S}}_j \\ &+ \frac{J_3'}{2}\sum_{\langle\langle\langle i,j\rangle\rangle\rangle}\hat{\mathbf{S}}_i\cdot\hat{\mathbf{S}}_j + \Delta'\sum_i(\hat{\mathbf{S}}_i\cdot\hat{\mathbf{z}}_i)^2 \\ &+ \frac{D'r_1^3}{2}\sum_{i,j}\frac{\hat{\mathbf{S}}_i\cdot\hat{\mathbf{S}}_j - 3(\hat{\mathbf{S}}_i\cdot\hat{\mathbf{r}}_{ij})(\hat{\mathbf{S}}_j\cdot\hat{\mathbf{r}}_{ij})}{r_{ij}^3}.\end{aligned} \tag{5.1}$$

This model consists of direct exchange interactions ($J'_{1,2,3}$) between classical spin vectors ($\hat{\mathbf{S}}_i$), where $\langle\dots\rangle$ indicates nearest-neighbour spin-pairs, $\langle\langle\dots\rangle\rangle$ indicates next-nearest-neighbour spin-pairs, and $\langle\langle\langle\dots\rangle\rangle\rangle$ indicates third-neighbour, cross-hexagon, spin-pairs. We also include a single-ion anisotropy term (Δ') which is defined by the vector connecting spin i to the centres of the two tetrahedra which both have spin i as a vertex (the local-$\langle 111\rangle$ axis ($\hat{\mathbf{z}}_i$)), and the magnitude, at the nearest-neighbour separation (r_1), of the dipolar interaction (D'). The prime superscripts on the parameters indicate that these are classical approximations of the quantum parameters. Comparison between these parameters and those presented in literature is facilitated by defining a scaling relationship between classical and quantum terms.[218]

$$J'_{1,2,3} = J_{1,2,3}S(S+1), \tag{5.2}$$

$$\Delta' = \Delta S^2, \tag{5.3}$$

$$D' = DS^2. \tag{5.4}$$

We fix $D = \mu_0(g\mu_b)^2/4\pi r_1^3 k_b = 0.05275\,\mathrm{K}$, based on the lattice parameter

$a = 10.225\,\text{Å}$ at 50 mK, with $D' = 0.64612\,\text{K}$. From previous reports of GSO and GTO we can compare the J and Δ parameters to those which have been suggested for GPO. In GSO, it is reported that $J_1 = 0.248(9)\,\text{K}$, and $\Delta = 0.14\,\text{K}$ (note, these are the values taken without considering the magnitude of the spins). While in GTO, $J_1 = 0.304\,\text{K}$, and $\Delta = 0.122\,\text{K}$. In both cases, we see that J_1 is relatively strongly antiferromagnetic, and there is a moderate single-ion anisotropy which favours alignment perpendicular to the local $\langle 111 \rangle$ axis, *i.e.* an easy-plane anisotropy. Since the lattice constant of GPO is closer in magnitude to that of GTO ($a = 10.17\,\text{Å}$) than GSO ($a = 10.44\,\text{Å}$), we might expect to see a similar J_1 value, as that exchange pathway will be very similar in both materials. Biswas *et al.* have also identified that *e.g.* crystal field parameters tend to follow an approximately linear trend with respect to the lattice constant.[220]

The general phase-diagram for this system is shown in Figure 1.15 b) (page 34), as given by Wills *et al.*[119] We see that an antiferromagnetic J_1 and either an antiferromagnetic J_2 or ferromagnetic J_3 will stabilise the $\mathbf{k} = (0\,0\,0)$, Palmer-Chalker state. There are, however, many possible combinations of J_2 and J_3 which favour the Palmer-Chalker state.

In this chapter I will present the results of our inelastic neutron scattering experiment carried out within the magnetically ordered regime as well as the results of polarised neutron scattering experiments for both the ordered ($T = 50\,\text{mK}$) and correlated paramagnetic ($T = 1.8\,\text{K}$) regimes. We find that the low-temperature state of GPO is the coplanar, antiferromagnetic, Palmer-Chalker state with a $\mathbf{k} = (0\,0\,0)$ ordering vector. Above the magnetic transition, significant diffuse magnetic scattering is observed, implying that there is a strongly-correlated paramagnetic state

persisting above T_N. Our analysis of this state allows us to characterise the Hamiltonian relevant to $Gd_2Pt_2O_7$, including the magnitude of the prefactors in Equation 5.1. We show that the single-ion anisotropy term for GPO is significantly enhanced relative to GSO and GTO, and the next-nearest-neighbour interaction strength is increased relative to GSO, which we attribute to the ability of Pt^{4+} to form Gd–O–Pt–O–Gd superexchange pathways.

5.2 Results and Discussion

5.2.1 Synthesis

The sample used in our neutron scattering experiments was synthesised as detailed in Section 2.4.3 by Wei-Tin Chen and Jason Gardner at the Centre for Condensed Matter Sciences, National Taiwan University.

5.2.2 High Temperature Structural Characterisation

In order to confirm the phase purity of the polycrystalline sample, X-ray and neutron diffraction data were collected at both beamline I11, Diamond, Didcot, UK, and the Polaris instrument, ISIS Neutron and Muon Source, Didcot, UK, respectively. To minimise absorption during our X-ray diffraction measurements, a portion of our sample was loaded into a 0.1 mm capillary, and data were collected using a MAC detector and a wavelength of $\lambda = 0.82658$ Å. These data were used for joint X-ray and neutron Rietveld refinements using TOPAS-ACADEMIC 6[221] and are shown in Figure 5.2. Both datasets suffered from a substantial degree of absorption and therefore a sequential approach to the Rietveld refinements was taken, exploiting the different sensitivities of X-rays and neutrons, in order to avoid the

a	10.263285(5) Å				
Atom	x	y	z	B_{iso}	Occ.
Gd	0.5	0.5	0.5	0.228(5)*	0.9999(70)‡
Pt	0	0	0	0.027(3)*	0.9999(70)‡
O	0.33646(6)†	0.125	0.125	0.273(5)†	1.005(6)†
O′	0.375	0.375	0.375	0.296(17)†	0.994(2)‡

Table 5.1: Atomic positions and occupancies from the joint Rietveld refinement of the X-ray and neutron diffraction pattern for GPO. In this setting of the $Fd\bar{3}m$ space group, the only adjustable atomic coordinate is the x position of O. $*$ indicates the parameter was extracted from X-ray diffraction data; † from neutron diffraction; and ‡ from combined X-ray and neutron diffraction.

over-correlation of parameters when absorption coefficients were refined. We refined and fixed the lattice parameter using only the I11 data, followed by using the data from Polaris to fix the position of O. Our X-ray data were then used to determined the thermal displacement parameters for platinum and gadolinium, with the neutron data used for the refinement of thermal displacements for O and O′. Finally we have used both datasets simultaneously to refine the occupancies of all atomic positions, including a site mixing term for Gd/Pt. All banks of Polaris were used for the refinements.

Across all measured temperatures GPO is structurally ordered in the $Fd\bar{3}m$ cubic space group; with lattice parameter $a = 10.263285(5)$ Å at 298 K and $a \approx 10.225$ Å at 50 mK, in very close agreement with previous results (*e.g.* $a = 10.2626(2)$ Å at 300 K).[216,217,222] Combined X-ray and neutron refinements are presented in Figure 5.2 and crystallographic details are given in Table 5.1.

5.2.3 Magnetic Ground State Characterisation

Further neutron scattering data have been collected on our polycrystalline sample of GPO (0.21 g) at 50 mK. These measurements were performed on the D7 diffuse

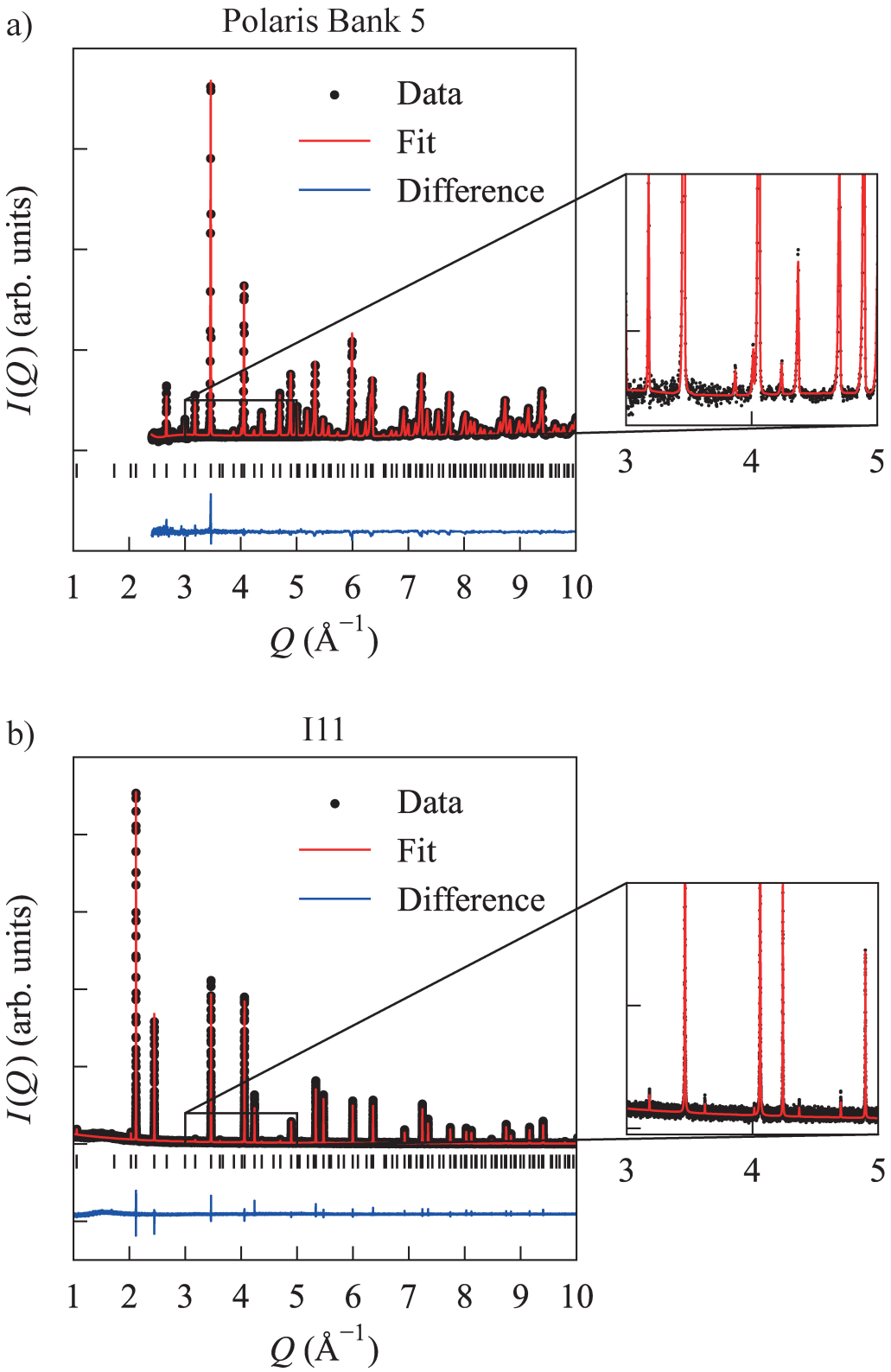


Figure 5.2: Joint X-ray and neutron Rietveld refinements to data collected on powder samples of GPO on both Polaris (high angle bank shown, **a)**) and I11 **b)**. Black points show the data, red lines are our Rietveld fits, and the difference is shown as a blue curve. The magnified regions highlight the peakshapes used and the different sensitivities of X-ray and neutron diffraction.

scattering spectrometer at the ILL, Grenoble, using an incident neutron wavelength of 4.86 Å.[144,223] D7 is able to perform xyz polarisation analysis and has support for a ^{3}He/^{4}He dilution refrigerator, both of which were used in our experiment. This incident wavelength and the solid angle covered by 132 ^{3}He detectors give access to a usable Q-range of $0.15 \leq Q \leq 2.5\,\text{Å}^{-1}$, with the low Q_{min} allowing determination of relatively long-range magnetic interactions.

xyz polarisation analysis enables the separation of the magnetic scattering from the nuclear and the spin-incoherent scattering contributions using the scattering cross sections given by Schärpf *et al.*[146] The collected data were corrected for detector and polarisation efficiency using standard samples (vanadium and amorphous silica, respectively), and have been placed on an absolute scale (barn sr^{-1} Gd^{-1}) by normalising the paramagnetic scattering to the paramagnetic moment expected for Gd^{3+}, which is only possible due to the very good separation of the magnetic, nuclear, and spin incoherent scattering possible on D7. The usual normalisation (to the incoherent scattering from the vanadium standard) could not be performed successfully due to the powder shifting during the sample loading process and thus not being fully in the neutron beam.

FULLPROF[202] was used to perform Rietveld refinements on our low temperature neutron measurements. We have used an interpolated background, and instrumental peakshape parameters[223] in our refinements. We have also used the bulk susceptibility data published by Hallas *et al.* in order to generate a data point for $I(Q = 0)$.[216] Using the relationship

$$S(Q) = \frac{k_B T}{(g\mu_B)^2 \mu_0 N_{\text{A}}} \chi(Q), \tag{5.5}$$

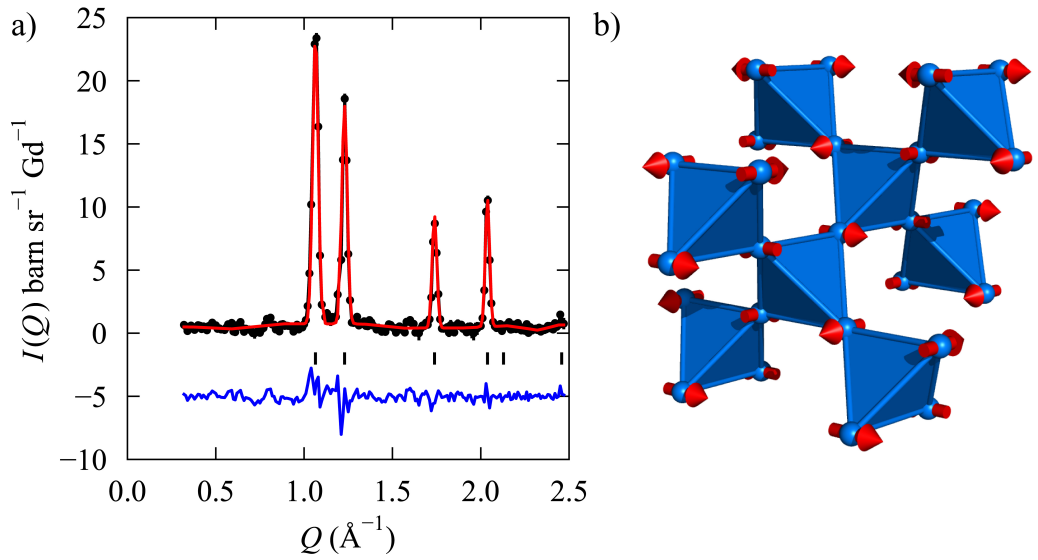


Figure 5.3: a) Magnetic neutron diffraction pattern collected at 50 mK, with the magnetic Rietveld fit using the Γ_7 irreducible representation show in red (see text), and the difference function between the data and the fit shown in blue. The black tick marks correspond to the Γ_7 irrep. **b)** A representation of the Γ_7 Palmer-Chalker coplanar, antiferromagnetic, state.

and converting the resulting structure factor into the measured scattering cross-section,

$$\left.\frac{d\sigma}{d\Omega}\right|_{Q=0} = \frac{16}{3}\left(\frac{\gamma r_0}{2}\right)^2 T\chi_{\mathrm{CGS}}, \tag{5.6}$$

where $\left(\frac{\gamma r_0}{2}\right)^2 = 0.07256$ barns, and χ_{CGS} gives the susceptibility in CGS units. We can then add a value to our measured diffuse magnetic scattering at $Q = 0$ (see Appendix A1 for full details).

We observe Bragg peaks in the magnetic scattering upon cooling our sample to 50 mK, indicating a transition into an ordered magnetic state. Using FULLPROF we have refined the magnetic scattering and determined that (as per Wills *et al.*[119]) the Γ_7 irreducible representation belonging to a $\mathbf{k} = (0\,0\,0)$ ordering vector provides the best fit to the data. This is the Palmer-Chalker state which has also been observed as the ordered magnetic state of GSO.[119] The magnetic diffraction pattern along with our Rietveld refinement and model of the structure are presented in Figure 5.3.

5.2.4 Magnetic Diffuse Scattering Above T_{N}

The magnetic diffraction from pyrochlore structures often shows broad diffuse-scattering features at temperatures just above the magnetic transition temperature, which arise due to correlated paramagnetism. The neutron-scattering data collected at 1.8 K are presented in Figure 5.4 a). These data show a broad feature centred around $Q \approx 1.1\,\text{Å}^{-1}$ along with a decrease in intensity as $Q \to 0$, which indicates that antiferromagnetic correlations persist over short distances.

In order to analyse this correlated paramagnetic regime we have used SPINVERT to perform reverse Monte Carlo (RMC) refinements of our data. We have also used SCATTY to calculate the expected single-crystal scattering from our boxes of spins.[189] The inherently stochastic nature of RMC allows it to generate the most disordered spin-configuration consistent with the data; we therefore use it to generate an upper bound on the degree of disorder in GPO.

Our RMC refinements were made up of $6 \times 6 \times 6$ magnetic unit-cells (containing 3456 spins), and 80 refinement runs were performed for the purposes of averaging. Since RMC refinements are not dependent on an interaction model, the spin-configurations generated are constrained by: i) the experimental data, ii) the pyrochlore lattice, and iii) a fixed length of Gd^{3+} spins. The stochastic nature of RMC refinements and the random initial spin-configurations produce results which will inherently be as disordered as possible, provided that the above constraints are satisfied. Runs were performed for 5000 moves per spin for equilibration, starting from randomly initialised spin-configurations, and the maximum spin move size and weight chosen so that approximately 80% of moves were accepted. In total, 80

separate calculations were performed in order to statistically average the obtained reciprocal- and real-space correlations.

SPINVERT gives direct access to spin-configuration models in real space, and from these models a 3D reciprocal-space map of correlations can be generated (*i.e.* a single-crystal diffuse-scattering pattern). In addition, real-space spin-spin correlation functions, as defined by

$$\langle \mathbf{S}(\mathbf{0}) \cdot \mathbf{S}(\mathbf{r}) \rangle = \frac{1}{N} \sum_{i=1}^{N} \sum_{j=1}^{Z_r} \frac{\hat{\mathbf{S}}_i \cdot \hat{\mathbf{S}}_j}{Z_{\mathbf{r}}}, \tag{5.7}$$

can be calculated. The correlation functions are averaged over Z_r symmetry equivalent neighbours and N spins as centres. Figure 5.4 shows the correlation functions for the high-symmetry directions of the pyrochlore lattice in real space. The decay of the correlations has been fitted using an Ornstein-Zernicke-type function

$$|\langle \mathbf{S}(\mathbf{0}) \cdot \mathbf{S}(\mathbf{r}) \rangle| \propto \frac{1}{|\mathbf{r}|} \exp\left[-\left(\frac{|\mathbf{r}|}{\xi} \right) \right], \tag{5.8}$$

where ξ describes the correlation length.

Figure 5.4 demonstrates that along $\mathbf{r}_1$ there are strong antiferromagnetic correlations with a long correlation length of $\xi = 12.03\,\text{Å}$. The change in vertical scale between the three panels shows that along $\mathbf{r}_2$ there are much weaker, ferromagnetic correlations with a correlation length of $\xi = 6.09\,\text{Å}$, and along $\mathbf{r}_3$ the correlations are poorly defined by RMC, however the first correlation is antiferromagnetic with further correlations being ferromagnetic. We observed a large variation in both the magnitude and the sign of the first correlation when the weight parameter for the

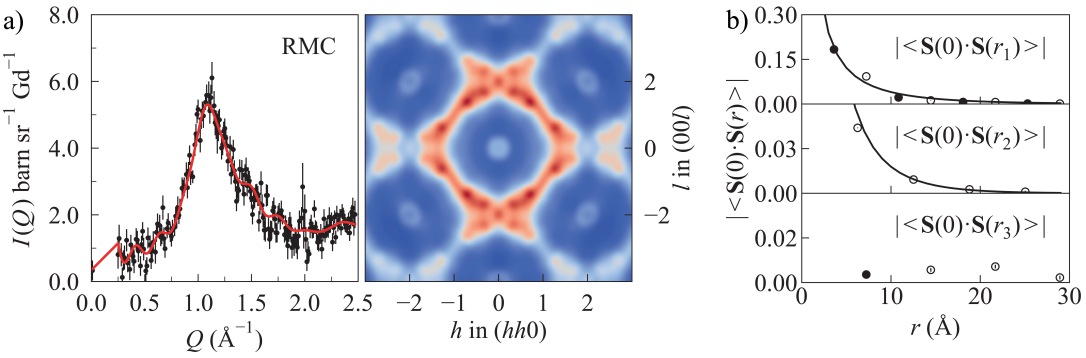


Figure 5.4: Results of our reverse Monte Carlo refinements to the data collected for GPO at 1.8 K. **a)** Left panel shows the fit to the diffuse magnetic powder neutron data collected using D7. Right panel shows the single crystal scattering calculated from our refinements boxes using SCATTY. **b)** Spin-spin correlation functions along high-symmetry directions in real space. Note the change of scale between the three directions. The black lines show the Ornstein-Zernicke (OZ) decay according to Equation 5.8. Filled and hollow symbols represent negative and positive correlations, respectively. Error bars are smaller than the size of the points.

refinement was altered, despite only minor changes in the fit. This is not unexpected due to the maximal disorder of RMC refinements, and was also observed in GSO.[218] Based on these spin-spin correlation functions, we suggest that interactions between next-nearest-neighbour spin-pairs are better defined by the diffuse scattering data than third-neighbour interactions.

We can also interrogate our real-space representations of the RMC refinements to confirm that our assumptions about the single-ion anisotropy are observed in the maximally stochastic refinements to the data. In Figure 5.5 we see that if we take the dot product of our spin vectors with the local z-axis, we obtain a distribution where the spin vectors are favourably aligned perpendicular to the z-axis (*i.e.* the spins have an easy-plane anisotropy). We also note that if we take the projection of the spins into the xy-plane, and then calculate the angle with respect to a local x-axis orthogonal to z, then we obtain a flat distribution—at $\sim \frac{1}{2\pi}$—as would be expected for a uniform distribution. So, our RMC results suggest that at 1.8 K, GPO is a

correlated paramagnet with XY anisotropy and nearest-neighbour antiferromagnetic correlations.

As discussed above, RMC refinements tend to produce the most disordered structures which are compatible with the data collected. Given the relatively large levels of uncertainty on our data, it is likely that a variety of structures will be appropriate, as they may all have very similar χ^2 values. It is common practice to average the diffuse scattering and correlation functions from a large number of independent refinements in order to prevent bias in our results. Independent refinement runs are likely to emphasise different features which are consistent with the data. Such features are mostly confined to fine, high-frequency, components of the RMC fit, for example at low-Q. These features will, in turn, correspond to long-range features in real space, and therefore may be associated with the high-r correlations along, *e.g.* r_3. We therefore do not see some of these correlations as statistically meaningful. RMC refinements have the appropriate degrees of freedom to fit high-frequency features in Q-space, however they are unlikely to be real features.

5.2.5 Inelastic Neutron Scattering

Our SPINVERT refinements indicated that the assumptions made based on other gadolinium pyrochlore systems, discussed in Section 5.1, are generally valid for GPO. While these model-free refinements, and the low-temperature order, indicate which region of the phase-diagram shown in Figure 1.15 b) GPO is situated, they do not provide estimates of the magnitudes of the exchange parameters. In order to fully characterise the Hamiltonian for GPO, we have also performed measurements using the cold neutron spectrometer LET, at the ISIS Neutron and Muon Source, Didcot,

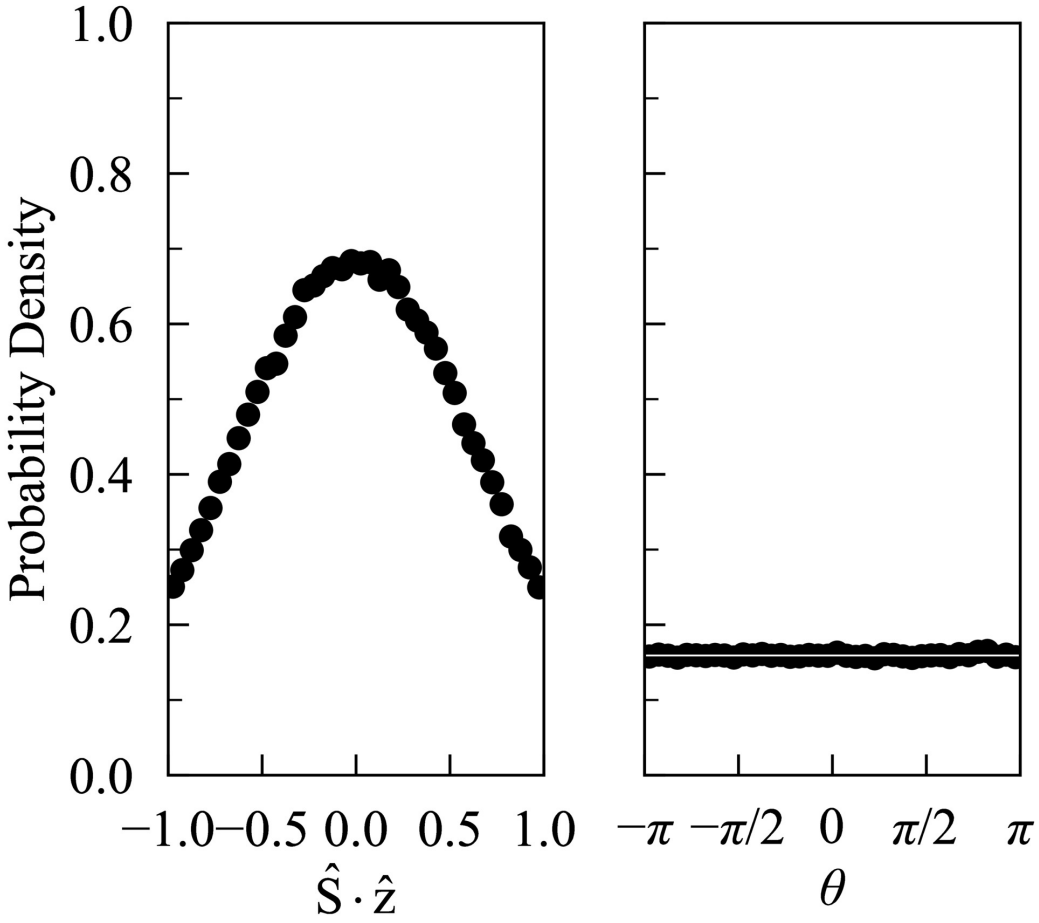


Figure 5.5: a) Probability density of the dot product of the spin vectors with the local z-axis at each vertex. **b)** Angular distribution of the spins in the xy-plane, relative to the local x-axis orthogonal to the local z-axis.

UK. Measurements were carried out at 250 mK using the dilution insert option on LET. Data were collected using repetition rate multiplication (RRM),[224] with $E_i = 9.46$ meV, giving access to repetitions at $E_i = 3.217, 1.603,$ and 0.957 meV. Data were summed and corrected using standard reduction scripts for LET. In contrast to the previous chapters, we have made use of inelastic neutron scattering, rather than DMC simulations of the diffuse magnetic scattering, to characterise the Hamiltonian. This is due to the fact that the spin-waves are more sensitive to the interaction parameters.

Visual analysis of the inelastic spectrum collected at $E_i = 1.603$ meV, shown in Figure 5.6 a), clearly shows several excitations in our sample—including an intense, approximately flat, band at $\Delta E = 0.25$ meV and a number of strongly dispersive bands.

Simulations of the inelastic data for comparison with our INS data collected on LET were performed using linear spin-wave theory (LSWT) as implemented in SpinW.[39] Fluctuations were calculated from the Palmer-Chalker state using nearest- and next-nearest-neighbour exchange parameters, as well as a single-ion anisotropy, and dipolar interactions, as described above [Eq. 5.1]. The convoluted powder spectra were calculated including approximations of the experimental FWHM of the excitations. Using SpinW, we initially simulated the inelastic scattering expected based on the exchange parameters applicable for GSO, so as to provide a benchmark for our calculations. These parameters reproduced the key features of the inelastic scattering (with the exception of the mode originating at $\Delta E \approx 0.45$ meV at low-Q), however the global energy scale was lower than observed experimentally.

In order to generate unbiased estimations of the principal exchange parameters

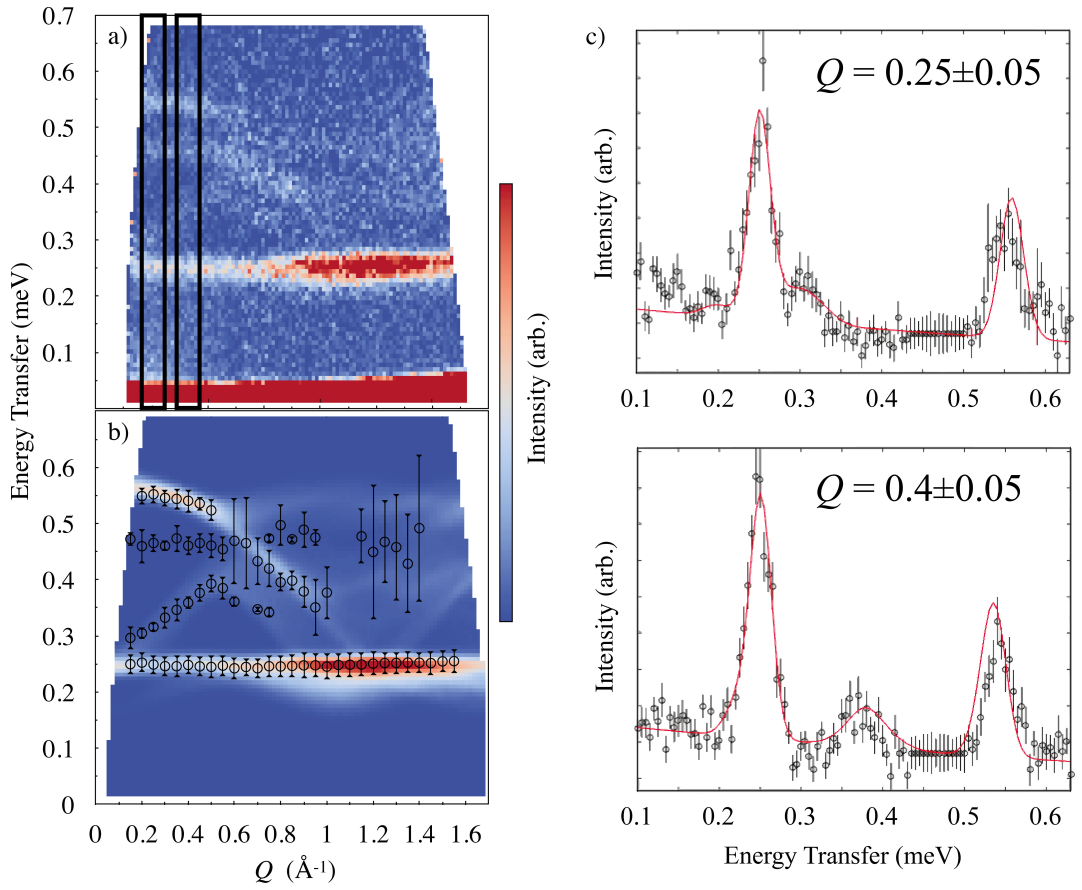


Figure 5.6: **a)** Data collected for GPO on LET with $E_i = 1.603$ meV. The black boxes represent the cuts shown in **c)**. **b)** Calculated powder inelastic neutron scattering from SpinW (colourmap), with points representing the centre of Gaussian fits to peaks observed in cuts of the data. The error bars represent the FWHM of the corresponding peak. **c)** Two representative cuts of the data, corresponding to the boxes shown in **a)**. The least-squares fit obtained using SpinW is shown in red. In these cuts, the band at 0.45 meV has been set to the level of the background, as explained in the main text.

and the single-ion anisotropy we have used a least-squares method to fit two representative cuts of the inelastic spectrum ($Q = 0.25 \pm 0.05 \text{Å}^{-1}$ and $Q = 0.40 \pm 0.05 \text{Å}^{-1}$). In both of these cuts, we have manually set the intensity of the mode around $\Delta E \approx 0.45\,\text{meV}$ to the approximate level of the background, for reasons to be discussed below. As shown in Figure 5.6 our model reproduces both the intensity and dispersion seen in our data. This model gives rise to exchange parameters $J_1' = 4.81(7)\,\text{K}$, $J_2' = 0.139(5)\,\text{K}$, and we have fixed $J_3' = 0\,\text{K}$, based on refinements where it refined to zero, within error. The magnitude of the single-ion anisotropy is calculated to be $\Delta' = 3.52(6)\,\text{K}$. This is an increase of ≈ 2 times the value which would have been expected from the interpolation of calculations of the crystal-field levels of $Gd_2Sn_2O_7$ and $Gd_2Ti_2O_7$. Applying these extracted parameters to the area of $(Q, \Delta E)$ space measured gives a very good fit to the rest of the spectrum, as shown in Figure 5.6 b). Since the parameter-space is highly correlated across all parameters—particularly J_1 and Δ—multiple values of the parameters give roughly equivalent fits. Also, the optimisation routine used is sensitive to local-minima, and thus may depend on the values with which the parameters are initialised.

Despite only being fit using two representative cuts, we can see that the model used provides a very good representation throughout reciprocal space, and thus we are confident that the parameters used give a good explanation of the interactions in the system. We have not, however, considered the approximately flat band at $\Delta E \approx 0.45\,\text{meV}$. Multiple explanations were sought for this band, including the possibility of it being a 'ghoston' of an intense mode in the 2^{nd} (or higher) Brillouin Zone (BZ),[42] or the possibility that there is a significant degree of anisotropy in the exchange matrix.[225] A search across BZs, and a detailed investigation into the

feasibility of an anisotropic exchange matrix were undertaken, but neither provided an appropriate explanation. Furthermore, our data suggest that this mode is a real, and not a spurious, excitation. Our multi-rep analysis shows that we observe this mode to be distinct from the higher energy mode and it is not simply a feature of instrumental resolution, as shown in Figure 5.7.

We believe that this band is, instead, a crystal-field level created by the admixture of states with $L > 0$ into the ground-sate. This is supported by point-charge calculations, performed by Dr Duc Le (ISIS Neutron and Muon Source), which suggest that, when the spin-orbit-coupling (SOC) on the Gd site is enhanced relative to a baseline value from Gd-doped LaF_3,[226] a crystal-field excitation can exist at approximately this energy.* We propose, therefore, that it is the approximations of LSWT which limit our ability to simulate this particular excitation. If we were to include accurately determined SOC parameters into our model, we believe that we should be able to model this crystal-field excitation; this remains an open problem.

5.2.6 Direct Monte Carlo Simulations at $T = 1.8\,\mathbf{K}$

We have used direct Monte Carlo (DMC) simulations in order to model GPO using the parameters extracted form our inelastic neutron scattering data. This allows us, as with our RMC refinements, to generate real-space spin-configurations, allowing the direct analysis of the spin-correlation functions along high-symmetry directions, as well as the calculation of the expected single-crystal diffuse magnetic

*We also note that this mode is predicted to exist for our model parameters (*i.e.* not considering the admixture of $L > 0$ states), albeit with zero intensity, when the single-crystal dispersions along high-symmetry directions of reciprocal-space are calculated. We anticipate that either symmetry breaking structural features—*e.g.* oxygen vacancies, site-mixing of gadolinium and platinum—or magnetic interactions beyond LSWT—*e.g.* two-magnon processes—could otherwise be responsible for the observed intensity. Joint X-ray and neutron Rietveld refinement of data collected at I11 and Polaris do not show evidence of such structural features, as shown in Table 5.1 and Figure 5.2.

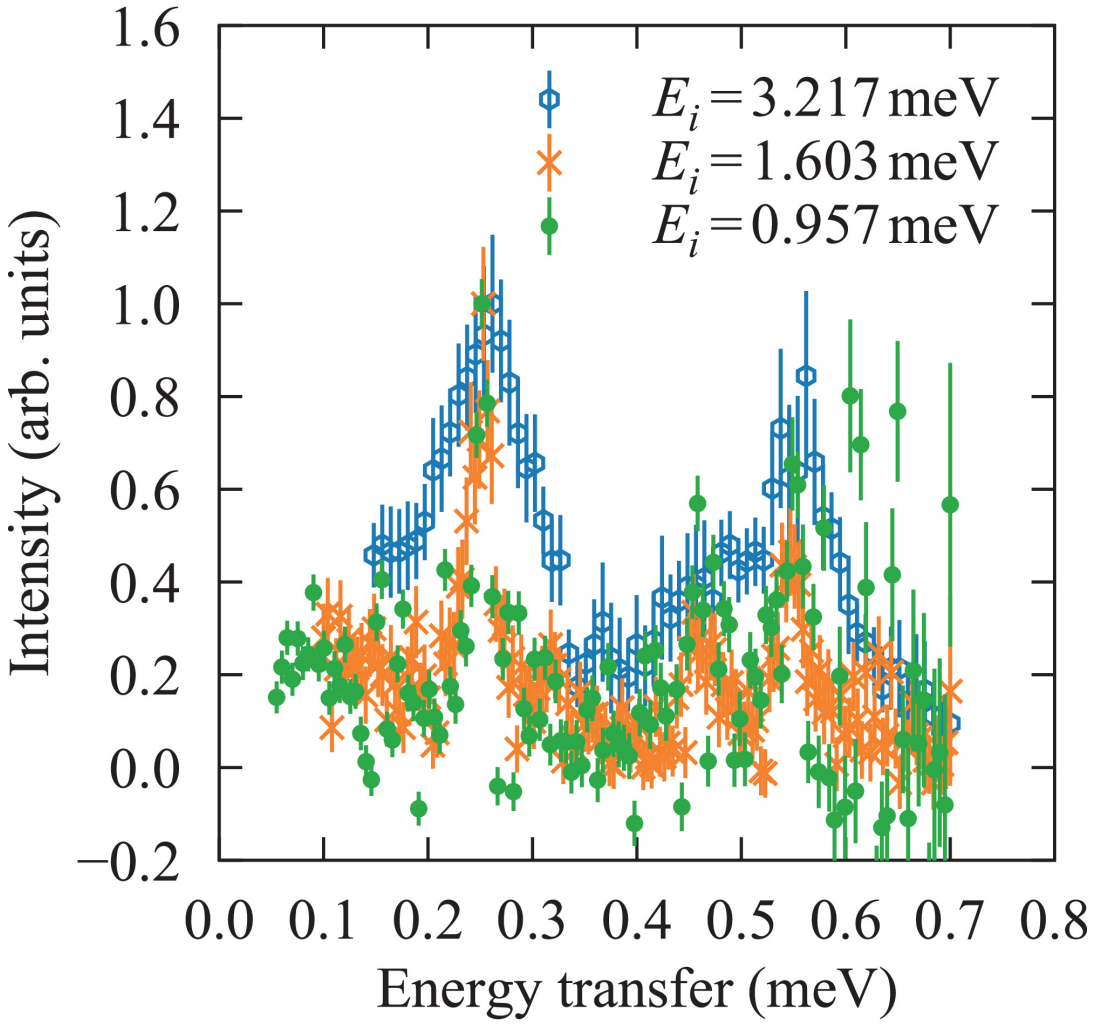


Figure 5.7: Comparison of the intensity of the inelastic signal for cuts between $Q = 0.2$ and $Q = 0.3$ for all measured incident energies, showing the presence of the peak at $\Delta E = 0.45\,\text{meV}$.

scattering patterns. Full computational details of the DMC analysis are contained in Refs. 143,152,218. Since we do not have a well defined magnetic moment for our sample, we have used the RMC algorithm implemented in SPINVERT in order to generate a scale factor for our simulations.*

In order to minimise the Hamiltonian [Eq. 5.1], we have used a Metropolis approach with our direct Monte Carlo algorithm. Long-range dipolar interactions were calculated using Ewald summation, with a simulated metallic boundary. The spin autocorrelation function was calculated from snapshots every $t = 500$ moves, and was checked for correlation, with a value of $\langle \mathbf{S}(0) \cdot \mathbf{S}(t) \rangle \lesssim 0.05$ indicating effective decorrelation of the snapshots. To allow for the direct comparison of our RMC refinements and our DMC simulations, the box size and other run parameters were kept the same as those used in Section 5.2.4. In all of our DMC simulations, we have used the same dipolar exchange constant as for the spin-wave modelling, and we have used the single-ion anisotropy value extracted from our spin-wave fits.†

Comparison with the phase diagram in Figure 1.15 b) shows that a small, antiferromagnetic, J_2 and/or a ferromagnetic J_3 should favour $\mathbf{k} = (000)$, when J_1 itself is antiferromagnetic. We therefore initially used the values obtained from least-squares fitting of the spin-waves as a starting point, and we obtain a very good match to our diffuse scattering data, as shown in Figure 5.8. In order to ensure that this is a robust set of exchange parameters, we have followed a systematic parameter-sweep-based approach in order to minimise χ^2. Since we expect that the

*As mentioned above the sample shifting prevented the refinement of the magnetic moment, which is used by SPINVERT to determine the scale using $g^2 S(S+1)$.

†Further values of Δ were tested, however none provided a meaningfully better fit to the diffuse scattering data.

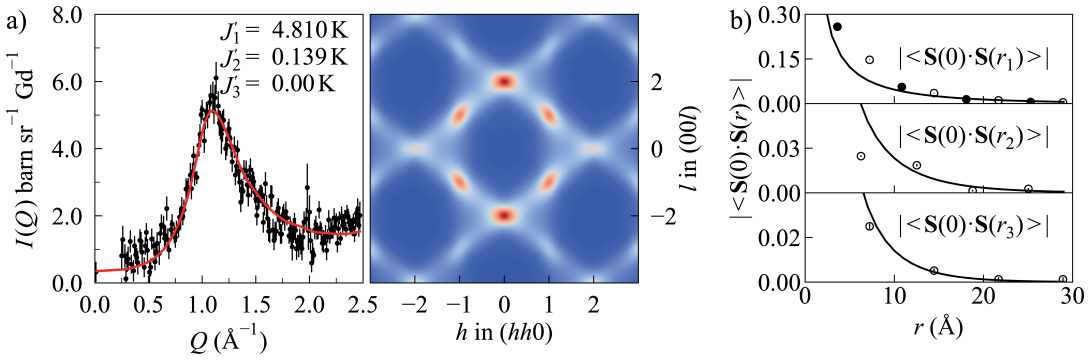


Figure 5.8: Results of our direct Monte Carlo simulations used to model GPO. **a)** Left panel shows the fit to the diffuse magnetic powder neutron data collected using D7. Right panel shows the single crystal scattering calculated from our simulation boxes using SCATTY. **b)** Spin-spin correlation functions along high-symmetry directions in real space. Spin-spin correlation functions along high-symmetry directions in real space. Note the change of scale between the three directions. The black lines show the Ornstein-Zernicke (OZ) decay according to Equation (5.8). Filled and hollow symbols represent negative and positive correlations, respectively. Error bars are smaller than the size of the points.

most important exchange parameter is J_1, we first scanned along this value alone to find the minimum in χ^2. For a given J_1 the ordering vector varies with both J_2 and J_3; we therefore performed a grid search across both parameters simultaneously. The parameter space searched is presented in Appendix A2. The values extracted from the fitting on the spin-waves do not give the lowest χ^2 value, however we observe a wide valley of stability around those parameters. Additionally, the difference in diffuse scattering between the values with lowest χ^2 and those from the fitting of spin-waves is minimal, and so we have proceeded with the values extracted by fitting of the spin-waves.

We have again extracted the real-space spin-spin correlation functions from our simulations. Figure 5.8 demonstrates that along $\mathbf{r}_1$ there are strong antiferromagnetic correlations with a long correlation length of $\xi = 18.66\,\text{Å}$. Along $\mathbf{r}_2$ there are much weaker, ferromagnetic correlations with a correlation length of $\xi = 8.10\,\text{Å}$, and along $\mathbf{r}_3$ we see ferromagnetic correlations with a shorter correlation length

than along $\mathbf{r}_2$, $\xi = 5.76\,\text{Å}$. These general features are consistent with those extracted from RMC refinements, and therefore demonstrate that the parameters are consistent with the measured data. The main difference is seen along $\mathbf{r}_3$, where the interactions in our RMC refinements are less well defined than for our DMC simulations. We also note that the correlation lengths are longer in our DMC simulations than in our RMC refinements. Both of these features are to be expected due to the stochastic nature of RMC, as discussed above.

Finally we have also extracted the bulk susceptibility from a DMC simulation employing a simulated annealing approach, and the result is shown in Figure 5.9. Comparison of our calculated susceptibility with the data published by Hallas *et al.*[216] confirms that our determined values of the exchange constants reproduce the experimental data very well.* Calculation of the Curie-Weiss temperature for our simulation gives $\Theta_{\text{CW}} = -11.85(4)\,\text{K}$ (*c.f.* $\Theta_{\text{CW}} = -10.75(10)\,\text{K}$ as determined from our fit of the data extracted from the paper of Hallas *et al.*). Finally, we can also extract the position of $T_{\text{N}} \approx 1.5\,\text{K}$ from the calculation of the magnetic heat capacity of the simulation, which is in very good agreement with the experimentally obtained values.

Despite the similarities between our data and those collected for the closely related GSO, there is a clear difference in the magnitude of the ordering temperature. In GPO the ordering temperature is raised by approximately 60% compared to GSO and GTO. This, in turn, appears to be primarily due to the increased strength of the single-ion anisotropy as well as the greater influence of the next-nearest-neighbour

*We find that Curie-Weiss fitting the data extracted from this paper gives rise to a slightly smaller value of Θ_{CW} than reported by Hallas *et al.*

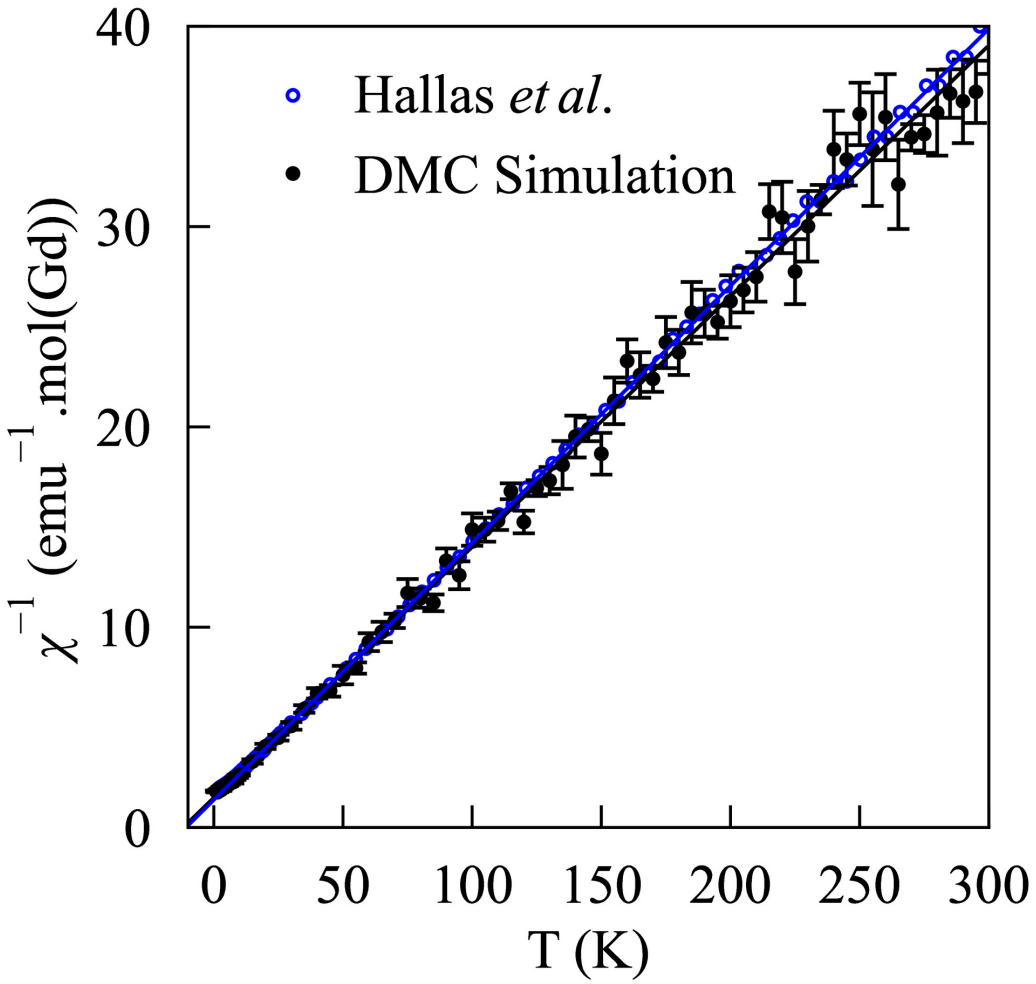


Figure 5.9: Comparison of the inverse magnetic susceptibility calculated from a DMC simulation, using simulated annealing, of GPO using our best interaction parameters (solid black points—for details see Ref. 60), with the experimental data collected by Hallas *et al.* for their sample of GPO (hollow blue points).[216]

exchange parameters (*cf.* J_2(GPO) ≈ 0.0088 K, while the minimum χ^2 value for GSO using a J_1+J_2 model is J_2(GSO) ≈ 0.0012 K, as shown in Ref. 218, Fig. 2(c)). Based on previous reports, we also propose that this increased strength of the exchange interactions between Gd centres is due to extra superexchange pathways, which are opened up by the presence of empty Pt^{4+}, e_g, orbitals (Gd–O–Pt–O–Gd).

5.3 Conclusion

We have investigated both the ordered magnetic and the correlated paramagnetic regimes of a ^{160}Gd enriched sample of $Gd_2Pt_2O_7$ using polarised neutron diffraction and inelastic neutron scattering. These data have been analysed using a combination of direct Monte Carlo, reverse Monte Carlo, and LSWT techniques. Below T_N we have demonstrated that GPO orders into the Palmer-Chalker state with a $\mathbf{k} = (000)$ ordering vector, as expected based on physical property measurements. Above T_N there is a persistence of correlated paramagnetic interactions, which give rise to a broad peak in the magnetic diffuse scattering. Since the next-nearest neighbour (J_2) and single-ion anisotropy (Δ) parameters we observe, as shown in Table 5.2, are much larger than those determined for GSO, we propose that these are the key features in the increase in T_N relative to other Gd-based pyrochlores. We suggest that superexchange pathways, created by the empty Pt^{4+}, e_g-like, orbitals, give rise to the increased ordering temperature by relieving some of the frustration in the pyrochlore system. Our RMC and DMC results support these conclusions.

Following on from this work, it would be of interest to measure the single-crystal neutron scattering of GPO as a direct probe of the single-crystal diffuse scattering pattern and the 3D spin-spin correlation functions. Such studies are limited by the

	a (Å)	J_1' (K)	J_2' (K)	J_3' (K)	D' (K)	Δ' (K)
GTO	10.17	4.80	-0.192	0	0.653	1.500
GSO	10.44	3.91	0	-0.02	0.575	1.715
GPO	10.225	4.81(7)	0.139(5)	0	0.646	3.52(6)

Table 5.2: Comparison of the interaction parameters of GPO with those of GTO and GSO. All values correspond to the 'classical' values—*i.e.* modified by $S(S+1)$ or S^2—as presented above.

availability of single-crystal samples (especially isotope enriched samples). Given a large enough, enriched, single-crystal, the measurement of the INS (in particular using time-of-flight neutrons) would allow the investigation of the spin-wave dispersions along the high-symmetry directions in reciprocal space, and thus might provide an explanation for the scattering intensity we observe which we cannot account for with our model. This work may also form the basis of future investigations into similar compounds such as GTO, where the nature of the interactions giving rise to an unusual, partially ordered, ground state, are not fully understood.

Chapter 6

Magnetic and electrical properties of single-crystalline spin chain compound Er_2BaNiO_5

Throughout the previous chapters of this thesis, I have examined a number of systems which support disordered states in two- or three-dimensions. In this chapter I will present our study of a material which has been proposed to host unconventional magnetic short-range order (SRO) in Ni^{2+} spin-chains connected to magnetically active Er^{3+} ions. It has been reported that Er_2BaNiO_5 possesses magnetic short-range order which is thermally decoupled from a lower temperature magnetic transition, giving rise to a ferroelectric ordering. We have investigated this system using single-crystal measurements of bulk magnetic and thermal properties, pyrocurrent measurements, and single-crystal neutron diffraction. We find that Er_2BaNiO_5 does not undergo a distortion to a polar space-group, and does not support ferroelectricity due to magnetic SRO.

6.1 Introduction

R_2BaNiO_5 oxides (R = rare earth) form a family of compounds which have long been investigated as examples of one-dimensional (1D) spin-chains within oxide systems.[227–230] One particularly well studied example is Y_2BaNiO_5, where non-magnetic Y^{3+} acts as a non-interacting spacer between the 1D chains of magnetic Ni^{2+} ions ($S = 1$), giving rise to an almost purely 1D antiferromagnetic chain of Ni–O–Ni, as demonstrated by magnetic susceptibility measurements and magnetic neutron

diffraction.[231,232] Such systems are of great theoretical and experimental interest, due to their potential to realise Haldane's prediction that integer-spin spin-chains should possess an excitation gap, while half-integer spin-chains should feature gapless excitations. Inelastic neutron scattering measurements of Y_2BaNiO_5 provide a direct observation of the Haldane gap.[233,234]

There has also been a significant interest in the doping of such systems in order to introduce chain terminations, disrupting the Haldane chains, or tune the interactions between chains by varying the interchain separation.[235,236] As outlined in Chapter 1 there are many reasons we may wish to investigate the magnetic interactions of low-dimensional systems. This can help in the determination of the fundamental physics associated with Haldane's original prediction of gapped excitations in integer-spin chains. Thus, the extension of both theory and experiment to determine the precise quantum effects in integer-spin chains has been of much interest.[237,238]

Most of the members of this family form room-temperature structures in the orthorhombic space-group $Immm$, with $a \approx 3.8\,\text{Å}$, $b \approx 5.8\,\text{Å}$, and $c \approx 11.3\,\text{Å}$ [Fig. 6.1 a)]. These unit-cell parameters are relatively consistent for most R,[228] as determined using powder and micro-crystalline samples synthesised using standard solid-state reactions. In the R_2BaNiO_5 structure, Ni^{2+} ions form chains along the a-axis, with a repeat length of $3.754\,\text{Å}$, and a 180° Ni–O–Ni bond. The nickel coordination environment is approximately octahedral.[230] The structure also contains sheets of edge-sharing R–O augmented triangular prisms (*i.e.* a triangular prism with a square pyramid attached to an equatorial face) in the ab-plane, which are vertex-sharing *via* the square pyramid, along the c-axis—which is where they intersect with the Ni–O chains. The structure is shown in Figure 6.1

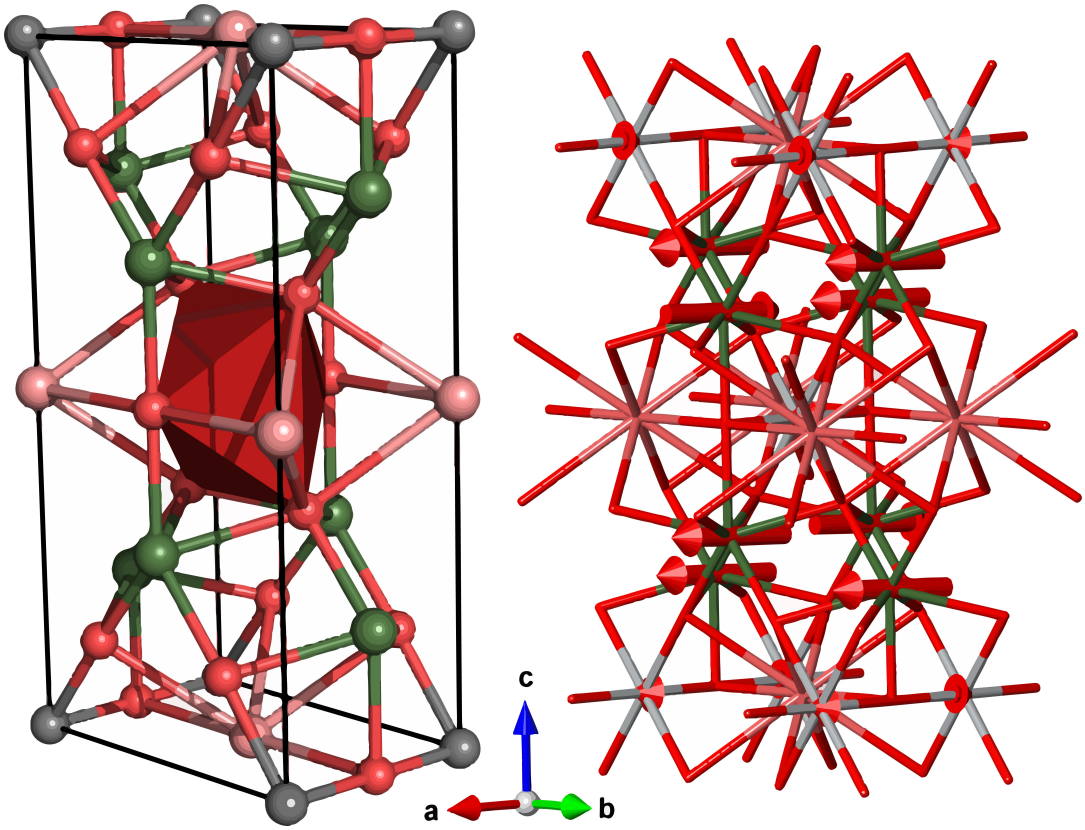


Figure 6.1: Nuclear (left) and magnetic (right) structures of Er_2BaNiO_5 shown for one unit cell of the nuclear structure. The flattened Ni–O octahedra are shown in red in the left-hand panel. Er^{3+} ions are shown in green, Ba^{2+} ions are shown in pink, Ni^{2+} ions are shown in grey, and O^{2-} ions are shown in red.

The simplest magnetic structure in this family comes from Y_2BaNiO_5, where Ni^{2+} ions are the only magnetically active component. Saez-Puche *et al.* demonstrated that the high-temperature magnetic susceptibility of Y_2BaNiO_5 behaves as expected for a one-dimensional antiferromagnetic chain with a coupling constant of $J/k_B = 322\,K$.[231] This behaviour was confirmed by Darriet and Regnault, who revised the value of $J/k_B = 285\,K$, and demonstrated using inelastic neutron scattering that there exists a Haldane gap of $\Delta_0 = 127(10)\,K$ with a single-ion anisotropy term of $D = 46(10)\,K$, due to the axial deformation of the Ni–O octahedra.[233]

The complexity of these systems can be increased dramatically by the inclusion of a magnetically active rare-earth ion in place of Y^{3+}, with Er_2BaNiO_5 being just

one example. As with other members of this family, Er_2BaNiO_5 has also been reported to form in the $Immm$ space-group, with $a = 3.7541(1)$ Å, $b = 5.7442(1)$ Å, and $c = 11.3019(2)$ Å.[239] While Y_2BaNiO_5 had not been observed to undergo a 3D magnetic ordering transition, Er_2BaNiO_5 was found to have a $T_N \approx 32\,K$, which was observed in neutron diffraction[229] and heat capacity[232] measurements. These heat capacity measurements also showed that a Schottky anomaly associated with the crystal-field splitting of the ground-state in the magnetically ordered regime can be observed, as shown in Figure 6.2.

The susceptibility and spectral properties of Er_2BaNiO_5 have also been measured,[240] which demonstrated that there is a large splitting of the ground-state doublet of Er^{3+}, of $\Delta \approx 16.5\,cm^{-1}$. More recent spectral studies confirmed that the exchange splitting for the $^4I_{15/2}$ ground state corresponds to $\Delta \approx 16.5\,cm^{-1} \approx 23.7\,K$.[241] It should be noted that measurements of the susceptibility of Er_2BaNiO_5 are often only taken to 300 K, as shown in Figure 6.2 a), and thus do not show the full contribution of the nickel spin-chains, which is expected to involve a broad peak at $T \approx 400\,K$.[242]

Chepurko *et al.*[240] have also modelled the magnetic susceptibility contribution of the rare-earth ions as

$$\begin{aligned}\chi_R(T) &= \frac{dm_R(T, H_{loc})}{dH_0} \\ &= \frac{\mu_R}{kT}\,\mathrm{sech}^2\left\{\frac{\mu_R(H_0 + \lambda m_{Ni}(T)}{kT}\right\}.\end{aligned} \tag{6.1}$$

μ_R is the magnetic moment of the rare-earth ions (in μ_B), H_0 is the applied magnetic field, and $\lambda \propto \overline{J_{Ni\text{-}R}}$. In this calculation, they set $m_{Ni} = 0$ for $T > T_N$, and for

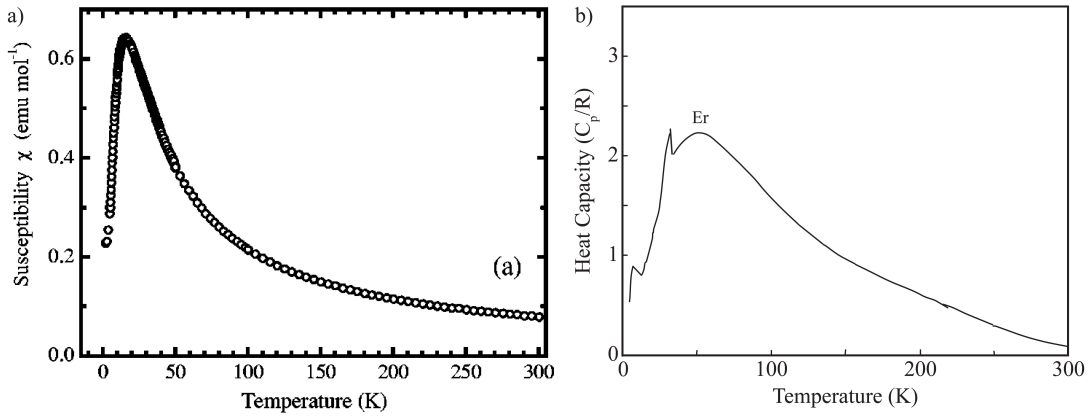


Figure 6.2: a) Magnetic susceptibility of Er_2BaNiO_5 below 300 K, taken from Popova *et al.*[241] **b)** Residual heat capacity of Er_2BaNiO_5 *i.e.* without lattice contributions, adapted from Castro *et al.*[232]

$T < T_{\mathrm{N}}$,

$$m_{\mathrm{Ni}}(T) = \frac{\mu_{\mathrm{Ni}}}{(1 + \exp\left(c(T - T_{\mathrm{N}})\right)}, \tag{6.2}$$

where $c \approx 0.5$. Chepurko *et al.* determine a value of $\lambda = 15.5\,\mathrm{kOe}/\mu_{\mathrm{B}}$. It is also observed that when the magnetisation is measured as a function of magnetic field, at low temperature (4.2 K), there exist two metamagnetic transitions at $H \approx 20$ and 35 kOe.

Neutron diffraction studies of R_2BaNiO_5 powders have tracked the thermal evolution of the magnetic structures as well as the distribution of the magnetic moments in compounds in which the rare-earth site is magnetic and there are relatively strong exchange interactions between Ni and R.[243] As given above, $T_{\mathrm{N}} = 32\,\mathrm{K}$ for Er_2BaNiO_5, and the magnetic space-group is reported as C_c2/c, with magnetic propagation vector $\mathbf{k} = (1/2, 0, 1/2)$. The coordinates and components of the spins for the magnetically active ions at 1.5 K are given in Table 6.1.

Recently there has been a renewed interest into this structural family in order to establish whether there is a coupling between their magnetic and electrical proper-

Atom	x	y	z	$\mathbf{m}_x$	$\mathbf{m}_y$	$\mathbf{m}_z$
Er	0.25	0	0.10145	7.23(5)	0	0.32(6)
Ni	0	0	0	−1.38(6)	0	−0.18(9)

Table 6.1: The positions of the magnetically active ions in Er_2BaNiO_5 in fractional coordinates (of the magnetic unit cell) along with the components of the magnetic moment in μ_B, as presented by García-Matres *et al.*[244]

ties, in an attempt to realise new examples of multiferroic compounds.[245–248] Various members of the family have been investigated, and in the case of Er_2BaNiO_5, it has been reported that magnetic short-range order (SRO) above T_N gives rise to ferroelectric interactions well above the (antiferro)magnetic ordering transition.[249] This SRO would be an interesting route to the realisation of a magnetoelectric multiferroic beyond the canonical magnetically-driven ferroelectrics, such as $TbMnO_3$.[250]

It has been proposed by Basu *et al.* that at $T \approx 60\,\mathrm{K}$ there exists a ferroelectric polarisation, which is created by a distortion of the basal oxygen ions in the Ni–O octahedra.[249] Globally, this distortion corresponds to a structural transition from the $Immm$ space-group to $Im2m$. Since $Im2m$ is a polar space-group, it is able to support a ferroelectric state. Their pyrocurrent measurements on a pressed and sintered powder sample show there is a large and broad peak in the pyrocurrent, which sets in at $T \approx 60\,\mathrm{K}$, as shown in Figure 6.3. Integrating this peak they demonstrate that there is an electric polarisation of $\sim 100\,\mu\mathrm{C/m^2}$ below 50 K.

In this chapter I will present the first experimental investigation of the magnetic and electrical properties of large single-crystals of Er_2BaNiO_5, using a combination of specific heat, magnetisation, pyrocurrent, and single-crystal neutron and X-ray diffraction measurements.

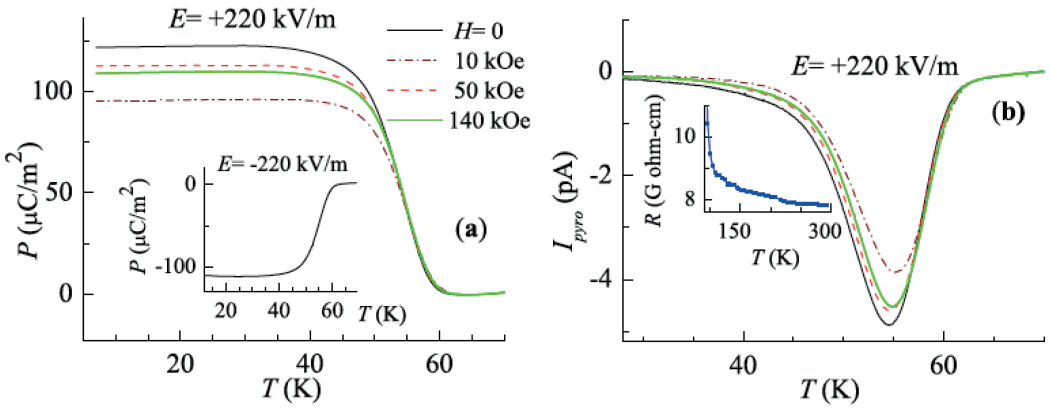


Figure 6.3: a) Electric polarisation, P, as a function of temperature, and **b)** Pyroelectric current as a function of temperature, as measured by Basu *et al.*[249]

6.2 Results and Discussion

6.2.1 Synthesis

Large single-crystal samples of Er_2BaNiO_5 have been prepared for the first time using the synthesis method reported in Section 2.4.1. As shown in Figure 6.4 the crystals formed are consistently faceted, and the use of an X-ray Laue camera allowed for the visual identification of the principal axes.

The composition of our crystals was confirmed by combining several small crystals from our synthesis and grinding them in an agate mortar to afford a homogeneous powder, a portion of which was used for the collection of powder X-ray diffraction data using a Bruker D8 Eco diffractometer. These data have been used in a Rietveld refinement using TOPAS-ACADEMIC 4[221*] and the resulting fits are shown in Figure 6.4. A further scan was performed for an extended period around $2\theta = 29.5°$ and confirmed the absence of Er_2O_3, *i.e.* unreacted starting material. We find that $a = 3.75462(4)$ Å, $b = 5.73766(5)$ Å, and $c = 11.29034(10)$ Å, in close

*Two different versions of TOPAS-ACADEMIC have been used for convenience rather than a technical reason.

agreement with previous results.[239]

We have also confirmed that the as-prepared crystals are of the correct composition using single-crystal X-ray diffraction data collected using an Oxford Diffraction (Agilent) SuperNova A diffractometer using Cu K-α radiation and reduced using the appropriate instrument manufacturer supplied software. An absorption correction of $\mu = 46.15\,\mathrm{mm}^{-1}$ was used and structures were solved using SIR92.[251] SIR92 uses a semi-invariant representation (SIR) technique based on Giacovazzo's method of representations[252] for a direct methods structure solution. Finally, the structure was refined using full-matrix least-squares refinement with CRYSTALS.[253] We also attempted to collect data on a small fragment of a crystal at the I19 beamline, Diamond, Harwell, UK, however even with the highest attenuation on the incident radiation, structure solution proved to be very difficult as the sample over-saturated individual pixels of the detector. It is therefore possible that our sample preparation methods, especially the slow cooling stage, led to a very high degree of crystallinity.

6.2.2 Bulk Thermal Properties

The heat capacity of a small, representative, single crystal was measured using a Quantum Design PPMS. The sample was mounted to the PPMS puck using a thin layer of grease, the background of which was measured prior to mounting the crystal, and subtracted from the final measurement. Previous measurements of the heat capacity had only been performed on powder or micro-crystalline samples.[229]

The results of our measurements are shown in Figure 6.5. We clearly see that there is a broad anomaly in C/T below $T \approx 30\,\mathrm{K}$ as well as a sharp feature at 32 K, which is consistent with the previous measurements of T_N.[254] We assign the broad

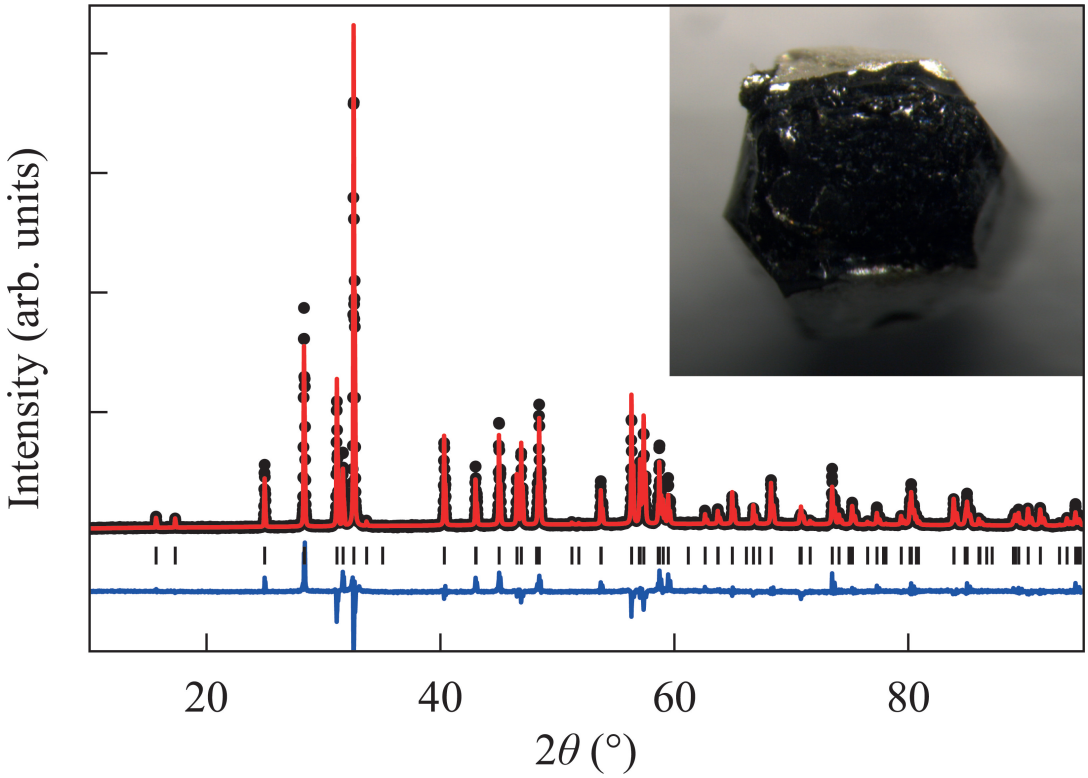


Figure 6.4: Rietveld refinement of a powder X-ray diffraction pattern for our ground single crystals, the fit is shown in red, with the difference function shown in blue. Inset: Representative single-crystal sample, viewed down the a-axis, showing the facets formed.

low-temperature peak to a two-level Schottky anomaly,

$$C_{\text{Schottky}} = R\left(\frac{\Delta}{T}\right)^2 \frac{e^{\Delta/T}}{[1+e^{\Delta/T}]^2}, \tag{6.3}$$

where R is the molar gas constant, and Δ is the energy gap between the two levels. Fitting this equation to the low-temperature portion of the measured heat capacity, and including a T^3 term to account for the lattice contribution to the heat capacity,[255] a gap of $\Delta = 24.1(1)\,\text{K}$ is observed, matching the value reported from spectroscopic measurements very well ($16.5\,\text{cm}^{-1} \approx 23.7\,\text{K}$).[240]

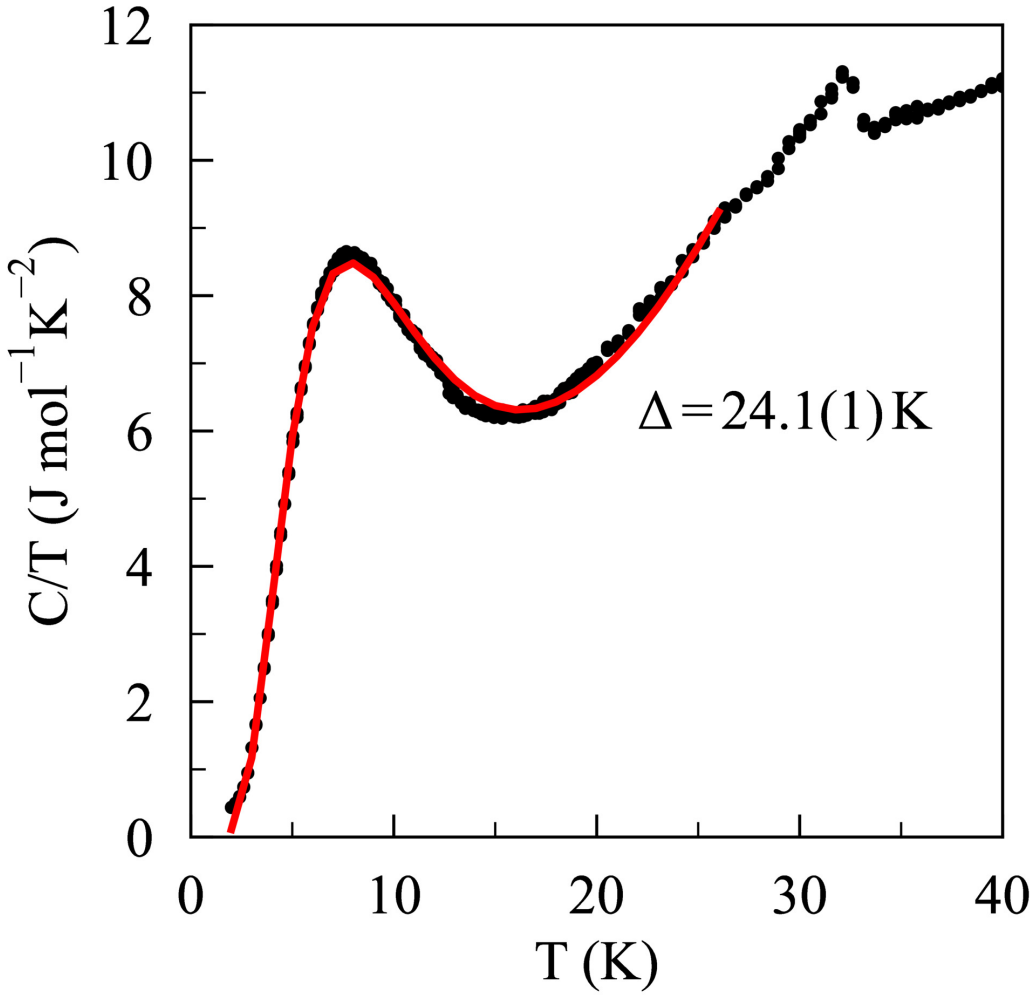


Figure 6.5: C/T as a function of temperature, showing both the Schottky anomaly (fitted curve in red) and the Néel temperature at 32 K.

6.2.3 Bulk Magnetic Properties

A Quantum Design MPMS 3 with a vibrating sample magnetometer (VSM) insert was used to measure the magnetic susceptibility under both zero-field cooled (ZFC) and field cooled (FC) conditions, as well as the magnetisation as a function of applied field across a range of temperatures. Our single-crystal sample was attached to the quartz sample holder using GE varnish. Measurements were performed with both the *a*-axis and *b*-axis aligned parallel with the field.

The temperature dependence of the magnetic susceptibility is shown in Figure 6.6. We observe very different behaviour parallel and perpendicular to the 'easy' *a*-axis, with a significantly greater increase in susceptibility at low temperature when the magnetic field is aligned parallel to this axis. The susceptibility in the high-temperature regime for measurements parallel to both the *a*- and *b*-axes is roughly consistent with Curie-Weiss behaviour, with $\Theta_{\mathrm{CW}} = 26.2\,\mathrm{K}$ and $-83.8\,\mathrm{K}$ respectively. The temperature range over which these values were calculated is, however, in the regime where there will be 1D order in the nickel sublattice, as the Ni–Ni interaction strength is $J \approx 300\,\mathrm{K}$. Therefore, the precise region over which the Curie-Weiss fit is performed has a strong influence on the calculated value, as it is not in a fully paramagnetic regime. In both cases, the overall magnitude of the magnetic moment is $\approx 14.7\,\mu_{\mathrm{B}}/f.u.$, in good agreement with previous measurements.[256]

We can compare these results with those of García-Matres *et al.* directly.[243] When we orient the field along the *a*-axis of our single crystal we see a significantly higher peak value of the susceptibility ($2.75\times10^{-3}\,\mathrm{emu/g}$ vs. $1.5\times10^{-3}\,\mathrm{emu/g}$). When the field is oriented parallel to the *b*-axis of our crystal the peak is much smaller, and

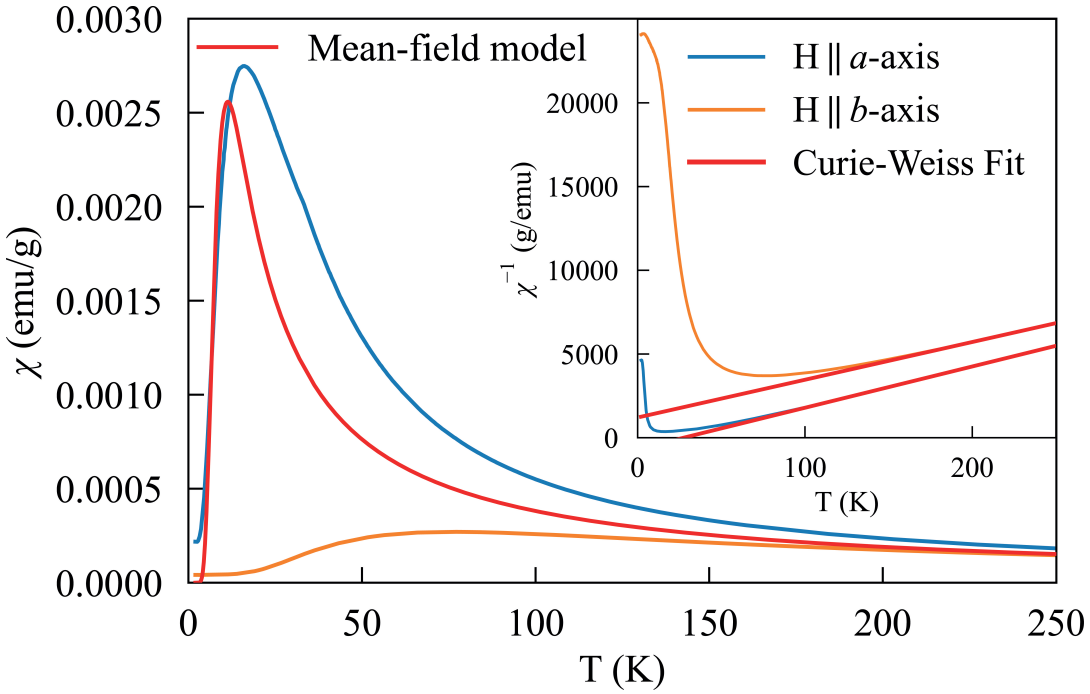


Figure 6.6: DC magnetic susceptibility as a function of temperature, with the field applied parallel to the a and b-axes for the upper and lower curves, shown in blue and orange, respectively. The red curve is the susceptibility of the mean-field model described in the text. **Inset:** The inverse susceptibility with the field applied parallel to the a and b-axes, with a Curie-Weiss fit to the high-temperature portion ($T > 200\,\mathrm{K}$) shown in red.

shifted to higher temperature. In the case of Y_2BaNiO_5 differences in susceptibility along single-crystal axes have been seen [Ref. 74, Fig. 1], however they are not as dramatic as those observed here in Er_2BaNiO_5.

If we use the Equation 6.1 to model the susceptibility of our measurements with $\mathbf{H} \parallel a$-axis we can extract a value of $\lambda = 12.1\,\mathrm{kOe}/\mu_\mathrm{B}$, which is below the reported value of $\lambda = 16.8\,\mathrm{kOe}/\mu_\mathrm{B}$.[240] We also do not fit the high temperature part of the susceptibility with this equation, indicating that we are, perhaps, dealing with a greater moment for Er^{3+}. This may also be a result of this mean-field model being isotropic, and hence not suited to our single-crystal measurements. Ideally we would have fitted this model to either powder data, or data averaged from all three crystallographic directions, however such data were not available. If we assume that

this mean-field parameter is directly equivalent to the average interaction parameter between Ni–Er, then we can say that $\overline{J_{\text{Ni-R}}} \approx 1\,\text{K}$, and is therefore approximately two orders of magnitude smaller than the Ni–Ni interactions.

We have also measured the response of the magnetisation to the strength of the applied magnetic field, as shown in Figure 6.7. Measuring the magnetisation as a function of applied magnetic field parallel to the crystallographic a-axis at 2 K, we observe two sharp jumps in the magnetisation as the field increases. Such sharp discontinuities have not been observed previously, however there have been reports of metamagnetic transitions—*i.e.* subtle changes in gradient of the curve—at the same values of applied magnetic field.[240] When measured with the crystal oriented with the magnetic field parallel to the b-axis, there are no sharp discontinuities, and therefore we may expect that a powder average of these measurements would lead to the small changes in gradient observed previously. We propose that these are spin-flip transitions, with the two jumps being due to the reorientation of Er^{3+} sublattices [Fig. 6.7 a)]. Similar behaviour has been observed in Nd_2BaNiO_5 by Popova *et al.*, who report that there are two different rare-earth sublattices; one with spins oriented approximately parallel with the field, and the other with the spins in the opposite direction.[257] There is also a significant hysteresis ($\sim 1\,\text{kOe}$) as the field is cycled, indicating that there is potentially a minor ferromagnetic component to the magnetisation with a small remnant field.

If we compare these results with the previous bulk magnetic measurements of Er_2BaNiO_5, we can see that our single-crystal measurements provide us with a much clearer depiction of several features. For example, we see very sharp changes in the magnetisation with increasing field strength, which have only previously been ob-

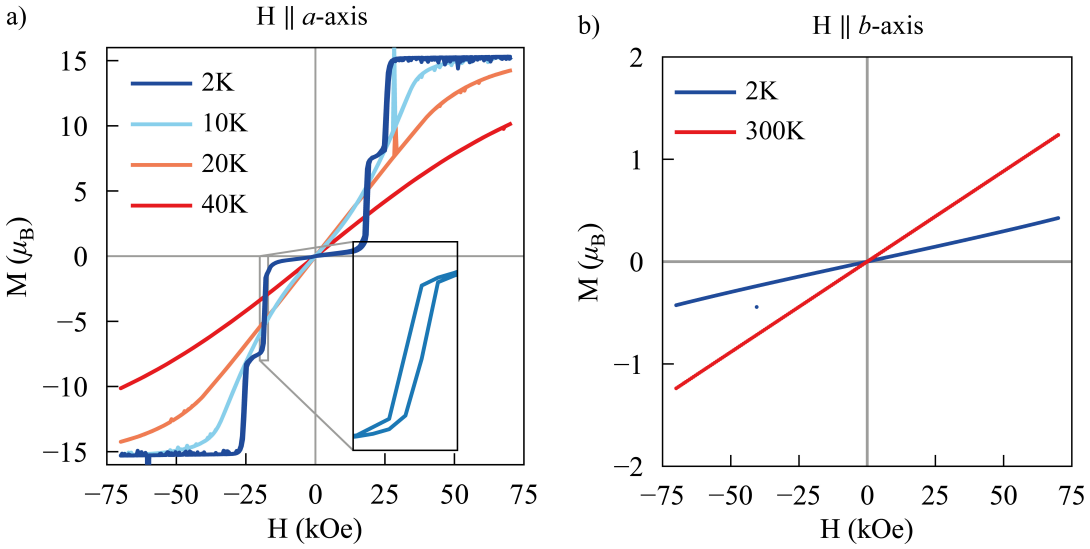


Figure 6.7: a) M vs H curves with the magnetic field parallel to the a-axis at four representative temperatures, showing two spin-flip transitions at the base temperature of our measurements. Inset: Expanded view of the first spin-flip transition, showing the hysteresis in the transition. **b)** M vs H curves with the magnetic field parallel to the b-axis at 2 K and 300 K. We see no evidence of transitions with increasing field along this direction.

served as subtle changes in the gradient. We can also pinpoint significant differences in the susceptibility when the magnetic field is aligned along different axes of the crystal.

By now we have established that our large single crystals are of the correct crystallographic form, and demonstrate the same bulk properties, including a low-temperature Schottky anomaly, and a magnetic ordering temperature of $T_N = 32$ K. We have also established that there is a significant anisotropy in the bulk magnetic properties of our single crystals.

6.2.4 Electrical Properties

We turn now to examine the electrical properties of Er_2BaNiO_5. Electrical measurements were performed using a Keithley 6517B electrometer. Prior to measurement, a powder sample was compressed into a disk and sintered at 1000 °C overnight. Both the sintered disk and single-crystal samples were mounted to a custom sample

holder using GE varnish, with silver paint used as the electrical contacts. In the case of the single crystal, the contact area of each axis was $\sim 1\,\mathrm{mm}^2$, while $d = 4\,\mathrm{mm}$ and $l \approx 2\,\mathrm{mm}$ for the sintered powder disk. For our pyrocurrent measurements, a bias voltage was set up across the sample using a high-voltage power supply. For our single-crystal measurements this was of approximately $220\,\mathrm{V\,mm^{-1}}$, to enable direct comparison with Basu *et al.*, while the field applied to the powder was approximately $110\,\mathrm{V\,mm^{-1}}$. The sample was then cooled under the bias voltage from 120 K to 10 K, where the electric field was removed and the sample shorted for sufficient time to allow the background to stabilise. The pyrocurrent was then measured as a function of temperature while heating in zero electric field. In order to confirm our measurements we additionally performed a pyrocurrent measurement with a bias electric field applied, as described in Ref. 151. In all cases, we have also measured the resistivity as a function of temperature.

The results of our electrical measurements are presented in Figures 6.8 and 6.9. Our resistivity measurements indicate that there is a difference in the electrical conductivity of our sample which depends on which axis we apply the electric field across. The temperature at which our resistivity increases sharply is higher than reported in Ref. 256 potentially due to sample dependent effects.

Our pyrocurrent data collected for a sintered powder sample are shown in Figure 6.8 a). While the general features are similar to those of Ref. 256, the peaks occur at a higher temperature—*viz.* 55 K *vs.* 70 K—and exist over a larger temperature range.* We also observe a secondary peak at approximately 100 K, which was not

*The difference in peak magnitude cannot be compared directly with Basu *et al.* due to the difference in applied field strength.

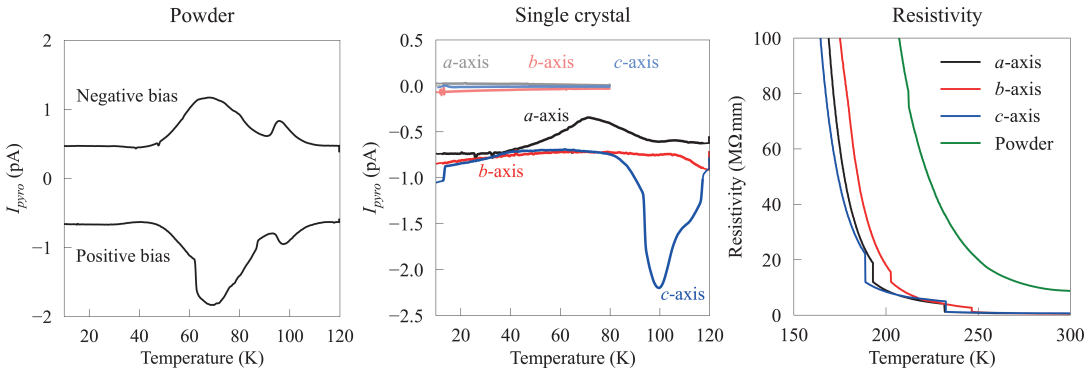


Figure 6.8: Temperature dependence of the electric current with heating for Er_2BaNiO_5. **Left panel:** Results of applying both a positive and negative bias electric field while cooling a powder sample of Er_2BaNiO_5. **Middle panel:** The results of applying a positive bias electric field while cooling our single crystal sample of Er_2BaNiO_5. **Right panel:** Resistivity of Er_2BaNiO_5 measured while cooling, the step changes are due to the instrument changing the measurement range. Below this temperature range, the resistivity increases above the measurement range of the instrument.

previously reported. As with the report by Basu *et al.* we observe that on switching the direction of the bias field, we reverse the direction of the pyrocurrent. We suggest that the main features of the powder pyrocurrent measurements—on which Ref. 256 relies for its evidence of inversion-symmetry breaking—are sample dependent.

In order to investigate this feature further, we have measured the pyrocurrent generation of our single-crystal samples. The electric transition reported by Basu *et al.* should retain the orthorhobmic symmetry of the system ($m2m$ point group), and the polarisation they propose should occur along the b-axis. More generally, in such a transition, the only possible directions of the polarisation are along the a, b, and c-axes. We have therefore measured the pyrocurrent across these directions of our crystal; our results are shown in Figure 6.8 b). We collected data by cooling under electric field from both 80 K and 120 K. The data collected show that when our sample was poled from 80 K to 10 K, we did not observe any features at all upon heating back to 80 K in zero field. Those data collected for poling from 120 K with the electric field applied along the b-axis while cooling show no features. We

do, however, observe features along both the *a*- and *c*-axes. Measuring across the *a*-axis we observe a positive deviation, despite the application of a positive bias while cooling. With the field applied along the *c*-axis we observe features in the pyrocurrent centred around 100 K. This is potentially related to the small feature shown in the powder measurements.

When a single-crystal sample of Er_2BaNiO_5 is subjected to a bias voltage on cooling, we do not observe pyrocurrent peaks consistent with the conclusions of Basu *et al.* when poling from 80 K; such peaks are only observed in powder samples. The observation that our powder sample shows features similar to those measured by Basu *et al.* implies that the effects observed are a result of polycrystallinity. We do not currently have a conclusive explanation for the features observed in the *a*-axis and *c*-axis when poling from 120 K. The feature observed in the *a*-axis appears at a similar temperature to that in the powder measurement, and may be related, however it is anomalous that the feature deviates in the positive direction. These measurements were performed on a separate day from the measurements up to 80 K, and the crystal had undergone many rounds of temperature cycling, which may have caused some internal strain. We did not have enough instrumental time to repeat these measurements sufficiently, or prepare multiple crystals for measurement. This remains an area of future research.

If we compare these features with Refs. 258 and 151 we can begin to propose why they are observed in a powder, and not in our single-crystal samples. Both De *et al.* and Terada *et al.* discuss the influence of thermally stimulated free charge (TSFC) carriers, which we believe are the cause of the apparent polarisation in Er_2BaNiO_5. TSFC carriers are, essentially, grain-boundary effects, where charge

carriers are unable to move across a grain boundary below a certain temperature. They are therefore trapped at low temperatures, and can be released when the temperature is raised.

One particular technique for the differentiation between a ferroelectric transition and TSFC carriers is the 'bias electric field' (BE) method. In this method, the sample is cooled without an electric field and is then heated in the presence of a bias electric field. If the observed pyrocurrent is a result of TSFC carriers, then the BE measurement should simply produce a smoothly varying curve, with no sharp peaks at the same positions as those seen in pyrocurrent measurements. This is demonstrated by Terada *et al.*, in particular for $SrMn_7O_{12}$.[151] In their example, peaks are observed in the pyrocurrent measurements, away from magnetic transitions, but no peaks are observed in the measurements of the bias electric field, indicating that the features observed in the pyrocurrent measurements are artefacts of the frozen-in charge carriers, and not ferroelectric transitions.

We have applied this technique to the *c*-axis of our single crystal and our powder sample, as they were the only measurements which gave rise to features in the standard pyrocurrent measurements. The results of these measurements are shown in Figure 6.9. In neither our single-crystal, nor our powder sample, do we see any sharp features in the BE measurements at any temperature at which the peaks are seen in the pyrocurrent measurements. The same is true at the magnetic ordering transition. We therefore conclude that the features we have seen are not the result of ferroelectric polarisation, but instead arise due to the trapping of TSFC carriers at grain boundaries.

Since the freezing-in of TSFC carriers is essentially a grain-boundary effect, it

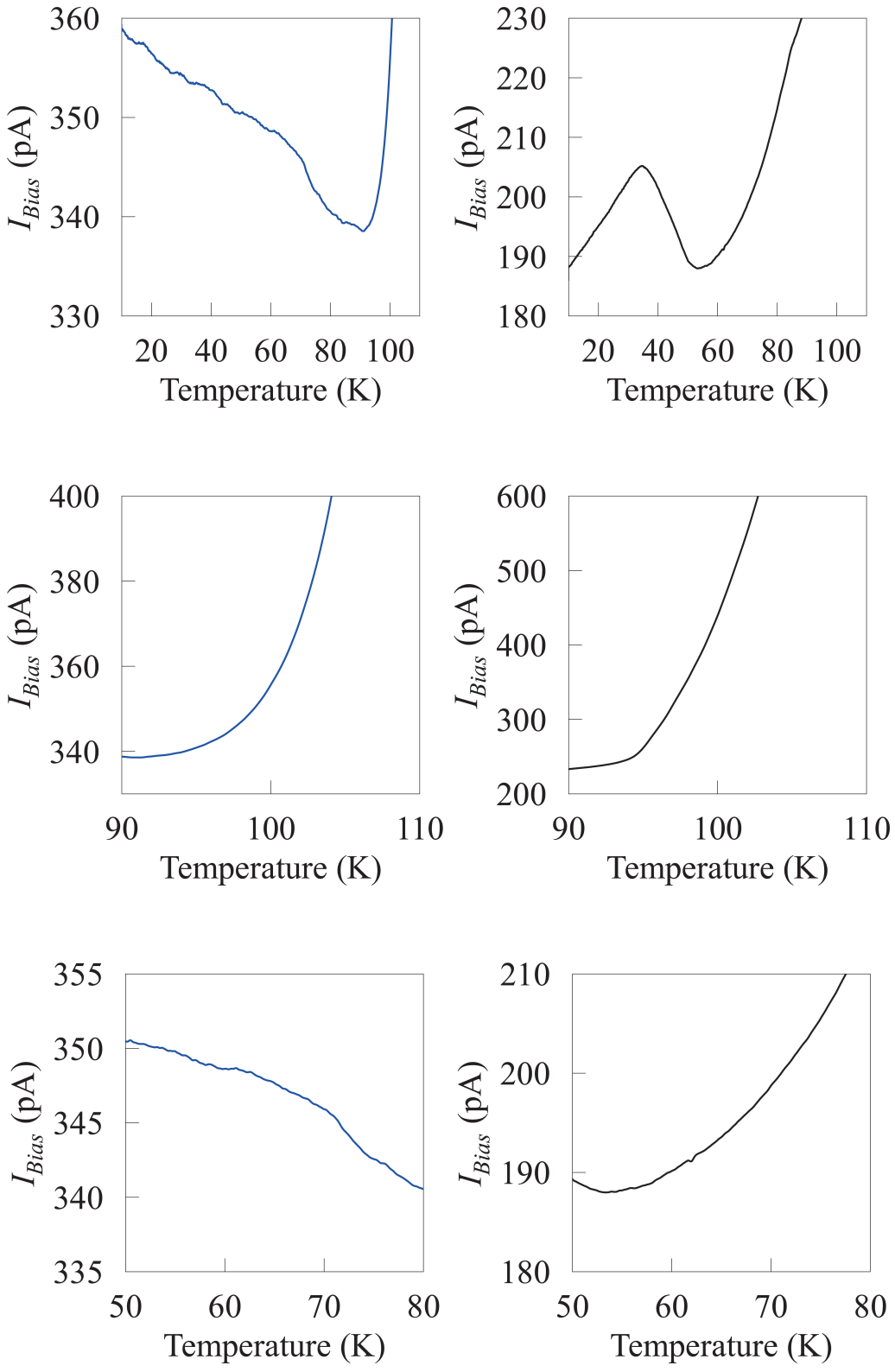


Figure 6.9: Dependence of the electric current on temperature, while heating Er_2BaNiO_5 while applying an electric field across the c-axis (left panels), or a powder sample (right panels). **Top:** BE measurements over the temperature range measured. **Middle:** BE measurements at the location of the high temperature features observed. **Bottom:** BE measurements at the location of the transition proposed by Basu *et al.*

is of no surprise that we would observe features of them in a powder sample. We may also expect to observe the trapping of charges as a surface effect, or due to potential defects within a single-crystal. This may also help to explain why these observations are sample dependent. We therefore propose that one of these effects is the cause of the feature seen in the pyrocurrent measurements along the c-axis.

6.2.5 Single-Crystal Neutron Diffraction

With our measurements of the electrical properties of Er_2BaNiO_5, we have ruled out the existence of a ferroelectric transition well above T_N, as was previously reported. In order to substantiate this claim further, we have performed single-crystal neutron diffraction measurements, which should allow us to define the upper limit of the mangitude of any potential oxygen ion displacements in Er_2BaNiO_5.

We now turn to the neutron diffraction data for our single crystals of Er_2BaNiO_5. We have collected data for an ~ 22 mg single crystal using the SXD beamline at the ISIS Neutron and Muon source, Harwell, UK. Data were collected at 290 K, 80 K (*i.e.* above the proposed T_c), 40 K (below T_c but above T_N), and 5 K (below T_N), with five orientations per temperature. These data were integrated and corrected for absorption using SXD2001,[259] and were analysed using Jana2006.[260] The high temperature dataset was also used to confirm our sample composition.

As for our single-crystal X-ray diffraction measurements, our neutron diffraction data at high temperature confirm the composition of our sample, the $Immm$ space-group, and the unit-cell parameters of $a = 3.7529(16)$Å, $b = 5.7286(32)$Å, and $c = 11.2853(45)$Å. We have also used our single-crystal neutron time-of-flight (ToF) Laue diffraction patterns at 5 K to refine the magnetic superstructure. Us-

Compound	Er_2BaNiO_5
Formula weight (g mol^{-1})	610.54
Crystal System	Orthorhombic
Space Group	$Immm$
Z	2
Radiation	TOF Neutrons
Crystal colour	Black
Crystal size (mm)	$7 \times 1 \times 0.5$
Temperature (K)	290
a (Å)	3.7529(16)
b (Å)	5.7286(32)
c (Å)	11.2853(45)
V (Å^3)	246.5
G_{iso}	0.013597
Reflections (obs, all)	2596, 2603
Refinement on	F
R_{all}, wR_{all}	12.43, 14.55
R_{obs}, wR_{obs}	12.40, 14.54
GOF_{obs}, GOF_{all}	4.93, 4.93

Table 6.2: Crystallographic details of the nuclear structure of Er_2BaNiO_5 measured at 290 K.

ing the previously published structure from García-Matres *et al.*[243] we were able to perform a robust refinement of the magnetic and nuclear structures below the Néel temperature. These results are presented in Table 6.2 and are discussed below.

In our low temperature, 5 K, measurements, the magnetic structure reported by García-Matres *et al.*[243] gives a very good fit to the data we have collected, and our refined moment sizes match very well with these previous results. The crystallographic details are shown in Tables 6.3 and 6.4. We observe a magnetic moment of magnitude 7.3 μ_B on Er^{3+} and a magnetic moment of magnitude 1.1 μ_B for Ni^{2+}.

In order to investigate whether there is a structural transition below T_c but above T_N, the existing structural model was used for the structure solution and refinement of the data collected at 80 K and 40 K, to provide a comparative reference for the refinements in the lower symmetry space group. Using the information given by

Compound	Er_2BaNiO_5
Formula weight (g mol^{-1})	610.54
Crystal System	Orthorhombic
Magnetic Space Group	C_c2/c
Z	2
Radiation	TOF Neutrons
Crystal colour	Black
Crystal size (mm)	$7 \times 1 \times 0.5$
Temperature (K)	5
a (Å)	7.4917(26)
b (Å)	5.7180(25)
c (Å)	22.5285(69)
V (Å^3)	965.1
G_{iso}	0.011554
G_{Mag}	1.575794
Nuclear Reflections (obs, all)	2898, 2902
Magnetic Reflections (obs, all)	594, 597
Refinement on	F
R_{all}, wR_{all}	12.06, 14.88
R_{obs}, wR_{obs}	12.04, 14.88
Nuclear refinement	
R_{all}, wR_{all}	11.51, 13.99
R_{obs}, wR_{obs}	11.50, 13.99
Magnetic refinement	
R_{all}, wR_{all}	18.27, 18.39
R_{obs}, wR_{obs}	18.16, 18.37
GOF_{obs}, GOF_{all}	5.21, 5.20

Table 6.3: Crystallographic details of the magnetic and nuclear structures of Er_2BaNiO_5 measured at 5 K.

Atom	x	y	z	$\mathbf{m}_x$	$\mathbf{m}_z$	$\lvert\mathbf{m}\rvert$
Er_1	0.25	0	0.1015	7.374(97)	0.579(77)	7.396(124)
Ni_1	0	0	0	−1.136(89)	0.082(123)	1.139(152)

Table 6.4: The positions of the magnetically active ions in Er_2BaNiO_5 in fractional coordinates along with the components of the magnetic moment in μ_B. For both atoms, $\mathbf{m}_y = 0$.

Temperature (K)	80
Space group	$Immm$
a (Å)	3.7476(14)
b (Å)	5.7169(29)
c (Å)	11.2649(39)
V (Å^3)	245.1
Reflections (obs, all)	3344, 3354
Refinement on	F
R_{all}, wR_{all}	13.26, 15.39
R_{obs}, wR_{obs}	13.23, 15.39
GOF_{obs}, GOF_{all}	4.89, 4.88
Temperature (K)	80
Space group	$Im2m$
R_{all}, wR_{all}	13.11, 15.23
R_{obs}, wR_{obs}	13.09, 15.23
GOF_{obs}, GOF_{all}	4.84, 4.83

Table 6.5: Crystallographic details of our refinements in the $Immm$ and $Im2m$ space groups at 80 K.

Basu *et al.*, we have used the $Im2m$ space group for refinements for both our 80 K and 40 K datasets in order to determine whether our sample shows any indications of undergoing the phase transition proposed.

In order to characterise this transition, we are relying on there being an observable difference in intensity at certain points in reciprocal space, as there is no change in reflection conditions between the two proposed space groups. In Tables 6.5 and 6.6 we have given the refinement parameters for our 80 K and 40 K datasets for both the $Immm$ and $Im2m$ structures.

As expected, we see that in both cases there is a slight improvement in R-factor when our refinement has more degrees of freedom in a lower symmetry space group. However, the refinements using $Im2m$ do not give positive definite values of the anisotropic atomic displacement parameters (ADPs) of the now-split oxygen positions. Therefore we have used isotropic oxygen APDs for the refinements. As shown in Table 6.7, for both our 80 K and 40 K datasets, we see that the refinement

Temperature (K)	40
Space group	$Immm$
a (Å)	3.7459(9)
b (Å)	5.7171(19)
c (Å)	11.2650(26)
V (Å^3)	241.2
Reflections (obs, all)	7524, 7542
Refinement on	F
R_{all}, wR_{all}	13.10, 15.59
R_{obs}, wR_{obs}	13.07, 15.59
GOF_{obs}, GOF_{all}	5.38, 5.37
Temperature (K)	40
Space group	$Im2m$
R_{all}, wR_{all}	13.02, 15.45
R_{obs}, wR_{obs}	12.99, 15.45
GOF_{obs}, GOF_{all}	5.28, 5.27

Table 6.6: Crystallographic details of our refinements in the $Immm$ and $Im2m$ space groups at 40 K.

T (K)	Space group	Ni–O dist. (Å)	ADP	$\sqrt{\mathrm{U(O)}}$ (Å)
290	$Immm$	2.1798(15)	Anisotropic	0.0871
80	$Immm$	2.1627(16)	Isotropic	0.0595
80	$Im2m$	2.153(5), 2.173(5)	Isotropic	0.0528
40	$Immm$	2.1634(10)	Isotropic	0.0593
40	$Im2m$	2.158(4), 2.169(3)	Isotropic	0.0539

Table 6.7: Comparison of the refined Ni–O bond lengths with the size of the ADPs on the oxygen positions. We have taken the average distance from the refined oxygen position to be the square-root of the mean-squared displacement in the direction of the distortion, denoted by U in the table.

structure does move the basal oxygen ions in the manner proposed by Basu *et al.*, and in both cases, the improvement in R-factor is very similar. One method for determining whether a lowering of the R-factor with an increase in the available degrees of freedom is Hamilton's R-factor test.[261] At all temperatures (including 290 K) the improvement in R-factor with the increased degrees of freedom of the $Im2m$ space group is statistically significant at the 95% level. However, the use of the Hamilton R-factor test has been cautioned against in situations where a decision is to be made between a centrosymmetric and a non-centrosymmetric space group.[262,263] We are, therefore, cautious about relying on the Hamilton R-test to determine whether the centre of inversion is lost upon cooling.*

We also note that for the oxygen ions involved in the proposed distortion the ADPs are larger than the change in Ni–O bond length by approximately an order of magnitude. In all cases the anisotropic ADP for the nickel position is elongated in the direction of the proposed distortion, and is slightly larger in the $Im2m$ space group (at 40 K, $\sqrt{\mathrm{U(Ni)}} = 0.0349$ Å in $Immm$ and $\sqrt{\mathrm{U(Ni)}} = 0.0389$ Å in $Im2m$). This leads us to the conclusion that we are not able to observe a distortion of the Ni–O bond lengths relative to the size of the ADPs using the data we have collected.

*We also note that the improvement in R-factor at 40 K is smaller than at 80 K.

One area of further investigation would be to perform a distortion mode refinement of our single-crystal data. Such a refinement would allow us to place an upper bound and an uncertainty on the magnitude of any possible displacement. Furthermore, such a refinement would limit the degrees of freedom of our refinements, which would serve to reduce the underlying source of error in our refinements.

6.3 Conclusions

Access to large single-crystal samples has enabled us to perform more detailed investigations of the directional dependence of the bulk magnetic and electrical properties, which we have compared with the previously published data from powder samples.

Our heat capacity measurements show that the single crystals have a well defined Schottky anomaly at low-temperature, as well as a clear magnetic ordering transition at 32 K, which is significantly sharper than the transition previously observed in powder samples.

We have determined that there is significant anisotropy in the susceptibility and magnetisation of the single crystals. The susceptibility is significantly enhanced along the Ni spin-chain (the a-axis), relative to previous powder-averaged measurements, implying that there is an easy-axis type anisotropy and that the spins can continuously reorient themselves towards a field applied along this axis. This is further demonstrated in our low-temperature measurements of the magnetisation as a function of applied magnetic field—we see a continuous, monotonic, increase in magnetisation with increasing magnetic field strength. Parallel to the easy-axis we observe two sharp, distinct, spin-flip transitions at 19 kOe and 26 kOe—in good

agreement with the metamagnetic transitions observed by Chepurko *et al.*[240]—with a saturation magnetisation equivalent to 15.31 $\mu_B/f.u.$. The upward gradient which lies between the two transitions is attributed to the contribution to the magnetisation from the Ni sublattice. Calculations show that a molecular field model, which takes into account the average $J_{\text{Ni–Er}}$ exchange parameters, can account relatively well for the susceptibility along a single axis of our crystal, however it falls short of describing the susceptibility fully, as it requires the powder averaged susceptibility.

In our electrical measurements, when poling our powder sample from 120 K we see that there is a double peak, centred around 70 K, which is reversible upon inversion of the applied voltage, and is absent in ZFC measurements. This is significantly different to the data collected by Basu *et al.* who observe a single peak at $T = 55$ K.

We have compared these features with our single-crystal samples. While poling from 120 K, we observe a pyrocurrent along the *c*-axis, along with anomalies along the *a*-axis. We propose that the observed pyrocurrent in both the powder along the *c*-axis arise due to thermally-stimulated free-charge (TSFC) carriers.[258] In order to elucidate the true nature of the observed pyrocurrent peaks, we have performed bias-pyrocurrent measurements, as previously described by Terada *et al.*[151] In these measurements, the sample was cooled without an electric field applied (ZFC) and with the sample shorted, in order to prevent the freezing of TSFCs. At base temperature, an electric field is applied across the sample, and the sample is heated. In a non-ferroelectric sample, we would expect to see a smoothly varying curve, absent of any sharp peaks at those temperatures at which features were observed in the pyrocurrent. In a truly ferroelectric sample, we would, however, expect that as we near T_c the dipoles in the sample would collectively polarise, followed by sponta-

neous depolarisation at T_c. This should give rise to a pyrocurrent peak, followed immediately by a trough. No such feature is observed in our data on top of the current changes associated with temperature changes.

Our SXD data show that if we refine both our 80 K and 40 K datasets in both $Immm$ and $Im2m$ there is an improvement in the R-factors, and a displacement of the oxygen ions involved in the proposed distortion in $Im2m$. However, the magnitude of the distortion, and the improvement in the fitting statistics, is very similar for both datasets. We propose that the size the ADPs, relative to the change in Ni–O bond lengths, means that we are unable to observe the lowering of symmetry which has been proposed, using the data collected.

Using ISODISTORT[264,265] we can identify that the the distortion mode for the proposed ferroelectric transition is the Γ_4- mode. Using this distortion mode, it would be possible to perform a symmetry mode refinement to the data collected, in order to gain a better understanding of the potential magnitude of the displacement. This remains an avenue of further investigation for this system.

Taken along with our measurements of the electrical properties of our single crystals, we believe that there is no ferroelectric ordering above T_N due to short-range magnetic order. Such a driving force for polarisation would have been unexpected, as in traditional multiferroics the polarisation emerges by coupling to magnetic symmetry breaking of specific types; short-range magnetic order does not break symmetry. Instead we believe that the features which were observed in a powder sample of Er_2BaNiO_5 are due to charge carries becoming trapped at grain boundaries, which is suppressed in our single crystal sample.

Chapter 7

Conclusion

In this thesis I have presented a number of studies of unconventional magnets using neutron scattering in conjunction with a variety of other experimental techniques. The magnetic materials I have examined have been linked by the common thread of their underlying lattice geometry strongly influencing the magnetic states observed.

In Chapter 3 I investigated $Tb(HCO_2)_3$, a metal–organic framework where the nuclear structure gives rise to strongly-correlated chains of Tb^{3+} ions which in turn form a triangular lattice antiferromagnet in the plane perpendicular to the chains. The analysis of our neutron diffraction experiments of $Tb(HCO_2)_3$ demonstrated that the magnetic state formed at 1.6 K is not long-range ordered in the triangular lattice plane. Instead, short-range magnetic order creates a state equivalent to the triangular Ising antiferromagnet, giving rise to sharp maxima in the continuous diffuse scattering function, which should not be interpreted as Bragg reflections indicative of a partially disordered state. This observation has potential implications for the design of magnetocaloric materials, as we must consider how the entropy of a long-range, or short-range, ordered system will influence the magnetocaloric properties.

In Chapter 4 we have used $CsCoCl_3$ in order to test whether the conclusions of Chapter 3 may be applied more broadly. From our neutron scattering data we have determined that: (i) antiferromagnetic order along the chain direction is observable at 25 K, and (ii) at 19 K the antiferromagnetic interactions perpendicular to the chains are best described in terms of the triangular Ising antiferromagnet. I have used this observation as a starting point for the analysis of the differences between

the long-range ordered state previously proposed, and the short-range order we have observed, in terms of the dynamics of the system. I have adapted a supercell approach for the analysis of phonons in order to calculate the differences in the magnon dispersion curves for these models. I find that gaps are observed in the magnon dispersion for the long-range ordered model, while no gaps are predicted for the triangular Ising antiferromagnet. This implies that measurement of the inelastic magnetic neutron scattering patterns may be able to discriminate between these states. It would be of particular interest to test this conclusion against experimental data for $CsCoCl_3$ directly, and this remains an avenue of further research.

Both of these chapters imply that, at least for magnetic systems, certain states may not be partially disordered, as determined by traditional crystallographic approaches. Instead, the observed sharp features in the magnetic neutron diffraction patterns may be due to local rules defining a short-range ordered state. These results should be tested against other systems, including where the charge[208] or orbital order[209] has been described in terms of a partially disordered triangular model. It should be noted that in these cases, there may be greater physical driving-forces for the formation of genuine partial disorder.

In Chapter 5 I have presented the first neutron scattering study of the frustrated pyrochlore, $Gd_2Pt_2O_7$. Using our polarised neutron diffraction measurements, we find that the ordered magnetic state below 1.6 K is the coplanar, $\mathbf{k} = (000)$, Palmer-Chalker state, as has been observed in the tin analogue, $Gd_2Sn_2O_7$. Inelastic neutron scattering data were also collected in the ordered magnetic regime, where we measured the magnon dispersion in our powder sample. Fitting these spin-waves using linear spin-wave theory, we have been able to determine the exchange constants

responsible for the magnetic structure of $Gd_2Pt_2O_7$. We find that the single-ion anisotropy is approximately twice as large as in $Gd_2Sn_2O_7$, which we attribute to Gd–O–Pt–O–Gd superexchange interactions. There is still an open problem regarding the explicit modelling of an approximately flat band in the inelastic spectrum, which we believe to be a crystal-field level associated with spin-orbit coupling. Finally, we have confirmed that the exchange constants extracted from the fitting of the inelastic spectrum can be used to account for the polarised neutron diffuse scattering data collected just above the magnetic ordering temperature. The analysis of this system would benefit greatly from the collection of data for a single-crystal sample, not least in order to investigate the proposed spin-orbit coupling further. However, the synthesis conditions required for this sample are unlikely to lead to single-crystals suitable for inelastic neutron scattering.

Finally, in Chapter 6 we have investigated a spin-chain system, Er_2BaNiO_5, which had been reported to host short-range magnetic order above T_N leading to magnetoelectic coupling. We synthesised large single crystals, in order to deduce the nature of the short-range ordered state. Measurements of the bulk susceptibility and magnetisation under field, as well as heat-capacity measurements, were in very good agreement with previous reports of this compound. We can also show that there are two spin-transitions as the magnetic field strength is increased, due to two Er^{3+} sublattices coupling to the external field. Our measurements of the pyrocurrent, however, do not fully support the identification of electric polarisation above the magnetic ordering transition. We observe a pyrocurrent for both a powder sample and along two crystal axes, however the temperature at which this current is observed differs significantly from the previous reports. Using the bias electric field

method, we do not observe current peaks consistent with ferroelectric order above T_N. Finally, we have collected single-crystal neutron scattering data in order to identify whether a transition into a polar, ferroelectric, state is observed above T_N. Based on our structure refinements, we cannot observe a distortion in the Ni–O bond lengths, consistent with the reported polarisation, that is greater than the change in refined atomic displacement parameters. Ideally, this work would benefit from being extended to collect pyrocurrent data across different single-crystal samples, in order to investigate any sample dependence. It could also be extended to include a study of whether oxygen annealing or sample doping influence the observed magnetic and electrical responses.

The results I have presented in this thesis suggest a number of interesting avenues for further work both within and beyond this field. Primarily, I have demonstrated that there are circumstances where inferring long-range order may lead to the spurious assignment of symmetry to systems which are dominated by short-range interactions. This has been readily demonstrated in magnetic examples, but may be more broadly applicable to other forms of order.[208,209] Even within magnetic systems, there are a number of examples where such misidentification may have occurred. A natural example for further study would be $CsCoBr_3$, which is reported to share many features with $CsCoCl_3$.[196,197] There are several other systems which have been described as potentially hosting partially disordered antiferromagnetic states, such as $RbCoBr_3$, where it would appear that there is a spin-lattice coupling associated with the transitions.[195] In such cases, it would be of great interest to reassess whether the structural transitions are potentially a result of short-range magnetic order.

Throughout this thesis, it is the underlying crystallographic structure which has had a large influence over the magnetic response of the materials studied. By linking structural features to the resulting magnetism, design rules may be established, and particular magnetic responses may be targeted. This is of particular relevance to the intersection of the MOF community and the magnetism community. Design rules for MOFs have already targeted gas adsorption properties, and similar rules for magnetic responses are being actively developed.[100] In this thesis, I have shown that there is also significant potential for the development of rules for designing magnetocaloric compounds.

The development of a supercell-based approach for the calculation of magnetic excitations may be of particular importance for a variety of investigations into frustrated magnetism. I have demonstrated that it is possible to translate the results of, for example, RMC refinements into the magnon dispersion curves expected for the system. As discussed, such techniques have had important applications in calculations related to the so-called waterfall phonons seen in relaxor ferroelectrics.[155] Extensions of the techniques presented in this thesis could help to provide real-space explanations of magnons observed in disordered spin-systems.

Bibliography

[1] Quessab, Y.; Xu, J.-W.; Ma, C. T.; Zhou, W.; Riley, G. A.; Shaw, J. M.; Nembach, H. T.; Poon, S. J.; Kent, A. D. Tuning interfacial Dzyaloshinskii-Moriya interactions in thin amorphous ferrimagnetic alloys. *Sci. Rep.* **2020**, *10*, 7447.

[2] Kramer, D. Helium users are at the mercy of suppliers. *Phys. Today* **2019**, *72*, 26 – 29.

[3] Shull, C. G.; Smart, J. S. Detection of Antiferromagnetism by Neutron Diffraction. *Phys. Rev.* **1949**, *76*, 1256 – 1257.

[4] Blundell, S. *Magnetism in condensed matter*; Oxford master series in condensed matter physics; Oxford University Press: Oxford ; New York, 2001.

[5] Orchard, A. F. *Magnetochemistry*; Oxford chemistry primers; 75; Oxford University Press: Oxford, 2003.

[6] Kittel, C.; McEuen, P. *Introduction to solid state physics*, 8th ed.; Wiley: New York ; Chichester, 2005.

[7] Néel, M. L., Propriétés magnétiques des ferrites; ferrimagnétisme et antiferromagnétisme. *Ann. Phys.* **1948**, *12*, 137 – 198.

[8] Bloch, F. On the Magnetic Scattering of Neutrons. *Phys. Rev.* **1936**, *50*, 259 – 260.

[9] Halpern, O.; Johnson, M. H. On the Magnetic Scattering of Neutrons. *Phys. Rev.* **1939**, *55*, 898 – 923.

[10] Alvarez, L. W.; Bloch, F. A Quantitative Determination of the Neutron Moment in Absolute Nuclear Magnetons. *Phys. Rev.* **1940**, *57*, 111 – 122.

[11] Wolf, W. P. Ferrimagnetism. *Rep. Prog. Phys.* **1961**, *24*, 212 – 303.

[12] Wildes, A. R.; Cowlam, N. Sperimagnetism in $Fe_{78}Er_5B_{17}$ and $Fe_{64}Er_{19}B_{17}$ metallic glasses: I. Moment values and non-collinear components. *J. Phys.: Condens. Matter* **2011**, *23*, 496004.

[13] Medvedev, M. V.; Goryainova, S. M. Asperomagnetism and Short-Range Magnetic Order in a Heisenberg Magnet with Random Exchange Bonds of Different Signs. *Phys. Status Solidi B* **1980**, *98*, 143 – 154.

[14] Aroyo, M. I. *International tables for crystallography. Volume A, Space-group symmetry*, sixth edition. ed.; 2016.

[15] Litvin, D. B. Tables of crystallographic properties of magnetic space groups. *Acta Crystallogr. A* **2008**, *64*, 419 – 424.

[16] Heisenberg, W. Zur Theorie des Ferromagnetismus. *Z. Phys.* **1928**, *49*, 619 – 636.

[17] Fischer, G.; Däne, M.; Ernst, A.; Bruno, P.; Lüders, M.; Szotek, Z.; Temmerman, W.; Hergert, W. Exchange coupling in transition metal monoxides: Electronic structure calculations. *Phys. Rev. B* **2009**, *80*, 014408.

[18] Frandsen, B. A.; Brunelli, M.; Page, K.; Uemura, Y. J.; Staunton, J. B.; Billinge, S. J. L. Verification of Anderson Superexchange in MnO via Magnetic Pair Distribution Function Analysis and ab initio Theory. *Phys. Rev. Lett.* **2016**, *116*, 197204.

[19] Kramers, H. A. L'interaction Entre les Atomes Magnétogènes dans un Cristal Paramagnétique. *Physica* **1934**, *1*, 182 – 192.

[20] Goodenough, J. B. Theory of the Role of Covalence in the Perovskite-Type Manganites [La, M(II)]MnO_3. *Phys. Rev.* **1955**, *100*, 564 – 573.

[21] Kanamori, J. Superexchange interaction and symmetry properties of electron orbitals. *J. Phys. Chem. Solids* **1959**, *10*, 87 – 98.

[22] Ising, E. Beitrag zur Theorie des Ferromagnetismus. *Z. Phys.* **1925**, *31*, 253 – 258.

[23] Potts, R. B. Some generalized order-disorder transformations. *Math. Proc. Cambridge Philos. Soc.* **1952**, *48*, 106 – 109.

[24] Wu, F. Y. The Potts model. *Rev. Mod. Phys.* **1982**, *54*, 235 – 268.

[25] Moriya, T.; Yosida, K. On the Origin of the Anisotropy Energy of $CuCl_2$-$2H_2O$. *Prog. Theor. Phys.* **1953**, *9*, 663 – 675.

[26] Tomasello, B.; Castelnovo, C.; Moessner, R.; Quintanilla, J. Single-ion anisotropy and magnetic field response in the spin-ice materials $Ho_2Ti_2O_7$ and $Dy_2Ti_2O_7$. *Phys. Rev. B* **2015**, *92*, 155120.

[27] Del Maestro, A. G.; Gingras, M. J. P. Quantum spin fluctuations in the dipolar Heisenberg-like rare earth pyrochlores. *J. Phys.: Condens. Matter* **2004**, *16*, 3339 – 3353.

[28] Chibotaru, L. F.; Iwahara, N. Ising exchange interaction in lanthanides and actinides. *New J. Phys.* **2015**, *17*, 103028.

[29] Ruderman, M. A.; Kittel, C. Indirect Exchange Coupling of Nuclear Magnetic Moments by Conduction Electrons. *Phys. Rev.* **1954**, *96*, 99 – 102.

[30] Kaplan, T. A. Frustrated classical Heisenberg model in one dimension with nearest-neighbor biquadratic exchange: Exact solution for the ground-state phase diagram. *Phys. Rev. B* **2009**, *80*, 012407.

[31] Wysocki, A. L.; Belashchenko, K. D.; Antropov, V. P. Consistent model of magnetism in ferropnictides. *Nat. Phys.* **2011**, *7*, 485 – 489.

[32] Dzyaloshinsky, I. A thermodynamic theory of "weak" ferromagnetism of antiferromagnetics. *J. Phys. Chem. Solids* **1958**, *4*, 241 – 255.

[33] Moriya, T. Anisotropic Superexchange Interaction and Weak Ferromagnetism. *Phys. Rev.* **1960**, *120*, 91 – 98.

[34] Karube, K.; White, J. S.; Reynolds, N.; Gavilano, J. L.; Oike, H.; Kikkawa, A.; Kagawa, F.; Tokunaga, Y.; Rønnow, H. M.; Tokura, Y.; Taguchi, Y. Robust metastable skyrmions and their triangular–square lattice structural transition in a high-temperature chiral magnet. *Nat. Mater.* **2016**, *15*, 1237 – 1242.

[35] Dove, M. T. *Introduction to lattice dynamics*; Cambridge topics in mineral physics and chemistry ; 4; Cambridge University Press: Cambridge, 1993.

[36] Sugawara, K. Effect of Crystal Field on the Inelastic Neutron Scattering Cross-Section. *Phys. Status Solidi B* **1977**, *81*, 313 – 321.

[37] Goodwin, A. L.; Tucker, M. G.; Dove, M. T.; Keen, D. A. Phonons from Powder Diffraction: A Quantitative Model-Independent Evaluation. *Phys. Rev. Lett.* **2004**, *93*, 075502.

[38] Walker, H. C.; Duncan, H. D.; Le, M. D.; Keen, D. A.; Voneshen, D. J.; Phillips, A. E. Magnetic structure and spin-wave excitations in the multiferroic magnetic metal-organic framework $(CD_3)_2ND_2[Mn(DCO_2)_3]$. *Phys. Rev. B* **2017**, *96*, 094423.

[39] Toth, S.; Lake, B. Linear spin wave theory for single-Q incommensurate magnetic structures. *J. Phys.: Condens. Matter* **2015**, *27*, 166002.

[40] Holstein, T.; Primakoff, H. Field Dependence of the Intrinsic Domain Magnetization of a Ferromagnet. *Phys. Rev.* **1940**, *58*, 1098 – 1113.

[41] Nguyen, T. M. H.; Sandilands, L. J.; Sohn, C. H.; Kim, C. H.; Wysocki, A. L.; Yang, I.-S.; Moon, S. J.; Ko, J.-H.; Yamaura, J.; Hiroi, Z.; Noh, T. W. Two-magnon scattering in the $5d$ all-in-all-out pyrochlore magnet $Cd_2Os_2O_7$. *Nat. Commun.* **2017**, *8*, 251.

[42] Rønnow, H. M.; Regnault, L. P.; Lorenzo, J. E. Chasing ghosts in reciprocal space—a novel inelastic neutron multiple scattering process. *Physica B Condens. Matter* **2004**, *350*, 11 – 16, Proceedings of the Third European Conference on Neutron Scattering.

[43] Rotter, M.; Le, M. D.; Boothroyd, A. T.; Blanco, J. A. Dynamical matrix diagonalization for the calculation of dispersive excitations. *J. Phys.: Condens. Matter* **2012**, *24*, 213201.

[44] Steiner, M.; Villain, J.; Windsor, C. G. Theoretical and experimental studies on one-dimensional magnetic systems. *Adv. Phys.* **1976**, *25*, 87 – 209.

[45] Kjems, J. K.; Steiner, M. Evidence for Soliton Modes in the One-Dimensional Ferromagnet $CsNiF_3$. *Phys. Rev. Lett.* **1978**, *41*, 1137 – 1140.

[46] Mikeska, H.-J.; Steiner, M. Solitary excitations in one-dimensional magnets. *Adv. Phys.* **1991**, *40*, 191 – 356.

[47] Ramirez, A. P.; Wolf, W. P. Specific Heat of $CsNiF_3$: Evidence for Spin Solitons. *Phys. Rev. Lett.* **1982**, *49*, 227 – 230.

[48] Sahling, S.; Remenyi, G.; Paulsen, C.; Monceau, P.; Saligrama, V.; Marin, C.; Revcolevschi, A.; Regnault, L. P.; Raymond, S.; Lorenzo, J. E. Experimental realization of long-distance entanglement between spins in antiferromagnetic quantum spin chains. *Nat. Phys.* **2015**, *11*, 255 – 260.

[49] Aasland, S.; Fjellvåg, H.; Hauback, B. Magnetic properties of the one-dimensional $Ca_3Co_2O_6$. *Solid State Commun.* **1997**, *101*, 187 – 192.

[50] Maignan, A.; Hardy, V.; Hebert, S.; Drillon, M.; Lees, M. R.; Petrenko, O.; Paul, D. M. K.; Khomskii, D. Quantum tunneling of the magnetization in the Ising chain compound $Ca_3Co_2O_6$. *J. Mater. Chem.* **2004**, *14*, 1231 – 1234.

[51] Chapon, L. C. Origin of the long-wavelength magnetic modulation in $Ca_3Co_2O_6$. *Phys. Rev. B* **2009**, *80*, 172405.

[52] Kageyama, H.; Yoshimura, K.; Stern, R.; Mushnikov, N. V.; Onizuka, K.; Kato, M.; Kosuge, K.; Slichter, C. P.; Goto, T.; Ueda, Y. Exact Dimer Ground State and Quantized Magnetization Plateaus in the Two-Dimensional Spin System $SrCu_2(BO_3)_2$. *Phys. Rev. Lett.* **1999**, *82*, 3168 – 3171.

[53] Sebastian, S. E.; Harrison, N.; Sengupta, P.; Batista, C. D.; Francoual, S.; Palm, E.; Murphy, T.; Marcano, N.; Dabkowska, H. A.; Gaulin, B. D. Fractalization drives crystalline states in a frustrated spin system. *Proc. Natl. Acad. Sci. U.S.A.* **2008**, *105*, 20157 – 20160.

[54] Mekata, M. Antiferro-Ferrimagnatic Transition in Triangular Ising Lattice. *J. Phys. Soc. Jpn.* **1977**, *42*, 76 – 82.

[55] Motoyama, N.; Eisaki, H.; Uchida, S. Magnetic Susceptibility of Ideal Spin 1 /2 Heisenberg Antiferromagnetic Chain Systems, Sr_2CuO_3 and $SrCuO_2$. *Phys. Rev. Lett.* **1996**, *76*, 3212 – 3215.

[56] Cao, G.; Durairaj, V.; Chikara, S.; Parkin, S.; Schlottmann, P. Partial antiferromagnetism in spin-chain $Sr_5Rh_4O_{12}$, $Ca_5Ir_3O_{12}$, and Ca_4IrO_6 single crystals. *Phys. Rev. B* **2007**, *75*, 134402.

[57] Baumbach, R. E.; Hamlin, J. J.; Shu, L.; Zocco, D. A.; O'Brien, J. R.; Ho, P.-C.; Maple, M. B. Unconventional $T-H$ Phase Diagram in the Noncentrosymmetric Compound $Yb_2Fe_{12}\mathbf{P}_7$. *Phys. Rev. Lett.* **2010**, *105*, 106403.

[58] Kudasov, Y. B.; Korshunov, A. S.; Pavlov, V. N.; Maslov, D. A. Frustrated lattices of Ising chains. *Phys.-Usp.* **2012**, *55*, 1169 – 1191.

[59] Nandi, M.; Mandal, P. Magnetic and magnetocaloric properties of quasi-one-dimensional Ising spin chain CoV_2O_6. *J. Appl. Phys.* **2016**, *119*, 133904.

[60] Paddison, J. A. M.; Agrestini, S.; Lees, M. R.; Fleck, C. L.; Deen, P. P.; Goodwin, A. L.; Stewart, J. R.; Petrenko, O. A. Spin correlations in $Ca_3Co_2O_6$: Polarized-neutron diffraction and Monte Carlo study. *Phys. Rev. B* **2014**, *90*, 014411.

[61] Coulon, C.; Miyasaka, H.; Clérac, R. In *Single-Molecule Magnets and Related Phenomena*; R., W., Ed.; Springer, Berlin, Heidelberg, 2006; Vol. 122; Chapter Single-Chain Magnets: Theoretical Approach to Experimental Systems.

[62] Mermin, N. D.; Wagner, H. Absence of Ferromagnetism or Antiferromagnetism in One- or Two-Dimensional Isotropic Heisenberg Models. *Phys. Rev. Lett.* **1966**, *17*, 1133 – 1136.

[63] Bethe, H. Zur Theorie der Metalle. *Z. Phys.* **1931**, *71*, 205 – 226.

[64] Lake, B.; Tsvelik, A. M.; Notbohm, S.; Tennant, A. D.; Perring, T. G.; Reehuis, M.; Sekar, C.; Krabbes, G.; Büchner, G. Confinement of fractional quantum number particles in a condensed-matter system. *Nat. Phys.* **2010**, *6*, 50 – 55.

[65] Mourigal, M.; Enderle, M.; Klöpperpieper, A.; Caux, J.-S.; Stunault, A.; Rønnow, H. M. Fractional spinon excitations in the quantum Heisenberg antiferromagnetic chain. *Nat. Phys.* **2013**, *9*, 435 – 441.

[66] des Cloizeaux, J.; Pearson, J. J. Spin-Wave Spectrum of the Antiferromagnetic Linear Chain. *Phys. Rev.* **1962**, *128*, 2131 – 2135.

[67] Melamud, M.; Pinto, H.; Makovsky, J.; Shaked, H. Magnetic Structure of $CsCoCl_3$ at 4.2 °K. *Phys. Status Solidi B* **1974**, *63*, 699 – 707.

[68] Goff, J. P.; Tennant, D. A.; Nagler, S. E. Exchange mixing and soliton dynamics in the quantum spin chain $CsCoCl_3$. *Phys. Rev. B* **1995**, *52*, 15992 – 16000.

[69] Braun, H.-B.; Kulda, J.; Roessli, B.; Visser, D.; Krämer, K. W.; Güdel, H.-U.; Böni, P. Emergence of soliton chirality in a quantum antiferromagnet. *Nat. Phys.* **2005**, *1*, 159 – 163.

[70] Haldane, F. D. M. Nonlinear Field Theory of Large-Spin Heisenberg Antiferromagnets: Semiclassically Quantized Solitons of the One-Dimensional Easy-Axis Néel State. *Phys. Rev. Lett.* **1983**, *50*, 1153 – 1156.

[71] Affleck, I.; Kennedy, T.; Lieb, E. H.; Tasaki, H. Valence bond ground states in isotropic quantum antiferromagnets. *Comm. Math. Phys.* **1988**, *115*, 477 – 528.

[72] Regnault, L. P.; Zaliznyak, I.; Renard, J. P.; Vettier, C. Inelastic-neutron-scattering study of the spin dynamics in the Haldane-gap system $Ni(C_2H_8N_2)_2NO_2ClO_4$. *Phys. Rev. B* **1994**, *50*, 9174 – 9187.

[73] Zaliznyak, I. A.; Dender, D. C.; Broholm, C.; Reich, D. H. Tuning the spin Hamiltonian of $Ni(C_2H_8N_2)_2NO_2ClO_4$ by external pressure: A neutron-scattering study. *Phys. Rev. B* **1998**, *57*, 5200 – 5204.

[74] Yokoo, T.; Sakaguchi, T.; Kakurai, K.; Akimitsu, J. Observation of the Haldane Gap in Y_2BaNiO_5 Single Crystal. *J. Phys. Soc. Jpn.* **1995**, *64*, 3651 – 3655.

[75] Yokoo, T.; Raymond, S.; Zheludev, A.; Maslov, S.; Ressouche, E.; Zaliznyak, I.; Erwin, R.; Nakamura, M.; Akimitsu, J. Magnetic ordering, spin waves, and Haldane-gap excitations in $(Nd_xY_{1-x})_2BaNiO_5$ linear-chain mixed-spin antiferromagnets. *Phys. Rev. B* **1998**, *58*, 14424 – 14435.

[76] Villar, V.; Mélin, R.; Paulsen, C.; Souletie, J.; Janod, E.; Payen, C. Unconventional antiferromagnetic correlations of the doped Haldane gapsystem $Y_2BaNi_{1-x}Zn_xO_5$. *Eur. Phys. J. B* **2002**, *25*, 39 – 51.

[77] Peierls, R. On Ising's model of ferromagnetism. *Proc. Cambridge Phil. Soc.* **1936**, *32*, 477 — 481.

[78] Berezinskiĭ, V. L. Destruction of Long-range Order in One-dimensional and Two-dimensional Systems having a Continuous Symmetry Group I. Classical Systems. *J. Exp. Theor. Phys* **1971**, *32*, 493.

[79] Kosterlitz, J. M.; Thouless, D. J. Ordering, metastability and phase transitions in two-dimensional systems. *J. Phys. C* **1973**, *6*, 1181 – 1203.

[80] Mooij, J. E.; van Wees, B. J.; Geerligs, L. J.; Peters, M.; Fazio, R.; Schön, G. Unbinding of charge-anticharge pairs in two-dimensional arrays of small tunnel junctions. *Phys. Rev. Lett.* **1990**, *65*, 645 – 648.

[81] Mironov, A. Y.; Silevitch, D. M.; Proslier, T.; Postolova, S. V.; Burdastyh, M. V.; Gutakovskii, A. K.; Rosenbaum, T. F.; Vinokur, V. V.; Baturina, T. I. Charge Berezinskii-Kosterlitz-Thouless transition in superconducting NbTiN films. *Sci. Rep* **2018**, *8*, 4082.

[82] Lobb, C. J.; Abraham, D. W.; Tinkham, M. Theoretical interpretation of resistive transition data from arrays of superconducting weak links. *Phys. Rev. B* **1983**, *27*, 150 – 157.

[83] Desbuquois, R.; Chomaz, L.; Yefsah, T.; Léonard, J.; Beugnon, J.; Weitenberg, C.; Dalibard, J. Superfluid behaviour of a two-dimensional Bose gas. *Nat. Phys.* **2012**, *8*, 645 – 648.

[84] Chernyshev, A. L.; Zhitomirsky, M. E. Spin waves in a triangular lattice antiferromagnet: Decays, spectrum renormalization, and singularities. *Phys. Rev. B* **2009**, *79*, 144416.

[85] Seabra, L.; Momoi, T.; Sindzingre, P.; Shannon, N. Phase diagram of the classical Heisenberg antiferromagnet on a triangular lattice in an applied magnetic field. *Phys. Rev. B* **2011**, *84*, 214418.

[86] Rosales, H. D.; Cabra, D. C.; Pujol, P. Three-sublattice skyrmion crystal in the antiferromagnetic triangular lattice. *Phys. Rev. B* **2015**, *92*, 214439.

[87] Mühlbauer, S.; Binz, B.; Jonietz, F.; Pfleiderer, C.; Rosch, A.; Neubauer, A.; Georgii, R.; Böni, P. Skyrmion Lattice in a Chiral Magnet. *Science* **2009**, *323*, 915 – 919.

[88] Li, H.; Eddaoudi, M.; O'Keeffe, M.; Yaghi, O. M. Design and synthesis of an exceptionally stable and highly porous metal-organic framework. *Nature* **1999**, *402*, 276 – 279.

[89] Eddaoudi, M.; Kim, J.; Rosi, N.; Vodak, D.; Wachter, J.; O'Keeffe, M.; Yaghi, O. M. Systematic Design of Pore Size and Functionality in Isoreticular MOFs and Their Application in Methane Storage. *Science* **2002**, *295*, 469 – 472.

[90] Yaghi, O. M.; O'Keeffe, M.; Ockwig, N. W.; Chae, H. K.; Eddaoudi, M.; Kim, J. Reticular synthesis and the design of new materials. *Nature* **2003**, *423*, 705 – 714.

[91] Cheetham, A. K.; Rao, C. N. R. There's Room in the Middle. *Science* **2007**, *318*, 58 – 59.

[92] Wunderlich, C.-H.; Weber, R.; Bergerhoff, G. Über Eisengallustinte. *Z. Anorg. Allge. Chemie* **1991**, *598*, 371 – 376.

[93] Zhao, M. and Huang, Y. and Peng, Y. and Huang, Z. and Ma, Q. and Zhang, H., Two-dimensional metal–organic framework nanosheets: synthesis and applications. *Chem. Soc. Rev.* **2018**, *47*, 6267 – 6295.

[94] Schoedel, A.; Li, M.; Li, D.; O'Keeffe, M.; Yaghi, O. M. Structures of Metal–Organic Frameworks with Rod Secondary Building Units. *Chem. Rev.* **2016**, *116*, 12466 – 12535.

[95] DeGayner, J. A.; Jeon, I.-R.; Sun, L.; Dincă, M.; Harris, T. D. 2D Conductive Iron-Quinoid Magnets Ordering up to Tc = 105 K via Heterogenous Redox Chemistry. *J. Am. Chem. Soc.* **2017**, *139*, 4175 – 4184.

[96] Ogborn, J. M.; Collings, I. E.; Moggach, S. A.; Thompson, A. L.; Goodwin, A. L. Supramolecular mechanics in a metal–organic framework. *Chem. Sci.* **2012**, *3*, 3011 – 3017.

[97] Saines, P. J.; Melot, B. C.; Seshadri, R.; Cheetham, A. K. Synthesis, structure and magnetic phase transitions of the manganese succinate hybrid framework, $Mn(C_4H_4O_4)$. *Chem. Eur. J* **2010**, *16*, 7579 – 7585.

[98] López-Cabrelles, J.; Mañas-Valero, S.; Vitórica-Yrezábal, I. J.; Bereciartua, P. J.; Rodríguez-Velamazán, J. A.; Waerenborgh, J. C.; Vieira, B. J. C.; Davidovikj, D.; Steeneken, P. G.; van der Zant, H. S. J.; Mínguez Espallargas, G.; Coronado, E. Isoreticular two-dimensional magnetic coordination polymers prepared through pre-synthetic ligand functionalization. *Nat. Chem.* **2018**, *10*, 1001 – 1007.

[99] Halder, G. J.; Kepert, C. J.; Moubaraki, B.; Murray, K. S.; Cashion, J. D. Guest-Dependent Spin Crossover in a Nanoporous Molecular Framework Material. *Science* **2002**, *298*, 1762 – 1765.

[100] Yamada, M. G.; Fujita, H.; Oshikawa, M. Designing Kitaev Spin Liquids in Metal-Organic Frameworks. *Phys. Rev. Lett.* **2017**, *119*, 057202.

[101] Moessner, R.; Ramierez, A. P. Geometrical frustration. *Phys. Today* **2006**, *59*, 24 – 29.

[102] Fazekas, P.; Anderson, P. W. On the ground state properties of the anisotropic triangular antiferromagnet. *Phil. Mag.* **1974**, *30*, 423 – 440.

[103] Wannier, G. H. Antiferromagnetism. The Triangular Ising Net. *Phys. Rev.* **1950**, *79*, 357 – 364.

[104] Keen, D. A.; Goodwin, A. L. The crystallography of correlated disorder. *Nature* **2015**, *521*, 303 – 309.

[105] Yoon, C.; Millane, R. P. Diffraction by a frustrated system: the triangular Ising antiferromagnet. *J. Opt. Soc. Am. A* **2014**, *31*, 1416 – 1426.

[106] Gardner, J. S.; Gingras, M. J. P.; Greedan, J. E. Magnetic pyrochlore oxides. *Rev. Mod. Phys.* **2010**, *82*, 53 – 107.

[107] Wöhler, F. Über den pyrochlor, eine neue mineralspecies. *Ann. Phys. Chem.* **1826**, *7*, 417 – 428.

[108] Von Gaertner, H. Die Kristallstrukturen von Loparit und Pyrochlor. *Neues. Jahrb. Mineral Geol. Palaeontol.* **1930**, *61*, 1 – 30.

[109] Hallas, A. M.; Gaudet, J.; Gaulin, B. D. Experimental Insights into Ground-State Selection of Quantum XY Pyrochlores. *Annu. Rev. Condens. Matter Phys.* **2018**, *9*, 105 – 124.

[110] Bramwell, S. T.; Gingras, M. J. P. Spin Ice State in Frustrated Magnetic Pyrochlore Materials. *Science* **2001**, *294*, 1495 – 1501.

[111] Anderson, P. W. Ordering and Antiferromagnetism in Ferrites. *Phys. Rev.* **1956**, *102*, 1008 – 1013.

[112] Harris, M. J.; Bramwell, S. T.; McMorrow, D. F.; Zeiske, T.; Godfrey, K. W. Geometrical Frustration in the Ferromagnetic Pyrochlore $Ho_2Ti_2O_7$. *Phys. Rev. Lett.* **1997**, *79*, 2554 – 2557.

[113] Huang, Y.; Chen, K.; Deng, Y.; Prokofév, N.; Svistunov, B. Spin-Ice State of the Quantum Heisenberg Antiferromagnet on the Pyrochlore Lattice. *Phys. Rev. Lett.* **2016**, *116*, 177203.

[114] Palmer, S. E.; Chalker, J. T. Order induced by dipolar interactions in a geometrically frustrated antiferromagnet. *Phys. Rev. B* **2000**, *62*, 488 – 492.

[115] Raju, N. P.; Dion, M.; Gingras, M. J. P.; Mason, T. E.; Greedan, J. E. Transition to long-range magnetic order in the highly frustrated insulating pyrochlore antiferromagnet $Gd_2Ti_2O_7$. *Phys. Rev. B* **1999**, *59*, 14489 – 14498.

[116] Champion, J. D. M.; Wills, A. S.; Fennell, T.; Bramwell, S. T.; Gardner, J. S.; Green, M. A. Order in the Heisenberg pyrochlore: The magnetic structure of $Gd_2Ti_2O_7$. *Phys. Rev. B* **2001**, *64*, 140407.

[117] Stewart, J. R.; Ehlers, G.; Wills, A. S.; Bramwell, S. T.; Gardner, J. S. Phase transitions, partial disorder and multi-k structures in $Gd_2Ti_2O_7$. *J. Phys.: Condens. Matter* **2004**, *16*, L321.

[118] Bonville, P.; Hodges, J. A.; Ocio, M.; Sanchez, J. P.; Vulliet, P.; Sosin, S.; Braithwaite, D. Low temperature magnetic properties of geometrically frustrated $Gd_2Sn_2O_7$ and $Gd_2Ti_2O_7$. *J. Phys.: Condens. Matter* **2003**, *15*, 7777 – 7787.

[119] Wills, A. S.; Zhitomirsky, M. E.; Canals, B.; Sanchez, J. P.; Bonville, P.; de Réotier, P. D.; Yaouanc, A. Magnetic ordering in $Gd_2Sn_2O_7$: the archetypal Heisenberg pyrochlore antiferromagnet. *J. Phys.: Condens. Matter* **2006**, *18*, L37.

[120] Champion, J. D. M. et al. $Er_2Ti_2O_7$: Evidence of quantum order by disorder in a frustrated antiferromagnet. *Phys. Rev. B* **2003**, *68*, 020401.

[121] Poole, A.; Wills, A. S.; Lelièvre-Berna, E. Magnetic ordering in the XY pyrochlore antiferromagnet $Er_2Ti_2O_7$: a spherical neutron polarimetry study. *J. Phys.: Condens. Matter* **2007**, *19*, 452201.

[122] Matsuhira, K.; Hinatsu, Y.; Tenya, K.; Amitsuka, H.; Sakakibara, T. Low-Temperature Magnetic Properties of Pyrochlore Stannates. *J. Phys. Soc. Jpn.* **2002**, *71*, 1576 – 1582.

[123] Mirebeau, I.; Apetrei, A.; Rodríguez-Carvajal, J.; Bonville, P.; Forget, A.; Colson, D.; Glazkov, V.; Sanchez, J. P.; Isnard, O.; Suard, E. Ordered Spin Ice State and Magnetic Fluctuations in $Tb_2Sn_2O_7$. *Phys. Rev. Lett.* **2005**, *94*, 246402.

[124] Mirebeau, I.; Apetrei, A.; Goncharenko, I. N.; Moessner, R. Two geometrically frustrated magnets studied by neutron diffraction. *Physica B: Condens. Matter* **2006**, *385 – 386*, 307 – 312.

[125] Paddison, J. A. M.; Ehlers, G.; Cairns, A. B.; Gardner, J. S.; Petrenko, O. A.; Butch, N. P.; Khalyavin, D. D.; Manuel, P.; Fischer, H. E.; Zhou, Z.; Goodwin, A. L.; Stewart, J. R. Nature of Partial Magnetic Order in the Frustrated Antiferromagnet $G_2Ti_2O_7$. 2020.

[126] Jin, H.-K.; Zhou, Y. Classical and quantum order in hyperkagome antiferromagnets. *Phys. Rev. B* **2020**, *101*, 054408.

[127] Canals, B.; Lacroix, C. Mean-field study of the disordered ground state in the $\beta-$Mn lattice. *Phys. Rev. B* **2000**, *61*, 11251 – 11254.

[128] Nakamura, H.; Yoshimoto, K.; Shiga, M.; Nishi, M.; Kakurai, K. Strong antiferromagnetic spin fluctuations and the quantum spin-liquid state in geometrically frustrated $\beta-$Mn, and the transition to a spin-glass state caused by non-magnetic impurity. *J. Phys.: Condens. Matter* **1997**, *9*, 4701–4728.

[129] Stewart, J. R.; Rainford, B. D.; Eccleston, R. S.; Cywinski, R. Non-Fermi-Liquid Behavior of Electron-Spin Fluctuations in an Elemental Paramagnet. *Phys. Rev. Lett.* **2002**, *89*, 186403.

[130] Paddison, J. A. M.; Stewart, J. R.; Manuel, P.; Courtois, P.; McIntyre, G. J.; Rainford, B. D.; Goodwin, A. L. Emergent Frustration in Co-doped β-Mn. *Phys. Rev. Lett.* **2013**, *110*, 1 – 5.

[131] Paddison, J. A. M.; Jacobsen, H.; Petrenko, O. A.; Fernández-Díaz, M. T.; Deen, P. P.; Goodwin, A. L. Hidden order in spin-liquid $Gd_3Ga_5O_{12}$. *Science* **2015**, *350*, 179 – 181.

[132] Hakuraku, Y.; Ogata, H. A rotary magnetic refrigerator for superfluid helium production. *J. Appl. Phys.* **1986**, *60*, 3266 – 3268.

[133] Shitade, A.; Katsura, H.; Kuneš, J.; Qi, X.-L.; Zhang, S.-C.; Nagaosa, N. Quantum Spin Hall Effect in a Transition Metal Oxide Na_2IrO_3. *Phys. Rev. Lett.* **2009**, *102*, 256403.

[134] Singh, Y.; Gegenwart, P. Antiferromagnetic Mott insulating state in single crystals of the honeycomb lattice material Na_2IrO_3. *Phys. Rev. B* **2010**, *82*, 064412.

[135] Chaloupka, J.; Jackeli, G.; Khaliullin, G. Kitaev-Heisenberg Model on a Honeycomb Lattice: Possible Exotic Phases in Iridium Oxides A_2IrO_3. *Phys. Rev. Lett.* **2010**, *105*, 027204.

[136] Zhitomirsky, M. E. Enhanced magnetocaloric effect in frustrated magnets. *Phys. Rev. B* **2003**, *67*, 104421.

[137] Saines, P. J.; Paddison, J. A. M.; Thygesen, P. M. M.; Tucker, M. G. Searching beyond Gd for magnetocaloric frameworks: magnetic properties and interactions of the $Ln(HCO_2)_3$ series. *Mater. Horiz.* **2015**, *2*, 528 – 535.

[138] Pakhira, S.; Mazumdar, C.; Ranganathan, R.; Avdeev, M. Magnetic frustration induced large magnetocaloric effect in the absence of long range magnetic order. *Sci. Rep.* **2017**, *7*, 7367.

[139] Bragg, W. H.; Bragg, W. L. *X rays and crystal structure*; G. Bell: London, 1915.

[140] Willis, B. T. M.; Carlile, C. J. *Experimental neutron scattering*; Oxford University Press: Oxford, 2008.

[141] Sivia, D. S. *Elementary scattering theory: for X-ray and neutron users*; Oxford University Press: Oxford, 2011.

[142] Blech, I. A.; Averbach, B. L. Spin correlations in MnO. *Physics Physique Fizika* **1964**, *1*, 31 – 44.

[143] Paddison, J. A. M.; Stewart, R. J.; Goodwin, A. L. SPINVERT. A program for refinement of paramagnetic diffuse scattering data. *J. Phys.: Condens. Matter* **2013**, *25*, 454220:1–15.

[144] Stewart, J. R.; Deen, P. P.; Andersen, K. H.; Schober, H.; Barthélémy, J.-F.; Hillier, J. M.; Murani, A. P.; Hayes, T.; Lindenau, B. Disordered materials studied using neutron polarization analysis on the multi-detector spectrometer, D7. *J. Appl. Crystallogr.* **2009**, *42*, 69–84.

[145] Hayter, J. B. Matrix analysis of neutron spin-echo. *Z. Phys.* **1978**, *31*, 117 – 125.

[146] Schärpf, O.; Capellmann, H. The XYZ-Difference Method with Polarized Neutrons and the Separation of Coherent, Spin Incoherent, and Magnetic Scattering Cross Sections in a Multidetector. *Phys. Status Solidi C* **1993**, *135*, 359–379.

[147] Moon, R. M.; Riste, T.; Koehler, W. C. Polarization Analysis of Thermal-Neutron Scattering. *Phys. Rev.* **1969**, *181*, 920 – 931.

[148] Van Hove, L. Correlations in Space and Time and Born Approximation Scattering in Systems of Interacting Particles. *Phys. Rev.* **1954**, *95*, 249 – 262.

[149] Clarke, J. SQUIDs. *Sci. Am.* **1994**, *271*, 46 – 53.

[150] Chmiel, F. Magnetic order in functional iron oxides. Ph.D. thesis, University of Oxford, 2018.

[151] Terada, N.; Glazkova, Y. S.; Belik, A. A. Differentiation between ferroelectricity and thermally stimulated current in pyrocurrent measurements of multiferroic $M\mathrm{Mn_7O_{12}}$ (M = Ca, Sr, Cd, Pb). *Phys. Rev. B* **2016**, *93*, 155127.

[152] Paddison, J. A. M.; Goodwin, A. L. Empirical magnetic structure solution of frustrated spin systems. *Phys. Rev. Lett.* **2012**, *108*, 017204.

[153] Metropolis, N.; Rosenbluth, A. W.; Rosenbluth, M. N.; Teller, A. H.; Teller, E. Equation of State Calculations by Fast Computing Machines. *J. Chem. Phys.* **1953**, *21*, 1087 – 1092.

[154] Hastings, W. K. Monte Carlo sampling methods using Markov chains and their applications. *Biometrika* **1970**, *57*, 97 – 109.

[155] Overy, A. R.; Cairns, A. B.; Cliffe, M. J.; Simonov, A.; Tucker, M. G.; Goodwin, A. L. Design of crystal-like aperiodic solids with selective disorder–phonon coupling. *Nat. Commun.* **2016**, *7*, 10445.

[156] Overy, A. R.; Simonov, A.; Chater, P. A.; Tucker, M. G.; Goodwin, A. L. Phonon broadening from supercell lattice dynamics: Random and correlated disorder. *Phys. Status Solidi B* **2017**, *254*, 1600586.

[157] Gale, J. D. GULP: A computer program for the symmetry-adapted simulation of solids. *J. Chem. Soc., Faraday Trans.* **1997**, *93*, 629 – 637.

[158] Seifert, H.-J. Über die Systeme Alkalimetallchlorid/Kobalt(II)-chlorid. *Z. Anorg. Allg. Chem.* **1961**, *307*, 137 – 144.

[159] McMurdie, H. F.; de Groot, J.; Morris, M.; Swanson, H. E. Crystallography and Preparation of Some $\mathrm{ABCl_3}$ Compounds. *J. Res. Nat. Bur. Stand.* **1969**, *73*, 621 – 626.

[160] Canepa, P.; Chabal, Y. J.; Thonhauser, T. When metal organic frameworks turn into linear magnets. *Phys. Rev. B* **2013**, *87*, 094407.

[161] Duan, Z.; Wang, Z.; Gao, S. Irreversible transformation of chiral to achiral polymorph of $\mathrm{K[Co(HCOO)_3]}$: synthesis, structures, and magnetic properties. *Dalton Trans.* **2011**, *40*, 4465 – 4473.

[162] Hursthouse, M. B.; Light, M. E.; Price, D. J. One-Dimensional Magnetism in Anhydrous Iron and Cobalt Ternary Oxalates with Rare Trigonal-Prismatic Metal Coordination Environment. *Angew. Chem. Int. Ed.* **2004**, *43*, 472 – 475.

[163] Saines, P. J.; Steinmann, M.; Tan, J.-C.; Yeung, H. H.-M.; Li, W.; Barton, P. T.; Cheetham, A. K. Isomer-Directed Structural Diversity and Its Effect on the Nanosheet Exfoliation and Magnetic Properties of 2,3-Dimethylsuccinate Hybrid Frameworks. *Inorg. Chem.* **2012**, *51*, 11198 – 11209.

[164] Saines, P. J.; Tan, J.-C.; Yeung, H. H.-M.; Barton, P. T.; Cheetham, A. K. Layered inorganic-organic frameworks based on the 2,2-dimethylsuccinate ligand: structural diversity and its effect on nanosheet exfoliation and magnetic properties. *Dalton Trans.* **2012**, *41*, 8585 – 8593.

[165] Huang, Y.-G.; Jiang, F.-L.; Hong, M.-C. Magnetic lanthanide–transition-metal organic–inorganic hybrid materials: From discrete clusters to extended frameworks. *Coord. Chem. Rev.* **2009**, *253*, 2814 – 2834, Functional Hybrid Nanomaterials:.

[166] Cliffe, M. J.; Lee, J.; Paddison, J. A. M.; Schott, S.; Mukherjee, P.; Gaultois, M. W.; Manuel, P.; Sirringhaus, H.; Dutton, S. E.; Grey, C. P. Low-dimensional quantum magnetism in $Cu(NCS)_2$: A molecular framework material. *Phys. Rev. B* **2018**, *97*, 144421.

[167] Trounov, V.; Tserkovnaya, E.; Gavrilov, S.; Vahrushev, S. Magnetic ordering in rare-earth formates. *Physica B* **1997**, *234 – 236*, 679 – 681.

[168] Kurbakov, A. I.; Rodríquez-Carvajal, J.; Trounov, V. A.; Starostina, N. V. Discovery and Investigation of the Magnetic Structure of Terbium Formate $Tb(DCOO)_3$. *Mater. Sci. Forum* **2000**, *321 – 324*, 971 – 975.

[169] Bolotovsky, R. L.; Bulkin, A. P.; Krutov, G. A.; Kudryashev, V. A.; Trunov, V. A.; Ul'yanov, V. A.; Antson, O.; Hiismäki, P.; Pöyry, H.; Tiitta, A.; Loshmanov, A. A.; Furmanova, N. G. Neutron diffraction study of the crystal structure of rare-earth and yttrium anhydrous deuterated formates. *Solid State Commun.* **1990**, *76*, 1045 – 1049.

[170] Lorusso, G.; Sharples, J. W.; Palacios, E.; Roubeau, O.; Brechin, E. K.; Sessoli, R.; Rossin, A.; Tuna, F.; McInnes, E. J. L.; Collison, D.; Evangelisti, M. A dense metal-organic framework for enhanced magnetic refrigeration. *Adv. Mater.* **2013**, *25*, 4653 – 4656.

[171] Moura, M. R.; Ayala, A. P.; Mendes Filho, J.; Guedes, I.; Paschoal, C. W. A.; Leyva, A. G.; Polla, G.; Vega, D.; de Perazzo, P. K.; Lanza, H. Thermal behavior in $Pr(HCOO)_3$ crystals. *J. Raman Spectrosc.* **2004**, *35*, 159 – 164.

[172] Todoroki, N.; Miyashita, S. Ordered Phases and Phase Transitions in The Stacked Triangular Antiferromagnet $CsCoCl_3$ and $CsCoBr_3$. *J. Phys. Soc. Jpn.* **2004**, *73*, 412 – 416.

[173] Goodwin, A. L.; Dove, M. T.; Chippindale, A. M.; Hibble, S. J.; Pohl, A. H.; Hannon, A. C. Aperiodicity, structure, and dynamics in $Ni(CN)_2$. *Phys. Rev. B* **2009**, *80*, 054101.

[174] Cairns, A. B.; Cliffe, M. J.; Paddison, J. A. M.; Daisenberger, D.; Tucker, M. G.; Coudert, F.-X.; Goodwin, A. L. Encoding complexity within supramolecular analogues of frustrated magnets. *Nat. Chem.* **2016**, *8*, 442 – 447.

[175] Kamieniarz, G.; Vanderzande, C. Quantum statistics of easy-plane ferromagnetic chains and specific heat of $CsNiF_3$ and $(C_6H_{11}NH_3)CuBr_3$. *Phys. Rev. B* **1987**, *35*, 3341 – 3346.

[176] Wysin, G. M.; Bishop, A. R. Quantum Monte Carlo and transfer-matrix calculations for one-dimensional easy-plane ferromagnets. *Phys. Rev. B* **1986**, *34*, 3377 – 3387.

[177] Chapon, L. C.; Manuel, P.; Radaelli, P. G.; Benson, C.; Perrott, L.; Ansell, S.; Rhodes, N. J.; Raspino, D.; Duxbury, D.; Spill, E.; Norris, J. Wish: The New Powder and Single Crystal Magnetic Diffractometer on the Second Target Station. *Neutron News* **2011**, *22*, 22 – 25.

[178] Larson, A. C.; Von Dreele, R. B. General Structure Analysis System (GSAS). *Los Alamos National Laboratory Report* **2000**, *LAUR 86-748*.

[179] Toby, B. H. *EXPGUI*, a graphical user interface for *GSAS. J. Appl. Crystallogr.* **2001**, *34*, 210 – 213.

[180] Saines, P. J.; Paddison, J. A. M.; Thygesen, P. M. M.; Tucker, M. G. Searching beyond Gd for magnetocaloric frameworks: magnetic properties and interactions of the $Ln(HCO_2)_3$ series. *Mater. Horiz.* **2015**, *2*, 528 – 535.

[181] Brown, P. J. In *International Tables for Crystallography, Volu. C*; Wilson, A. J. C., Ed.; Kluwer Academic Publishers: London, 1995; Chapter 4.4.5, pp 391 – 399.

[182] Baxter, R. J. *Exactly solved models in statistical mechanics*; Academic Press: London, 1982.

[183] Loveluck, J. M.; Lovesey, S. W.; Aubry, S. Spin correlations for a classical linear magnet with exchange and single-site anisotropy energies. *J. Phys. C* **1975**, *8*, 3841 – 3856.

[184] Sasaki, K. Statistical Mechanics of a Classical Heisenberg Chain with Anisotropies. *Prog. Theor. Phys.* **1982**, *68*, 1518 – 1532.

[185] Gingras, M. J. P.; den Hertog, B. C.; Faucher, M.; Gardner, J. S.; Dunsiger, S. R.; Chang, L. J.; Gaulin, B. D.; Raju, N. P.; Greedan, J. E. Thermodynamic and single-ion properties of Tb^{3+} within the collective paramagnetic-spin liquid state of the frustrated pyrochlore antiferromagnet $Tb_2Ti_2O_7$. *Phys. Rev. B* **2000**, *62*, 6496 – 6511.

[186] Tucker, M. G.; Keen, D. A.; Dove, M. T.; Goodwin, A. L.; Hui, Q. RMCProfile: reverse Monte Carlo for polycrystalline materials. *J. Phys.: Condes. Matter* **2007**, *19*, 335218.

[187] Wojtas, D. H.; Millane, R. P. Two-point correlation function for the triangular Ising antiferromagnet. *Phys. Rev. E* **2009**, *79*, 041123.

[188] Dixey, R. J. C.; Orlandi, F.; Manuel, P.; Mukherjee, P.; Dutton, S. E.; Saines, P. J. Emergent magnetic order and correlated disorder in formate metal-organic frameworks. *Phil. Trans. R. Soc. A.* **2019**, *377*, 20190007.

[189] Paddison, J. A. M. Ultrafast calculation of diffuse scattering from atomistic models. *Acta Cryst. A* **2019**, *75*, 14–24.

[190] Nguyen, T. N.; Lee, P. A.; zur Loye, H.-C. Design of a Random Quantum Spin Chain Paramagnet: $Sr_3CuPt_{0.5}Ir_{0.5}O_6$. *Science* **1996**, *271*, 489 – 491.

[191] Niitaka, S.; Kageyama, H.; Yoshimura, K.; Kosuge, K.; Kawano, S.; Aso, N.; Mitsuda, A.; Mitamura, H.; Goto, T. High-Field Magnetization and Neutron Diffraction Studies of One-Dimensional Compound Ca_3CoRhO_6. *J. Phys. Soc. Jpn.* **2001**, *70*, 1222 – 1225.

[192] Loewenhaupt, M.; Schäfer, W.; Niazi, A.; Sampathkumaran, E. V. Evidence for the coexistence of low-dimensional magnetism and long-range order in Ca_3CoRhO_6. *EPL - Europhys. Lett.* **2003**, *63*, 374.

[193] Nishiwaki, Y.; Kato, T.; Oohara, Y.; Iio, K. Neutron Diffraction Study of Distorted-Triangular-Lattice Ising-like Antiferromagnet $RbCoBr_3$. *J. Phys. Soc. Jpn.* **2004**, *73*, 2841 – 2844.

[194] Nishiwaki, Y.; Nakamura, T.; Oosawa, A.; Kakurai, K.; Todoroki, N.; Igawa, N.; Ishii, Y.; Kato, T. Partial Disordered Phase of Ising Spin System in Distorted Triangular Lattice $RbCoBr_3$. *J. Phys. Soc. Jpn.* **2008**, *77*, 104703.

[195] Nakamura, T.; Nishiwaki, Y. Spin-lattice model of magnetoelectric transitions in $RbCoBr_3$. *Phys. Rev. B* **2008**, *78*, 104422.

[196] Yelon, W. B.; Cox, D. E.; Eibschütz, M. Magnetic ordering in $CsCoBr_3$. *Phys. Rev. B* **1975**, *12*, 5007 – 5015.

[197] Farkas, A.; Gaulin, B. D.; Tun, Z.; Briat, B. Magnetic phase transitions in $CsCoBr_3$. *J. Appl. Phys.* **1991**, *69*, 6167 – 6169.

[198] Mekata, M.; Adachi, K. Magnetic Structure of $CsCoCl_3$. *J. Phys. Soc. Jpn.* **1978**, *44*, 806 – 812.

[199] Boucher, J. P.; Regnault, L.-P.; Pires, A.; Henry, J. Y.; Stirling, W. G.; Renard, J. P. *Narrow and Broad Solitons in the Antiferromagnetic Chains of CsCoCl3 and TMMC*; 1984; Vol. 54; pp 6 – 11.

[200] Villain, J. Propagative spin relaxation in the Ising-like antiferromagnetic linear chain. *Physica B+C* **1975**, *79*, 1 – 12.

[201] Kenzelmann, M.; Coldea, R.; Tennant, D. A.; Visser, D.; Hofmann, M.; Smeibidl, P.; Tylczynski, Z. Order-to-disorder transition in the XY-like quantum magnet Cs_2CoCl_4 induced by noncommuting applied fields. *Phys. Rev. B* **2002**, *65*, 144432.

[202] Rodríguez-Carvajal, J. Recent advances in magnetic structure determination by neutron powder diffraction. *Physica B: Condens. Matter* **1993**, *192*, 55 – 69.

[203] Chung, J. S.; Thorpe, M. F. Local atomic structure of semiconductor alloys using pair distribution functions. *Phys. Rev. B* **1997**, *55*, 1545 – 1553.

[204] Farrow, C. L.; Billinge, S. J. L. Relationship between the atomic pair distribution function and small-angle scattering: implications for modeling of nanoparticles. *Acta Crystallogr. A* **2009**, *65*, 232 – 239.

[205] Goodwin, A. L.; Dove, M. T.; Tucker, M. G.; Keen, D. A. MnO spin-wave dispersion curves from neutron powder diffraction. *Phys. Rev. B* **2007**, *75*, 075423.

[206] Shiba, H.; Ueda, Y.; Okunishi, K.; Kimura, S.; Kindo, K. Exchange Interaction via Crystal-Field Excited States and Its Importance in $CsCoCl_3$. *J. Phys. Soc. Jpn.* **2003**, *72*, 2326 – 2333.

[207] Arnold, O. et al. Mantid – Data analysis and visualization package for neutron scattering and μSR experiments. *Nucl. Instrum. Methods Phys. Res.* **2014**, *764*, 156 – 166.

[208] Pascut, G. L.; Coldea, R.; Radaelli, P. G.; Bombardi, A.; Beutier, G.; Mazin, I. I.; Johannes, M. D.; Jansen, M. Direct Observation of Charge Order in Triangular Metallic $AgNiO_2$ by Single-Crystal Resonant X-Ray Scattering. *Phys. Rev. Lett.* **2011**, *106*, 157206.

[209] Nakatsuji, S. et al. Spin-Orbital Short-Range Order on a Honeycomb-Based Lattice. *Science* **2012**, *336*, 559 – 563.

[210] Balents, L. Spin liquids in frustrated magnets. *Nature* **2010**, *464*, 199.

[211] Castelnovo, C.; Moessner, R.; Sondhi, S. L. Magnetic monopoles in spin ice. *Nature* **2008**, *451*, 42.

[212] Petit, S.; Lhotel, E.; Canals, B.; Ciomaga Hatnean, M.; Ollivier, J.; Mutka, H.; Ressouche, E.; Wildes, A. R.; Lees, M. R.; Balakrishnan, G. Observation of magnetic fragmentation in spin ice. *Nat. Phys.* **2016**, *12*, 746 – 750.

[213] Ramirez, A. P. Strongly Geometrically Frustrated Magnets. *Annu. Rev. Mater. Sci.* **1994**, *24*, 453 – 480.

[214] Moessner, R.; Chalker, J. T. Properties of a Classical Spin Liquid: The Heisenberg Pyrochlore Antiferromagnet. *Phys. Rev. Lett.* **1998**, *80*, 2929 – 2932.

[215] Moessner, R.; Chalker, J. T. Low-temperature properties of classical geometrically frustrated antiferromagnets. *Phys. Rev. B* **1998**, *58*, 12049–12062.

[216] Hallas, A. M.; Sharma, A. Z.; Cai, Y.; Munsie, T. J.; Wilson, M. N.; Tachibana, M.; Wiebe, C. R.; Luke, G. M. Relief of frustration in the Heisenberg pyrochlore antiferromagnet $Gd_2Pt_2O_7$. *Phys. Rev. B* **2016**, *94*, 134417.

[217] Li, X.; Cai, Y. Q.; Cui, Q.; Lin, C. J.; Dun, Z. L.; Matsubayashi, K.; Uwatoko, Y.; Sato, Y.; Kawae, T.; Lv, S. J.; Jin, C. Q.; Zhou, J.-S.; Goodenough, J. B.; Zhou, H. D.; Cheng, J.-G. Long-range magnetic order in the Heisenberg pyrochlore antiferromagnets $Gd_2Ge_2O_7$ and $Gd_2Pt_2O_7$ synthesized under high pressure. *Phys. Rev. B* **2016**, *94*, 214429.

[218] Paddison, J. A. M.; Ehlers, G.; Petrenko, O. A.; Wildes, A. R.; Gardner, J. S.; Stewart, J. R. Spin correlations in the dipolar pyrochlore antiferromagnet $Gd_2Sn_2O_7$. *J. Phys. Condes. Matter* **2017**, *29*, 144001.

[219] Moessner, R.; Berlinsky, A. J. Magnetic Susceptibility of Diluted Pyrochlore and $SrCr_{9-x}Ga_{3+9x}O_{19}$ Antiferromagnets. *Phys. Rev. Lett.* **1999**, *83*, 3293 – 3296.

[220] Biswas, A. A.; Jana, Y. M. Estimation of single-ion anisotropies, crystal-field and exchange interactions in Gd-based frustrated pyrochlore anti-ferromagnets $Gd_2M_2O_7$ (M=Ti, Sn, Hf, Zr). *J. Magn. Magn. Mater.* **2011**, *323*, 3202 – 3209.

[221] Coelho, A. A. *TOPAS* and *TOPAS-Academic*: an optimization program integrating computer algebra and crystallographic objects written in C++. *J. Appl. Crystallogr.* **2018**, *51*, 210 – 218.

[222] Hoekstra, H. R.; Gallagher, F. Synthesis of some pyrochlore-type oxides of platinum(IV) at high pressure. *Inorganic Chemistry* **1968**, *7*, 2553 – 2557.

[223] Fennell, T.; Mangin-Thro, L.; Mutka, H.; Nilsen, G. J.; Wildes, A. R. Wavevector and energy resolution of the polarized diffuse scattering spectrometer D7. *Nucl. Instrum. Methods Phys. Res* **2017**, *857*, 24 – 30.

[224] Russina, M.; Mezei, F. Implementation of Repetition Rate Multiplication in Cold, Thermal and Hot Neutron Spectroscopy. *J. Phys.: Conf. Ser.* **2010**, *251*, 1 – 4.

[225] Yan, H.; Benton, O.; Jaubert, L.; Shannon, N. Theory of multiple-phase competition in pyrochlore magnets with anisotropic exchange with application to $Yb_2Ti_2O_7$, $Er_2Ti_2O_7$, and $Er_2Sn_2O_7$. *Phys. Rev. B* **2017**, *95*, 0994422.

[226] Carnall, W. T.; Goodman, G. L.; Rajnak, K.; Rana, R. S. A systematic analysis of the spectra of the lanthanides doped into single crystal LaF_3. *J. Chem. Phys.* **1989**, *90*, 3443 – 3457.

[227] Schiffler, S. T.; Müller-Buschbaum, H. K. $BaNiYb_2O_5$ – eine Verbindung, die nicht im $BaNiLn_2O_5$-Typ kristallisiert Mit einem Beitrag über $BaCuSm_2O_5$. *Z. Anorg. Allg. Chem.* **1986**, *540*, 243 – 250.

[228] Schiffler, S.; Müller-Buschbaum, H. New compounds of the $BaNiNd_2O_5$-type: $BaNiLn_2O_5$ (Ln=Sm, Gd, Ho, Er, Tm). *Monatsh. Chem.* **1987**, *118*, 741 – 747.

[229] Amador, J.; Gutiérrez-Puebla, E.; Monge, M. A.; Rasines, I.; Ruiz-Valero, C.; Fernández, F.; Sáez-Puche, R.; Campá, J. A. Evidence of low-dimensional antiferromagnetic ordering and crystal structure in the R_2BaNiO_5 (R=Y,Er) oxides. *Phys. Rev. B* **1990**, *42*, 7918 – 7924.

[230] Buttrey, D. J.; Sullivan, J. D.; Rheingold, A. L. Phase equilibrium study of the YBaNiO system and structural characterization of the new quasi-one-dimensional oxide Y_2BaNiO_5. *J. Solid State Chem.* **1990**, *88*, 291 – 302.

[231] Saez-Puche, R.; Martin-Llorente, J. M.; Coronado, J. M. Magnetic properties and structural characterization of the solid solution $Er_{2-x}Y_xBaNiO_5$ ($0 \leq x \leq 2$). *J. Less Common Met.* **1991**, *175*, 131 – 136.

[232] Castro, M.; Burriel, R.; Salinas-Sánchez, A.; Sáez-Puche, R. Heat-capacity measurement of R_2BaNiO_5 (R = Y, Ho, Er) oxides. *J. Magn. Magn. Mater.* **1992**, *104*, 619 – 620.

[233] Darriet, J.; Regnault, L. P. The compound Y_2BaNiO_5: A new example of a haldane gap in A S = 1 magnetic chain. *Solid State Commun.* **1993**, *86*, 409 – 412.

[234] Xu, G.; DiTusa, J. F.; Ito, T.; Oka, K.; Takagi, H.; Broholm, C.; Aeppli, G. Y_2BaNiO_5: A nearly ideal realization of the $S = 1$ Heisenberg chain with antiferromagnetic interactions. *Phys. Rev. B* **1996**, *54*, R6827 – R6830.

[235] Yoshida, M.; Shiraki, K.; Okubo, S.; Ohta, H.; Ito, T.; Takagi, H.; Kaburagi, M.; Ajiro, Y. Energy Structure of a Finite Haldane Chain in $Y_2BaNi_{0.96}Mg_{0.04}O_5$ Studied by High Field Electron Spin Resonance. *Phys. Rev. Lett.* **2005**, *95*, 117202.

[236] Popova, E. A.; Klimin, S. A.; Popova, M. N.; Vasiliev, A. N. The Contribution of the Nickel Subsystem into Magnetic Properties of Quasi One-Dimensional Magnets $(Y_{1-x}Nd_x)_2BaNiO_5$. *J. Low Temp. Phys.* **2016**, *185*, 692 – 700.

[237] Affleck, I. Quantum spin chains and the Haldane gap. *J. Phys. Condens. Matter* **1989**, *1*, 3047 – 3072.

[238] Yamashita, M.; Ishii, T.; Matsuzaka, H. Haldane gap systems. *Coord. Chem. Rev.* **2000**, *198*, 347 – 366.

[239] García-Matres, E.; Martínez, J. L.; Rodríguez-Carvajal, J.; Alonso, J. A.; Salinas-Sánchez, A.; Saez-Puche, R. Structural Characterization and Polymorphism of R_2BaNiO_5 (R = Nd, Gd, Dy, Y, Ho, Er, Tm, Yb) Studied by Neutron Diffraction. *J. Solid State Chem.* **1993**, *103*, 322 – 333.

[240] Chepurko, G. G.; Kazei, Z. A.; Kudrjavtsev, D. A.; Levitin, R. Z.; Mill, B. V.; Popova, M. N.; Snegirev, V. V. Magnetic and spectral studies of Er_2BaNiO_5 and other rare earth nickelates. *Phys. Lett. A* **1991**, *157*, 81 – 84.

[241] Popova, M. N.; Klimin, S. A.; Chukalina, E. P.; Malkin, B. Z.; Levitin, R. Z.; Mill, B. V.; Antic-Fidancev, E. High-resolution spectral study of Er^{3+} crystal-field levels and magnetic ordering in $(Er_xY_{1-x})_2BaNiO_5$ chain compounds. *Phys. Rev. B* **2003**, *68*, 155103.

[242] Saez-Puche, R.; Coronado, J. M.; Otero-Díaz, C. L.; Martín Llorente, J. M. Structural change and magnetic properties of $Y_2BaNi_{1-x}Zn_xO_5$ oxides. *J. Solid State Chem.* **1991**, *93*, 461 – 468.

[243] García-Matres, E.; García-Muñoz, J. L.; Martínez, J. L.; Rodríguez-Carvajal, J. Magnetic susceptibility and field-induced transitions in R_2BaNiO_5 compounds (R = Tm, Er, Ho, Dy, Tb, Gd, Sm, Nd, Pr). *J. Magn. Magn. Mater.* **1995**, *149*, 363 – 372.

[244] García-Matres, E.; Martínez, J. L.; Rodríguez-Carvajal, J. Neutron diffraction studt of the magnetic ordering in the series R_2BaNiO_5 (R = Rare Earth). *Eur. Phys. J. B* **2001**, *24*, 59 – 70.

[245] Singh, K.; Basu, T.; Chowki, S.; Mahapotra, N.; Iyer, K. K.; Paulose, P. L.; Sampathkumaran, E. V. Magnetoelectric coupling in the Haldane spin-chain system Dy_2BaNiO_5. *Phys. Rev. B* **2013**, *88*, 094438.

[246] Chowki, S.; Basu, T.; Singh, K.; Mohapatra, N.; Sampathkumaran, E. V. Multiferroicity and magneto-electric effect in Gd2BaNiO5. *J. Appl. Phys.* **2014**, *115*, 214107.

[247] Basu, T.; Mohapatra, N.; Singh, K.; Sampathkumaran, E. V. Magnetic and magnetodielectric coupling anomalies in the Haldane spin-chain system Nd_2BaNiO_5. *AIP Advances* **2015**, *5*, 037128.

[248] Upadhyay, S. K.; Sampathkumaran, E. V. Absence of ferroelectric features in Eu_2BaNiO_5: An anomalous case within this rare-earth family. *AIP Conf. Proc.* **2018**, *1942*, 130061.

[249] Basu, T.; Kishore, V. V. R.; Gohil, S.; Singh, K.; Mohapatra, N.; Bhattacharjee, S.; Gonde, B.; Lalla, N. P.; Mahadevan, P.; Ghosh, S.; Sampathkumaran, E. V. Displacive-type ferroelectricity from magnetic correlations within spin-chain. *Sci. Rep.* **2014**, *4*, 1 – 6.

[250] Kimura, T.; Goto, T.; Shintani, H.; Ishizaka, K.; Arima, T.; Tokura, Y. Magnetic control of ferroelectric polarization. *Nature* **2003**, *426*, 55 – 58.

[251] Altomare, A.; Cascarano, G.; Giacovazzo, C.; Guagliardi, A.; Burla, M. C.; Polidori, G.; Camalli, M. *SIR*92 – a program for automatic solution of crystal structures by direct methods. *J. Appl. Crystallogr.* **1994**, *27*, 435.

[252] Giacovazzo, C. A general approach to phase relationships: the method of representations. *Acta Crystallogr. A* **1977**, *33*, 933 – 944.

[253] Betteridge, P. W.; Carruthers, J. R.; Cooper, R. I.; Prout, K.; Watkin, D. J. CRYSTALS version 12: software for guided crystal structure analysis. *J. Appl. Crystallogr.* **2003**, *36*, 1487.

[254] Alonso, J. A.; Amador, J.; Martínez, J. L.; Rasines, I.; Rodríguez-Carvajal, J.; Sáez-Puche, R. Neutron diffraction study of the magnetic structure of Er_2BaNiO_5. *Solid State Commun.* **1990**, *76*, 467 – 474.

[255] Debye, P. Zur Theorie der spezifischen Wärmen. *Ann. Phys.* **1912**, *344*, 789 – 839.

[256] Basu, T.; Singh, K.; Mohapatra, N.; Sampathkumaran, E. V. Magnetic and dielectric behaviour of the spin-chain compound Er_2BaNiO_5 well below its Néel temperature. *J. Appl. Phys.* **2014**, *116*, 1 – 5.

[257] Popova, E. A.; Klimin, S. A.; Popova, M. N.; Klingeler, R.; Tristan, N.; Büchner, B.; Vasil'ev, A. N. Behavior of the magnetic subsystems in Nd_2BaNiO_5. *J. Exp. Theor. Phys.* **2014**, *118*, 611 – 620.

[258] De, C.; Ghara, S.; Sundaresan, A. Effect of internal electric field on ferroelectric polarization in multiferroic $TbMnO_3$. *Solid State Commun.* **2015**, *205*, 61 – 65.

[259] Gutmann, M. SXD2001 - a program for treating data from TOF neutron single-crystal diffraction. *Acta Crystallogr. A* **2005**, *61*, c164.

[260] Petříček, V.; Dušek, M.; Palatinus, L. Crystallographic Computing System JANA2006: General features. *Z. Kristallogr.* **2014**, *229*, 345 – 352.

[261] Hamilton, W. C. Significance tests on the crystallographic R factor. *Acta Crystallogr.* **1965**, *18*, 502 – 510.

[262] Marsh, R. E. Centrosymmetric or noncentrosymmetric? *Acta Crystallogr. B* **1986**, *42*, 193 – 198.

[263] Marsh, R. E. Some thoughts on choosing the correct space group. *Acta Crystallogr. B* **1995**, *51*, 897 – 907.

[264] Stokes, H. T.; Hatch, D. M.; Campbell, B. J. ISODISTORT, ISOTROPY Software Suite, iso.byu.edu.

[265] Campbell, B. J.; Stokes, H. T.; Tanner, D. E.; Hatch, D. M. *ISODISPLACE*: a web-based tool for exploring structural distortions. *J. Appl. Crystallogr.* **2006**, *39*, 607 – 614.

[266] Ahmed, N.; Hicks, T. J. Polarization analysis of neutron scattering from Cu Mn alloys. *Solid State Commun.* **1974**, *15*, 415 – 419.

Appendix A

A1 $Q = 0$ magnetic scattering and susceptibility

The following is the derivation of the $Q = 0$ scattering intensity for magnetic neutron scattering in paramagnets calculated from the bulk susceptibility. We start with the expression for the magnetic cross-section of a paramagnet at $Q = 0$.

$$\frac{d\sigma}{d\Omega} = \frac{2}{3}\left(\frac{\gamma r_0}{2}\right)^2 g_s^2 S(S+1) \tag{A1.1}$$

where the factor $\left(\frac{\gamma r_0}{2}\right)^2 = 0.07265$ barns. The expression for the magnetic susceptibility in SI is given by the Curie Law (or the Curie-Weiss law)

$$\chi_{\mathrm{SI}} = \frac{\mu_0 \mu_B^2}{3k_B} g_s^2 S(S+1)\frac{1}{T}. \tag{A1.2}$$

Substituting Eq. A1.2 into Eq. A1.1 we get,

$$\left.\frac{d\sigma}{d\Omega}\right|_{Q=0} = 2\left(\frac{\gamma r_0}{2}\right)^2 \frac{k_B T}{\mu_0 \mu_B^2}\chi_{\mathrm{SI}}. \tag{A1.3}$$

Note that both the cross-section and the susceptibility are assumed to be normalised per spin. This equation is (within a factor of g_s^2) the same expression as the CGS version given in Ref. 266. It is equivalent to the expression derived *via* the fluctuation-dissapation theorem and the Kramers-Krönig relation. It is valid under the quasi-

static approximation, given by the condition $\hbar\omega << k_BT$. Expanding to first order we can therefore write,

$$[1 + n(\omega)] = \frac{1}{1 - \exp(-\frac{\hbar\omega}{k_BT})} \simeq \frac{k_BT}{\hbar\omega}. \tag{A1.4}$$

Generally, the magnetic neutron scattering intensity (differential cross-section) is normalised **per magnetic ion** (spin), which corresponds to the SI susceptibility given by Eq. A1.2 and which has dimensions [m^3 $spin^{-1}$].

Susceptibility is generally given in CGS units [emu mol^{-1}] or in [emu mol^{-1}_{spins}], which are related by,

$$\chi_{\rm CGS}[\text{emu mol}^{-1}_{\rm spins}] = \frac{1}{N_{\rm mag}}\chi_{\rm CGS}[\text{emu mol}^{-1}], \tag{A1.5}$$

where $N_{\rm mag}$ is the number of magnetic ions per formula unit. The CGS expression for the Curie Law, with $\chi_{\rm CGS}$ in [emu mol^{-1}_{spins}] is given by,

$$\chi_{\rm CGS} = \frac{N_A\mu_B^2}{3k_B} g_s^2 S(S+1)\frac{1}{T}, \tag{A1.6}$$

where all the constants are now in CGS; $\mu_B = 9.274 \times 10^{-21}$ erg G^{-1}, $k_B = 1.38 \times 10^{-16}$ erg K^{-1} and $N_A = 6.022 \times 10^{23}$ mol^{-1}. Gathering these constants together we can write

$$\frac{N_A\mu_B^2}{3k_B} = \frac{6.022 \times 10^{23} \times 86.0 \times 10^{-42}}{3 \times 1.38 \times 10^{-16}} \simeq \frac{1}{8}, \tag{A1.7}$$

where this approximation is good to 0.07%. From Eqs. A1.2 and A1.6, we can now write an expression for converting χ_{SI} to χ_{CGS}.

$$\chi_{\mathrm{SI}} = \frac{\mu_0 \mu_B^2}{3k_B} \times 8\chi_{\mathrm{CGS}}. \tag{A1.8}$$

Finally we can substitute Eq. A1.8 into Eq. A1.3 to get the expression for the $Q = 0$ cross-section of a paramagnet

$$\left.\frac{d\sigma}{d\Omega}\right|_{Q=0} = 2\left(\frac{\gamma r_0}{2}\right)^2 \frac{k_B T}{\mu_0 \mu_B^2} 8 \frac{\mu_0 \mu_B^2}{3k_B} \chi_{\mathrm{CGS}} \tag{A1.9}$$

$$= \frac{16}{3}\left(\frac{\gamma r_0}{2}\right)^2 T \chi_{\mathrm{CGS}}. \tag{A1.10}$$

A2 DMC grid search for $Gd_2Pt_2O_7$

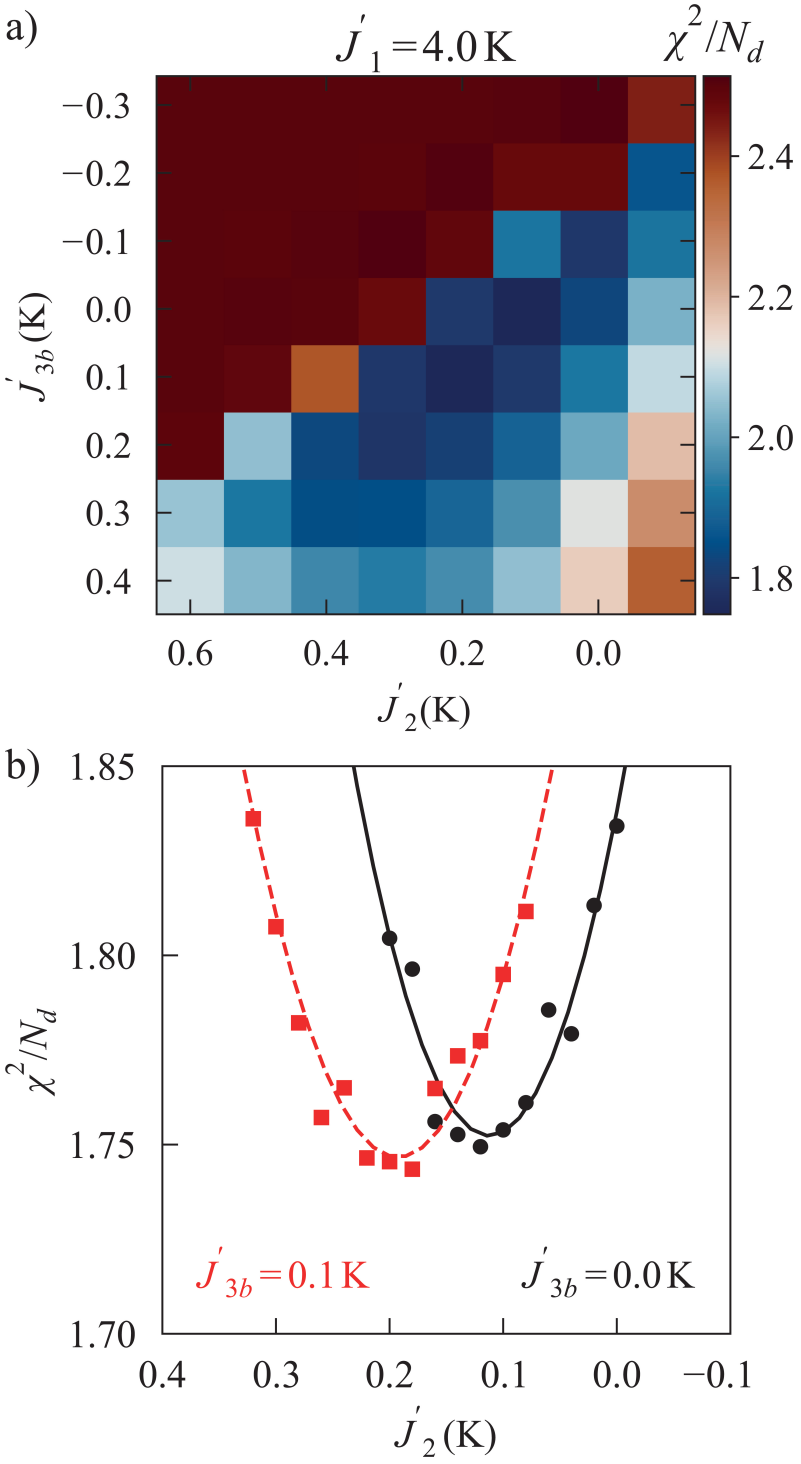


Figure A2.1: Grid search through J_2, J_3 parameter space to identify the lowest χ^2 relative to the diffuse scattering data at 1.8 K.

Appendix B

B1 SpinW code used for the calculation of a dynamical matrix for use in supercell spin dynamics calculations

```
%% Calculation of the dynamical matrix for a 12x12 supercell of a TIA system
% The loop in this section is a function for generating the unit cell
% positions consistently

for i=0:11
    for j=0:11
        fprintf("TIA.addatom('r', [%i/12 %i/12 0],'S', 1,'label','MCu2','color','blue')\n",i,j)
    end
end

%% Define the triangular lattice and the magnetic ions
% A single cell of this strucutre would have a unit cell of 3x3x8 Angstrom.

TIA = spinw;
TIA.genlattice('lat_const',[36 36 8],'angled',[90 90 120],'spgr',0)
TIA.addatom('r', [0/12 0/12 0],'S', 1,'label','MCu2','color','blue')
TIA.addatom('r', [0/12 1/12 0],'S', 1,'label','MCu2','color','blue')
TIA.addatom('r', [0/12 2/12 0],'S', 1,'label','MCu2','color','blue')
TIA.addatom('r', [0/12 3/12 0],'S', 1,'label','MCu2','color','blue')
TIA.addatom('r', [0/12 4/12 0],'S', 1,'label','MCu2','color','blue')
```

```
TIA.addatom('r', [0/12 5/12 0],'S', 1,'label','MCu2','color','blue')
TIA.addatom('r', [0/12 6/12 0],'S', 1,'label','MCu2','color','blue')
TIA.addatom('r', [0/12 7/12 0],'S', 1,'label','MCu2','color','blue')
TIA.addatom('r', [0/12 8/12 0],'S', 1,'label','MCu2','color','blue')
TIA.addatom('r', [0/12 9/12 0],'S', 1,'label','MCu2','color','blue')
TIA.addatom('r', [0/12 10/12 0],'S', 1,'label','MCu2','color','blue')
TIA.addatom('r', [0/12 11/12 0],'S', 1,'label','MCu2','color','blue')
TIA.addatom('r', [1/12 0/12 0],'S', 1,'label','MCu2','color','blue')
TIA.addatom('r', [1/12 1/12 0],'S', 1,'label','MCu2','color','blue')
TIA.addatom('r', [1/12 2/12 0],'S', 1,'label','MCu2','color','blue')
TIA.addatom('r', [1/12 3/12 0],'S', 1,'label','MCu2','color','blue')
TIA.addatom('r', [1/12 4/12 0],'S', 1,'label','MCu2','color','blue')
TIA.addatom('r', [1/12 5/12 0],'S', 1,'label','MCu2','color','blue')
TIA.addatom('r', [1/12 6/12 0],'S', 1,'label','MCu2','color','blue')
TIA.addatom('r', [1/12 7/12 0],'S', 1,'label','MCu2','color','blue')
TIA.addatom('r', [1/12 8/12 0],'S', 1,'label','MCu2','color','blue')
TIA.addatom('r', [1/12 9/12 0],'S', 1,'label','MCu2','color','blue')
TIA.addatom('r', [1/12 10/12 0],'S', 1,'label','MCu2','color','blue')
TIA.addatom('r', [1/12 11/12 0],'S', 1,'label','MCu2','color','blue')
TIA.addatom('r', [2/12 0/12 0],'S', 1,'label','MCu2','color','blue')
TIA.addatom('r', [2/12 1/12 0],'S', 1,'label','MCu2','color','blue')
TIA.addatom('r', [2/12 2/12 0],'S', 1,'label','MCu2','color','blue')
TIA.addatom('r', [2/12 3/12 0],'S', 1,'label','MCu2','color','blue')
TIA.addatom('r', [2/12 4/12 0],'S', 1,'label','MCu2','color','blue')
TIA.addatom('r', [2/12 5/12 0],'S', 1,'label','MCu2','color','blue')
TIA.addatom('r', [2/12 6/12 0],'S', 1,'label','MCu2','color','blue')
TIA.addatom('r', [2/12 7/12 0],'S', 1,'label','MCu2','color','blue')
TIA.addatom('r', [2/12 8/12 0],'S', 1,'label','MCu2','color','blue')
TIA.addatom('r', [2/12 9/12 0],'S', 1,'label','MCu2','color','blue')
TIA.addatom('r', [2/12 10/12 0],'S', 1,'label','MCu2','color','blue')
TIA.addatom('r', [2/12 11/12 0],'S', 1,'label','MCu2','color','blue')
TIA.addatom('r', [3/12 0/12 0],'S', 1,'label','MCu2','color','blue')
TIA.addatom('r', [3/12 1/12 0],'S', 1,'label','MCu2','color','blue')
TIA.addatom('r', [3/12 2/12 0],'S', 1,'label','MCu2','color','blue')
TIA.addatom('r', [3/12 3/12 0],'S', 1,'label','MCu2','color','blue')
TIA.addatom('r', [3/12 4/12 0],'S', 1,'label','MCu2','color','blue')
```

```
TIA.addatom('r', [3/12 5/12 0],'S', 1,'label','MCu2','color','blue')
TIA.addatom('r', [3/12 6/12 0],'S', 1,'label','MCu2','color','blue')
TIA.addatom('r', [3/12 7/12 0],'S', 1,'label','MCu2','color','blue')
TIA.addatom('r', [3/12 8/12 0],'S', 1,'label','MCu2','color','blue')
TIA.addatom('r', [3/12 9/12 0],'S', 1,'label','MCu2','color','blue')
TIA.addatom('r', [3/12 10/12 0],'S', 1,'label','MCu2','color','blue')
TIA.addatom('r', [3/12 11/12 0],'S', 1,'label','MCu2','color','blue')
TIA.addatom('r', [4/12 0/12 0],'S', 1,'label','MCu2','color','blue')
TIA.addatom('r', [4/12 1/12 0],'S', 1,'label','MCu2','color','blue')
TIA.addatom('r', [4/12 2/12 0],'S', 1,'label','MCu2','color','blue')
TIA.addatom('r', [4/12 3/12 0],'S', 1,'label','MCu2','color','blue')
TIA.addatom('r', [4/12 4/12 0],'S', 1,'label','MCu2','color','blue')
TIA.addatom('r', [4/12 5/12 0],'S', 1,'label','MCu2','color','blue')
TIA.addatom('r', [4/12 6/12 0],'S', 1,'label','MCu2','color','blue')
TIA.addatom('r', [4/12 7/12 0],'S', 1,'label','MCu2','color','blue')
TIA.addatom('r', [4/12 8/12 0],'S', 1,'label','MCu2','color','blue')
TIA.addatom('r', [4/12 9/12 0],'S', 1,'label','MCu2','color','blue')
TIA.addatom('r', [4/12 10/12 0],'S', 1,'label','MCu2','color','blue')
TIA.addatom('r', [4/12 11/12 0],'S', 1,'label','MCu2','color','blue')
TIA.addatom('r', [5/12 0/12 0],'S', 1,'label','MCu2','color','blue')
TIA.addatom('r', [5/12 1/12 0],'S', 1,'label','MCu2','color','blue')
TIA.addatom('r', [5/12 2/12 0],'S', 1,'label','MCu2','color','blue')
TIA.addatom('r', [5/12 3/12 0],'S', 1,'label','MCu2','color','blue')
TIA.addatom('r', [5/12 4/12 0],'S', 1,'label','MCu2','color','blue')
TIA.addatom('r', [5/12 5/12 0],'S', 1,'label','MCu2','color','blue')
TIA.addatom('r', [5/12 6/12 0],'S', 1,'label','MCu2','color','blue')
TIA.addatom('r', [5/12 7/12 0],'S', 1,'label','MCu2','color','blue')
TIA.addatom('r', [5/12 8/12 0],'S', 1,'label','MCu2','color','blue')
TIA.addatom('r', [5/12 9/12 0],'S', 1,'label','MCu2','color','blue')
TIA.addatom('r', [5/12 10/12 0],'S', 1,'label','MCu2','color','blue')
TIA.addatom('r', [5/12 11/12 0],'S', 1,'label','MCu2','color','blue')
TIA.addatom('r', [6/12 0/12 0],'S', 1,'label','MCu2','color','blue')
TIA.addatom('r', [6/12 1/12 0],'S', 1,'label','MCu2','color','blue')
TIA.addatom('r', [6/12 2/12 0],'S', 1,'label','MCu2','color','blue')
TIA.addatom('r', [6/12 3/12 0],'S', 1,'label','MCu2','color','blue')
TIA.addatom('r', [6/12 4/12 0],'S', 1,'label','MCu2','color','blue')
```

```
TIA.addatom('r', [6/12 5/12 0],'S', 1,'label','MCu2','color','blue')
TIA.addatom('r', [6/12 6/12 0],'S', 1,'label','MCu2','color','blue')
TIA.addatom('r', [6/12 7/12 0],'S', 1,'label','MCu2','color','blue')
TIA.addatom('r', [6/12 8/12 0],'S', 1,'label','MCu2','color','blue')
TIA.addatom('r', [6/12 9/12 0],'S', 1,'label','MCu2','color','blue')
TIA.addatom('r', [6/12 10/12 0],'S', 1,'label','MCu2','color','blue')
TIA.addatom('r', [6/12 11/12 0],'S', 1,'label','MCu2','color','blue')
TIA.addatom('r', [7/12 0/12 0],'S', 1,'label','MCu2','color','blue')
TIA.addatom('r', [7/12 1/12 0],'S', 1,'label','MCu2','color','blue')
TIA.addatom('r', [7/12 2/12 0],'S', 1,'label','MCu2','color','blue')
TIA.addatom('r', [7/12 3/12 0],'S', 1,'label','MCu2','color','blue')
TIA.addatom('r', [7/12 4/12 0],'S', 1,'label','MCu2','color','blue')
TIA.addatom('r', [7/12 5/12 0],'S', 1,'label','MCu2','color','blue')
TIA.addatom('r', [7/12 6/12 0],'S', 1,'label','MCu2','color','blue')
TIA.addatom('r', [7/12 7/12 0],'S', 1,'label','MCu2','color','blue')
TIA.addatom('r', [7/12 8/12 0],'S', 1,'label','MCu2','color','blue')
TIA.addatom('r', [7/12 9/12 0],'S', 1,'label','MCu2','color','blue')
TIA.addatom('r', [7/12 10/12 0],'S', 1,'label','MCu2','color','blue')
TIA.addatom('r', [7/12 11/12 0],'S', 1,'label','MCu2','color','blue')
TIA.addatom('r', [8/12 0/12 0],'S', 1,'label','MCu2','color','blue')
TIA.addatom('r', [8/12 1/12 0],'S', 1,'label','MCu2','color','blue')
TIA.addatom('r', [8/12 2/12 0],'S', 1,'label','MCu2','color','blue')
TIA.addatom('r', [8/12 3/12 0],'S', 1,'label','MCu2','color','blue')
TIA.addatom('r', [8/12 4/12 0],'S', 1,'label','MCu2','color','blue')
TIA.addatom('r', [8/12 5/12 0],'S', 1,'label','MCu2','color','blue')
TIA.addatom('r', [8/12 6/12 0],'S', 1,'label','MCu2','color','blue')
TIA.addatom('r', [8/12 7/12 0],'S', 1,'label','MCu2','color','blue')
TIA.addatom('r', [8/12 8/12 0],'S', 1,'label','MCu2','color','blue')
TIA.addatom('r', [8/12 9/12 0],'S', 1,'label','MCu2','color','blue')
TIA.addatom('r', [8/12 10/12 0],'S', 1,'label','MCu2','color','blue')
TIA.addatom('r', [8/12 11/12 0],'S', 1,'label','MCu2','color','blue')
TIA.addatom('r', [9/12 0/12 0],'S', 1,'label','MCu2','color','blue')
TIA.addatom('r', [9/12 1/12 0],'S', 1,'label','MCu2','color','blue')
TIA.addatom('r', [9/12 2/12 0],'S', 1,'label','MCu2','color','blue')
TIA.addatom('r', [9/12 3/12 0],'S', 1,'label','MCu2','color','blue')
TIA.addatom('r', [9/12 4/12 0],'S', 1,'label','MCu2','color','blue')
```

```
129 TIA.addatom('r', [9/12 5/12 0],'S', 1,'label','MCu2','color','blue')
130 TIA.addatom('r', [9/12 6/12 0],'S', 1,'label','MCu2','color','blue')
131 TIA.addatom('r', [9/12 7/12 0],'S', 1,'label','MCu2','color','blue')
132 TIA.addatom('r', [9/12 8/12 0],'S', 1,'label','MCu2','color','blue')
133 TIA.addatom('r', [9/12 9/12 0],'S', 1,'label','MCu2','color','blue')
134 TIA.addatom('r', [9/12 10/12 0],'S', 1,'label','MCu2','color','blue')
135 TIA.addatom('r', [9/12 11/12 0],'S', 1,'label','MCu2','color','blue')
136 TIA.addatom('r', [10/12 0/12 0],'S', 1,'label','MCu2','color','blue')
137 TIA.addatom('r', [10/12 1/12 0],'S', 1,'label','MCu2','color','blue')
138 TIA.addatom('r', [10/12 2/12 0],'S', 1,'label','MCu2','color','blue')
139 TIA.addatom('r', [10/12 3/12 0],'S', 1,'label','MCu2','color','blue')
140 TIA.addatom('r', [10/12 4/12 0],'S', 1,'label','MCu2','color','blue')
141 TIA.addatom('r', [10/12 5/12 0],'S', 1,'label','MCu2','color','blue')
142 TIA.addatom('r', [10/12 6/12 0],'S', 1,'label','MCu2','color','blue')
143 TIA.addatom('r', [10/12 7/12 0],'S', 1,'label','MCu2','color','blue')
144 TIA.addatom('r', [10/12 8/12 0],'S', 1,'label','MCu2','color','blue')
145 TIA.addatom('r', [10/12 9/12 0],'S', 1,'label','MCu2','color','blue')
146 TIA.addatom('r', [10/12 10/12 0],'S', 1,'label','MCu2','color','blue')
147 TIA.addatom('r', [10/12 11/12 0],'S', 1,'label','MCu2','color','blue')
148 TIA.addatom('r', [11/12 0/12 0],'S', 1,'label','MCu2','color','blue')
149 TIA.addatom('r', [11/12 1/12 0],'S', 1,'label','MCu2','color','blue')
150 TIA.addatom('r', [11/12 2/12 0],'S', 1,'label','MCu2','color','blue')
151 TIA.addatom('r', [11/12 3/12 0],'S', 1,'label','MCu2','color','blue')
152 TIA.addatom('r', [11/12 4/12 0],'S', 1,'label','MCu2','color','blue')
153 TIA.addatom('r', [11/12 5/12 0],'S', 1,'label','MCu2','color','blue')
154 TIA.addatom('r', [11/12 6/12 0],'S', 1,'label','MCu2','color','blue')
155 TIA.addatom('r', [11/12 7/12 0],'S', 1,'label','MCu2','color','blue')
156 TIA.addatom('r', [11/12 8/12 0],'S', 1,'label','MCu2','color','blue')
157 TIA.addatom('r', [11/12 9/12 0],'S', 1,'label','MCu2','color','blue')
158 TIA.addatom('r', [11/12 10/12 0],'S', 1,'label','MCu2','color','blue')
159 TIA.addatom('r', [11/12 11/12 0],'S', 1,'label','MCu2','color','blue')
160
161 TIA.plot('range',[1 1 1])
162
163 %% Determine the list of bonds based on length
164 % To consider bonds up to 7 Angstrom length we use the sw.gencoupling()
```

```
% function. Since no symmetry operators are defined, it sorts all bonds
% according to increasing length, all bonds are equivalent that has the
% same length within an error bar.

TIA.gencoupling('maxDistance',8)

% list the 1st and 2nd neighbor bonds
TIA.table('bond',1:3)

%% Defining the spin Hamiltonian
 % We create a matrix with a label 'Ja', an antiferromagnetic heisenberg
% interaction, J = 1 meV and assing it to the first neghbor bonds as
% spin-spin exchange interaction. And plot the crystal
% structure with the added bonds.

TIA.addmatrix('value',eye(3),'label','Ja','color','green')

TIA.addcoupling('mat','Ja','bond',1);
plot(TIA,'range',[1 1 0.5],'cellMode','none','baseMode','none')
% To prevent the structure optimisation routines from destroying the
% 'unstable' frustrated system, we need to add in a single-ion anisotropy
% term
D = -100;
TIA.addmatrix('value',D*[0 0 0 ; 0 0 0 ; 0 0 1],...
               'label','D1','color','r');
TIA.addaniso('D1');

%% Definition of TIA magnetic structure
% We read in the spin vectors based on modelling the supercell using a
% FORTRAN script

k=1;
zeros = zeros([1 144]);
%up = ones([1 144])
fileID = fopen(strcat('CsCoCl3_spinw_01.txt'),'r');
formatSpec = '%d';
```

```
spins = fscanf(fileID,formatSpec);
fclose(fileID);
spins=spins.';

TIA.genmagstr('mode','direct', 'k',[0 0 0],'n',[0 0 1],'S',[zeros; zeros; spins], '
    nExt',0.01);

disp('Magnetic structure:')
TIA.table('mag')

%% The energy of the ground state per spin
% The spinw.energy() function gives the ground state energy per spin, the
% value is dynamically calculated at every call.

energy1 = TIA.energy;
TIA.optmagsteep('nRun',1e3);
energy2 = TIA.energy;

fprintf('\n Energy before optimisation: %0.4f \n',energy1)
fprintf(' Energy after optimisation: %0.4f \n',energy2)

if (abs(energy1 - energy2) > 0.001)
    DISP('Warning - magnetic structure changed by optmagsteep....')
end

%% Calculate spin wave dispersion and spin-spin correlation function
% We calculate spin wave dispersion and correlation function along the
% chain, momentum transfer value is Q = (H 0 0). Then we calculate the
% neutron scattering cross section and select 'Sperp' the neutron
% scattering intensity for plotting. Then we plot spin wave dispersion and
% the value of the correlation function with the 1-Q^2 neutron scattering
% cross section in units of hbar/spin.

TIAspec = TIA.spinwave({[0 0 0] [1/2 1/2 0] [1/2 0 0] [0 0 0]},'hermit',false, '
    saveV', true,'saveH',true);
TIAspec = sw_neutron(TIAspec);
```

```
TIAspec = sw_egrid(TIAspec,'component','Sperp','imagChk',false);

figure;
sw_plotspec(TIAspec,'mode',1,'colormap','vik')
axis([0 5 0 100])

%% Calculate powder average spectrum
% We calculate powder spectrum for Q = 0:2.5 Angstrom^-1 100 steps
% resolution 1000 random Q points for every step. Then we plot the spectrum
% convoluted with 0.1 meV Gaussian along energy.

TIApowspec = TIA.powspec(linspace(0,2.5,100),'Evect',linspace(0,4.5,250),'nRand'
    ,1000,'hermit',false);
figure;
sw_plotspec(TIApowspec,'dE',0.1)
axis([0 2.5 0 4.5]);
caxis([0 .05]);

%% Output V and D matrices to suitable files
% We extract the dynamical matrix as the 'H' matrix produced by SpinW,
% the eigenvectors and values of this matrix at k=0 are the values we
% require for band unfolding.
dynmat = TIAspec.H(1:144,1:144,1);
[V,D] = eig(dynmat);
eigvals = diag(D);
writematrix(V,'eigenvectors_tia12_4.txt','Delimiter','space');
fileID = fopen('eigenvalues_tia12_4.txt','w');
fprintf(fileID,'%8.6f \n',eigvals);
fclose(fileID)
```

Listing 1: SpinW code example

Appendix C

C1 Python code used for supercell spin dynamics calculations

```
import pandas as pd
import numpy as np
import itertools
%matplotlib inline
%pylab inline
%timeit
import cmath
import os
from matplotlib import rc
rc('font',**{'family':'serif','serif':['Times New Roman']})
rc('mathtext',**{'it':'Times New Roman:italic','rm':'serif','sf':'serif','bf':'
    serif','fallback_to_cm':'False','tt':'serif'})
plt.rcParams.update({'font.size': 15})

num_struct = 50
for numconf in range(num_struct):
    print(type(numconf))
    numcells = 144
    atomspercell = 1
    location = os.getcwd() + '/PDA/eigenvalues_pda12_%s.txt' % str(numconf)
    print(location)
    n=int(numcells*atomspercell)
    #gammatox = np.zeros((200,numatoms),dtype=np.float)

```

```
    p = np.zeros((n,n,n),dtype=np.complex)
    eigvec = np.zeros(n, dtype=np.float)

    try:
        eigval = np.asarray(pd.read_csv(location, header = None))
        #eigval = np.asarray(eigvaldf)
        #eigval = np.hsplit(eigval,numatoms)
        #eigval = 50 * eigval
        print(eigval.shape)
        #print('File exists '+location)
    except:
        print('File does not exist.')

    location = os.getcwd() + '/PDA/eigenvectors_pda12_%s.txt' % str(numconf)
    try:
        eigvec = np.loadtxt(location,delimiter=' ')
    except:
        print('File does not exist.2')

    eigvec = np.transpose(eigvec)
    print(eigvec.shape)

    pk = np.zeros((n,n,n),dtype=np.float)
    kvec=np.zeros(2, dtype=np.float)

    l = int(sqrt(n))
    r = np.zeros((n,2), dtype=np.integer)
    k = np.zeros((n,2), dtype=np.float)
    i=0
    for y in range(l):
        for x in range(l):
            r[i,0] = x
            r[i,1] = y
            if x/l > 0.5:
                k[i,0] = 0.5 - x/l
            else:
```

```
60                  k[i,0] = x/l
61              if y/l > 0.5:
62                  k[i,1] = 0.5 - y/l
63              else:
64                  k[i,1] = y/l
65              i+=1
66      #print(k,r)
67      a=0
68      kr = np.zeros(n**2, dtype=np.float)
69      for i in range(n):
70          for j in range(n):
71              kr[a]=k[i].dot(r[j])
72              a+=1
73      kr = kr.reshape(n,n)
74
75
76      modesum=np.zeros((n,n), dtype=np.float)
77
78      modesumc=np.zeros((n,n), dtype=np.complex)
79      ksum=np.zeros((n,n), dtype=np.float)
80
81      for i in range(n):
82          a=0
83          for j in range(n):
84              for l in range(n):
85                  p[i,j,l] = eigvec[j,l] * cmath.exp(complex(0,2*math.pi*kr[i,l]))
86
87              #modesum[i,j]=sum(real(p[i,j])) + sum(imag(p[i,j]))
88              modesumc[i,j]=sum(p[i,j])
89              modesum[i,j]=abs(modesumc[i,j])**2
90              modesum[i,j] = round((modesum[i,j]),3)
91              #if dp3 !=0.00:
92                  #print('Mode ',j,' is non-zero',modesum[i,j], dp3)
93                  #ksum[i,j]=ksum[i,j]+modesum[i,j]
94                  #print('')
95      #print(ksum.shape)
```

```
    for i in range(n):
        modesum[i]=modesum[i]/sum(modesum[i])
        #print(modesum[i],sum(modesum[i]))
    binwidth = 0.2
    Emax = 207
    Emin = 192
    nbins = int((Emax-Emin)/binwidth)
    if numconf==0:
        Ebin = np.zeros((n,nbins), dtype=np.float)
        Ebinx = np.zeros((n,nbins), dtype=np.float)
        DensityOfStates = np.zeros((nbins), dtype=np.float)
        DoStmp = np.zeros((nbins), dtype=np.float)
        DoSErr = np.zeros((nbins), dtype=np.float)
    Ebinx.fill(0)
    DoStmp.fill(0)
    for i in range(n):
        dosx = int((eigval[i]-Emin)/binwidth)
        DoStmp[dosx]+=1
        for j in range(n):
            m = int((eigval[j]-Emin)/binwidth)
            if m > nbins:
                m=nbins-1
            Ebinx[i,m]=Ebinx[i,m]+modesum[i,j]
            #print(Ebin[i],k[i])
            #print(sum(Ebin[i]))
    Ebin=Ebin + Ebinx
    DensityOfStates= DensityOfStates + DoStmp
    DoSErr = DoSErr + DoStmp**2
    #print(sum(Ebin[i]))

Ebin=Ebin/(num_struct)
DensityOfStates=DensityOfStates/(num_struct)
DoSErr = DoSErr - (num_struct*DensityOfStates**2)
DoSErr = DoSErr/(num_struct-1)
DoSErr = sqrt(DoSErr)

```

```
from scipy import interpolate
from sklearn import metrics
histox=[]
histoy=[]
for i in range(nbins):
    if isnan((sum(Ebin[:,i])/i)):
        histox.append(0)
    else:
        histox.append((sum(Ebin[:,i])/i))
    histoy.append((i*binwidth))
f = interpolate.interp1d(histoy,histox,fill_value=0)
xnew = np.arange(0, (nbins)*binwidth, 0.2)
ynew = f(xnew)
plt.plot(ynew,xnew)#, linestyle='-',marker='None')
plt.ylabel(r'E (meV)')
plt.xlabel(r'g($\omega$)')
axes=plt.gca()
axes.set_ylim([0,15])
axes.set_xlim([0,0.35])
ylocator = MultipleLocator(2)
axes.xaxis.set_ticks_position('both')
axes.yaxis.set_ticks_position('both')
axes.tick_params(which='minor',direction='in', length=4)
axes.tick_params(which='major',direction='in', length=6, pad=10)
axes.yaxis.set_major_locator(ylocator)
print(metrics.auc(histoy,histox))
plt.savefig('Figures/PDA_12_50Avg_hist.eps',format='eps', dpi=1000, transparent=
    True,bbox_inches='tight')

j,m,l,u,v,w=0,0,0,0,0,0

gk_x=np.full((nbins*int(sqrt(n)+1),3),nan, dtype=np.float)
k_xk_y=np.full((nbins*int(sqrt(n)+1),3),nan, dtype=np.float)
k_yg=np.full((nbins*int(sqrt(n)+1),3),nan, dtype=np.float)
gm=np.full((nbins*int(sqrt(n)+1),3),nan, dtype=np.float)
mk_y=np.full((nbins*int(sqrt(n)+1),3),nan, dtype=np.float)
```

```
Ebin = Ebin/Ebin.max()
#[0,0] to [1/2,0]
for i in range(n):
    if k[i,0]==0 and k[i,1]==0:
        for ee in range(nbins):
            if Ebin[i,ee]!=0:
                #print(ee*binwidth,k[i])
                gk_x[j,0]=ee*binwidth #Abs energy
                gk_x[j,1]=k[i,0] #k point
                gk_x[j,2]=Ebin[i,ee] #Energy density
                j+=1
        for ee in range(nbins):
            if Ebin[i,ee]!=0:
            #print(ee*binwidth,k[i])
                k_yg[u,0]=ee*binwidth
                k_yg[u,1]=1/2
                k_yg[u,2]=Ebin[i,ee]
                u+=1
        ###for ee in range(nbins):
        ###         if Ebin[i,ee]!=0:
        ###             gm[v,0]=ee*binwidth
        ###             gm[v,1]=k[i,1]
        ###             gm[v,2]=Ebin[i,ee]
        ###             v+=1

    elif k[i,0]>0 and k[i,1]==0:
        #print(Ebin[i],k[i])
        if k[i,1]==0 and k[i,0]==0.5:
            for ee in range(nbins):
                if Ebin[i,ee]!=0:
                    #print(ee*binwidth,k[i])
                    gk_x[j,0]=ee*binwidth
                    gk_x[j,1]=k[i,0]
                    gk_x[j,2]=Ebin[i,ee]
                    j+=1
            for ee in range(nbins):
```

```
                if Ebin[i,ee]!=0:
                    k_xk_y[m,0]=ee*binwidth
                    k_xk_y[m,1]=k[i,1]
                    k_xk_y[m,2]=Ebin[i,ee]
                    m+=1
        else:
            for ee in range(nbins):
                if Ebin[i,ee]!=0:
                    #print(ee*binwidth,k[i])
                    gk_x[j,0]=ee*binwidth
                    gk_x[j,1]=k[i,0]
                    gk_x[j,2]=Ebin[i,ee]
                    j+=1
            #if k[i,1]==0 and k[i,0]==0:
            #    for ee in range(nbins):
            #        if Ebin[i,ee]!=0:
            #            #print(ee*binwidth,k[i])
            #            gk_x[j,0]=ee*binwidth
            #            gk_x[j,1]=k[i,0]
            #            gk_x[j,2]=Ebin[i,ee]
            #            j+=1
    #[1/2,0] to [0,1/2]
    elif k[i,0]>0 and k[i,1]>0:
        for s in range(int(sqrt(n)/2)):
            if round(k[i,0],4)==round((0.5-(s/sqrt(n))),4) and round(k[i,1],4)==
    round((0+(s/sqrt(n))),4):
                for ee in range(nbins):
                    if Ebin[i,ee]!=0:
                        k_xk_y[m,0]=ee*binwidth
                        k_xk_y[m,1]=round(s/sqrt(n),4)
                        k_xk_y[m,2]=Ebin[i,ee]
                        m+=1
    elif k[i,0]==0 and k[i,1]>0:
        #print(k[i,1])
        if k[i,0]==0 and k[i,1]==0.5:
            for ee in range(nbins):
```

```
                if Ebin[i,ee]!=0:
                    k_xk_y[m,0]=ee*binwidth
                    k_xk_y[m,1]=k[i,1]
                    k_xk_y[m,2]=Ebin[i,ee]
                    m+=1
            for ee in range(nbins):
                if Ebin[i,ee]!=0:
            #print(ee*binwidth,k[i])
                    k_yg[u,0]=ee*binwidth
                    k_yg[u,1]=k[i,0]
                    k_yg[u,2]=Ebin[i,ee]
                    u+=1
        else:
            for ee in range(nbins):
            #print(Ebin[i,ee])
                if Ebin[i,ee]!=0:
                #print(ee*binwidth,k[i])
                    k_yg[u,0]=ee*binwidth
                    k_yg[u,1]=1/2 - k[i,1]
                    k_yg[u,2]=Ebin[i,ee]
                    u+=1

fig, ax = plt.subplots(nrows=1,ncols=3,sharey=True)
fig.subplots_adjust(wspace=0)
rgb = np.ones((len(gk_x),3))
rgb1 = np.ones((len(k_xk_y),3))
rgb2 = np.ones((len(k_yg),3))

for j in range(len(gk_x)):
#print(j)
    if (gk_x[j,2]>1):
        rgb[j,2]=0
        rgb[j,0]=0
        rgb[j,1]=0
    elif (np.isnan(gk_x[j,2])):
        rgb[j,2]=1
```

```
        rgb[j,0]=1
        rgb[j,1]=1
    else:
        rgb[j,0]=1-(1*(gk_x[j,2]))
        rgb[j,1]=1-(1*(gk_x[j,2]))
        rgb[j,2]=1-(1*(gk_x[j,2]))

    if (k_xk_y[j,2]>1):
        rgb1[j,2]=0
        rgb1[j,0]=0
        rgb1[j,1]=0
    elif (np.isnan(k_xk_y[j,2])):
        rgb1[j,2]=1
        rgb1[j,0]=1
        rgb1[j,1]=1
    else:
        rgb1[j,0]=1-(1*(k_xk_y[j,2]))
        rgb1[j,1]=1-(1*(k_xk_y[j,2]))
        rgb1[j,2]=1-(1*(k_xk_y[j,2]))

    if (k_yg[j,2]>1):
        rgb2[j,2]=0
        rgb2[j,0]=0
        rgb2[j,1]=0
    elif (np.isnan(k_yg[j,2])):
        rgb2[j,2]=1
        rgb2[j,0]=1
        rgb2[j,1]=1
    else:
        #print(k_yg[j,2])
        rgb2[j,0]=1-(1*(k_yg[j,2]))
        rgb2[j,1]=1-(1*(k_yg[j,2]))
        rgb2[j,2]=1-(1*(k_yg[j,2]))

    ax[0].bar((gk_x[j,1]),binwidth,facecolor=rgb[j],bottom=(gk_x[j,0]),width=1/sqrt
    (n))
```

```
309     ax[1].bar((k_xk_y[j,1]),binwidth,facecolor=rgb1[j],bottom=(k_xk_y[j,0]),width
        =1/sqrt(n))
310     ax[2].bar((k_yg[j,1]),binwidth,facecolor=rgb2[j],bottom=(k_yg[j,0]),width=1/
        sqrt(n))
311
312 #for j in range(len(k_xk_y)):
313 #print(j)
314
315
316 #for j in range(len(k_yg)):
317 #print(j)
318
319
320 for xx in range(3):
321     ax[xx].set_xlim([0,0.5])
322     ax[xx].set_ylim([Emin-Emin,Emax-Emin])
323     majorLocator = MultipleLocator(0.25)
324     ax[xx].xaxis.set_major_locator(majorLocator)
325     ax[xx].xaxis.set_ticks_position('both')
326     ax[xx].yaxis.set_ticks_position('both')
327     ax[xx].tick_params(which='minor',direction='in', length=4)
328     ax[xx].tick_params(which='major',direction='in', length=6, pad=10)
329 ax[0].set_xticks(np.arange(0.0, 0.75, 0.25))
330 ax[1].set_xticks(np.arange(0.25, 0.5, 0.25))
331 ax[2].set_xticks(np.arange(0.0, 0.75, 0.25))
332 ylocator = MultipleLocator(2)
333 ax[0].yaxis.set_major_locator(ylocator)
334 ax[0].set_xlabel(r'$\xi\;$ in: $(\xi,\,0)$')
335 ax[1].set_xlabel(r'$(1/2-\xi,\,\xi)$')
336 ax[2].set_xlabel(r'$(0,\,1/2 - \xi)$')
337 fig.suptitle('PDA 12x12 - 50 Config. Average')
338
339 plt.savefig('Figures/PDA_12_50Avg.eps',format='eps', dpi=1000, transparent=True,
        bbox_inches='tight')
```

Listing 2: Supercell spin dynamics (SCSD) code